Relative Trajectory Design and Control near Periodic Orbits in Multi-Body Systems using Local Toroidal Coordinates

by

Ian Lee Elliott

B.S., Aerospace Engineering, Virginia Tech, 2017

M.S., Aerospace Engineering Sciences, University of Colorado, 2019

A thesis submitted to the
Faculty of the Graduate School of the
University of Colorado in partial fulfillment
of the requirements for the degree of
Doctor of Philosophy
Ann and H.J. Smead Department of Aerospace Engineering Sciences
2022

Committee Members:
Natasha Bosanac, Chair
James D. Meiss
Hanspeter Schaub
Daniel J. Scheeres
Jeffrey R. Stuart

Elliott, Ian Lee (Ph.D., Aerospace Engineering Sciences)

Relative Trajectory Design and Control near Periodic Orbits in Multi-Body Systems using Local Toroidal Coordinates

Thesis directed by Prof. Natasha Bosanac

Spacecraft activity in multi-body environments is likely to expand to include the operation of multiple spacecraft in close proximity to conduct tasks such as rendezvous, docking, and station-keeping of specific configurations for scientific observations. Quasi-periodic orbits have been identified as a useful dynamical structure for locating natural bounded motions for spacecraft to reduce propellant usage during proximity operations. However, the computation of quasi-periodic orbits in even approximate dynamical models of a multi-body system is generally a complex process. Thus, in this dissertation, new coordinate systems are introduced to describe motion relative to a periodic orbit that are derived from the first-order approximation of an invariant curve associated with a nearby invariant 2-torus in the circular restricted three-body problem. The introduced coordinates are variations of modal coordinates which possess similar definitions to local toroidal coordinate systems previously applied in other disciplines. A key advantage of the coordinates is that motion within a center eigenspace of a periodic orbit is constant over time in a linearized dynamical model and motion near the center eigenspace in a nonlinear dynamical model is slowly time-varying. To further support the use of quasi-periodic orbits for relative trajectory design, strategies to characterize the first-order approximation of an invariant curve and define bounds of possible motion within the center eigenspace are presented. Finally, several strategies for the control of spacecraft near periodic orbits are formulated using the introduced coordinate systems, including continuous feedback control strategies and impulsive control strategies. Throughout this investigation, the presented spacecraft control strategies are evaluated in higher-fidelity, ephemeris models of spacecraft motion in a multi-body environment.

Dedication

To Mom and Dad. Now there is another response to “which Dr. Elliott?”

Acknowledgements

I would like to distinctly thank Prof. Bosanac for the incredible amount of guidance and support you have given me over these past years. Thank you for introducing me to so many interesting research topics and people. I would also like to thank everyone on my committee for your feedback and direction in guiding this work, Dr. Black for your mentorship and support during such a pivotal time in my career, and Roger for your continued friendship.

I have been endlessly supported by so many people during my time in Boulder. I have learned so much, both inside and outside of school, from my friends. Jack, Stefano, Thomas, Kristen, Renee, and Giuliana, thank you all for your friendships and invaluable feedback. I would like to express my particular gratitude to Jack for all our discussions and for tirelessly listening to every single one of my research ideas over the last five years. Thank you Mark, Luke, Erica, Kieran, Don, Hermann, Ken, Spencer, and many others too numerous to list for your friendships. I am also very grateful for the members of ORCCA who befriended and helped our emerging research group during the early semesters when we shared our basement lab space. I cannot thank Lubna enough, who is not only an ORCCA peer and trusted source of advice, but also a truly wonderful partner. I am so excited to keep exploring space with you. And finally to my parents, thank you for your never-ending love and support. Nothing that I've accomplished would have been possible without you.

I also gratefully acknowledge the Graduate Assistance in Areas of National Need Fellowship from the Smead Aerospace Engineering Sciences Department and the Beverly Sears Graduate Student Grant from the University of Colorado Boulder for supporting this work.

Contents

Chapter

Tables

Table

Figures

Figure

Chapter 1

Introduction

The near-future of space activity will include a significant increase in missions beyond the primary gravitational influence of a single celestial body. In multi-body systems, such as the Earth-Moon and Sun-Earth systems, bounded orbits enable long-term perspectives of various scientific phenomena. Trajectories in these multi-body environments that remain bounded over time may resemble periodic orbits or quasi-periodic orbits that are derived from approximate dynamical models such as the circular restricted three-body problem (CR3BP). Formations of spacecraft near these reference orbits also enable distributed architectures to support science objectives that require multi-point measurements as well as the in-space assembly and servicing of space assets. Yet, the relative motion between multiple spacecraft located near these bounded motions is much more complex than relative motion in two-body environments and is not currently well-understood. Thus, this research focuses on supporting formations operating near periodic orbits by using insight from dynamical structures that exist in the CR3BP to introduce a new framework for the characterization and control of relative motion near periodic orbits.

1.1 Motivation and background

Missions that involve spacecraft operating in multi-body gravitational environments and beyond the primary gravitational influence of the Earth have been of increasing interest for scientific, technological, and exploration purposes. Early use of periodic orbits that exist within the CR3BP have been leveraged in the trajectory design of previous scientific missions include the International

Sun-Earth Explorer-3 (ISEE-3) and the Solar and Heliospheric Observatory (SOHO) [1]. Recently, periodic orbits and quasi-periodic orbits in the CR3BP have been leveraraged in the design of the trajectories for space-based observatories and telescopes including the Deep Space Climate Observatory (DSCOVR) [2], the James Webb Space Telescope [3], and the upcoming Nancy Grace Roman Space Telescope [4, 5]. To support and extend the lifetime of space assets located near periodic orbits, in-space assembly within the Earth-Moon and Sun-Earth multi-body environments has been identified as a key technology [6, 7]. Additional assets such as servicing vehicles, supplementary components, or starshades may rendezvous with or maintain a desired path relative to the primary spacecraft [8, 9].

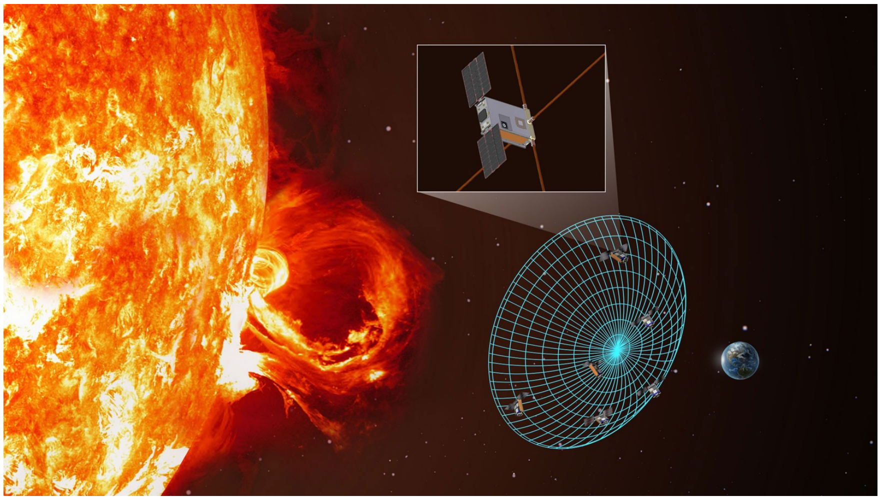

Figure 1.1: Conceptual image of the space-based interferometer formed by the six spacecraft of the SunRISE mission flying in close proximity about a supersynchronous Earth orbit [10].

Constellations of closely-clustered spacecraft are emerging as an enabling technology to form space-based interferometers [11]. Spacecraft constellation operating in multi-body environments may provide unqiue perspectives of points of scientific interest. Proposed missions emplying distributed space systems in multi-body environments include Terrestrial Planet Finder [12], MAXIM [13], Stellar Imager [14], and Darwin [15]. These concepts focused on placing formations of spacecraft in multi-body environments to search for potentially habitable planets, study stellar magnetic activity, and achieve other scientific objectives. In these scenarios, generalized and geometrically-interpretable insight into the relative motion between spacecraft in these complex dynamical environments may be useful to support the development of proximity operation guidelines and formation flying guidance and control schemes.

A notable application of spacecraft formation flying near periodic orbits is the upcoming Gateway space station. As a component of NASA's Artemis program, Gateway is currently planned to include a crewed space station operating in an Earth-Moon near-rectilinear halo orbit (NRHO) and serving as a hub for travel to and from Earth and the lunar surface [16, 17]. Gateway, and spacecraft that will likely rendezvous and dock with it, have inspired a surge of interest and research into relative motion and control near periodic orbits in multi-body systems. Similar to the International Space Station, Gateway will provide an experimental proving ground for space technology within a chaotic, multi-body environment, with the first modules of the station expected to be launched in the mid-2020s [18]. As activity near Gateway increases, and practical experience of formation flying at periodic orbits is gained, formation flying strategies near periodic orbits in multi-body systems may continue to be a significant and relevant topic in astrodynamics research.

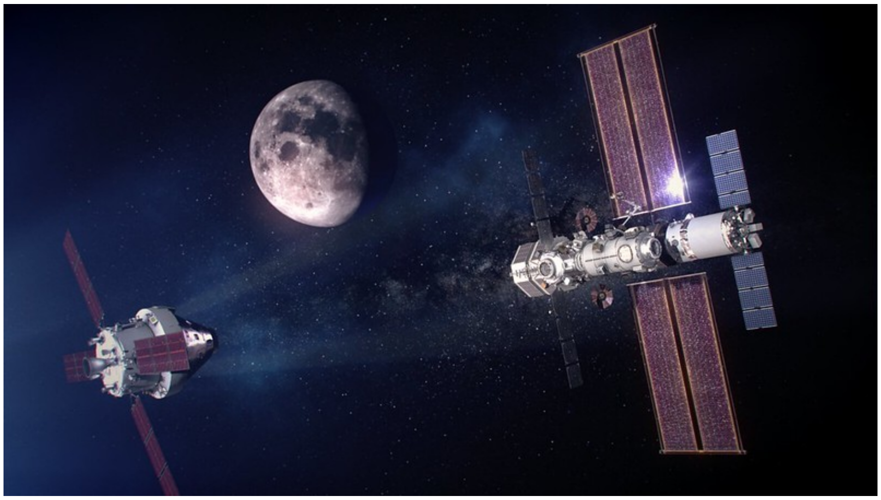

Figure 1.2: Conceptual image of the Orion spacecraft rendezvousing with Gateway located on an Earth-Moon NRHO [19].

1.2 Previous contributions

The study of spacecraft motion in multi-body environments includes early investigation into the three-body problem, including works by Euler [20], Poincaré [21], and Lagrange [22], to modern, state-of-the-art analyses for the Artemis program and other upcoming endeavors. In this section, an overview of previous contributions on the topics of relative trajectory design and control strategies near periodic orbits in multi-body environments is presented.

1.2.1 Leveraging the CR3BP in spacecraft trajectory design

The CR3BP is employed in this investigation as a fundamental approximate model of the motion of spacecraft due to the gravity of two primaries. Thorough analyses of the CR3BP and the solution space admitted by this autonomous dynamical model have been conducted in the astrodynamics community [23, 24]. In addition to the CR3BP, other variations of approximate models of spacecraft dynamics in multi-body environments have been studied, including the elliptic restricted three-body problem [25] and bicircular restricted four-body problem [26]. While these models offer increases in the fidelity of spacecraft dynamical modelling, the CR3BP often supplies a useful, autonomous approximation of spacecraft motion in ephemeris models with additional perturbations [27, 28, 29]. In fact, solutions of the CR3BP have seen widespread use within the trajectory design of many spacecraft missions due to the approximate retention of solutions of the CR3BP within higher-fidelity, ephemeris dynamical models [30].

The CR3BP admits several fundamental solutions, including five equilibrium points and an infinite variety of periodic and quasi-periodic orbits. Periodic orbits in the CR3BP have been identified as advantageous locations for the placement of spacecraft in cislunar space by Farquhar [31], Breakwell and Brown [32], and Howell [33]. Trajectories resembling periodic orbits in the vicinity of the Sun-Earth L_1 and L_2 equilibrium points have also been identified as favorable locations for the placement of spacecraft for scientific observations [34]. In fact, since SOHO began operation at a Sun-Earth L_1 halo orbit in 1996, spacecraft have been continuously operated in mission orbits that resemble periodic orbits [35]. In addition to periodic orbits, quasi-periodic orbits in the CR3BP have been employed within the trajectory design of several spacecraft missions, such as Advanced Composition Explorer (ACE) [36] and the Wilkinson Microwave Anisotropy Probe (WMAP) [37], to achieve a diversity of scientific perspectives. Due to the relevance of periodic orbits and quasi-periodic orbits in the design of spacecraft trajectories in multi-body environments, these types of solution are a primary focus of this investigation.

1.2.2 Analysis of motion relative to periodic orbits

Spacecraft formations have been operating near the Earth for decades [38] and in low lunar orbit during the Apollo missions [39]. In these regimes, where the two-body problem offers a useful approximate dynamical model, the relative motion between two spacecraft and perturbation models are well-understood using equations of relative motion expressing the motion of a chaser spacecraft relative to a target spacecraft [40, 41]. In fact, linearization of dynamics about circular and elliptical orbits have enabled the development of widely-used approximate models of relative motion, such as the Clohessy-Wiltshire equations [42] and Tschauner-Hempel equtions [43]. Additionally, in two-body environments, the relative state between spacecraft is often expressed in a local-vertical, local horizontal (LVLH) coordinate frame defined by the target spacecraft relative to the primary body [41]. Relative orbital element sets and geometry-based coordinate sets may also be used in two-body environments to introduce geometric insight into the description of spacecraft relative motion [44, 45]. For instance, Keplerian orbital element differences between spacecraft within a formation admit relative state representations with a constant description in the two-body problem and vary slowly with time in perturbed environments [46]. These slowly-varying state descriptions are particularly useful for formation flying guidance and control stategies [47, 48, 49]. Dynamical systems theory-based approaches have also been applied for relative trajectory design about orbits in two-body environments [50]. Comprehensive surveys compiled by Carter [51] and Sullivan et al. [52] capture the state-of-the-art of relative motion models in predominantly two-body environments.

Relative motion in multi-body environments is significantly more complex to examine than in Keplerian regimes due to the chaotic nature of the underlying solution space; as a result, there is currently less heuristic insight into relative motion in these environments. Investigations into the impact of third-body gravitational perturbations on spacecraft formations have been examined via conic-based differential orbital elements [53] and hybrid orbital element systems [54]. However, as general trajectories in multi-body systems are not well-approximated by conics, they are often analyzed in a rotating frame defined by two celestial bodies using approximated dynamical models such as the CR3BP [55, 56]. Nonlinear and linear equations of relative motion formulated in an LVLH frame defined by a target spacecraft relative to a primary body of a three-body environent have also been introduced for spacecraft governed by the CR3BP [57]. In Hamiltonian systems, action-angle coordinates are a fundamental method for describing states that lie on the surface of a torus [58]. However, in multi-body gravitational environments, numerically computing these coordinates via normal form expansions tends to be computationally intensive [59, 60]. Ultimately, the sensitivity and variety of the solution space for relative trajectory design in three-body environments still presents challenges for the extraction of meaningful heuristics.

The analysis of motion relative to periodic orbits constrains the solution space to the analysis of motion about a time-periodic solution. Thus, the application of Floquet theory is useful for gaining insight into the relative motion about periodic orbits in the context of the stability and local manifolds of the periodic orbit [61, 62]. Notably, the Floquet modes of a periodic orbit may be used to construct a basis for a set of modal coordinates which express the projection of the relative state of a chaser spacecraft along each eigenspace of the orbit [63]. These modal coordinates supply intuition into relative motion about periodic orbits, however, geometric insight into the exact relative configuration of spacecraft may still remain difficult to extract.

To reduce propellant requirements, a key focus for spacecraft formation flying is the identification of naturally bounded relative motion [64, 65]. In two-body environments, the design of such trajectories is well understood using insight from Keplerian orbital elements and the Clohessy-Wiltshire equations. In multi-body environments, quasi-periodic orbits that exist in the vicinity of periodic orbits have been historically identified as a useful mechanism for locating passive bounded motions for spacecraft formations [66]. However, quasi-periodic motions possess complex and time-varying descriptions relative to periodic orbits when expressed using Cartesian coordinates. Furthermore, as demonstrated by previous investigations, including works by Gomez et al. [67], Jorba and Masdemont [68], Kolemen et al. [69], and Olikara and Scheeres [70], the computation of quasi-periodic orbits in the nonlinear CR3BP is generally an expensive numerical process. Investigations by Barden and Howell [71, 72, 73] demonstrate that spacecraft following quasi-periodic orbits in the CR3BP remain naturally bounded and exhibit quasi-periodic motion relative to an associated periodic orbit. Further investigation by Howell and Marchand [74] determine that first-order approximations of invariant tori supply sufficient representations of solutions that exist in the local neighborhood of a periodic orbit in the nonlinear CR3BP, as well as in higher fidelity ephemeris models. Building upon these works, additional investigations into relative trajectory design have used invariant tori in a variety of nonlinear gravitational models and scenarios [75, 76, 77, 78, 79]. These results motivate leveraging approximations of quasi-periodic motion as computationally-inexpensive mechanisms for studying bounded relative motion for formation flying near periodic orbits in multi-body systems.

To leverage the geometry of invariant tori that exist near periodic orbits that possess an oscillatory mode in trajectory design and analysis, this investigation uses variations of toroidal coordinate systems. Toroidal coordinates are common tool used within the study of magnetic fields [80] and plasma confinement [81]. In this investigation, formulations of local toroidal coordinates are employed to describe the state of a spacecraft relative to a spacecraft or reference trajectory following a periodic orbit that possesses an oscillatory mode. Investigation of the first-order approximation of invariant tori relative to a periodic orbit reveals an elliptical cross section, i.e., a first-order approximation of an invariant curve. Thus, the local toroidal coordinates share similarities with previously defined elliptical local toroidal coordinate systems [82].

To study the elliptical geometry of the first-order approximation of the invariant curve relative to a periodic orbit, singular value decomposition (SVD) is employed throughout this investigation. The mathematical concept of an SVD has been used in a variety of applications to gain geometric insight into flow properties, linear transformations, and data that exist within a hyperellipse [83]. In the study of astrodynamics, SVD has been employed to examine stretching distances between nearby trajectories using the SVD of the Cauchy-Green tensor [84, 85, 86] and to identify regions of low relative drift [87]. In this investigation, SVD is used to analytically determine the principal axes of the instantaneous approximation of the invariant curve associated with an invariant torus to extract information on the size and shape relative to a periodic orbit. One application of this analysis is to construct a set of parameters to describe the size, shape, and orientation of the approximated invariant curve relative to the periodic orbit. This description is similar to a set of linearized relative orbital elements introduced by Hsiao and Scheeres to describe oscillatory motion stabilized relative to a periodic orbit via feedback control, resulting in solutions with similar characteristics to motion within a natural center eigenspace [88, 89].

1.2.3 Controlling spacecraft near periodic orbits

Due to the sensitivity of multi-body environments to perturbations, spacecraft are are typically required to apply control to maintain long-term boundedness near a desired reference trajectory, such as one that resembles a periodic orbit from an approximate dynamical model. Dunham and Roberts provide a thorough discussion of the station-keeping control algorithms used by early spacecraft in multi-body environments to maintain their desired orbits [90]. Surveys by Folta [91] and Shirobokov et al. [92] present compilations of station-keeping strategies for spacecraft near periodic orbits in the CR3BP, capturing the current state-of-the-art in station-keeping strategies. Presently, only individual spacecraft have operated on reference trajectories representative of periodic orbit and quasi-periodic orbits in the CR3BP. However, for multiple spacecraft to operate near periodic orbits, control strategies will be required that consider the relative motion between two or more spacecraft.

At a high-level, control strategies for spacecraft on or near periodic orbits use continuous or impulsive maneuvers. For precise station-keeping, continuous control strategies may be employed to eliminate drift from a reference trajectory between impulsive maneuvers [93]. Optimal continuous control techniques have been investigated to stabilize formations of spacecraft near unstable orbits in the CR3BP by Marchand and Howell [94], Millard and Howell [95], and Bando and Ichikawa [96]. However, incorporating naturally-bounded configurations within control schemes provides stability and long-term propellant usage benefits. Continuous control strategies based on Floquet theory have been developed for general time periodic systems by Calico and Wiesel [97] and Weisel and Shelton [63], and applied to periodic orbits in multi-body environments by Howell and Millard [98]. Scheeres et al. [89] also developed a nontraditional feedback control law to stabilize the motion of a spacecraft around an unstable periodic orbit in the Hill three-body problem by incorporating stability information of the periodic orbit corresponding to the stable and unstable modes. For spacecraft formation flying applications, continuous feedback control laws have been developed using control Lyapunov functions, including variations formulated using relative Cartesian states [41] and Keplerian orbital element differences [99].

Floquet theory has been applied to develop impulsive control strategies for station-keeping spacecraft near periodic orbits in multi-body environments by Simó et al [100]. In this implementation, the projection of the relative state of a spacecraft from a periodic orbit along the unstable eigenspace is eliminated using the Floquet modal coordinates. Building upon this strategy, Howell and Marchand [74] apply Floquet mode control modified to eliminate the projection along the unstable and trivial eigenspaces. The remaining state, exciting the stable and oscillatory modes, results in bounded, oscillatory motion about the periodic orbit that lies along the center eigenspace. Knowledge of the eigenspaces of perioidic orbits is also applied within impulsive station-keeping methods, such as those presented by Farrés and Jorba [101] and Pavlak and Howell [102]. Pavlak and Howell demonstrate that the stable eigenvector of a reference periodic orbit may be used as an initial guess to generate maneuvers for long-term bounded motion in a multi-body environment in the presence of random impulsive perturbations [102, 29].

While modal control strategies such as Floquet-based control methods are well-suited to stabilizing spacecraft relative to a reference periodic orbit, formations of spacecraft near an associated periodic orbit may require stricter constraints to maintain formation geometry maintenance and satisfy collision-avoidance considerations. These constraints may require spacecraft to be capable of tracking specific deviations from a reference periodic orbit. Targeting methods, such as formulations presented by Howell and Barden [103] and Qi et al. [104], support tracking of specific deviations from a periodic orbit. Furthermore, target point methods, introduced by Howell and Pernicka [105] and modified by Howell and Gordon [106], formulate the targeting problem into a optimization problem. Unlike Floquet mode control strategies, these targeting schemes do not require knowledge of the local stability of the reference trajectory. However, as identified by Koon et al. [24], a control strategy that combines aspects of target point and Floquet control methods may provide the advantages of both strategies.

1.3 Dissertation overview

Increasing interest in formations within multi-body systems motivates the development of consistent and intuitive design of bounded motion relative to trajectories resembling periodic orbits in multi-body environments. Geometrically-interpretable state representations have proven valuable for relative trajectory design in two-body environments, and may be similarly valuable for the description of spacecraft formations near periodic orbits in multi-body environments and development of spacecraft control strategies. The goal of this dissertation is to construct a framework for describing and controlling spacecraft motion near periodic orbits in multi-body environments by leveraging a new family of local toroidal coordinates. To accomplish this goal, this dissertation is organized as follows:

Chapter 2: Coordinate frames and dynamical models relevant to the analysis of spacecraft motion in a multi-body environment are described. A derivation of the equations of motion of the CR3BP are presented, including a discussion on nondimensionalization. Equations of relative motion for two spacecraft, each governed by the CR3BP, are also presented. A point mass ephemeris model with an approximated model of solar radiation pressure (SRP) is detailed.

Chapter 3: Particular solutions of the CR3BP relevant to this investigation are summarized.

Additionally, the numerical process used to compute these solutions are also detailed, including numerical shooting methods, psuedo-arclength continuation, and numerical integration schemes. Three reference periodic orbits in the Earth-Moon and Sun-Earth CR3BP are also defined for use throughout this investigation to demonstrate the presented strategies.

Chapter 4: A family of local toroidal coordinate systems for the description of motion relative to periodic orbits in a multi-body environment is introduced. Two formulations are derived: a nonsingular formulation and a geometric formulation. Ancillary analyses related to the coordinate systems are also presented. The description of relative motion via the new coordinate systems is demonstrated via the analysis of motion relative to periodic orbits in the Earth-Moon L_2 southern halo orbit family.

Chapter 5: Methods for characterizing relative oscillatory motion on the center eigenspace of a periodic orbit in the CR3BP are investigated. The presented characterization methods leverage the local toroidal coordinates to parameterize the size, shape, and orientation of the first-order approximation of an invariant curve relative to a periodic orbit. These parameters are then used to derive bounds of different relative motion characteristics for spacecraft tracing an invariant torus.

Chapter 6: Continuous and impulsive control strategies leveraging the introduced local toroidal coordinate systems are presented for spacecraft operating near periodic orbits. Incorporating local toroidal coordinates within the formulation of these control strategies facilitates the design of spacecraft maneuvers within and near the center eigenspace of a periodic orbit. The control strategies presented in this chapter are derived using insight from the CR3BP and are demonstrated in both the CR3BP and point mass ephemeris model.

Chapter 7: A survey of the evolution of the size, shape, and orientation of the first-order approximation of an invariant curve over a revolution of a periodic orbit is conducted for members of orbit families in the Earth-Moon and Sun-Earth CR3BP.

Chapter 8: The presented coordinate systems, characterization methods, and control strategies are employed within a comprehensive example considering the trajectory design process of a constellation surrounding a Sun-Earth L_1 southern halo orbit. Then, the constellation is simulated with control in a point mass ephemeris model with perturbations from SRP along with simulated navigation and thruster firing errors.

Chapter 9: Conclusions to the investigation are presented, including a summary of the completed work and recommendations for further investigation and applications.

1.4 Summary of contributions

The contributions of this dissertation to the astrodynamics community include:

(1) Definition of the local coordinate systems that supply intuitive descriptions of motion relative to periodic orbits in the CR3BP and trajectories resembling periodic orbits in higher-fidelity dynamical models. The straightforward derivation of these coordinate systems and their useful properties may enable future relative motion analysis in multi-body systems.

(2) Introduction of methods for characterizing naturally bounded oscillatory relative motion near periodic orbits. These methods may support future spacecraft constellations by increasing understanding into the expected motion between spacecraft operating near trajectories resembling periodic orbits.

(3) Development of control strategies for spacecraft operating near trajectories resembling periodic orbits. These approaches combine the benefits of previously derived strategies and provide new geometric insight into spacecraft maneuvers in multi-body systems.

(4) Surveys of first-order oscillatory motion relative to periodic orbits in the Earth-Moon and Sun-Earth systems. This investigation illustrates the complex solution space for formations leveraging quasi-periodic motion in a multi-body system and increases heuristics into favorable locations these formations.

Chapter 2

Dynamical Models of Spacecraft in Multi-Body Environments

Various dynamical models and reference frames support the analysis and design of spacecraft motion in multi-body environments. For preliminary trajectory design, the CR3BP supplies an approximation of the motion of a spacecraft under the gravitational influence of two celestial bodies, which are assumed to travel on circular orbits about their mutual barycenter. While the CR3BP serves as a useful tool for low-fidelity analysis, higher-fidelity dynamical models incorporating ephemeris information and additional perturbations provide a more accurate representation of the real-world motion of spacecraft. In this chapter, first, an overview of the derivation and properties of the CR3BP are presented. Next, nonlinear and linearized equations of relative motion between two spacecraft governed by the CR3BP are derived, formulated in both a rotating frame and a local Hill frame. While general for motion in the CR3BP, in this analysis, the expressions for the linearized equations of motion are applied to describe the dynamics relative to a target spacecraft following a periodic orbit. Finally, higher-fidelity modeling of spacecraft motion is discussed, including the equations of motion for a spacecraft in point mass ephemeris model with SRP.

2.1 The circular restricted three-body problem

The CR3BP is a model of a three-body problem consisting of two celestial bodies and a single spacecraft or particle of negligible mass. The dynamics of the spacecraft due to the two celestial bodies are often examined in a rotating reference frame defined by the celestial bodies to develop a set of autonomous equations of motion for the spacecraft. The CR3BP approximates the two celestial bodies as point masses that travel in circular orbits about their mutual barycenter; these celestial bodies are denoted as the primary bodies, P_1 and P_2, where P_1 is defined as the more massive body. The masses of P_1 and P_2 are defined as m_1 and m_2, respectively, and are assumed to be constant over time. The third body of the three-body problem represents a spacecraft or small particle, denoted as P_3, that is assumed to have a negligible mass compared to the mass of the P_1, P_2 system and does not gravitationally influence the motion of the primaries.

A nondimensionalization scheme is commonly applied to quantities of length, time, and mass in the CR3BP using characteristic quantities derived from the P_1-P_2 system. This nondimensionalization facilitates numerical integration and other numerical processes within analysis. A characteristic length quantity, labeled as l^*, is typically set equal to the distance between P_1 and P_2. Under the assumption of circular orbits for the primaries, this distance is equal to the semi-major axis of the P_1-P_2 system, a, calculated as

$$a = r_1 + r_2 \tag{2.1}$$

where r_1 and r_2 are the distances of P_1 and P_2, respectively, from their mutual barycenter. A characteristic time quantity, t^*, is typically set equal to the inverse of the mean motion, n, of the P_1-P_2 system. The mean motion of the system is defined as

$$n = \sqrt{\frac{G(m_1 + m_2)}{a^3}} \tag{2.2}$$

where G is the universal gravitational constant. Lastly, a characteristic mass quantity, m^*, is typically set equal to the combined mass of P_1 and P_2, defined as $m^* = m_1 + m_2$. Using these definitions, dimensional quantities of length, time, and mass are divided by their respective characteristic quantities. Following this nondimensionalization, the semi-major axis and mean motion of the system are equal to unity and the nondimensional rotational period of the system is equal to 2π. Finally, a mass ratio, μ, is defined as the ratio of the mass of P_2 to the total system mass as

$$\mu = \frac{m_2}{m_1 + m_2} \tag{2.3}$$

Values of the characteristic quantities and mass ratio used in this investigation for the Earth-Moon and Sun-Earth CR3BP are summarized in Table 2.1.

Table 2.1: Characteristic quantities and mass ratio of the Earth-Moon and Sun-Earth systems.

Parameter	Earth-Moon system	Sun-Earth system
μ	$1.215060379 \times 10^{-2}$	$3.003459885 \times 10^{-6}$
l^*	3.84400×10^{5} km	1.49598023×10^{8} km
t^*	$3.751326414 \times 10^{5}$ s	$5.021854393 \times 10^{6}$ s
m^*	6.047683×10^{24} kg	$1.989105974 \times 10^{30}$ kg

The nondimensional mass and separation of P_1 and P_2 from their mutual barycenter may be straightforwardly expressed as a function of the system mass ratio. Solving the system of equations formed by Eq. (2.2) and Eq. (2.3), the gravitational parameters of P_1 and P_2, Gm_1 and Gm_2, respectively, are defined using nondimensionalized quantities as

$$Gm_1 = 1 - \mu \tag{2.4}$$

$$Gm_2 = \mu \tag{2.5}$$

The distances of the primary bodies from the barycenter may also be represented as a function of the mass parameter. For the scalar distances r_1 and r_2, measured in opposite directions from the system barycenter, the center of mass relationship is expressed as

$$(1 - \mu)\, r_1 = \mu\, r_2 \tag{2.6}$$

Solving the system of equations formed by Eq. (2.1) and Eq. (2.6), the nondimensional distances of P_1 and P_2 from the system barycenter are equal to $r_1 = \mu$ and $r_2 = 1 - \mu$, respectively.

$$r_1 = \mu \tag{2.7}$$

$$r_2 = 1 - \mu \tag{2.8}$$

Throughout this investigation, nondimensionalized quantities are generally employed within the derivation of the various equations of motion. However, dimensional quantities are generally used to report and visualize results.

2.1.1 The P_1-P_2 rotating frame

The CR3BP typically formulates the motion of a spacecraft in a rotating frame defined by the two primary bodies. This rotating frame, denoted $\mathcal{R}$, is defined with axes $\{\hat{\boldsymbol{x}}, \hat{\boldsymbol{y}}, \hat{\boldsymbol{z}}\}$, equal to

$$\hat{\boldsymbol{x}} = \frac{\boldsymbol{r}_{12}}{r_{12}} \tag{2.9a}$$

$$\hat{\boldsymbol{y}} = \hat{\boldsymbol{z}} \times \hat{\boldsymbol{x}} \tag{2.9b}$$

$$\hat{\boldsymbol{z}} = \frac{\boldsymbol{h}_{12}}{h_{12}} \tag{2.9c}$$

where $\boldsymbol{r}_{12}$ is the relative position of P_2 measured from P_1. Note that this relative position vector is calculated as

$$\boldsymbol{r}_{ij} = \boldsymbol{r}_j - \boldsymbol{r}_i \tag{2.10}$$

The orbital angular momentum vector of P_2 with respect to P_1, $\boldsymbol{h}_{12}$, is defined as

$$\boldsymbol{h}_{12} = \boldsymbol{r}_{12} \times \dot{\boldsymbol{r}}_{12} \tag{2.11}$$

Note that the dot vector notation, $\dot{(\ )}$, indicates a time derivative of a vector for an observer fixed in the inertial frame. These axes form an orthogonal, right-handed triad. Under the assumption of circular motion, P_1 and P_2 are located at fixed position vectors along the $\hat{\boldsymbol{x}}$ axis of the rotating frame. The position vector of P_1 with respect to the system barycenter is equal to

$$\boldsymbol{r}_1 = -\mu\hat{\boldsymbol{x}} \tag{2.12}$$

The position vector of P_2 with respect to the system barycenter is equal to

$$\boldsymbol{r}_2 = (1-\mu)\hat{\boldsymbol{x}} \tag{2.13}$$

When expressed in the rotating frame, the components of these position vectors are constant over time in the CR3BP.

An arbitrary inertial frame is defined to supply an inertial reference for expressed motion as seen by an observer fixed in the rotating frame. Specifically, this inertial frame is denoted $\mathcal{N}$ with axes $\{\hat{\boldsymbol{X}}, \hat{\boldsymbol{Y}}, \hat{\boldsymbol{Z}}\}$ and is defined such that the three axes of the rotating frame are aligned with the axes of the inertial frame at a specific epoch, denoted t_0. Because the primary bodies are assumed to travel in circular orbits about their mutual barycenter, the angular velocity of the rotating frame with respect to the inertial frame is defined by the mean motion of the system. Thus, the nondimensional angular velocity of rotating frame with respect to the inertial frame, $\boldsymbol{\omega}_{RN}$, in the CR3BP is expressed as

$$\boldsymbol{\omega}_{RN} = 1\hat{\boldsymbol{z}} \tag{2.14}$$

and is constant over time. Using this definition, the third axes of the inertial and rotating frames, $\hat{\boldsymbol{Z}}$ and $\hat{\boldsymbol{z}}$, respectively, are equal for all time.

The orientation of the rotating frame with respect to the defined inertial frame may be expressed as a single-axis rotation about the orbital angular momentum axis, $\hat{\boldsymbol{Z}}$. Because the nondimensional mean motion of the system is equal to unity, the angle of the rotation about the $\hat{\boldsymbol{Z}}$ axis, θ, is equivalent to the difference of the current time and initial time, expressed as $\theta = (t - t_0)$. A position vector defined in the inertial frame may be transformed into the rotating frame via a rotation matrix, labeled $[\boldsymbol{C}]$, which is expressed via an elementary single-axis rotation in the CR3BP, equal to

$$[\boldsymbol{C}] = \begin{bmatrix} \cos\theta & \sin\theta & 0 \\ -\sin\theta & \cos\theta & 0 \\ 0 & 0 & 1 \end{bmatrix} \tag{2.15}$$

The transformation of a position vector expressed in the inertial frame to a position vector expressed in the rotating frame is

$${}^{\mathcal{R}}\boldsymbol{r} = [\boldsymbol{C}]\left({}^{\mathcal{N}}\boldsymbol{r}\right) \tag{2.16}$$

The left superscript is used to explicitly indicate the frame for which the components of a vector is expressed in when a frame definition is required. A schematic of the rotating frame with respect to the inertial frame is included in Figure 2.1, with each coordinate frame originating from the P_1-P_2 barycenter. The locations of P_1 and P_2 at the arbitrary epoch, t_0, i.e., when the rotating and inertial frames are aligned, are indicated by white circles, whereas the locations of P_1 and P_2 at time t are represented with black circles.

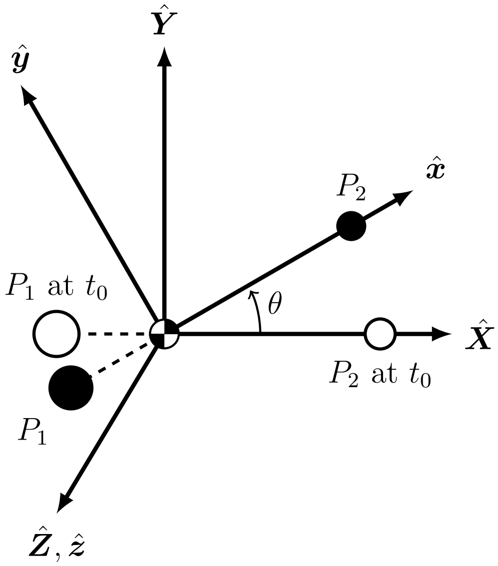

Figure 2.1: Schematic of the rotating frame and the arbitrary inertial frame aligned with the rotating frame at time t_0.

2.1.2 Equations of motion

A Newtonian derivation of the equations of motion of P_3 with respect to the P_1-P_2 barycenter under the approximations of the CR3BP is presented. First, the nondimensional gravitational potential of P_3, U_3, in the P_1-P_2 system is defined as [107]

$$U_3 = \frac{1-\mu}{r_{13}} + \frac{\mu}{r_{23}} \tag{2.17}$$

where the distances r_{13} and r_{23} are the distances of P_3 from P_1 and P_2, respectively. Given this potential, the inertial acceleration of the spacecraft, $\ddot{\boldsymbol{r}}_3$, due to the gravitational influence of the two bodies is defined as the gradient of the potential, $\partial U_3/\partial \boldsymbol{r}_3$. This nondimensional inertial acceleration is expressed as

$$\ddot{\boldsymbol{r}}_3 = -(1-\mu)\frac{\boldsymbol{r}_{13}}{r_{13}^3} - \mu\frac{\boldsymbol{r}_{23}}{r_{23}^3} \tag{2.18}$$

At this step, this acceleration is expressed independent of reference frame and assumptions on the motion of the two celestial bodies, thus, is valid for any restricted three-body problem.

The position vector of P_3 with respect to the P_1-P_2 barycenter is formulated in the rotating frame. This vector may be expressed as a linear combination of the basis of the rotating frame and three coordinates, (x, y, z), as

$$\boldsymbol{r}_3 = x\hat{\boldsymbol{x}} + y\hat{\boldsymbol{y}} + z\hat{\boldsymbol{z}} \tag{2.19}$$

The three coordinates may also be expressed as a 3×1 column vector as

$$^{\mathcal{R}}\boldsymbol{r}_3 = \begin{bmatrix} x & y & z \end{bmatrix}^T \tag{2.20}$$

The first time derivative of $\boldsymbol{r}_3$ for an observer fixed in the rotating frame is expressed in components of the rotating frame

$$^{\mathcal{R}}\boldsymbol{r}_3' = \begin{bmatrix} \dot{x} & \dot{y} & \dot{z} \end{bmatrix}^T \tag{2.21}$$

The notation $^{\mathcal{R}}(\ )' = {}^{\mathcal{R}}\mathrm{d}/\mathrm{dt}(\ )$ is used to denote a time derivative with an observer fixed in the $\mathcal{R}$ frame. Because the time derivative of a scalar is the same regardless of what frame the observer is fixed in, the scalar dot notation, $\dot{(\ )}$ and $\ddot{(\ )}$, is used to indicate the first and second time derivative of a scalar quantity, respectively [40]. The second time derivative of the position vector of P_3 for an observer in the rotating frame, $^{\mathcal{R}}\boldsymbol{r}_3''$, is defined as

$$^{\mathcal{R}}\boldsymbol{r}_3'' = \begin{bmatrix} \ddot{x} & \ddot{y} & \ddot{z} \end{bmatrix}^T \tag{2.22}$$

To simplify notation, the frame in which the time derivative of a vector is expressed is assumed to be the same as the frame of the observer. The nondimensional angular velocity vector of the rotating frame with respect to the inertial frame, $\boldsymbol{\omega}_{RN}$, is expressed in the rotating frame as

$$^{\mathcal{R}}\boldsymbol{\omega}_{RN} = \begin{bmatrix} 0 & 0 & 1 \end{bmatrix}^T \tag{2.23}$$

This is the same formulation of the angular velocity vector expressed in the inertial frame, $^{\mathcal{N}}\boldsymbol{\omega}_{RN}$. Note that the time derivative of the angular velocity in the rotating or inertial frame is equal to zero in the CR3BP.

Next, the acceleration of a spacecraft for an observer fixed in the rotating frame is derived. The relation between the derivatives of a vector with respect to time as seen by an observer in the rotating and inertial frame is defined as

$$\frac{^{\mathcal{N}}\mathrm{d}\boldsymbol{r}}{\mathrm{dt}} = \frac{^{\mathcal{R}}\mathrm{d}\boldsymbol{r}}{\mathrm{dt}} + \boldsymbol{\omega}_{RN} \times \boldsymbol{r} \tag{2.24}$$

This relationship is referred to as the basic kinematic equation or transport theorem [40]. Applying transport theorem twice, the acceleration of the P_3 for an observer fixed in the rotating frame, ${}^{\mathcal{R}}\boldsymbol{r}_3''$, is equal to

$$ {}^{\mathcal{R}}\boldsymbol{r}_3'' = {}^{\mathcal{R}}\ddot{\boldsymbol{r}}_3 - 2\left({}^{\mathcal{R}}\boldsymbol{\omega}_{RN} \times {}^{\mathcal{R}}\boldsymbol{r}_3'\right) - {}^{\mathcal{R}}\boldsymbol{\omega}_{RN} \times \left({}^{\mathcal{R}}\boldsymbol{\omega}_{RN} \times {}^{\mathcal{R}}\boldsymbol{r}_3\right) \tag{2.25} $$

This second-order vector differential equation supplies the nonlinear equations motion of P_3 in the CR3BP. These nondimensional equations of motion of the CR3BP are commonly written as a set of three second-order, scalar differential equations as

$$ \ddot{x} = -(1-\mu)\frac{(x+\mu)}{r_{13}^3} - \mu\frac{(x-1+\mu)}{r_{23}^3} + 2\dot{y} + x \tag{2.26a} $$

$$ \ddot{y} = -(1-\mu)\frac{y}{r_{13}^3} - \mu\frac{y}{r_{23}^3} - 2\dot{x} + y \tag{2.26b} $$

$$ \ddot{z} = -(1-\mu)\frac{z}{r_{13}^3} - \mu\frac{z}{r_{23}^3} \tag{2.26c} $$

where the distances r_{13} and r_{23} are equal to

$$ r_{13} = \sqrt{(x+\mu)^2 + y^2 + x^2} \tag{2.27} $$

$$ r_{23} = \sqrt{(x-1+\mu)^2 + y^2 + x^2} \tag{2.28} $$

These equations of motion may also be concisely expressed as functions of the partial derivatives of a pseudo-potential, labeled U^*, defined as

$$ U^* = \frac{1}{2}\left(x^2 + y^2\right) + \frac{1-\mu}{r_{13}} + \frac{\mu}{r_{23}} \tag{2.29} $$

which incorporates the gravitational potential of P_1 and P_2, as well as the effects of the rotation of the $\mathcal{R}$ frame. Using this pseudo-potential function, the equations of motion of the CR3BP may be equivalently expressed as

$$ \ddot{x} = \frac{\partial U^*}{\partial x} + 2\dot{y} \tag{2.30a} $$

$$ \ddot{y} = \frac{\partial U^*}{\partial y} - 2\dot{x} \tag{2.30b} $$

$$ \ddot{z} = \frac{\partial U^*}{\partial z} \tag{2.30c} $$

When formulated in the rotating frame, time does not explicitly appear in the equations of motion, producing an autonomous dynamical model. This dynamical model admits several fundamental solutions, including equilibrium points, periodic orbits, and quasi-periodic orbits, which are detailed in Chapter 3.

The CR3BP possesses an integral of motion due to its autonomous Hamiltonian structure [24]. In the astrodynamics comminunity, the integral of motion for the CR3BP is labeled the Jacobi constant, and is commonly expressed using the state components of P_3 formulated in the rotating frame as [24]

$$C_J = 2U^* - v^2 \tag{2.31}$$

The final term within this expression, v^2, is the square of the magnitude of the velocity of the spacecraft with respect to the barycenter for an observer fixed in the rotating frame, expressed as $v^2 = \dot{x}^2 + \dot{y}^2 + \dot{z}^2$. The value of the Jacobi constant is typically reported using the nondimensionalized quantities. The Jacobi constant is commonly derived from the equations of the motion of the CR3BP by first differentiating v^2 as

$$\frac{\mathrm{d}}{\mathrm{dt}}\left(\frac{1}{2}v^2\right) = \dot{x}\ddot{x} + \dot{y}\ddot{y} + \dot{z}\ddot{z}$$

Substituting in the equations of motion of the CR3BP, the expression simplifies to the total derivative of the pseudo-potential as [28]

$$\frac{\mathrm{d}}{\mathrm{dt}}\left(\frac{1}{2}v^2\right) = \dot{x}\left(\frac{\partial U^*}{\partial x} + 2\dot{y}\right) + \dot{y}\left(\frac{\partial U^*}{\partial y} - 2\dot{x}\right) + \dot{z}\frac{\partial U^*}{\partial z} = \frac{\mathrm{d}U^*}{\mathrm{dt}}$$

Integrating this equation with respect to time yields the relationship between the pseudo-potential, speed, and a constant of integration, C, as

$$\frac{1}{2}v^2 = U^* + C$$

The constant produced by the integration may be formulated into the Jacobi constant as expressed in Eq. (2.31). The Jacobi constant is an an energy-like term that is preserved for natural motion in the CR3BP and is inversely related to energy, such that a lower value of C_J indicates a higher energy and vice versa. Furthermore, the Jacobi constant also supplies insight into allowable natural motion of a spacecraft in the three body environment at a specific engergy level via the definition of zero velocity surfaces and planar zero velocity curves [28].

Linearization of the equations of motion of the CR3BP is useful in analyzing the stability of equilibrium solutions in the CR3BP. First, a state vector, $\boldsymbol{x}$, locating P_3 in phase space measured from the system barycenter in the rotating frame is defined as

$$\boldsymbol{x} = \begin{bmatrix} x & y & z & \dot{x} & \dot{y} & \dot{z} \end{bmatrix}^T \tag{2.32}$$

The time derivative of each of the components of the state vector is defined as

$$\boldsymbol{x}' = \begin{bmatrix} \dot{x} & \dot{y} & \dot{z} & \ddot{x} & \ddot{y} & \ddot{z} \end{bmatrix}^T \tag{2.33}$$

Using these definitions, a Jacobian matrix, $[\boldsymbol{A}]$, reflects the partial derivative of the rate of change of each state component with respect to each state component, written as

$$[\boldsymbol{A}] = \frac{\partial \boldsymbol{x}'}{\partial \boldsymbol{x}} \tag{2.34}$$

This Jacobian may be decomposed into four, 3×3 quadrants of vector partial derivatives as

$$[\boldsymbol{A}] = \begin{bmatrix} [\boldsymbol{0}_3] & [\boldsymbol{I}_3] \\ \frac{\partial({}^{\mathcal{R}}\boldsymbol{r}_3'')}{\partial({}^{\mathcal{R}}\boldsymbol{r}_3)} & \frac{\partial({}^{\mathcal{R}}\boldsymbol{r}'')}{\partial({}^{\mathcal{R}}\boldsymbol{r}')} \end{bmatrix} \tag{2.35}$$

where $[\boldsymbol{I}_n]$ represents the $n \times n$ identity matrix and $[\boldsymbol{0}_n]$ represents the zero matrix of size $n \times n$. The lower-left quadrant is equal to the partial derivative of the acceleration of the spacecraft for an observer fixed in the rotating frame with respect to the position vector. This quadrant is expressed in nondimensional quantities as

$$\frac{\partial({}^{\mathcal{R}}\boldsymbol{r}_3'')}{\partial({}^{\mathcal{R}}\boldsymbol{r}_3)} = -(1-\mu)\left(\frac{[\boldsymbol{I}_3]}{r_{13}^3} - \frac{3({}^{\mathcal{R}}\boldsymbol{r}_{13})({}^{\mathcal{R}}\boldsymbol{r}_{13})^T}{r_{13}^5}\right) - \mu\left(\frac{[\boldsymbol{I}_3]}{r_{23}^3} - \frac{3({}^{\mathcal{R}}\boldsymbol{r}_{23})({}^{\mathcal{R}}\boldsymbol{r}_{23})^T}{r_{23}^5}\right) - [{}^{\mathcal{R}}\tilde{\boldsymbol{\omega}}_{RN}][{}^{\mathcal{R}}\tilde{\boldsymbol{\omega}}_{RN}] \tag{2.36}$$

The matrix tilde notation, $[\tilde{\ }]$, indicates the skew-symmetric representation of the cross product of a vector. For a general vector defined as $\boldsymbol{a} = [a_1, a_2, a_3]^T$, the skew symmetric representation is expressed as [40]

$$\tilde{\boldsymbol{a}} = \begin{bmatrix} 0 & -a_3 & a_2 \\ a_3 & 0 & -a_1 \\ -a_2 & a_1 & 0 \end{bmatrix} \tag{2.37}$$

Finally, the lower-right quadrant of the Jacobian matrix is equal to the partial derivative of the acceleration with respect to the velocity vector of P_3 for an observer fixed in the rotating frame [24]

$$\frac{\partial({}^{\mathcal{R}}\boldsymbol{r}_3'')}{\partial({}^{\mathcal{R}}\boldsymbol{r}_3')} = -2[{}^{\mathcal{R}}\tilde{\boldsymbol{\omega}}_{RN}] = \begin{bmatrix} 0 & 2 & 0 \\ -2 & 0 & 0 \\ 0 & 0 & 0 \end{bmatrix} \tag{2.38}$$

This Jacobian is used throughout this investigation within the computation of the state transition matrix and in formulating linear equations of relative motion.

2.2 Relative motion in a three-body environment

The study of relative motion in a three-body environment considers the relative motion between two or more spacecraft under the gravitational influence of two celestial bodies. In this investigation, each spacecraft is assumed to possess a negligible mass compared to the two primaries; thus, the dynamics of each spacecraft may be modeled using via independent three-body systems. To distinguish between multiple spacecraft in a formation, two subsets of spacecraft are defined: target spacecraft and chaser spacecraft. A target spacecraft is typically defined as the primary spacecraft or non-physical reference point, e.g., a space station, in-space servicing target vehicle, or cluster center, which often, but are not required to, follow a natural trajectory. The state of a chaser spacecraft, e.g., a rendezvousing spacecraft, is then expressed relative to the target spacecraft to study the relative motion problem.

In this section, two formulations of equations of relative motion for spacecraft in multi-body environments are presented assuming each spacecraft is governed by the CR3BP. The first formulation expresses the equations of motion in the rotating frame defined by two primary bodies.

The second formulation defines equations of relative motion formulated in a Hill frame defined by the target spacecraft with respect to one of the primary gravitational bodies. Additionally, the linearization of the CR3BP about the target spacecraft formulated in each of the two coordinate frames in presented. When the motion of each spacecraft is governed by the CR3BP, the nonlinear and linear equations of relative motion may be implemented such that the description of the relative state between the target and chaser spacecraft is autonomous. Part of the material in this section was first published by Celestial Mechanics and Dynamical Astronomy in 2022 by Springer Nature [108].

2.2.1 Equations of relative motion in the rotating frame

The CR3BP is used in this section as a foundation for formulating the equations of relative motion between two spacecraft in a system with two massive primary bodies. There are a variety of implementations that may be used to analyze relative motion between spacecraft. However, a common practice for the analysis of relative motion in two-body environments is the development of equations of relative motion. In this section, the target spacecraft and the chaser spacecraft are both assumed to follow uncontrolled natural reference paths in the CR3BP, assuming that the spacecraft do not gravitationally interact with each other. Nonlinear and linearized equations of relative motion are then presented for an observer in the rotating frame. The resulting equations of relative motion are autonomous, enabling an analysis of relative motion in the CR3BP independent of epoch.

The relative position vector of the chaser spacecraft measured from the target spacecraft and expressed in the rotating frame is investigated. The target spacecraft is denoted by the subscript t, while the chaser spacecraft is denoted by the subscript c. The position vector of the chaser spacecraft relative to the target spacecraft is denoted as $\boldsymbol{\rho}$, and is defined as

$$\boldsymbol{\rho} = \boldsymbol{r}_c - \boldsymbol{r}_t \tag{2.39}$$

where $\boldsymbol{r}_t$ and $\boldsymbol{r}_c$ are the position vectors of the target and chaser spacecraft, respectively, from the

P_1-P_2 barycenter. This relative position vector is equivalent to the difference of the position vectors of the target and chaser spacecraft measured from either of the two primaries and is conceptually illustrated in Figure 2.2. The relative position vector may be expressed in the rotating frame by a set of relative coordinates, $(\delta x, \delta y, \delta z)$, as

$$\boldsymbol{\rho} = \delta x \hat{\boldsymbol{x}} + \delta y \hat{\boldsymbol{y}} + \delta z \hat{\boldsymbol{z}} \tag{2.40}$$

Using these relative coordinate definitions, the relative position vector expressed in the rotating frame may be expressed as a 3×1 column vector as

$$^{\mathcal{R}}\boldsymbol{\rho} = \begin{bmatrix} \delta x & \delta y & \delta z \end{bmatrix}^T \tag{2.41}$$

The first and second time derivatives of the relative position vector as seen by an observer in the rotating frame, $^{\mathcal{R}}\boldsymbol{\rho}'$ and $^{\mathcal{R}}\boldsymbol{\rho}''$, respectively, are expressed as

$$^{\mathcal{R}}\boldsymbol{\rho}' = \begin{bmatrix} \delta \dot{x} & \delta \dot{y} & \delta \dot{z} \end{bmatrix}^T \tag{2.42}$$

$$^{\mathcal{R}}\boldsymbol{\rho}'' = \begin{bmatrix} \delta \ddot{x} & \delta \ddot{y} & \delta \ddot{z} \end{bmatrix}^T \tag{2.43}$$

To simplify notation, the frame for which the vector is expressed in is assumed to be the same frame as the observer.

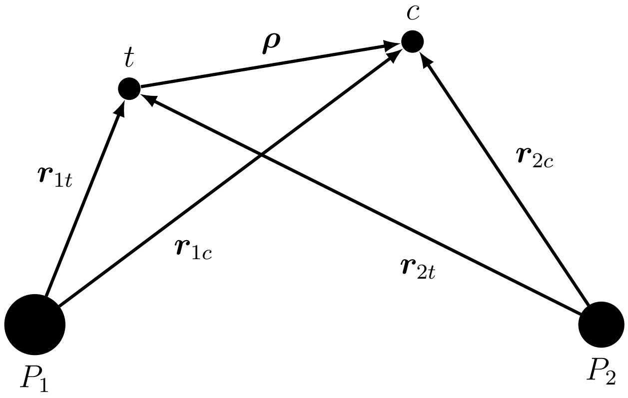

Figure 2.2: Schematic of the relative position of the chaser spacecraft, c, measured from the target spacecraft, t.

An expression for the relative acceleration between two spacecraft for an observer fixed in the rotating frame is derived via a Newtonian approach. The inertial and nondimensional relative acceleration, $\ddot{\boldsymbol{\rho}}$, is calculated as the difference between the inertial accelerations of the target and chaser spacecraft, each governed by Eq. (2.18), expressed as

$$\ddot{\boldsymbol{\rho}} = -\mu \left(\frac{\boldsymbol{r}_{2c}}{r_{2c}^3} - \frac{\boldsymbol{r}_{2t}}{r_{2t}^3} \right) - (1-\mu) \left(\frac{\boldsymbol{r}_{1c}}{r_{1c}^3} - \frac{\boldsymbol{r}_{1t}}{r_{1t}^3} \right) \tag{2.44}$$

The relative acceleration, $\boldsymbol{\rho}''$, between the two spacecraft for an observer fixed in the rotating frame is then calculated as

$$^{\mathcal{R}}\boldsymbol{\rho}'' = {}^{\mathcal{R}}\ddot{\boldsymbol{\rho}} - 2\left({}^{\mathcal{R}}\boldsymbol{\omega}_{RN} \times {}^{\mathcal{R}}\boldsymbol{\rho}'\right) - {}^{\mathcal{R}}\boldsymbol{\omega}_{RN} \times \left({}^{\mathcal{R}}\boldsymbol{\omega}_{RN} \times {}^{\mathcal{R}}\boldsymbol{\rho}\right) \tag{2.45}$$

This second-order vector differential equation supplies the nonlinear equations of relative motion for the chaser spacecraft. When the state of the target spacecraft is integrated via the equations of motion of the CR3BP from Eq. (2.26), and the relative state of the chaser spacecraft from the target spacecraft is simultaneously integrated via the equations of relative motion from Eq. (2.45), the paths of the two spacecraft are generated using an augmented system of 12 scalar and autonomous first-order differential equations.

A six-dimensional state vector is defined as the difference of the state vectors of the chaser and target spacecraft measured from the system barycenter and formulated in the rotating frame. This relative state vector, labeled $\delta\boldsymbol{x}$, is defined as

$$\delta\boldsymbol{x} = \boldsymbol{x}_c - \boldsymbol{x}_t \tag{2.46}$$

where $\boldsymbol{x}_c$ and $\boldsymbol{x}_t$ are the state vectors of the chaser and target spacecraft, respectively. The components of this 6×1 relative state vector are defined as

$$\delta\boldsymbol{x} = \begin{bmatrix} \delta x & \delta y & \delta z & \delta\dot{x} & \delta\dot{y} & \delta\dot{z} \end{bmatrix}^T \tag{2.47}$$

The time derivative of this relative state vector is defined in vector form as

$$\delta\boldsymbol{x}' = \begin{bmatrix} \delta\dot{x} & \delta\dot{y} & \delta\dot{z} & \delta\ddot{x} & \delta\ddot{y} & \delta\ddot{z} \end{bmatrix}^T \tag{2.48}$$

The relative state vector is used to construct a first-order approximation of the dynamics of a spacecraft relative to the target spacecraft traveling on a natural reference trajectory in the CR3BP.

The equations of relative motion may be well approximated by their linearization about the target spacecraft for relative motion in the neighborhood of the target spacecraft [109]. For the nonlinear equations of relative motion expressed in Eq. (2.45), the associated linearized equations of relative motion are written in the form

$$\delta \boldsymbol{x}' \approx [\boldsymbol{A}_t]\delta \boldsymbol{x} \tag{2.49}$$

where $[\boldsymbol{A}_t]$ is the Jacobian matrix defined in Eq. (2.35) evaluated at the state of the target spacecraft in the CR3BP. The process of deriving this first-order approximation of relative motion is detailed further in the following chapter within the discussion of the stability of periodic orbits. The first-order approximation of the relative path of a chaser spacecraft may be generated by simultaneously integrating the relative state of the chaser spacecraft and absolute state of target spacecraft. A 12×1 system of equations is formed by the nonlinear equations of motion governing the target spacecraft state in the CR3BP, as expressed by Eq. (2.26), and the linearized equations of relative motion governing the relative state of the chaser spacecraft, as expressed in Eq. (2.49). The result is a system of 12 scalar and autonomous first-order differential equations where the motion of the target spacecraft is recovered to within the accuracy of numerical integration in the CR3BP and the motion of the chaser spacecraft is approximated via linearization about the target spacecraft.

2.2.2 The Hill frame

A Hill frame is defined for a target spacecraft in a three-body environment using the state of the target spacecraft relative to P_2. This formulation of the Hill frame is of interest for the analysis of motion near the less massive body of a three-body system, e.g., the Moon in the Earth-Moon system or the Earth in the Sun-Earth system. However, a Hill frame may also be defined using P_1 as the primary body.

The axes of the Hill frame are defined as a function of the instantaneous state of a target spacecraft with respect to P_2. The Hill frame, denoted $\mathcal{O}$, is defined with axes $\{\hat{\boldsymbol{o}}_r, \hat{\boldsymbol{o}}_\theta, \hat{\boldsymbol{o}}_h\}$, where $\hat{\boldsymbol{o}}_r$ is the radial direction, $\hat{\boldsymbol{o}}_\theta$ is the along-track direction, and $\hat{\boldsymbol{o}}_h$ is the cross-track direction. These three basis vectors are calculated as

$$\hat{\boldsymbol{o}}_r = \frac{\boldsymbol{r}_{2t}}{r_{2t}} \tag{2.50a}$$

$$\hat{\boldsymbol{o}}_\theta = \hat{\boldsymbol{o}}_h \times \hat{\boldsymbol{o}}_r \tag{2.50b}$$

$$\hat{\boldsymbol{o}}_h = \frac{\boldsymbol{h}_{2t}}{h_{2t}} \tag{2.50c}$$

where the specific, inertial orbital angular momentum of the target spacecraft relative to P_2 is defined as

$$\boldsymbol{h}_{2t} = \boldsymbol{r}_{2t} \times \dot{\boldsymbol{r}}_{2t} \tag{2.51}$$

A schematic of the axes of the Hill frame defined by the target spacecraft with respect to P_2 is illustrated in Figure 2.3. As this coordinate frame is a function of the instantaneous state of the target spacecraft, the axes of the coordinate frame will generally evolve over time relative to the rotating frame and inertial frame.

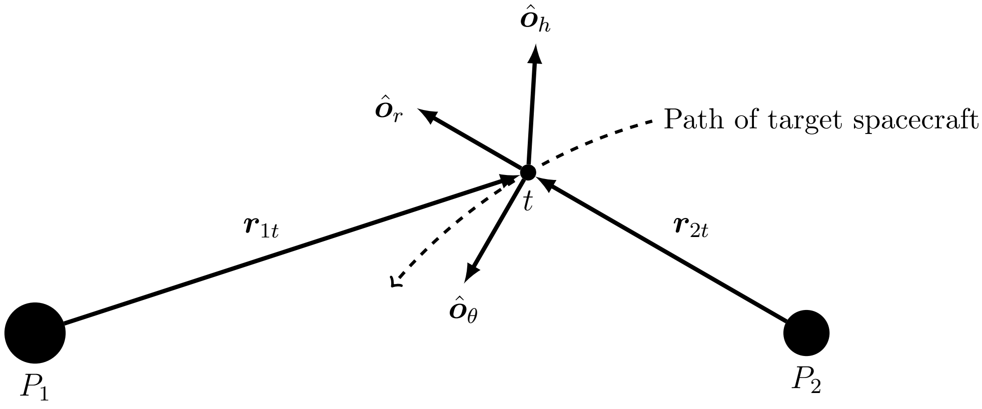

Figure 2.3: Schematic of the Hill frame defined by the state of the target spacecraft measured with respect to P_2.

The angular velocity of the Hill frame in a three-body environment is derived considering the gravitational influence of both P_1 and P_2 on the target spacecraft. The angular velocity of the Hill frame with respect to the inertial frame, $\boldsymbol{\omega}_{ON}$, is expressed as [40]

$$\boldsymbol{\omega}_{ON} = \frac{\boldsymbol{h}_{2t}}{r_{2t}^2} + \frac{\boldsymbol{r}_{2t}}{h_{2t}}(\ddot{\boldsymbol{r}}_{2t} \cdot \hat{\boldsymbol{o}}_h) \tag{2.52}$$

The angular velocity of the Hill frame is influenced by the gravity of P_2 in the radial direction as well as the gravity of P_1, which produces a nonzero angular velocity term in the $\hat{\boldsymbol{o}}_h$ direction. The acceleration, $\ddot{\boldsymbol{r}}_{2t}$, is written in nondimensional quantities as [107]

$$\ddot{\boldsymbol{r}}_{2t} = -\mu \frac{\boldsymbol{r}_{2t}}{r_{2t}^3} - (1-\mu)\left(\frac{\boldsymbol{r}_{1t}}{r_{1t}^3} + \frac{\boldsymbol{r}_{21}}{r_{21}^3}\right) \tag{2.53}$$

Unlike the angular velocity of the rotating frame with respect to the inertial frame, the angular velocity of the Hill frame with respect to the inertial frame has a nonzero time derivative for an observer fixed in the inertial frame. This inertial time rate of change of, $\dot{\boldsymbol{\omega}}_{ON}$, is written as

$$\dot{\boldsymbol{\omega}}_{ON} = \frac{\dot{\boldsymbol{h}}_{2t}}{r_{2t}^2} - 2\frac{(\boldsymbol{r}_{2t}\cdot\dot{\boldsymbol{r}}_{2t})\boldsymbol{h}_{2t}}{r_{2t}^4} + \left(\frac{\dot{\boldsymbol{r}}_{2t}}{h_{2t}} - \frac{\boldsymbol{r}_{2t}(\boldsymbol{h}_{2t}\cdot\dot{\boldsymbol{h}}_{2t})}{h_{2t}^3}\right)(\ddot{\boldsymbol{r}}_{2t}\cdot\hat{\boldsymbol{o}}_h) + \frac{\boldsymbol{r}_{2t}}{h_{2t}}\left(\dddot{\boldsymbol{r}}_{2t}\cdot\hat{\boldsymbol{o}}_h + \ddot{\boldsymbol{r}}_{2t}\cdot\dot{\hat{\boldsymbol{o}}}_h\right) \tag{2.54}$$

where the inertial time rate of change of the angular momentum unit vector is defined as

$$\dot{\hat{\boldsymbol{o}}}_h = \boldsymbol{\omega}_{ON} \times \hat{\boldsymbol{o}}_h \tag{2.55}$$

Note that the time derivative of the angular velocity vector, $\dot{\boldsymbol{\omega}}_{ON}$, is the same for an observer fixed in the inertial frame as for an observer fixed in the Hill frame. This expression requires the inertial jerk, or third time derivative, $\dddot{\boldsymbol{r}}_{2t}$, of the position vector of the target spacecraft with respect to P_2. This vector is expressed in nondimensional quantities as

$$\dddot{\boldsymbol{r}}_{2t} = -\mu\left(\frac{\dot{\boldsymbol{r}}_{2t}}{r_{2t}^3} - 3\frac{\boldsymbol{r}_{2t}(\boldsymbol{r}_{2t}\cdot\dot{\boldsymbol{r}}_{2t})}{r_{2t}^5}\right) - (1-\mu)\left(\frac{\dot{\boldsymbol{r}}_{1t}}{r_{1t}^3} - 3\frac{\boldsymbol{r}_{1t}(\boldsymbol{r}_{1t}\cdot\dot{\boldsymbol{r}}_{1t})}{r_{1t}^5} + \frac{\dot{\boldsymbol{r}}_{21}}{r_{21}^3} - 3\frac{\boldsymbol{r}_{21}(\boldsymbol{r}_{21}\cdot\dot{\boldsymbol{r}}_{21})}{r_{21}^5}\right) \tag{2.56}$$

where the time derivative of the orbital angular momentum of the target spacecraft with respect to P_2 is required is expressed as

$$\dot{\boldsymbol{h}}_{2t} = \boldsymbol{r}_{2t} \times \ddot{\boldsymbol{r}}_{2t} \tag{2.57}$$

These quantities supply information that is required to formulate the equations of relative motion for the CR3BP in the Hill frame.

2.2.3 Equations of relative motion in the Hill frame

An expression for the relative acceleration between two spacecraft, given an observer that is fixed in the Hill frame, is derived via a Newtonian approach. The relative position vector, $\boldsymbol{\rho}$, may be expressed in the Hill frame using a set of relative Hill frame coordinates, (ξ, η, ζ), as

$$\boldsymbol{\rho} = \xi \hat{\boldsymbol{o}}_r + \eta \hat{\boldsymbol{o}}_\theta + \zeta \hat{\boldsymbol{o}}_h \tag{2.58}$$

or in column vector notation as

$$^{\mathcal{O}}\boldsymbol{\rho} = \begin{bmatrix} \xi & \eta & \zeta \end{bmatrix}^T \tag{2.59}$$

These coordinates possess a time rate of change of

$$^{\mathcal{O}}\boldsymbol{\rho}' = \begin{bmatrix} \dot{\xi} & \dot{\eta} & \dot{\zeta} \end{bmatrix}^T \tag{2.60}$$

where $^{\mathcal{O}}(\;)'$ indicates a time derivative for an observer fixed in the Hill frame. The second time derivative of the relative position vector for an observer in the Hill frame is expressed as

$$^{\mathcal{O}}\boldsymbol{\rho}'' = \begin{bmatrix} \ddot{\xi} & \ddot{\eta} & \ddot{\zeta} \end{bmatrix}^T \tag{2.61}$$

Using these definition, the relative acceleration between the two spacecraft for an observer fixed in the Hill frame is calculated as

$$^{\mathcal{O}}\boldsymbol{\rho}'' = {}^{\mathcal{O}}\ddot{\boldsymbol{\rho}} - {}^{\mathcal{O}}\dot{\boldsymbol{\omega}}_{ON} \times {}^{\mathcal{O}}\boldsymbol{\rho} - 2\left({}^{\mathcal{O}}\boldsymbol{\omega}_{ON} \times {}^{\mathcal{O}}\boldsymbol{\rho}'\right) - {}^{\mathcal{O}}\boldsymbol{\omega}_{ON} \times \left({}^{\mathcal{O}}\boldsymbol{\omega}_{ON} \times {}^{\mathcal{O}}\boldsymbol{\rho}\right) \tag{2.62}$$

This second-order, vector differential equation supplies nonlinear equations of relative motion for the chaser spacecraft formulated in the Hill frame.

In the nonlinear CR3BP, the relative path of the chaser spacecraft is generated by simultaneously integrating the relative state of the chaser spacecraft and the absolute state of the target spacecraft. When the state of the target spacecraft is integrated via the equations of motion of the CR3BP from Eq. (2.26), and the relative state of the chaser spacecraft from the target spacecraft is integrated via the equations of relative motion from Eq. (2.62), the paths of the two spacecraft are generated using a system of 12 scalar and autonomous first-order differential equations.

A first-order approximation of relative motion is constructed in the Hill frame. A six-dimensional state vector, $\boldsymbol{q}$, of the chaser spacecraft relative to the target spacecraft formulated in the Hill frame is defined as

$$\boldsymbol{q} = \begin{bmatrix} \xi & \eta & \zeta & \dot{\xi} & \dot{\eta} & \dot{\zeta} \end{bmatrix}^T \tag{2.63}$$

The time derivatives of the scalar components of this relative state vector are equal to

$$\boldsymbol{q}' = \begin{bmatrix} \dot{\xi} & \dot{\eta} & \dot{\zeta} & \ddot{\xi} & \ddot{\eta} & \ddot{\zeta} \end{bmatrix}^T \tag{2.64}$$

Using these definitions, equations of relative motion that are linearized about a target spacecraft are derived using a Taylor-series expansion about the target spacecraft. These linear equations of relative motion for a state vector formulating in the Hill frame are written as

$$\boldsymbol{q}' \approx [\boldsymbol{A}_t]\boldsymbol{q} \tag{2.65}$$

where the Jacobian matrix, $[\boldsymbol{A}_t]$, is formulated using the equations of relative motion in the CR3BP that are expressed in the Hill frame and evaluated at the state of the target spacecraft, i.e., at $\boldsymbol{q} = \boldsymbol{0}$. This Jacobian matrix is equal to

$$[\boldsymbol{A}_t] = \begin{bmatrix} [\boldsymbol{0}_3] & [\boldsymbol{I}_3] \\ \frac{\partial({}^{\mathcal{O}}\boldsymbol{\rho}'')}{\partial({}^{\mathcal{O}}\boldsymbol{\rho})}\Big|_t & \frac{\partial({}^{\mathcal{O}}\boldsymbol{\rho}'')}{\partial({}^{\mathcal{O}}\boldsymbol{\rho}')}\Big|_t \end{bmatrix} \tag{2.66}$$

The lower left quadrant of the Jacobian corresponds to the partial derivative of the relative acceleration with respect to the relative position vector. Assuming an observer in the Hill frame, when evaluated at the state of the target spacecraft, the partial derivative with respect to the relative position vector is written in nondimensional quantities as

$$\frac{\partial\left({}^{\mathcal{O}}\boldsymbol{\rho}''\right)}{\partial({}^{\mathcal{O}}\boldsymbol{\rho})}\bigg|_t = -\mu\left(\frac{[\boldsymbol{I}_3]}{r_{2t}^3} - \frac{3({}^{\mathcal{O}}\boldsymbol{r}_{2t})({}^{\mathcal{O}}\boldsymbol{r}_{2t})^T}{r_{2t}^5}\right) - (1-\mu)\left(\frac{[\boldsymbol{I}_3]}{r_{1t}^3} - \frac{3({}^{\mathcal{O}}\boldsymbol{r}_{1t})({}^{\mathcal{O}}\boldsymbol{r}_{1t})^T}{r_{1t}^5}\right) - [{}^{\mathcal{O}}\tilde{\dot{\boldsymbol{\omega}}}_{ON}] - [{}^{\mathcal{O}}\tilde{\boldsymbol{\omega}}_{ON}][{}^{\mathcal{O}}\tilde{\boldsymbol{\omega}}_{ON}] \tag{2.67}$$

where $[{}^{\mathcal{O}}\tilde{\boldsymbol{\omega}}_{ON}]$ and $[{}^{\mathcal{O}}\tilde{\dot{\boldsymbol{\omega}}}_{ON}]$ are the skew-symmetric matrix representations of the cross products of ${}^{\mathcal{O}}\boldsymbol{\omega}_{ON}$ and ${}^{\mathcal{O}}\dot{\boldsymbol{\omega}}_{ON}$, respectively. Lasty, the partial derivative of the acceleration for an observer in the Hill frame with respect to the relative velocity vector, which constructs the lower right quadrant of the Jacobian, is equal to

$$\frac{\partial\left({}^{\mathcal{O}}\boldsymbol{\rho}''\right)}{\partial\left({}^{\mathcal{O}}\boldsymbol{\rho}'\right)}\bigg|_t = -2[{}^{\mathcal{O}}\tilde{\boldsymbol{\omega}}_{ON}] \tag{2.68}$$

The first-order approximation of the relative path of a chaser spacecraft is generated by simultaneously integrating the relative state of the chaser spacecraft and absolute state of target spacecraft.

Recall that these state vectors are combined to form the augmented state vector. Then, a 12×1 system of equations is formed by the nonlinear equations of motion governing the target spacecraft state in the CR3BP, as expressed by Eq. (2.26), and the linearized equations of relative motion, governing the relative state of the spacecraft and expressed in Eq. (2.65). The result is a system of 12 scalar and autonomous first-order differential equations where the motion of the target spacecraft is recovered to within the accuracy of numerical integration in the CR3BP and the motion of the chaser spacecraft is approximated via linearization about the target spacecraft.

2.3 Higher-fidelity dynamical models

While the CR3BP provides a suitable approximation of the motion of spacecraft in a three-body environment for preliminary and rapid analysis, a point mass ephemeris model of the Sun, Earth, and Moon is used to model spacecraft motion in higher-fidelity. In addition to the ephemeris configuration of gravitational bodies, acceleration due to SRP on spacecraft near the Sun-Earth libration point orbits is non-negligible, and is included in this ephemeris model using a spherical, "cannonball" approximation.

2.3.1 Inertial reference frame

In implementation, the state of spacecraft in the ephemeris model is expressed and integrated in the International Celestial Reference Frame (ICRF) [107]. The ephemeris information of celestial bodies may be used to convert between the ICRF and an instantaneous P_1-P_2 rotating frame defined by two primary bodies, i.e., the Earth and Moon or Sun and Earth. In this analyis, the NASA Jet Propulsion Laboratory DE421 ephemerides are specifcally employed, accessed via the SPICE toolkit [110]. The rotation matrix, $[\boldsymbol{C}]$, between the ICRF and a P_1-P_2 rotating frame is generally calculated using the basis vectors of the rotating frame expressed in the ICRF as

$$[\boldsymbol{C}] = \begin{bmatrix} {}^{\mathcal{N}}\hat{\boldsymbol{x}}^T \\ {}^{\mathcal{N}}\hat{\boldsymbol{y}}^T \\ {}^{\mathcal{N}}\hat{\boldsymbol{z}}^T \end{bmatrix} \tag{2.69}$$

where the rotating frame axes $\hat{\boldsymbol{x}}$, $\hat{\boldsymbol{y}}$, $\hat{\boldsymbol{z}}$ possess the same definitions as expressed in Eq. (2.9) in Section 2.1.1. Unlike the CR3BP, the celestial bodies in an ephemeris model are not assumed to travel on circular orbits and all three basis vectors expressed in the ICRF are generally time-varying. Using this rotation matrix, the transformation between the components of a position vector, $\boldsymbol{r}$, expressed in the rotating frame and the ICRF are defined as

$$ {}^{\mathcal{R}}\boldsymbol{r} = [\boldsymbol{C}] \left({}^{\mathcal{N}}\boldsymbol{r} \right) \tag{2.70} $$

$$ {}^{\mathcal{N}}\boldsymbol{r} = [\boldsymbol{C}]^T \left({}^{\mathcal{R}}\boldsymbol{r} \right) \tag{2.71} $$

where the left superscript indicates the frame in which the position vector is expressed. The instantaneous angular velocity of the rotating frame with respect to the ICRF, $\boldsymbol{\omega}_{RN}$, is used to transform the velocity vector between an observer fixed the rotating frame and an inertial observer fixed in the ICRF. This angular velocity vector is modeled as [27]

$$ \boldsymbol{\omega}_{RN} = \frac{\boldsymbol{h}_{12}}{r_{12}^2} \tag{2.72} $$

The velocity of the particle as seen by an observer in a rotating frame and expressed in the rotating frame, ${}^{\mathcal{R}}\boldsymbol{r}'$, may be computed using the inertial velocity of the particle expressed in the ICRF, ${}^{\mathcal{N}}\dot{\boldsymbol{r}}$, as

$$ {}^{\mathcal{R}}\boldsymbol{r}' = [\boldsymbol{C}] \left({}^{\mathcal{N}}\dot{\boldsymbol{r}} \right) - {}^{\mathcal{R}}\boldsymbol{\omega}_{RN} \times {}^{\mathcal{R}}\boldsymbol{r} \tag{2.73} $$

Inversely, the inertial velocity of the particle is found as a function of the velocity for an observer in the rotating frame as

$$ {}^{\mathcal{N}}\dot{\boldsymbol{r}} = [\boldsymbol{C}]^T \left({}^{\mathcal{R}}\boldsymbol{r}' + {}^{\mathcal{R}}\boldsymbol{\omega}_{RN} \times {}^{\mathcal{R}}\boldsymbol{r} \right) \tag{2.74} $$

To simplify notation, the left superscript of the term ${}^{\mathcal{R}}\boldsymbol{r}'$, is used to indicate both the observer and the frame the velocity is expressed in, i.e., ${}^{\mathcal{R}}\boldsymbol{r}' = {}^{\mathcal{R}}\mathrm{d}\,{}^{\mathcal{R}}\boldsymbol{r}/\mathrm{dt}$.

2.3.2 Point mass ephemeris model

To simulate the motion of spacecraft to a higher fidelity, a point mass ephemeris model of the Sun, Earth, and Moon with SRP is employed. Two formulations of the point mass ephemeris model are defined with different origins: a model formulated with the Earth as the central body and a model formulated with the Moon as the central body. Each model is defined by equations of motion of a spacecraft formulated in the ICRF using the NASA Jet Propulsion Laboratory DE421 ephemerides [110]. The equations of motion of the two ephemeris models are presented using dimensional quantities. However, during integration, quantities of length and time may be nondimensionalized by the constant, average characteristic quantities of the system to facilitate numerical integration and numerical correction schemes.

For integration with respect to Earth as the primary body, the state of the spacecraft is formulated and integrated in the Geocentric Celestial Reference Frame (GCRF), which uses the Earth as the origin and the axes of the ICRF. The total inertial acceleration of a spacecraft, denoted by subscript sc, relative to the Earth is expressed as [107]

$$\ddot{\boldsymbol{r}}_{E,sc} = -Gm_E \frac{\boldsymbol{r}_{E,sc}}{r^3_{E,sc}} + Gm_S \left(\frac{\boldsymbol{r}_{sc,S}}{r^3_{sc,S}} - \frac{\boldsymbol{r}_{E,S}}{r^3_{E,S}} \right) + Gm_M \left(\frac{\boldsymbol{r}_{sc,M}}{r^3_{sc,M}} - \frac{\boldsymbol{r}_{E,M}}{r^3_{E,M}} \right) + \boldsymbol{a}_{\text{srp}} \tag{2.75}$$

where subscripts E, S, and M correspond to the Earth, Sun, and Moon, respectively, and $\boldsymbol{a}_{\text{srp}}$ is the acceleration of the spacecraft due to SRP. These equations of motion assume that the mass of the spacecraft is negligible in comparison to the mass of the point mass bodies, i.e., $m_{sc} \ll m_i$. For a Moon-centered model, the equations of motion in the Moon-centered ICRF are written as

$$\ddot{\boldsymbol{r}}_{M,sc} = -Gm_M \frac{\boldsymbol{r}_{M,sc}}{r^3_{M,sc}} + Gm_S \left(\frac{\boldsymbol{r}_{sc,S}}{r^3_{sc,S}} - \frac{\boldsymbol{r}_{M,S}}{r^3_{M,S}} \right) + Gm_E \left(\frac{\boldsymbol{r}_{sc,E}}{r^3_{sc,E}} - \frac{\boldsymbol{r}_{M,E}}{r^3_{M,E}} \right) + \boldsymbol{a}_{\text{srp}} \tag{2.76}$$

For this investigation, the acceleration of the spacecraft due to SRP is approximated using a spherical model, defined as [111]

$$\boldsymbol{a}_{\text{srp}} = C_R P_S r^2_{AU} \frac{A}{m} \left(\frac{\boldsymbol{r}_{S,sc}}{r^3_{S,sc}} \right) \tag{2.77}$$

The SRP model requires the solar flux at 1 AU, P_R, and the mean distance from the Sun to the Earth, r_{AU}. The reflectivity coefficient of the spacecraft, C_R, the surface-area-to-mass ratio of the spacecraft, A/m, are dependent on the specific spacecraft model. The SRP and gravitational parameters, Gm, values are consistent with the NASA Goddard General Mission Analysis Tool

(GMAT) [112]. These values are summarized in Table 2.2. Throughout this investigation, this dynamical model is referred to as the ephemeris model for brevity.

Table 2.2: Parameters of the point mass ephemeris model with SRP used in this investigation.

Parameter	Value
G	6.6730×10^{-20} km^3/(kg s^2)
M_E	3.986004415×10^5 km^2/s^3
M_S	$1.3271244001799 \times 10^{11}$ km^2/s^3
M_M	$4.9028005821478 \times 10^3$ km^2/s^3
P_R	$4.5598211813587 \times 10^{-3}$ kg /(km s^2)
r_{AU}	$1.49597870691 \times 10^8$ km

Chapter 3

Particular Solutions and Numerical Methods

The CR3BP admits several fundamental solutions, including five equilibrium points and an infinite variety of periodic orbits, quasi-periodic orbits, and chaotic motion. Of particular interest are periodic orbits, which may enable the identification of bounded reference motion for spacecraft missions, and the complex design space associated with the motion of spacecraft relative to a periodic orbit. This chapter presents an overview of particular solutions of the CR3BP, with a specific focus on motion relative to a periodic orbit. First, the locations of the five equilibrium points of the CR3BP are derived. Next, a discussion on Floquet Theory and evaluating the stability of a periodic orbit in the CR3BP is presented. The local stability of periodic orbits supplies information for the computation of other solutions in the CR3BP, including quasi-periodic orbits. This section also details the various numerical methods employed in this investigation to compute solutions in the CR3BP and to transition solutions from the CR3BP to higher-fidelity models.

3.1 Equilibrium points

The CR3BP admits five equilibrium points for motion formulated in the rotating frame. These equilibrium points are determined via analysis of the pseudo-potential of the CR3BP, U^*. At each equilibrium point, the partial derivatives of the pseudo-potential equal zero, i.e.,

$$\frac{\partial U^*}{\partial x} = \frac{\partial U^*}{\partial y} = \frac{\partial U^*}{\partial z} = 0 \tag{3.1}$$

A spacecraft placed at one of these points with zero velocity will remain at the point indefinitely in the CR3BP. Analysis of the pseudo-potential along the x-axis reveals the existence of three equilibrium points, labeled the collinear equilibrium points [24]. Along this axis, $y = z = 0$ and the partial derivatives of the pseudo-potential, $\partial U^*/\partial y$ and $\partial U^*/\partial z$, equal zero. Evaluating the partial derivative of the pseudo-potential with respect to x, $\partial U^*/\partial x$, along the x-axis, two singularities are observed at the locations of P_1 and P_2, located at $x = \mu$ and $x = 1 - \mu$, respectively. The partial derivative of the pseudo-potential, $\partial U^*/\partial x$, possesses three distinct zeros along this axis, indicating the existence of the three collinear equilibrium points, identified as L_1, L_2, and L_3. The L_1 equilibrium point lies on the $\hat{\boldsymbol{x}}$-axis within the range $-\mu < x_{L1} < (1 - \mu)$, L_2 possesses an x coordinate greater than P_2 such that $(1 - \mu) < x_{L2}$, and L_3 lies to the left of P_1 when visualized in the rotating frame such that $x_{L3} < -\mu$. Because no analytical solution exists to solve for the location of the collinear equilibrium points along the $\hat{\boldsymbol{x}}$-axis, a root-finding method, such as a Newton-Raphson method, may be employed to compute the solutions to $\partial U^*/\partial x = 0$.

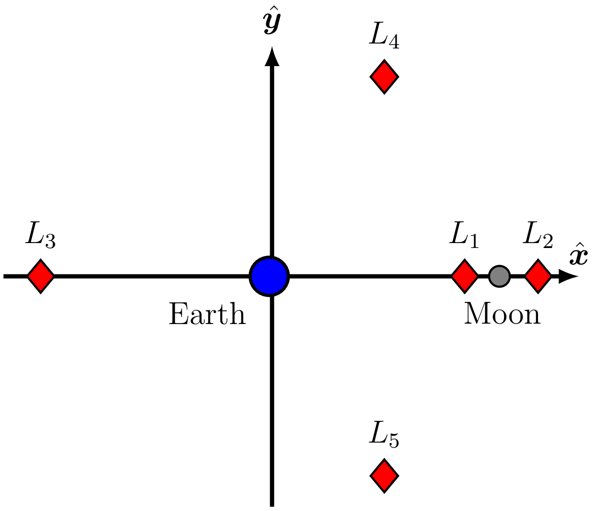

Figure 3.1: Locations of the Earth, Moon, and five equilibrium points in the Earth-Moon CR3BP.

Two additional equilibrium points of the CR3BP exist in the rotating frame. These equilibrium points are denoted as the triangular equilibrium points, L_4 and L_5. Together with the locations of P_1 and P_2, the triangular equilibrium points form equilateral triangles in the configuration space [24]. The x-coordinates of L_4 and L_5 are both equal to $x = (1/2 - \mu)$ and the y-coordinates of L_4 and L_5 are equal to $y = \sqrt{3}/2$ and $y = -\sqrt{3}/2$, respectively. The locations of the five equilibrium points of the Earth-Moon CR3BP are illustrated along with the locations of the Earth and Moon in the rotating frame in Figure 3.1.

3.2 Periodic orbits

Periodic orbits are a fundamental solution of the CR3BP that exactly repeat in the rotating frame after one orbital period and exist in continuous, single-parameter families. A fixed point is defined as a state along the periodic orbit that supplies an initial condition, $\boldsymbol{x}(t_0)$, that when integrated in the CR3BP satisfies the condition $\boldsymbol{x}(t_0) = \boldsymbol{x}(t_0 + T)$, where T is the period of the orbit in the rotating frame. Periodic orbits in the CR3BP exhibit an infinite variety of geometries and exist in continuous families distributed across the P_1-P_2 system. Periodic orbit families may emanate from the equilibrium points, primary bodies, or bifurcations from different periodic orbit families [113].

To support discussion, three periodic orbits are specified for use as reference orbits in the analysis throughout this investigation. The three orbits are members of different families in the Earth-Moon and Sun-Earth systems and are selected due to their current interest in the community, as well as potential relevance in upcoming mission. The three periodic orbits are selected as:

(1) An Earth-Moon L_2 southern near-rectilinear halo orbit with a period of 8 days and is of particular interest due to the upcoming Gateway infrastructure [18]. Specifically, the trajectory of Gateway is derived from a member of the orbit family labeled near-rectilinear and is characterized by a low perilune and very high apolune. This orbit is plotted in the Earth-Moon rotating frame in Figure 3.2.

(2) A distant retrograde orbit in the Earth-Moon system with a period of 7 days. This orbit lies within the xy plane of the Earth-Moon rotating frame, and when visualized in the rotating frame, closely orbits the Moon in a near-circular, retrograde motion. This orbit is a good candidate for the description and analysis of relative motion formulated in a P_2 Hill frame because of the close proximity of the orbit to the primary. From this perspective,

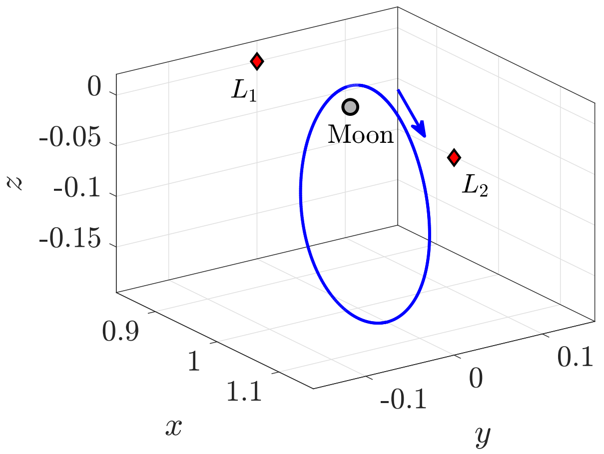

Figure 3.2: An 8-day Earth-Moon L_2 southern near-rectilinear halo orbit.

interesting parallels may be drawn between relative motion in the CR3BP and Keplerian relative motion near circular orbits. This orbit is plotted in the Earth-Moon rotating frame in Figure 3.3.

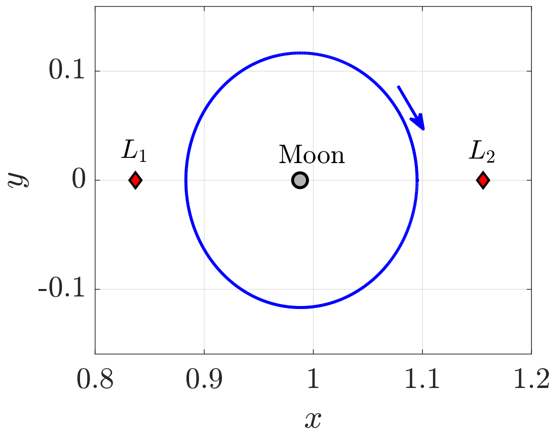

Figure 3.3: A 7-day Earth-Moon distant retrograde orbit.

(3) A Sun-Earth L_1 southern halo orbit with a period of 177 days. Members of the associated orbit family have been previously used as a reference for the trajectory design of previous missions, including ISEE-3 and SOHO [90]. This orbit is plotted in the Sun-Earth rotating frame in Figure 3.4.

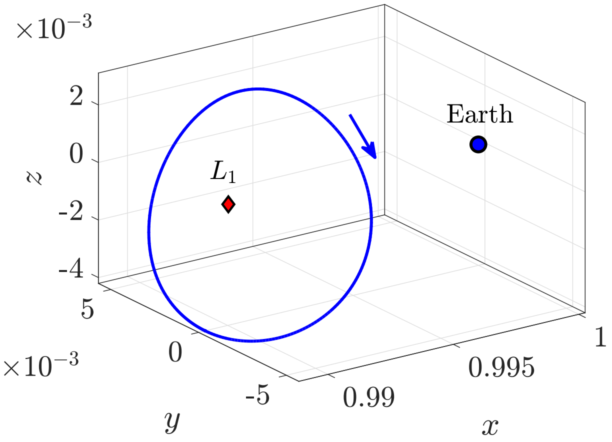

Figure 3.4: A 177-day Sun-Earth L_1 southern halo orbit.

These reference orbits supply a variety of geometric and stability characteristics to support demonstrations of the relative motion analysis in this investigation. For each orbit, the period in days, the Jacobi constant, and a fixed point along each orbit are summarized in Table 3.1.

Table 3.1: Summary of reference periodic orbits in the CR3BP used throughout this investigation.

System	Orbit family	Period (days)	Jacobi constant	Initial conditions, $\boldsymbol{x}_0$ (nondimensional)
Earth-Moon	L_2 southern halo	8	3.0271	$[1.0465, 0, -0.1950, 0, -0.1507, 0]^T$
Earth-Moon	Distant retrograde	7	2.9976	$[1.0951, 0, 0, 0, -0.4611, 0]^T$
Sun-Earth	L_1 southern halo	177	3.0007	$[0.9891, 0, -0.0042, 0, 0.0110, 0]^T$

3.2.1 Periodic orbit stability

As the dynamics of spacecraft in close proximity to a periodic orbit is largely governed by linearization about the periodic orbit, stability analysis of periodic orbits is closely coupled with relative motion analyses. To evaluate the stability of a periodic orbit, the motion of a state perturbed from a periodic orbit is investigated following the process detailed by Koon et. al [24]. Let $\boldsymbol{x}_r(t)$ be an initial condition along a reference periodic orbit and $\delta\boldsymbol{x}(t)$ define a small displacement from $\boldsymbol{x}_r(t)$. The initial condition of a trajectory corresponding to this displacement that neighbors the periodic orbit is equal to

$$\boldsymbol{x}(t) = \boldsymbol{x}_r(t) + \delta\boldsymbol{x}(t) \tag{3.2}$$

The time derivative of this expression for an observer in the rotating frame may be expressed as

$$\boldsymbol{x}'(t) = \boldsymbol{f}(\boldsymbol{x}_r(t) + \delta\boldsymbol{x}(t)) \tag{3.3}$$

where $\boldsymbol{f}$ represents the nonlinear differential equations for a state vector in the CR3BP. Next, the first-order Taylor series expansion of $\boldsymbol{x}'(t)$ about the reference trajectory is expressed as

$$\boldsymbol{x}'(t) \approx \boldsymbol{x}_r'(t) + \frac{\partial\boldsymbol{x}_r'(t)}{\partial\boldsymbol{x}_r(t)}\delta\boldsymbol{x}(t) \tag{3.4}$$

The partial derivative, $\partial\boldsymbol{x}_r'(t)/\partial\boldsymbol{x}_r(t)$, is equal to the Jacobian matrix, $[\boldsymbol{A}]$, expressed in Eq. (2.35), evaluated at the reference periodic orbit in the CR3BP. Rearranging Eq. (3.4), the first-order approximation of the rate of change of the displaced state, defined as $\delta\boldsymbol{x}'(t) = \boldsymbol{x}'(t) - \boldsymbol{x}_r'(t)$, is then equal to

$$\delta\boldsymbol{x}'(t) = [\boldsymbol{A}(t)]\delta\boldsymbol{x}(t) \tag{3.5}$$

This vector differential equation also serves as the linear equations of relative motion for the CR3BP, as discussed in Section 2.2.1.

With the evolution of a displacement from a periodic orbit shown to be a function of the Jacobian evaluated at the periodic orbit, the discrete mapping between two instances of time is investigated. Consider the state $\boldsymbol{x}(t_0)$ at an initial time, t_0. The state of the associated trajectory at time t may be expressed in terms of this initial condition and the flow map from t_0 to t, $\boldsymbol{\phi}$, as

$$\boldsymbol{x}(t) = \boldsymbol{\phi}(\boldsymbol{x}(t_0), t) \tag{3.6}$$

The first-order Taylor series expansion of this expression for $\delta\boldsymbol{x}(t)$ about the reference trajectory is expressed as

$$\boldsymbol{x}(t) \approx \boldsymbol{\phi}(\boldsymbol{x}_r(t_0), t) + \frac{\partial\boldsymbol{\phi}(\boldsymbol{x}_r(t_0), t)}{\partial\boldsymbol{x}_r(t_0)}\delta\boldsymbol{x}(t_0) \tag{3.7}$$

This expression may be rearranged to solve for the first-order approximation of the displacement at time t as

$$\delta\boldsymbol{x}(t) = \frac{\partial\boldsymbol{x}_r(t)}{\partial\boldsymbol{x}_r(t_0)}\delta\boldsymbol{x}(t_0) \tag{3.8}$$

The partial derivative, $\partial \boldsymbol{x}_r(t)/\partial \boldsymbol{x}_r(t_0)$, is labeled the state transition matrix (STM), $[\boldsymbol{\Phi}]$. Thus, the STM offers a linear mapping of the displacement from the periodic orbit between two times. In this investigation, mapping between an initial displacement, $\delta\boldsymbol{x}(t_0)$ at time t_0, to a displacement, $\delta\boldsymbol{x}(t)$ at time t, is expressed using the following notation

$$\delta\boldsymbol{x}(t) = [\boldsymbol{\Phi}(t,t_0)]\delta\boldsymbol{x}(t_0) \tag{3.9}$$

A mapping of a displacement from t_0 to t using an STM produces equivalent results as integrating the initial displacement for a time $(t-t_0)$ via the Jacobian matrix [114]. Equation (3.9) also reveals that the mapping of the displacement backwards in time, from t to t_0, is found by inverting the STM as

$$\delta\boldsymbol{x}(t_0) = [\boldsymbol{\Phi}(t,t_0)]^{-1}\delta\boldsymbol{x}(t) \tag{3.10}$$

Or alternatively, the inverse of the STM may be expressed as $[\boldsymbol{\Phi}(t,t_0)]^{-1} = [\boldsymbol{\Phi}(t_0,t)]$.

The state transition matrix along a periodic orbit in the CR3BP may be computed via numerical integration. To derive the differential equations which are used to compute the STM, first consider the time derivative of Eq. (3.9), which reveals the relation:

$$\delta\boldsymbol{x}'(t) = \frac{\mathrm{d}[\boldsymbol{\Phi}(t,t_0)]}{\mathrm{dt}}\delta\boldsymbol{x}(t_0) \tag{3.11}$$

Note that $\mathrm{d}\left(\delta\boldsymbol{x}(t_0)\right)/\mathrm{dt}$ drops out because $\boldsymbol{x}(t_0)$ is a constant [114]. Substituting in Eq. (3.5) and Eq. (3.9), this expression may be rewritten as

$$[\boldsymbol{A}(t)][\boldsymbol{\Phi}(t,t_0)]\delta\boldsymbol{x}(t_0) = \frac{\mathrm{d}[\boldsymbol{\Phi}(t,t_0)]}{\mathrm{dt}}\delta\boldsymbol{x}(t_0)$$

Thus, the STM satisfies the matrix differential equation [24]:

$$\frac{\mathrm{d}}{\mathrm{dt}}[\boldsymbol{\Phi}(t,t_0)] = [\boldsymbol{A}(t)][\boldsymbol{\Phi}(t,t_0)] \tag{3.12}$$

The initial condition of this differential equation, $[\boldsymbol{\Phi}(t_0,t_0)]$, is simply the 6 × 6 identity matrix [114]. In implementation, the state of the reference periodic orbit and the components of the STM are integrated simultaneously in an augmented ODE from the initial to the final time. This implementation returns the exact value of the STM to within the tolerances of the numerical integration scheme. Alternatively, the STM mapping between two times may be approximated via numerical finite-differencing schemes.

The STM evaluated along a periodic orbit for one period is labeled the monodromy matrix and is an important solution for evaluating the stability of a periodic orbit. The monodromy matrix, $[\boldsymbol{M}]$, may be calculated from any initial point along the periodic orbit. For an initial time, t, and orbit period, T, the monodromy matrix is defined as

$$[\boldsymbol{M}(t)] = [\boldsymbol{\Phi}(t+T,t)] \tag{3.13}$$

The eigenvalues, λ, and eigenvectors, $\boldsymbol{w}$, of the monodromy matrix indicate the stability of the periodic orbit. The eigenvalues of the monodromy matrix do not depend on the associated fixed point at which the matrix is computed. Consider the relationship between the monodromy matrix evaluated at two times, t_1 and t_2, labeled $[\boldsymbol{M}(t_1)]$ and $[\boldsymbol{M}(t_2)]$, respectively, that is mathematically expressed as

$$\begin{aligned}
[\boldsymbol{M}(t_2)] &= [\boldsymbol{\Phi}(t_2+T,t_2)] \\
&= [\boldsymbol{\Phi}(t_2+T,t_1+T)][\boldsymbol{\Phi}(t_1+T,t_1)][\boldsymbol{\Phi}(t_1,t_2)] \\
&= [\boldsymbol{\Phi}(t_1,t_2)]^{-1}[\boldsymbol{M}(t_1)][\boldsymbol{\Phi}(t_1,t_2)]
\end{aligned}$$

This similarity transformation reveals that the eigenvalues of the monodromy matrix are preserved along the orbit. Furthermore, the eigenvalues of the monodromy matrix are also preserved when reformulated in a different reference frame in which the periodicity of the orbit is preserved. For instance, the eigenvalues of the monodromy matrix formulated in the rotating frame are equivalent to the eigenvalues of the monodromy matrix formulated the Hill frame. In this case, another similarity transformation reveals the preservation of the eigenvalues between the transformation between the two frames.

The eigenvectors of the monodromy matrix reflect the span of each eigenspace of the periodic orbit at the associated fixed point. The eigenvectors, and thus the span of each eigenspace, evolves along each orbit. Thus, the location at which the monodromy matrix and associated eigenvectors are computed along a periodic orbit must be considered when assessing the direction of each eigenspace. For an eigenvector, $\boldsymbol{w}(t_0)$, of the monodromy matrix evaluated at a fixed point, $\boldsymbol{x}(t_0)$, the eigenvector at a different fixed point, $\boldsymbol{x}(t)$, is found via a mapping of the STM as [115]

$$\boldsymbol{w}(t) = [\boldsymbol{\Phi}(t, t_0)]\boldsymbol{w}(t_0) \tag{3.14}$$

Furthermore, consider the relationship of an eigenvalue and eigenvector pair of the monodromy matrix, expressed as

$$[\boldsymbol{M}(t_0)]\boldsymbol{w}(t_0) = \lambda \boldsymbol{w}(t_0) \tag{3.15}$$

The left side of this expression maps the eigenvector at time t_0 to one period forward in time. Accordingly, an eigenvector after one period of the orbit, $\boldsymbol{w}(t_0 + T)$, is related to the eigenvector, $\boldsymbol{w}(t_0)$, at the initial time and the associated eigenvalue as

$$\boldsymbol{w}(t_0 + T) = \lambda \boldsymbol{w}(t_0) \tag{3.16}$$

This mapping may reflect expansion, contraction, or oscillations depending on the specific mode.

Because of the symplectic nature of STMs in the CR3BP, each eigenvalue of an STM exists in a reciprocal pair [115]. Furthermore, the monodromy matrix of a periodic orbit will always admit a pair of trivial eigenvalues equal to unity, indicating the periodicity of the orbit and existence of the orbit in a single-parameter family [63]. The four remaining nontrivial eigenvalues of the monodromy matrix indicate the existence of stable, unstable, oscillatory, or spiral modes. Stable and unstable modes are identified by a pair of real, reciprocal eigenvalues. An eigenvalue corresponding to a stable mode, λ_s, will possess a magnitude of less than 1. An eigenvalue corresponding to an unstable mode will possess a magnitude of greater than one, equal to the inverse of the stable eigenvalue, i.e., $\lambda_u = 1/\lambda_s$. Complex eigenvalues that lie on the unit circle possess a magnitude equal to unity, thus exist in complex conjugate pairs corresponding to an oscillatory mode. Finally, in the case of complex eigenvalues that do not lie on the unit circle, for a single eigenvalue, both the complex conjugate and the reciprocal of this eigenvalue exist as eigenvalues of the monodromy matrix, such that a set of four complex eigenvalues is formed [115]. These eigenvalues correspond to spiral modes that combine both oscillatory motion with stable or unstable motion, determined by the magnitude of the eigenvalue. Example locations of these types of eigenvalues in the complex plane are illustrated in Figure 3.5. Along the real axis, the two trivial eigenvalues are plotted in black, a stable eigenvalue is plotted in blue, unstable eigenvalues is plotted in red, Along the unit circle, complex eigenvalues corresponding to an oscillatory mode are plotted. Finally, in the most general case, four complex conjugate pairs that do not lie on the unit circle are plotted in cyan.

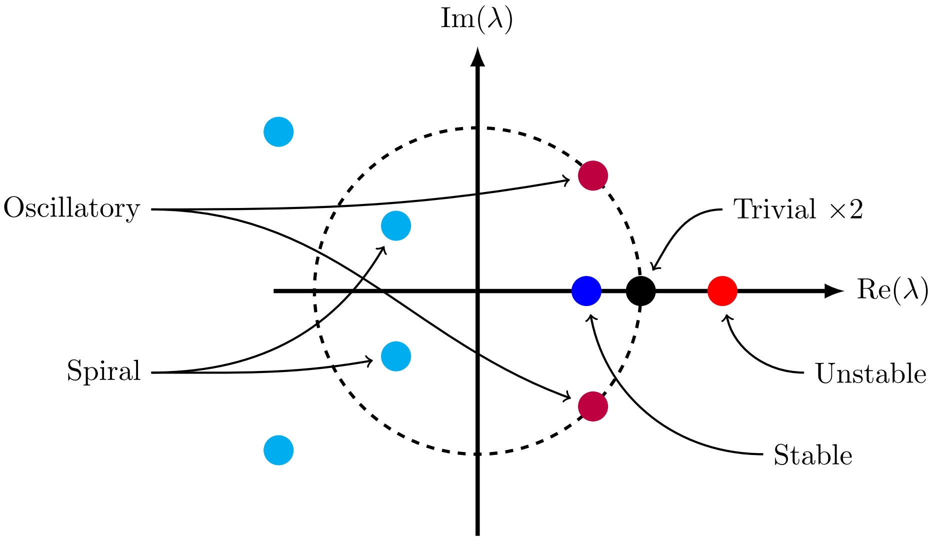

Figure 3.5: Examples of the types of eigenvalues of the monodromy matrix of a periodic orbit in the CR3BP, plotted within the complex plane.

In this investigation, the stability of a periodic orbit is summarized via two stability indices. The two stability indices, labeled s_1 and s_2, are defined as the sum of each pair of nontrivial eigenvalues [33]. For a stable/unstable eigenvalue pair, λ_s and λ_u, respectively, the corresponding stability index is equal to

$$s = \lambda_s + \lambda_u = \lambda_s + \frac{1}{\lambda_s} \tag{3.17}$$

For a complex conjugate eigenvalue pair, λ_{ij}, the corresponding stability index is equal to

$$s = \lambda_i + \lambda_j = 2\,\mathrm{Re}(\lambda_i) \tag{3.18}$$

Note that this formulation of the stability index does not capture the instability of orbits that possess complex eigenvalues with magnitudes greater than one, i.e., that possess spiraling modes. For the stability characterization of perioidc orbits that possess these types of modes, alternative stability index definitions may be applied [116]. However, for periodic orbits that do not possess complex eigenvalues of the monodromy matrix that lie off of the unit circle, this formulation of stability indices indicates an unstable orbit if either of the indices possess a magnitude greater than two. A stable orbit is identified when both stability indices possess a magnitude of less than or equal to two.

Table 3.2: Stability indices of the reference periodic orbits used throughout this investigation.

System	Orbit family	Period (days)	s_1	s_2
Earth-Moon	L_2 southern halo	8	0.65937	-3.38227
Earth-Moon	Distant retrograde	7	0.69689	0.04099
Sun-Earth	L_1 southern halo	177	1099.39	1.72345

The stability of the three reference orbits of this investigation is assessed via computation of their stability indices. The three periodic orbits admit stable, unstable, and oscillatory modes; none of the reference orbits possess a monodromy matrix with complex eigenvalues that lie off of the unit circle. The stability indices of each orbit are listed in Table 3.2. The Earth-Moon NRHO is observed to be weakly stable, since the s_1 index possesses a magnitude of less than two and the s_1 index possesses a magnitude that is just greater than two. Next, the stability indices of the Earth-Moon DRO indicate a stable orbit that possesses two oscillatory modes. One of the oscillatory modes of the DRO is restricted to motion in the xy plane while the other oscillatory mode corresponds to out-of-plane motion. Finally, the stability indices of the Sun-Earth L_1 halo orbit indicates the existence of a pair of stable/unstable modes and a pair of oscillatory modes. Thus, the orbit is unstable and admits hyperbolic stable and unstable manifolds as well as nearby quasi-periodic motion.

3.2.2 Floquet theory

Floquet theory supplies useful analyses for linear time-periodic systems, such as linear motion in the vicinity of a periodic orbit in the CR3BP. Recall Eq. (3.5), which expresses the differential equations that governs linear motion relative to a periodic orbit in terms of the Jacobian matrix, $[\boldsymbol{A}]$, evaluated along a periodic orbit in the CR3BP. When evaluated along a periodic orbit, the Jacobian matrix is periodic with T, i.e., $[\boldsymbol{A}(t_0)] = [\boldsymbol{A}(t_0 + T)]$. Floquet theory states the an STM evaluated in a linear time periodic system between time t_0 to time t may be decomposed as [24]

$$[\boldsymbol{\Phi}(t, t_0)] = [\boldsymbol{P}(t)] \exp\left([\boldsymbol{B}](t - t_0)\right) \tag{3.19}$$

where $[\boldsymbol{P}]$ is a time periodic matrix of period T and $[\boldsymbol{B}]$ is a constant matrix [24]. When $t = t_0$, Eq. (3.19) yields the initial condition $[\boldsymbol{P}(t_0)] = [\boldsymbol{\Phi}(t, t_0)] = [\boldsymbol{I}_6]$. Floquet theory additionally states that the STM may also be decomposed as [62]

$$[\boldsymbol{\Phi}(t, t_0)] = [\boldsymbol{F}(t)] \exp([\boldsymbol{J}](t - t_0))[\boldsymbol{F}(t_0)]^{-1} \tag{3.20}$$

where $[\boldsymbol{F}]$ is a time periodic matrix that contains the Floquet modes of the periodic orbit in each column and $[\boldsymbol{J}]$ is a constant block diagonal matrix of the eigenvalues of $[\boldsymbol{B}]$. Evaluating Eq. (3.20) at time $(t_0 + T)$, reveals that $[\boldsymbol{F}(t_0)]$ is equal to the generalized eigenvectors of the monodromy matrix computed at t_0 and $\exp([\boldsymbol{J}]T)$ is a block diagonal matrix formed from the eigenvalues of the monodromy matrix. Thus, $[\boldsymbol{J}]$ is also diagonal. The diagonal terms of $[\boldsymbol{J}]$ are labeled the Floquet exponents of the periodic orbit, σ, and relate the eigenvalues of the monodromy matrix, λ, as [61]

$$\sigma_i = \frac{\ln(\lambda_i)}{T} \tag{3.21}$$

With this definition, Floquet exponents equal to zero correspond to the trivial, unity eigenvalues of the monodromy matrix, purely imaginary Floquet exponents correspond to oscillatory motion, and stable and unstable modes are identified by positive or negative Floquet exponents, respectively. To constrain the values of $[\boldsymbol{F}]$ and $[\boldsymbol{J}]$ to be real valued, the real Jordan normal forms of $[\boldsymbol{F}]$ and $[\boldsymbol{J}]$ may be used [61].

The Floquet modes of a periodic orbit form a time periodic basis that captures the span of each mode. Each Floquet mode, labeled $\overline{\boldsymbol{w}}$, may be calculated from the associated Floquet exponent and eigenvector as [24]

$$\overline{\boldsymbol{w}}_i(t) = \exp\left(-\sigma_i(t - t_0)\right) \boldsymbol{w}_i(t) \tag{3.22}$$

This relationship illustrates that the direction of each Floquet mode, $\overline{\boldsymbol{w}}$, is the same as the associated eigenvector, $\boldsymbol{w}(t)$. While Floquet modes are time periodic over T, eigenvectors are not, and instead may grow or decay exponentially or oscillate over time depending on the type of mode. When using the real Jordan normal form of $[\boldsymbol{F}]$ and $[\boldsymbol{J}]$, the matrix of Floquet modes at time t is equal to [117]

$$[\boldsymbol{F}(t)] = [\boldsymbol{\Phi}(t, t_0)][\boldsymbol{F}(t_0)] \exp(-[\boldsymbol{J}](t - t_0)) \tag{3.23}$$

where the initial conditions, $[\boldsymbol{F}(t_0)]$, are the set of linearly independent generalized eigenvectors of the monodromy matrix. Alternatively, the Floquet modes may be computed as [93]

$$[\boldsymbol{F}(t)] = [\boldsymbol{P}(t)][\boldsymbol{F}(t_0)] \tag{3.24}$$

Note that Floquet modes normalized at an initial time will not stay normalized over the entire period of the orbit [97].

As the two trivial unity eigenvalues of the monodromy matrix correspond to a repeated eigenvector, the monodromy matrix is defective, i.e., a full set of linearly independent eigenvectors does not exist [118]. This a property of the existence of the periodic orbit in a single parameter family in a Hamiltonian system [63]. Furthermore, due to the limitations of numerical eigenvalue solvers, an eigendecomposition of the monodromy matrix typically returns values of trivial eigenvalues with a small numerical error such that the trivial eigenvalues lie close to $\lambda = 1$ to within a small numerical tolerance. As a result, the eigenvectors corresponding to the two unity eigenvalues will differ by a large enough numerical error that the set of eigenvectors incorrectly forms a full-rank matrix. Thus, careful implementation of Floquet mode analyses is required to account for this numerical inconsistency and to construct a set of linearly independent generalized eigenvectors.

To compute the generalized eigenvector associated with the trivial eigenvalue pair of a periodic orbit in the CR3BP, first, the limitations of the numerical eigendecomposition solver must be recognized. Several procedures for computating a generalized eigenvector of the monodromy matrix have been presented, including approaches by Wiesel and Pohlen [62] and Dichmann et al. [119]. Following the process presented by Wiesel and Pohlen, a generalized eigenvector, $\boldsymbol{g}$, corresponding to the trivial eigenvalues may be computed using the relationship with the repeated eigenvector, $\boldsymbol{w}$, as [62]:

$$([\boldsymbol{M}] - [\boldsymbol{I}_6])\,\boldsymbol{g} = T\boldsymbol{w} \tag{3.25}$$

where the inclusion of the period, T, enables the generalized eigenvector to be periodic [62]. Since $([\boldsymbol{M}] - [\boldsymbol{I}_6])$ is not full rank, the constraint $\boldsymbol{w}^T\boldsymbol{g} = 0$ is substituted as the first row of $([\boldsymbol{M}] - \lambda_1[\boldsymbol{I}_6])$ to constrain the generalized eigenvector to lie orthogonal to the repeated eigenvector [62]. Solving this system of equations produces a generalized eigenvector corresponding to $\lambda = 1$ that lies tangent to the direction of the orbit family.

The repeated eigenvector and associated generalized eigenvector possess useful phyiscal interpretations of different motions relative to a periodic orbit. A conceptual illustration of the repeated eigenvector and the associated generalized eigenvector is included in Figure 3.6 to visualize the interpretation of each vector. Exciting motion along the span of the repeated eigenvector corresponds to motion along the direction of the periodic orbit. Linearizing the dynamics about the periodic orbit, relative motion that excites this mode is periodic with respect to the motion of the original fixed point used to compute the eigenvectors. This type of relative motion may be leveraged to design "string-of-pearls" formations, in which multiple spacecraft form a bounded configuration by traveling along the same orbit at different phasing [50]. The generalized eigenvector points in the direction of a nearby periodic orbit of the same orbit family [62]. Exciting motion along the span of the generalized eigenvector produces mildly unstable relative motion caused by the difference in periods of the two periodic orbits. Initial conditions along this span will result in secular drift from the periodic orbit, which may be leveraged for orbit phasing reconfiguration.

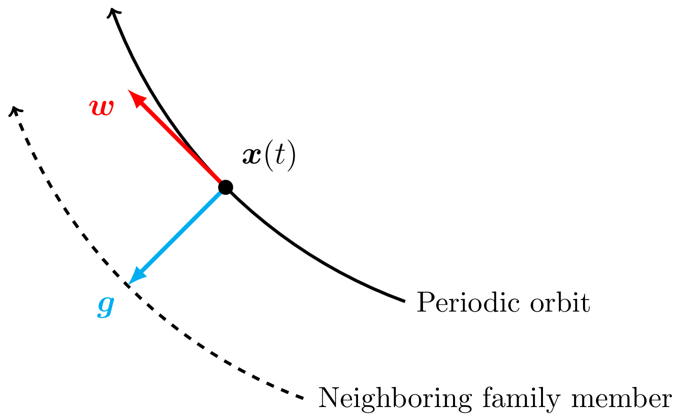

Figure 3.6: Conceptual interpretation of the repeated eigenvector, $\boldsymbol{w}$, associated with the trivial eigenvlaues of the monodromy matrix and the corresponding generalized eigenvector, $\boldsymbol{g}$. Adapted from [63].

The Floquet modes of a periodic orbit may be used to form a basis set to compute a set of modal coordinates to describe motion relative to a periodic orbit. The modal coordinates, labeled $\boldsymbol{c}$, which indicate the direction of the displacement from the periodic orbit along each mode, are computed as [63]

$$\boldsymbol{c}(t) = [\boldsymbol{F}(t)]^{-1}\delta\boldsymbol{x}(t) \tag{3.26}$$

where $\delta\boldsymbol{x}(t)$ is a displacement from the periodic orbit. The evolution of these coordinates is described as [63]

$$\frac{\mathrm{d}}{\mathrm{dt}}\boldsymbol{c}(t) = [\boldsymbol{J}]\boldsymbol{c}(t) \tag{3.27}$$

Because $[\boldsymbol{J}]$ is a constant matrix, the modal coordinates may be mapped between two times as

$$\boldsymbol{c}(t) = \exp\left([\boldsymbol{J}](t - t_0)\right)\boldsymbol{c}(t_0) \tag{3.28}$$

Thus, the monodromy matrix formulated in this state representation is equal to $[\boldsymbol{M}] = \exp([\boldsymbol{J}]T)$, which is simply the Jordan normal form of the Floquet exponents of the periodic orbit. These Floquet modal coordinates are useful for the design of relative motion about a general time-periodic orbit as well as Floquet model control schemes as demonstrated by Simó et al. [100]. However, the time-varying description of motion along the center eigenspace and ambiguity of the eigenvectors of the monodromy matrix motivate the presented investigation into new strategies and coordinate systems for describing motion relative to periodic orbits.

3.3 Quasi-periodic orbits

Center manifolds exist in the vicinity of a periodic orbit that possesses an oscillatory mode [120]. In the CR3BP, motion within a center manifold of a periodic orbit includes quasi-periodic orbits that trace the surface of an invariant torus. A periodic orbit with a single oscillatory mode will admit nearby invariant 2-tori, while a stable periodic orbit with two oscillatory modes admits nearby quasi-periodic orbits that trace the surface of higher-dimensional 3-tori, governed by additional fundamental frequencies [70]. Part of the material in this section was first published by Celestial Mechanics and Dynamical Astronomy in 2022 by Springer Nature [108].

3.3.1 Invariant 2-tori

The computation of invariant tori in the nonlinear CR3BP has been the focus of several studies [67, 68, 69, 70]. The process formulated by Olikara and Scheeres focuses on computing an invariant torus by directly calculating an invariant curve, defined as a set of states for which motion initialized on the set returns to the same set after a stroboscopic mapping time, rotated by an angle governed by the other fundamental frequencies of the torus. Through this approach, a two-dimensional invariant 2-torus may be computed via a numerical corrections process using a first-order approximation of an invariant curve as an initial guess. This initial guess is constructed using the complex eigenvector of the monodromy matrix, computed at a selected fixed point of the periodic orbit. The first fundamental frequency of a torus close to the periodic orbit is approximated by the period of the orbit. The rotation angle after each return to the invariant curve is approximated by the rotation of oscillatory motion in the linear systems, calculated from the complex eigenvalue corresponding to the oscillatory mode. Using this initial guess, an invariant torus in the nonlinear CR3BP may be computed by constraining nonlinear invariance conditions and varying both the fundamental frequencies of the solution and the locations of a discrete number of states along the invariant curve via a numerical shooting scheme [70]. While quasi-periodic orbits in the vicinity of a periodic orbit share similar geometric characteristics as the associated periodic orbit, quasi-periodic orbits associated with 2-tori exist in two-parameter continuous families in the CR3BP [121]. Continuation schemes may be applied to compute quasi-periodic orbits along these familes, revealing complex evolutions in the geoemtry of the tori along the families [122].

Examples of quasi-periodic orbits in the Sun-Earth CR3BP and their associated invariant 2-torus are examined. Quasi-periodic orbits exist that within a two-dimensional family emanating from a 177-day Sun-Earth L_1 southern halo orbit are computed using the process introduced by Olikara and Scheeres [70]. The stability analysis of this halo orbit, summarized in Table 3.2, reveals the periodic orbit possesses an oscillatory mode associated with s_2, and thus, admits nearby invariant 2-tori. Twelve quasi-periodic orbits that possess the same Jacobi constant as the L_1 halo orbit and a stroboscopic mapping time equal to 178.2 days are computed and propagated for one mapping time, plotted in blue in Figure 3.7a in the Sun-Earth rotating frame along with the halo orbit in black. Each quasi-periodic orbit is numerically integrated from an initial invariant curve defined near apogee of the L_1 halo orbit for one stroboscopic mapping time. Over infinite time, each quasi-periodic orbit traces the entire surface of the associated invariant 2-torus, visualized in Figure 3.7b.

Quasi-periodic orbits possess complicated state descriptions in the rotating frame which vary without repeating over time. Action-angle coordinates have been a useful representation for the description and interpretation of motion tracing the surface of an invariant torus in a Hamiltonian system [58]. In an action-angle representation, for an n-dimensional torus, n action coordinates are used to describe the surface of an invariant torus and n an angle coordinates locate a state on the torus, varying over time at a constant rate governed by each of the fundamental frequencies of the torus [58]. Action-angle coordinates offer a useful representation of a torus, however, mapping action-angle coordinates to the position and velocity of a quasi-periodic orbit in the CR3BP is generally a computationally intensive process [59, 60]. For analysis at a small separation from a periodic orbit, linear approximations of action-angle coordinates have also been investigated [123].

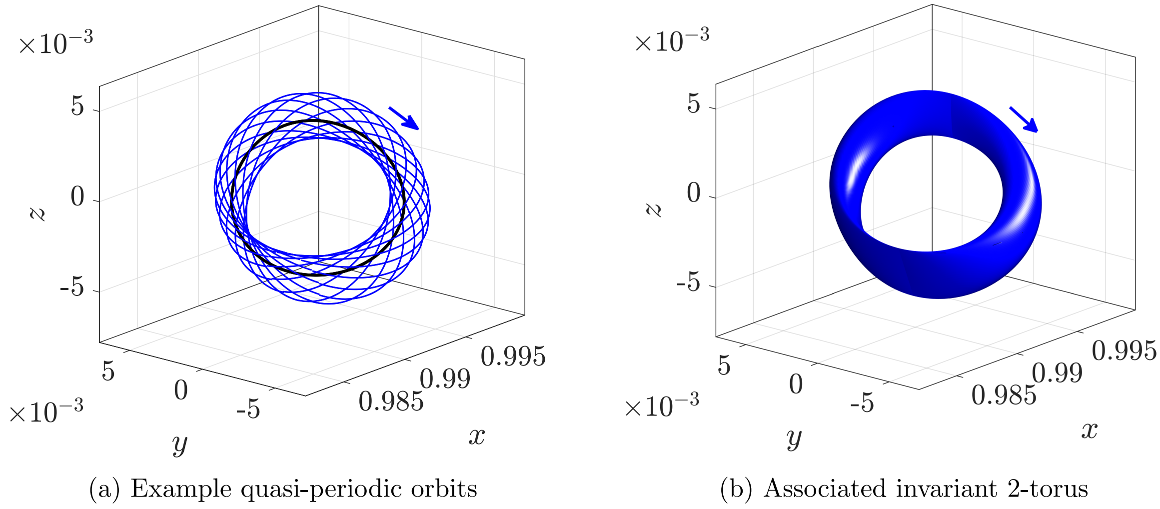

(a) Example quasi-periodic orbits (b) Associated invariant 2-torus

Figure 3.7: Example quasi-periodic orbits and their associated invariant 2-torus in the Sun-Earth CR3BP near a 177-day L_1 southern halo orbit.

The coordinate systems presented in this dissertation describe motion relative to a periodic orbit with an oscillatory mode in the CR3BP and possess some connections to action-angle coordinates. The first coordinate of the geometric local toroidal coordinate set, introduced in Section 4.3, possesses a similar interpretation with the action associated with the latitudinal direction of a torus. This coordinate reflects the separation of an invariant torus measured from an associated periodic orbit and is constant over time for a spacecraft tracing an approximated invariant 2-torus in dynamics linearized about the periodic orbit. The second coordinate of the geometric local toroidal coordinate set reflects a specific location on an instantaneous approximated invariant curve. However, unlike the angle coordinate in an action-angle set, the angular geometric toroidal coordinate is constant over time in linearized dynamics for motion tracing an approximated invariant 2-torus, due to the evolution of the toroidal coordinate frame axes with the natural relative dynamics about the periodic orbit. Furthermore, due to the linear approximation of dynamics relative to a periodic orbit within the formulation of the toroidal coordinates, the computation of toroidal coordinates is less computationally intensive compared to the computation of action-angle coordinates.

3.3.2 First-order approximation of an invariant 2-torus

A first-order approximation of an invariant 2-torus is calculated using the eigenvectors associated with an oscillatory mode of the monodromy matrix for a selected state along a periodic orbit. At this fixed point, a complex eigenvector associated with the oscillatory mode, $\boldsymbol{w}$, is used to generate a set of relative states, $\boldsymbol{\varphi}$, that lie within the center eigenspace of the periodic orbit evaluated at the associated fixed point, defined as

$$\boldsymbol{\varphi} = \epsilon \left(\mathrm{Re}(\boldsymbol{w}) \cos \vartheta + \mathrm{Im}(\boldsymbol{w}) \sin \vartheta \right) \tag{3.29}$$

where $\vartheta \in [0, 2\pi]$ radians and ϵ is a scaling term that influences the size of the first-order approximation of the nearby torus relative to the periodic orbit [115]. For a constant value of ϵ, the set of states $\boldsymbol{\varphi}$ forms a first-order approximation of an invariant curve [73]. For this linear approximation, the stroboscopic mapping time is equal to the period of the associated periodic orbit [115]. Furthermore, each state in this set returns to the same set after one period of the associated orbit rotated by the angle, ϱ, calcuated as [70]

$$\varrho = \tan^{-1} \left(\frac{\mathrm{Im}(\lambda)}{\mathrm{Re}(\lambda)} \right) \tag{3.30}$$

where λ is the associated complex eigenvalue of the monodromy matrix.

The real and imaginary vector components of rthe complex eigenvector form a conjugate diameter of a unique ellipse centered at the fixed point, i.e., the first-order approximation of an invariant curve [124]. To construct a first-order approximation of an invariant 2-torus relative to a periodic orbit, the complex eigenvector may be calculated at various states along one revolution of the periodic orbit by either integrating the eigenvector using the linear equations of relative motion or using mappings of the state transition matrix [24]. Using this information, the set $\boldsymbol{\varphi}$ is computed at a constant value of ϵ at multiple fixed points along the periodic orbit. The resulting ellipses formed by the set $\boldsymbol{\varphi}$ for a constant value of ϵ may vary in size, eccentricity, and orientation over time, corresponding to an evolving geometry of the first-order approximation of an invariant torus relative to the periodic orbit [73].

States in the set $\boldsymbol{\varphi}$ and, therefore, the center eigenspace associated with the specific fixed point, lie within a two-dimensional plane embedded within the six-dimensional phase space [73]. The projection of the center eigenspace onto the configuration space forms a reference plane that is used to define the coordinate systems presented in this paper. Calculating this plane begins by writing the complex eigenvector in terms of four 3×1 vectors corresponding to the real and imaginary position and velocity components as

$$\boldsymbol{w} = \begin{bmatrix} \boldsymbol{r}_r \\ \\ \boldsymbol{v}_r \end{bmatrix} + i \begin{bmatrix} \boldsymbol{r}_i \\ \\ \boldsymbol{v}_i \end{bmatrix} \tag{3.31}$$

For a single fixed point, $\boldsymbol{r}_r$ and $\boldsymbol{r}_i$ span the plane formed by the projection of the center eigenspace onto the configuration space. The unit vector perpendicular to this plane is defined as

$$\hat{\boldsymbol{n}} = \frac{\boldsymbol{n}}{n} = \frac{\boldsymbol{r}_r \times \boldsymbol{r}_i}{|\boldsymbol{r}_r \times \boldsymbol{r}_i|} \tag{3.32}$$

The orientation of the plane normal to $\hat{\boldsymbol{n}}$ is periodic in the rotating frame with the same period as the reference periodic orbit.

The periodicity of the plane spanned by the projection of the center eigenspace onto the configuration space is shown to be periodic by examining the evolution normal vector after one revolution. First, define the normal vector at an arbitrary initial time as $\boldsymbol{n}(t_0)$. The normal vector after one revolution of the periodic orbit is then defined as $\boldsymbol{n}(t_0 + T) = \boldsymbol{n}(t_f)$. The normal vector evaluated at these two times may be expressed as the components of the complex eigenvector at the respective times as

$$\boldsymbol{n}(t_0) = \boldsymbol{r}_r(t_0) \times \boldsymbol{r}_i(t_0)$$

$$\boldsymbol{n}(t_f) = \boldsymbol{r}_r(t_f) \times \boldsymbol{r}_i(t_f)$$

The relationship between the complex eigenvector at the final and initial time is $\boldsymbol{w}(t_f) = \lambda \boldsymbol{w}(t_0)$, where λ is the complex eigenvalue associated with the complex eigenvector. Let the real and imaginary components of the complex eigenvalue be defined as λ_r and λ_i, respectively, such that

$$\lambda = \lambda_r + i\,\lambda_i \tag{3.33}$$

Using this relationship, the final real and imaginary position vectors are calculated as

$$\boldsymbol{r}_r(t_f) = \lambda_r \boldsymbol{r}_r(t_0) - \lambda_i \boldsymbol{r}_i(t_0)$$

$$\boldsymbol{r}_i(t_f) = \lambda_r \boldsymbol{r}_i(t_0) + \lambda_i \boldsymbol{r}_r(t_0)$$

Then, the normal vector after one revolution of the periodic orbit may be rewritten as

$$\begin{aligned}\boldsymbol{n}(t_f) &= \boldsymbol{r}_r(t_f) \times \boldsymbol{r}_i(t_f) \\ &= \left(\lambda_r \boldsymbol{r}_r(t_0) - \lambda_i \boldsymbol{r}_i(t_0)\right) \times \left(\lambda_r \boldsymbol{r}_i(t_0) + \lambda_i \boldsymbol{r}_r(t_0)\right) \\ &= \left(\lambda_r^2 + \lambda_i^2\right) \boldsymbol{n}(t_0)\end{aligned}$$

Since the eigenvalue associated with the oscillatory mode lies on the unit circle, $\lambda_r^2 + \lambda_i^2 = 1$. Thus, $\boldsymbol{n}(t_f) = \boldsymbol{n}(t_0)$ and

$$\hat{\boldsymbol{n}}(t_0) = \hat{\boldsymbol{n}}(t_0 + T) \tag{3.34}$$

Thus, the plane spanned by the projection of the center eigenspace onto the configuration space is time-periodic.

3.3.2.1 Approximations of invariant 2-tori in the Earth-Moon system

Several first-order approximations of invariant 2-tori are constructed relative to members of the Earth-Moon L_2 southern halo orbit family. Members of this family evolve away from a bifurcation with the L_2 Lyapunov orbit family and towards the Moon, possessing a maximum z-extension that occurs below the Earth-Moon plane [32]. In Figure 3.8, selected members of the southern L_2 halo orbit family are plotted in the Earth-Moon rotating frame relative to the system barycenter. The plotted halo orbits vary in orbit period between approximately 6 and 14.8 days. Four specific halo orbits within this family are highlighted for further analysis.

The stability of each orbit highlighted in Figure 3.8 is calculated. The two stability indices computed for each orbit are summarized in Table 3.3. Each orbit admits at least one stability index with a magnitude of less than 2, indicating that each orbit admits at least one oscillatory mode and, therefore, nearby quasi-periodic relative motion. The oscillatory modes of the halo orbit near the bifurcation with the L_2 Lyapunov orbit family (blue), and the centrally located halo orbit (cyan)

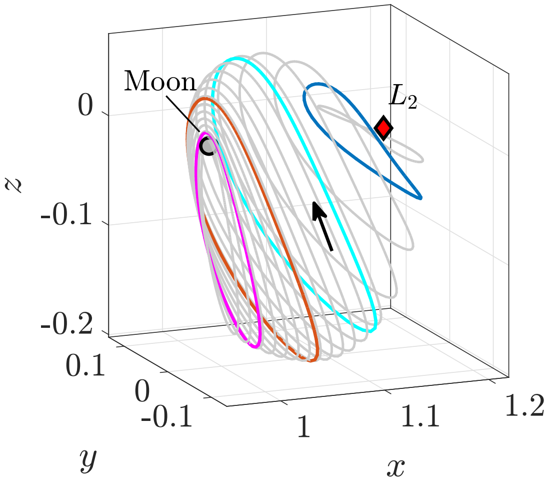

Figure 3.8: Selected members of the Earth-Moon southern L_2 halo orbit family. Reproduced with permission from Springer Nature [108].

correspond to the s_2 index, while the oscillatory mode of the NRHO (magenta) corresponds to s_1. The halo orbit (red), is located in a region of stable orbits in the L_2 halo orbit family where the orbits admit two pairs of oscillatory modes corresponding to both indices. The orbits represented in blue and cyan each possess a stability index corresponding to a stable/unstable eigenvalue pair and are classified as unstable. The orbit represented by magenta possesses a stability index with a magnitude of just greater than 2 in addition to the index indicating an oscillatory mode, thus, this orbit is classified as weakly stable.

Table 3.3: Stability of the specified Earth-Moon southern L_2 halo orbits.

Marker color	Period (days)	s_1	s_2	Stability
Magenta	7	1.1908	-3.0211	Weakly stable
Red	10	0.51663	-1.2669	Stable
Cyan	13	69.074	-1.4715	Unstable
Blue	14.7	924.79	1.8523	Unstable

For each highlighted orbit, a first-order approximation of an invariant 2-torus is constructed using the process described in Section 3.3.2. These tori are plotted at the boundaries of Figure 3.9, visualized using the axes of the rotating frame with the periodic orbit associated with each tori represented at the origin. At the center of Figure 3.9, the stability indices of periodic orbits within the computed segment of the southern L_2 halo family are plotted as a function of the orbit period. The tori are identified by markers in the center of Figure 3.9 using a color scheme consistent with Figure 3.8 and indicating the stability index corresponding with the oscillatory mode associated with the torus. The varying geometries of the approximated tori illustrate the complex solution space for spacecraft formations leveraging the center eigenspace of a periodic orbit in a multi-body system and motivates the presented investigation into methods for the straightforward and intuitive description of motion tracing the surfaces of these tori, as well as methods for the characterization of the tori. Furthermore, an infinite number of nested 2-tori of different size exist relative to each orbit, motivating methods for the characterization of the size of approximated tori. Finally, this stability analysis reveals that within the computed segment of the Earth-Moon southern L_2 halo orbit family, every orbit possess at least one oscillatory mode, thus admits nearby invariant 2-tori, indicating a wide range of applicable orbits for formation design leveraging the center eigenspace of a periodic orbit in the CR3BP.

3.4 Numerical methods for trajectory analysis

In this section, the fundamental numerical methods used to compute various solutions of the CR3BP are discussed. First, a brief discussion on the numerical integration schemes used within this investigation is included. Next, an overview of numerical shooting methods is presented, followed by a description of the application of single shooting to compute periodic orbits in the CR3BP and a discussion of the use of pseudo-arclength continuation to compute families of periodic orbits is included. Finally, a multiple shooting algorithm used to transition natural solutions from the CR3BP to the ephemeris model is presented.

3.4.1 Numerical integration

Numerical integration is required to solve sets of ordinary differential equations and compute trajectories in the CR3BP and ephemeris models. In this investigation, two numerical integration

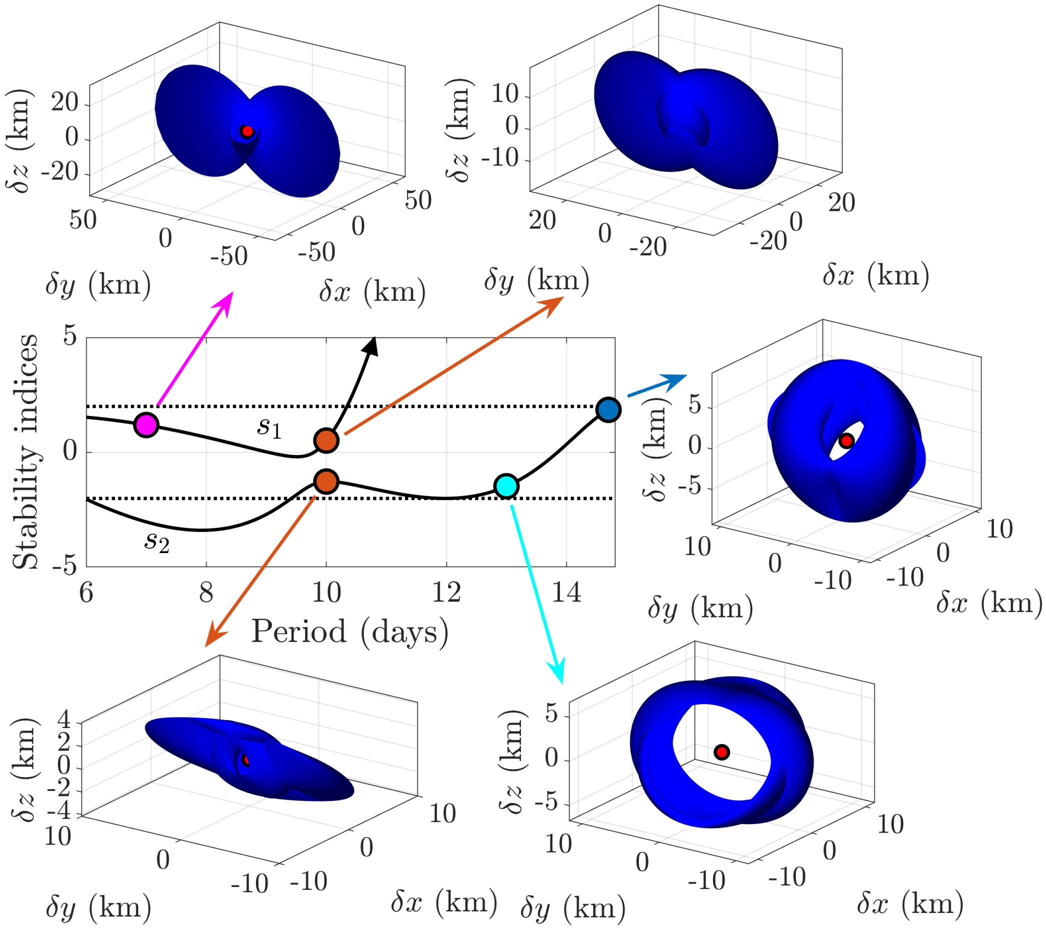

Figure 3.9: Stability indices of periodic orbits across the Earth-Moon southern L_2 halo orbit family with selected first-order approximations of invariant 2-tori visualized relative to the associated periodic orbit in the rotating frame. Reproduced with permission from Springer Nature [108].

schemes are used. The first is an Adams-Bashforth-Moulton method with varying order between one and 13, accessed via MATLAB's `ode113` [125]. This scheme is used broadly to integrate various ordinary differential equations and generate the results presented in this investigation. Additionally, a C++ implementation of an eighth-order Dormand-Prince Runge Kutta method is accessed via the GNU Scientific Library's `gsl_odeiv2_step_rk8pd` [126]. This scheme is primarily used to integrate trajectories in the ephemeris model to reduce computational time. For trajectories in the ephemeris model, results are validated using a similar integration scheme in GMAT [127]. In general, for both numerical integration methods, strict tolerances are selected to minimize truncation error.

3.4.2 Shooting methods

Shooting methods are used to solved two-point boundary variable problems in the CR3BP such the computation of periodic orbits, quasi-periodic orbits, and spacecraft transfers. In this investigation, free variable and constraint formulations of single and multiple shooting are implemented to compute a desired trajectory via a vectorial root-finding problem. In a general free variable and constraint shooting formulation, a trajectory is defined via a set of n scalar free variables, V, organized in an $n \times 1$ free variable vector, labeled $\boldsymbol{V}$, written as

$$\boldsymbol{V} = \begin{bmatrix} V_1 & V_2 & \dots & V_{n-1} & V_n \end{bmatrix}^T \tag{3.35}$$

Next, the conditions that the trajectory must satisfy are specified via m scalar constraint functions, labeled F, where $m \leq n$. Each constraint is a function of the free variables that is formulated such that $F_i(\boldsymbol{V}) = 0$ when satisfied. The constraints are organized in an $m \times 1$ constraint vector, $\boldsymbol{F}(\boldsymbol{V})$, written as

$$\boldsymbol{F}(\boldsymbol{V}) = \begin{bmatrix} F_1 & F_2 & \dots & F_{m-1} & F_m \end{bmatrix}^T \tag{3.36}$$

such that $\boldsymbol{F}(\boldsymbol{V}) = \boldsymbol{0}$ when all constraints are satisfied. The gradient of the constraint vector with respect to the free variables is often used to update the free variable vector. Thus, the partial derivative of each constraint with respect to each free variable is employed. This $m \times n$ Jacobian matrix, labeled $[\boldsymbol{DF}(\boldsymbol{V})]$, is expressed generally as

$$[\boldsymbol{DF}(\boldsymbol{V})] = \frac{\partial \boldsymbol{F}(\boldsymbol{V})}{\partial \boldsymbol{V}} = \begin{bmatrix} \frac{\partial F_1}{\partial V_1} & \dots & \frac{\partial F_1}{\partial V_n} \\ \vdots & \ddots & \vdots \\ \frac{\partial F_m}{\partial V_1} & \dots & \frac{\partial F_m}{\partial V_n} \end{bmatrix}_{m \times n} \tag{3.37}$$

The partial derivatives within $[\boldsymbol{DF}(\boldsymbol{V})]$ may be analytically defined, or alternatively, approximated via a finite-differencing scheme. If the constraints are linearly independent, $[\boldsymbol{DF}(\boldsymbol{V})]$ will be rank m.

Numerical shooting methods iteratively update the free variables from an initial guess until a solution that satisfies the constraints is found. To update the free variables, a multi-variate

Newton's method is employed in this investigation. Successful application of Newton's method relies on three assumptions [128]:

(1) The initial guess of the free variables is "sufficiently" close to a solution.

(2) The constraints are continuous with respect to the free variables.

(3) The Jacobian matrix of constraints with respect to the free variables is always full-rank.

When these assumptions are satisfied, the free variables are iteratively updated via an update equation, and will nominally converge quadratically on a feasible solution [128]. For an underconstrained system, where the number of constraints is less than the number of free variables (i.e., $m < n$) a minimum-norm update using the pseudo inverse of $[\boldsymbol{DF}(\boldsymbol{V})]$ is used. For the i-th update, the next free variable vector at the next iteration is computed as

$$\boldsymbol{V}_{i+1} = \boldsymbol{V}_i - [\boldsymbol{DF}(\boldsymbol{V}_i)]^T \left([\boldsymbol{DF}(\boldsymbol{V}_i)][\boldsymbol{DF}(\boldsymbol{V}_i)]^T \right)^{-1} \boldsymbol{F}(\boldsymbol{V}_i) \tag{3.38}$$

where $\boldsymbol{F}(\boldsymbol{V}_i)$ and $[\boldsymbol{DF}(\boldsymbol{V}_i)]$ are the constraint vector and Jacobian matrix, respectively, evaluated using the variables at the i-th iteration. If the same number of constraints exist as the number of free variables (i.e., $m = n$), this update equation simplifies to

$$\boldsymbol{V}_{i+1} = \boldsymbol{V}_i - [\boldsymbol{DF}(\boldsymbol{V}_i)]^{-1} \boldsymbol{F}(\boldsymbol{V}_i) \tag{3.39}$$

The update equation is applied until the constraints are satisfied, such that $||\boldsymbol{F}(\boldsymbol{V}_i)|| = 0$ to within an appropriate numerical tolerance.

3.4.3 Computing periodic orbits

Single shooting is used to compute periodic orbits in the CR3BP. A conceptual illustration of an initial guess of a periodic orbit and a nearby solution is included in Figure 3.10. The trajectory corresponding to the initial guess of the free variables, represented in black, is discontinuous However, it is expected to lie near a periodic solution. The subscripts 0 and f indicate a state along the trajectory at times t_0 and t_f, respectively. The objective of single shooting is to vary the initial conditions and integration time until the associated trajectory is a periodic solution. The intermediate trajectories corresponding to each iteration of the shooting method are represented as dashed black lines. With each iteration, the solution is updated until a periodic solution is reached, represented in blue.

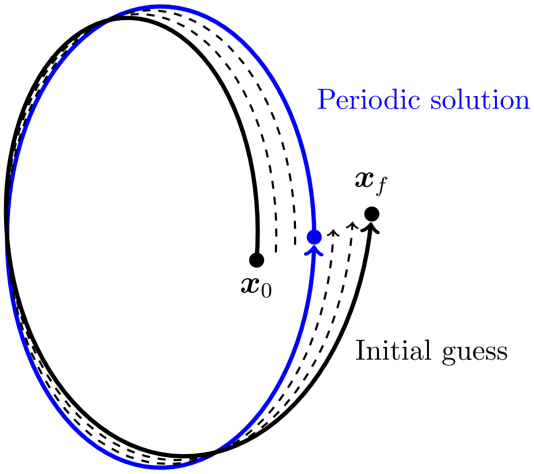

Figure 3.10: Conceptual illustration of a single shooting approach to computing a periodic orbit in the CR3BP.

Periodicity is straightforwardly defined via a constraint vector that is equal to the difference between the initial state and final state along a trajectory in the rotating frame. However, since the Jacobi constant is preserved along this natural trajectory, only five of the six state components must be constrained [28]. This allows for an additional constraint to replace an appropriately selected continuity constraint. For instance, the initial state along a symmetric periodic orbit may be constrained to lie along the x-axis of the rotating frame in place of continuity in the y component of velocity. Alternative constraint formulations may be tailored to compute periodic orbits with different geometries or in different regions of the P_1-P_2 system. Including this modification also ensures that the nullspace of the $[\boldsymbol{DF}(\boldsymbol{V})]$ is one-dimensional, which facilitates numerical continuation along an orbit family. Of course, an infinite variety of implementations may be formulated to solve for a desired solution.

Consider the computation of a periodic orbit in the CR3BP using single shooting. One form of a free variable vector allows the six initial states of the trajectory to vary, as well as the integration time of the trajectory, t_{int}, is written as

$$\boldsymbol{V} = \begin{bmatrix} x_0 & y_0 & z_0 & \dot{x}_0 & \dot{y}_0 & \dot{z}_0 & t_{\text{int}} \end{bmatrix}^T$$

If the desired solution is a periodic orbit that possesses a crossing of the xz plane with a large $\dot{y}$ magnitude (e.g., a Lyapunov or halo orbit), the constraint on $\dot{y}_f = \dot{y}_0$ is replaced with a constraint on the initial state to lie in the xz plane, i.e., $y = 0$. Thus, a complete constraint vector may be expressed as

$$\boldsymbol{F}(\boldsymbol{V}) = \begin{bmatrix} x_f - x_0 \\ y_f - y_0 \\ z_f - z_0 \\ \dot{x}_f - \dot{x}_0 \\ y_0 \\ \dot{z}_f - \dot{z}_0 \end{bmatrix}$$

The $[\boldsymbol{DF}(\boldsymbol{V})]$ matrix for this formulation is then defined as

$$[\boldsymbol{DF}(\boldsymbol{V})] = \begin{bmatrix} \Phi_{11} - 1 & \Phi_{12} & \Phi_{13} & \Phi_{14} & \Phi_{15} & \Phi_{16} & \dot{x}_f \\ \Phi_{21} & \Phi_{22} - 1 & \Phi_{23} & \Phi_{24} & \Phi_{25} & \Phi_{26} & \dot{y}_f \\ \Phi_{31} & \Phi_{32} & \Phi_{33} - 1 & \Phi_{34} & \Phi_{35} & \Phi_{36} & \dot{z}_f \\ \Phi_{41} & \Phi_{42} & \Phi_{43} & \Phi_{44} - 1 & \Phi_{45} & \Phi_{46} & \ddot{x}_f \\ 0 & 1 & 0 & 0 & 0 & 0 & 0 \\ \Phi_{61} & \Phi_{62} & \Phi_{63} & \Phi_{64} & \Phi_{65} & \Phi_{66} - 1 & \ddot{z}_f \end{bmatrix}$$

where Φ_{ij} are the components of the STM evaluated along the current trajectory between the initial and final time, i.e., $[\boldsymbol{\Phi}(t_0 + t_{\text{int}}, t_0)]$. For this example, there are less constraints defined than variables, thus, an infinite number of solutions exist and the pseudo-inverse update equation expressed in Eq. (3.38) may be employed. Furthermore, the Jacobian matrix associated with this formulation of the free variable and constraint vectors possesses a one-dimensional nullspace, such that it may be employed during pseudo-arclength continuation.

An additional constraint may be appended to the constraint vector to compute a periodic orbit with a specific orbit period or Jacobi constant. For these problems, the Jacobian matrix will require the associated partial derivatives of the new constraint and will be full-rank if the constraints form a linearly independent set. With this addition of another constraint, since there are the same number of constraints as variables, application of Newton's method with a sufficient initial guess will have a unique solution using the update equation written in Eq. (3.39).

3.4.4 Continuation of periodic orbit families

Pseudo-arclength continuation is leveraged in this investigation to compute families of periodic orbits in the CR3BP. Pseudo-arclength continuation uses the gradient of the orbit family to predict and compute subsequent members of a family. By using this gradient information, pseudo-arclength continuation is able to succeed in computing additional members of a family along turning points in the family, while methods such as natural parameter continuation may fail [129, 130]. In this investigation, pseudo arclength is used in combination with single shooting.

A member an orbit family is required to initialize a pseudo-arclength continuation algorithm, thus, pseudo-arclength continuation is not self-starting. A known member of the orbit family is used to construct free variable and constraint formulation, $\boldsymbol{V}$ and $\boldsymbol{F}(\boldsymbol{V})$, respectively, that produces a Jacobian matrix with a one-dimensional nullspace, (i.e., $n-m=1$). The nullspace of the Jacobian matrix, labeled $\boldsymbol{\nu}$, captures the gradient along the orbit family and possess the same dimension as the free variable vector. After each iteration of the continuation method, a small step is taken along the tangent direction of the family to predict the next member of the family and seed the initial guess of the free variable vector of the next iteration. Then, during corrections, pseudo-arclength continuation uses an additional constraint that limits the projection of the change in the free variables between the two iterations onto the nullspace to equal a specified step size, Δs. This constraint is formulated as [131]

$$(\boldsymbol{V}-\boldsymbol{V}^{*})^{T}\boldsymbol{\nu}^{*}-\Delta s=0 \tag{3.40}$$

where $\boldsymbol{V}$ is the free variable vector of the current solution being solved, $\boldsymbol{V}^{*}$ is the free variable vector of the previous orbit solution, and $\boldsymbol{n}^{*}$ is the nullspace of the Jacobian matrix evaluated at

$\boldsymbol{V}^*$. Thus, Δs influences step size along the orbit family. The exact value of Δs must be sufficiently small to allow Newton's method to converge.

To compute each orbit during continuation, an augmented constraint vector is defined as a combination of the desired constraints and the additional pseudo arclength constraint. This augmented constraint vector, labeled $\boldsymbol{H}(\boldsymbol{V})$, is defined generally as [131]

$$\boldsymbol{H}(\boldsymbol{V}) = \begin{bmatrix} \boldsymbol{F}(\boldsymbol{V}) \\ (\boldsymbol{V} - \boldsymbol{V}^*)^T \boldsymbol{\nu}^* - \Delta s \end{bmatrix} \tag{3.41}$$

The Jacobian matrix of the partial derivatives of the augmented constraint vector with respect to the free variables vector, $[\boldsymbol{DH}(\boldsymbol{V})]$, is constructed accordingly as

$$[\boldsymbol{DH}(\boldsymbol{V})] = \begin{bmatrix} [\boldsymbol{DF}(\boldsymbol{V})] \\ (\boldsymbol{\nu}^*)^T \end{bmatrix} \tag{3.42}$$

This augmented Jacobian matrix is square and full-rank, such that Newton's method will converge to a unique solution. The update equation written in Eq. (3.39) is used to iteratively update the free variables until the Euclidean norm of $\boldsymbol{H}(\boldsymbol{V})$ is sufficiently small. Using this converged solution, the nullspace of the Jacobian matrix of the non-augmented constraint vector and the free variables, $[\boldsymbol{DF}(\boldsymbol{V})]$, is used in finding the next orbit.

Pseudo-arclength continuation benefits from additional checks to achieve the desired performance. First, the direction of the nullspace as returned from a nullspace solver routine must be compared to the direction of the nullspace of the previous iteration to ensure that they lie in the same direction. Otherwise, the direction of continuation may flutter. Additionally, implementation of an adaptive step size may facilitate computation along a periodic orbit family by reducing the number of orbits required to be computed.

3.4.5 Computing trajectories in a higher-fidelity model

To recover a natural trajectory in the ephemeris model that shares similar geometric characteristics with a periodic orbit in the CR3BP, a multiple shooting numerical corrections scheme is used. This multiple shooting approach, relying on discretizing the path into multiple arcs, significantly reduces the sensitivity of the corrections problem. A conceptual illustration of this multiple shooting formulation is included in Figure 3.11. The initial guess constructed in the CR3BP, represented in black, will produce a discontinuous trajectory in the ephemeris model. Using the detailed multiple shooting approach, this discontinuous guess is iteratively updated until a nearby continuous solution is recovered, represented in blue, that retains the structure of the initial guess.

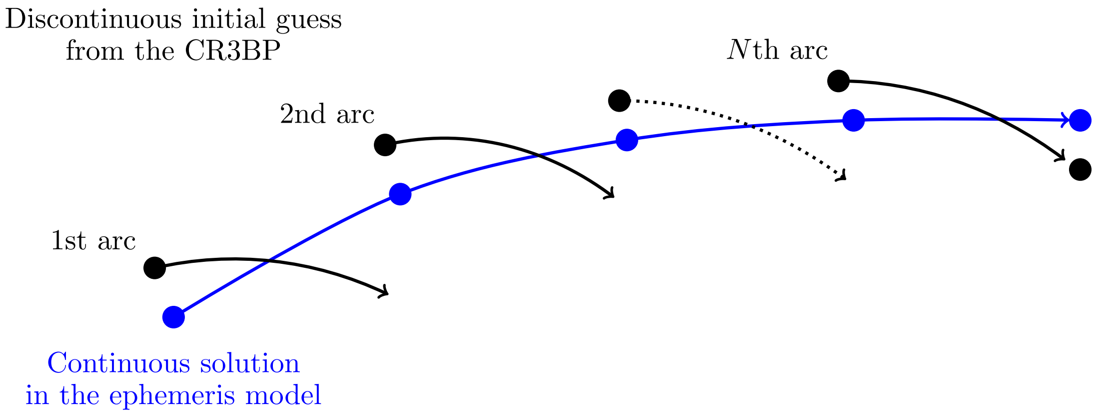

Figure 3.11: Conceptual illustration of the presented multiple shooting scheme used to recover trajectories resembling periodic orbits in the ephemeris model.

To recover a continuous trajectory in the ephemeris model that resembles a periodic orbit in the CR3BP, first, several revolutions of a periodic orbit are generated in the CR3BP. This trajectory in the CR3BP is then discretized into a sequence of N arcs and a final node. The initial state of each arc is transformed into a P_2-centered ICRF using ephemeris information of the instantaneous states of the body, e.g. the Moon in the Earth-Moon system or the Earth in the Sun-Earth system. Next, a free variable and constraint vector formulation is constructed to vary the initial state, initial epoch, and integration time of each arc and constrain state and epoch continuity across the recovered trajectory in the ephemeris model. In this implementation, quantities of length and time are nondimensionalized within the multiple shooting algorithm to facilitate Newton's method by reducing ill-conditioning in the Jacobian matrix.

A free variable vector is constructed to reflect the variables describing each arc along the solution. This free variable vector is formed by combining the individual vectors, $\boldsymbol{V}_i$, describing each arc for $i = 1, \dots, N$. For the i-th arc, $\boldsymbol{V}_i$ is written as:

$$\boldsymbol{V}_i = \begin{bmatrix} \boldsymbol{X}_{0,i} \\ t_i \\ \Delta t_i \\ \beta_i \end{bmatrix} \tag{3.43}$$

where $\boldsymbol{X}_{0,i}$ is the nondimensional state vector of the spacecraft at the beginning of the arc formulated in the P_2-centered ICRF and Δt_i is the nondimensional integration time along the arc [131]. The variable, t_i, is the nondimensional time at the beginning of the arc measured from an initial epoch, defined as

$$t_i = \tau_i - \tau_0 \tag{3.44}$$

where τ_i is the epoch of the i-th node and τ_0 is an initial epoch. The final variable for the arc, β_i, is a slack variable used to ensure a positive integration time along the i-th arc. For the final node, the β_i and Δt_i variables are excluded such that the free variables associated with the final node, $\boldsymbol{V}_f$, is written as

$$\boldsymbol{V}_f = \begin{bmatrix} \boldsymbol{X}_{0,i} \\ t_i \end{bmatrix} \tag{3.45}$$

The complete free variable vector of the multiple shooting scheme, $\boldsymbol{V}$, is then assembled as

$$\boldsymbol{V} = \begin{bmatrix} \boldsymbol{V}_1 \\ \vdots \\ \boldsymbol{V}_N \\ \boldsymbol{V}_f \end{bmatrix} \tag{3.46}$$

If there are N arcs and one final node, the dimension of $\boldsymbol{V}$ is $(9N + 7) \times 1$.

The constraint vector, $\boldsymbol{F}(\boldsymbol{V})$, is constructed to enforce continuity between neighboring arcs, a positive integration time along each arc and to fix the initial conditions. Individual components,

$\boldsymbol{F}_i$, of the constraint vector capture the discontinuity between the end of the i-th arc and the subsequent node. The constraint vector corresponding to the i-th arc, $\boldsymbol{F}_i$, is defined as

$$\boldsymbol{F}_i = \begin{bmatrix} \boldsymbol{X}_{f,i} - \boldsymbol{X}_{0,i+1} \\ (t_i + \Delta t_i) - t_{i+1} \\ \Delta t_i - \beta_i^2 \end{bmatrix} \tag{3.47}$$

where $\boldsymbol{X}_{f,i}$ is the inertial state at the end of the i-th arc. For the final arc, i.e., $i = N$, the state and epoch information of the final node is used to compute the subsequent state and time past the initial epoch, $\boldsymbol{X}_{0,i+1}$ and t_{i+1}, respectively. The final element of this vector constrains the integration time to retain a positive value; the slack variable β_i is used to write this requirement as an equality constraint.

Two additional constraints may be incorporated to, if desired, constrain the initial epoch of the trajectory and constrain the initial state of the trajectory to lie along the xz plane of the P_1-P_2 rotating frame. The epoch constraint is implemented by constraining the time past the initial epoch of the initial state of the first arc, t_i, equal to zero, defined as

$$f_\tau = t_i \tag{3.48}$$

such that τ_0 may be selected as the desired initial epoch of the trajectory. The constraint to force the initial conditions of the trajectory to lie on the xz plane of the instantaneous rotating frame is defined as

$$f_y = y_0 \tag{3.49}$$

where y_0 is the y component of the initial state of the trajectory expressed in the P_1-P_2 rotating frame. This initial condition constraint may be modified to accommodate the recovery of trajectories in different regions of the P_1-P_2 system. With these two additional constraints, the complete constraint vector is constructed as

$$\boldsymbol{F}(\boldsymbol{V}) = \begin{bmatrix} \boldsymbol{F}_1 \\ \vdots \\ \boldsymbol{F}_N \\ f_\tau \\ f_y \end{bmatrix} \tag{3.50}$$

For N arcs and one final node, $\boldsymbol{F}(\boldsymbol{V})$ possesses a dimension of $(8N + 2) \times 1$ when both additional constraints are included.

For this multiple shooting formulation, Newton's method is employed to perform iterative updates to the free variable vector until the norm of the constraint vector is approximately zero to within a sufficiently small tolerance. A Jacobian matrix, $[\boldsymbol{DF}(\boldsymbol{V})]$, is formed to reflect a linear approximation of the sensitivity of each constraint to the free variables.

$$[\boldsymbol{DF}(\boldsymbol{V})] = \begin{bmatrix} \frac{\partial \boldsymbol{F}_1}{\partial \boldsymbol{V}_1} & \frac{\partial \boldsymbol{F}_1}{\partial \boldsymbol{V}_2} & \dots & \boldsymbol{0} & \boldsymbol{0} \\ \boldsymbol{0} & \frac{\partial \boldsymbol{F}_2}{\partial \boldsymbol{V}_2} & \dots & \boldsymbol{0} & \boldsymbol{0} \\ \vdots & \vdots & \ddots & \vdots & \vdots \\ \boldsymbol{0} & \boldsymbol{0} & \dots & \frac{\partial \boldsymbol{F}_N}{\partial \boldsymbol{V}_N} & \frac{\partial \boldsymbol{F}_N}{\partial \boldsymbol{V}_f} \\ \frac{\partial f_\tau}{\partial \boldsymbol{V}_1} & \boldsymbol{0} & \dots & \boldsymbol{0} & \boldsymbol{0} \\ \frac{\partial f_y}{\partial \boldsymbol{V}_1} & \boldsymbol{0} & \dots & \boldsymbol{0} & \boldsymbol{0} \end{bmatrix} \tag{3.51}$$

This matrix is constructed using a combination of analytical expressions and approximations via forward finite differencing. The matrix has dimensions of $(9N + 7) \times (8N + 2)$ and is generally sparse. Using this definition for the free variable vector, constraint vector, and Jacobian matrix, the minimum-norm update equation is applied until the Euclidean norm of the constraint vector $\boldsymbol{F}(\boldsymbol{V})$ equals zero to within an appropriate tolerance, e.g., 10^{-10}, indicating recovery of a continuous trajectory that satisfies all of the constraints.

The outlined multiple shooting algorithm is applied to recover continuous trajectories in the ephemeris model using the three reference periodic orbits. Each trajectory uses a point mass ephemeris model of the Sun, Earth, and Moon. For the periodic orbits in the Earth-Moon system, the Moon is used as the central body during numerical corrections; for the Sun-Earth periodic orbit, the Earth is used. For these trajectories, acceleration due to SRP is not modeled. Ten revolutions of the reference orbit in the P_1-P_2 rotating frame are captured. Each trajectory is constrained to lie along the xz plane of the associated rotating frame at an initial epoch of January 1st, 2025 at 00:00:00.000 UTC.

The trajectories recovered in the ephemeris model, representative of the Earth-Moon L_2 southern NRHO, Earth-Moon DRO, and Sun-Earth L_1 southern halo orbit, are plotted in Figure 3.12, Figure 3.13, and Figure 3.14, respectively. Specifically, each trajectory is visualized in the rotating frame with respect to the approximated location of the barycenter of the primaries using dimensional quantities. The initial conditions of each trajectory are indicated with a black marker. Using the detailed multiple shooting algorithm, each computed trajectory in the ephemeris model is observed to well-recover the geometric features of the associated periodic orbit. These trajectories are used throughout this investigation to demonstrate the application of the introduced strategies in higher-fidelity dynamics.

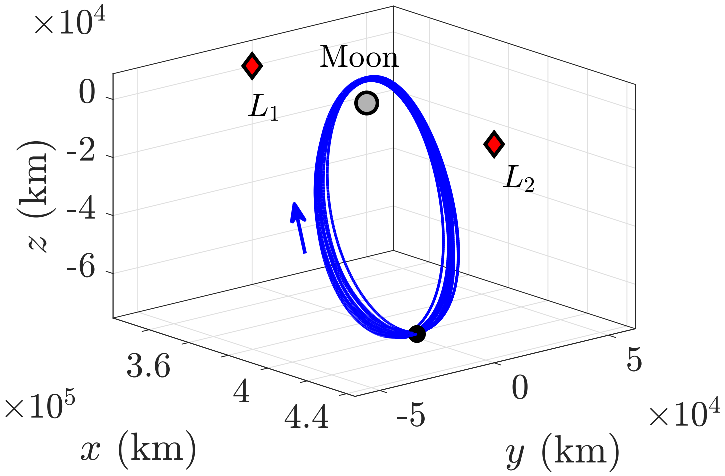

Figure 3.12: Trajectory in the ephemeris model recovered in the vicinity of an Earth-Moon L_2 southern NRHO with a period of 8 days, plotted in the Earth-Moon rotating frame.

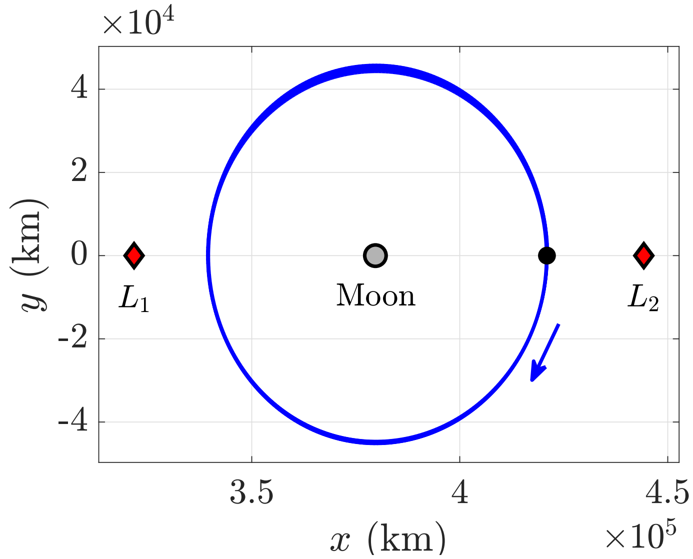

Figure 3.13: Trajectory in the ephemeris model recovered in the vicinity of an Earth-Moon DRO with a period of 7 days, plotted in the Earth-Moon rotating frame.

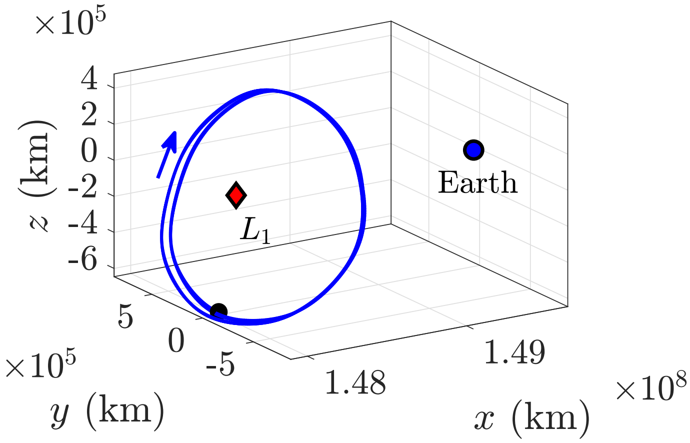

Figure 3.14: Trajectory in the ephemeris model recovered in the vicinity of a Sun-Earth L_1 southern halo orbit with a period of 177 days, plotted in the Sun-Earth rotating frame.

Chapter 4

Local Toroidal Coordinate Systems for Relative Motion Near Periodic Orbits

In this chapter, a family a local toroidal coordinate systems are introduced to support the description of motion relative to periodic orbits that possess an oscillatory mode. These descriptions are comparable to toroidal coordinate sets that are used to study magnetic fields and plasma physics [80, 81]. The presented toroidal coordinate systems are non-orthogonal coordinate systems formulated using the first-order approximation of invariant 2-tori in the CR3BP. The coordinate systems are formulated to supply geometric insight into the state of a chaser spacecraft relative to a periodic orbit that admits an oscillatory mode while also possessing a consistent interpretation across various periodic orbits. The first coordinate set, denoted as the nonsingular local toroidal coordinates, possesses an oblique basis and maps linearly with Cartesian coordinates relative to a fixed point as a function of the complex eigenvector of the monodromy matrix. The second coordinate set, denoted as the geometric local toroidal coordinates, expresses the state of the chaser spacecraft relative to a fixed point using the amplitude, angle, and axial components of a reference 2-torus. However, in contrast to toroidal coordinate systems that describe a state measured from an origin on the revolution axis of the torus, the presented local toroidal coordinates are formulated to describe a state measured from a reference along the center ring of the torus, i.e., a fixed point along a periodic orbit in the CR3BP.

To derive the local toroidal coordinate systems, first, a process for normalizing a complex eigenvector of the monodromy matrix that corresponds to an oscillatory mode is presented, required for consistent definition of the toroidal coordinate systems. Then, derivations of the nonsingular and geometric local toroidal coordinate systems are detailed, including calculations of the coordinate and their respective rates of change. Finally, several analyses related to local toroidal coordinates are presented, including the derivation of equations of relative motion, demonstration that motion on the center eigenspace has a constant description using local toroidal coordinates, and an investigation of error in the nonlinear CR3BP associated with the linear assumptions within the formulation of the coordinate systems. Part of the material in this chapter was first published by Celestial Mechanics and Dynamical Astronomy in 2022 by Springer Nature [108].

4.1 Normalizing the complex eigenvector

For consistent implementation when defining the local toroidal coordinate systems, a normalization scheme is applied to the complex eigenvector of the monodromy matrix associated with an oscillatory mode to remove ambiguity. Prior to the normalization, the fixed point along the periodic orbit at which the monodromy matrix is computed must be defined. The presented normalization process of the complex eigenvector of the monodromy matrix is summarized as:

(1) Aligning the eigenvector associated with the oscillatory mode with the principal axes of the first-order invariant curve approximation at the specified fixed point

(2) Constraining the magnitude of the real, position components of the eigenvector

(3) Applying a series of case-specific sign checks to remove ambiguity in the sign of the real and imaginary components of the eigenvector

The resulting real and imaginary vector components of the complex eigenvector supply a useful set of basis vectors for the center eigenspace and enable construction of a unique reference first-order approximation of a 2-torus relative to the periodic orbit.

The principal axes of the ellipse formed by the first-order approximation of the invariant curve are computed via an SVD of a matrix containing columns that span the center eigenspace in the phase space. Consider a fixed point of a periodic orbit that admits at least one oscillatory mode as indicated by the eigendecomposition of the monodromy matrix. One complex eigenvector from a complex conjugate pair that lies on the unit circle is selected and denoted as $\boldsymbol{w}^*$. Then, a 6×2 matrix is defined as

$$[\boldsymbol{E}] = \begin{bmatrix} \mathrm{Re}(\boldsymbol{w}^*) & \mathrm{Im}(\boldsymbol{w}^*) \end{bmatrix}^T \tag{4.1}$$

The SVD of $[\boldsymbol{E}]$ is used to compute the lengths and directions of the principal axes of the ellipse formed by the instantaneous approximated invariant curve in terms of $\boldsymbol{w}^*$ [132]. First, the matrix $[\boldsymbol{E}]$ is decomposed as [118]

$$[\boldsymbol{E}] = [\boldsymbol{U}][\boldsymbol{\Sigma}][\boldsymbol{V}]^T \tag{4.2}$$

In this expression, the matrix $[\boldsymbol{U}]$ is a 6×2 semi-orthogonal matrix that contains basis vectors that are aligned with nonunique principal semi-axes of the ellipse formed by the approximation of the invariant curve centered at the fixed point. Specifically, the columns of $[\boldsymbol{U}]$ are ordered with the basis vector aligned with a semi-major axis of the ellipse in the left column and the basis vector aligned with a semi-minor axis of the same ellipse in the right column.[1] The matrix $[\boldsymbol{\Sigma}]$ is a 2×2 diagonal matrix containing the magnitudes of the semi-major and semi-minor axes of this ellipse in the upper-left and lower-right quadrants, respectively. Finally, the matrix $[\boldsymbol{V}]$ is a 2×2 orthogonal matrix, which may be expressed as a rotation matrix as [118]

$$[\boldsymbol{V}] = \begin{bmatrix} \cos\Theta & -\sin\Theta \\ \sin\Theta & \cos\Theta \end{bmatrix} \tag{4.3}$$

where Θ is the angle between the axes defined by the real and imaginary components of the input complex eigenvector and the principal axes of the ellipse.

A complex scaling factor is applied to the complex eigenvector to recover basis vectors of the center eigenspace that are aligned with the principal axes of the ellipse formed by the invariant curve. Rearranging the SVD of $[\boldsymbol{E}]$ produces the relationship $[\boldsymbol{E}][\boldsymbol{V}] = [\boldsymbol{U}][\boldsymbol{\Sigma}]$. The right hand side of this expression, $[\boldsymbol{U}][\boldsymbol{\Sigma}]$, is equivalent to a 6×2 matrix containing a vector $\boldsymbol{a}$ in the left column that is measured from the center of the ellipse formed by the invariant curve and directed

---

[1] Note that in this context, the terminology semi-major axis is not related to the Keplerian orbital element; rather, the semi-major axis is associated with the ellipse formed by the approximated invariant curve.

along the major axis, as well as a vector $\boldsymbol{b}$ in the right column that is directed along the minor axis. This analysis reveals that the matrix $[\boldsymbol{E}]$, right multiplied by $[\boldsymbol{V}]$, is equal to the matrix $[\boldsymbol{U}][\boldsymbol{\Sigma}]$ containing an orthogonal set of principal axes of the ellipse formed by the invariant curve. Accordingly, an eigenvector with real and imaginary components that are aligned with the principal axes of the ellipse formed by the invariant curve is computed by multiplying $\boldsymbol{w}^*$ by the complex scalar quantity c, defined as

$$c = e^{-i\Theta} \tag{4.4}$$

where Θ is extracted from $[\boldsymbol{V}]$ as

$$\Theta = \tan^{-1}\left(\frac{V_{21}}{V_{11}}\right) \tag{4.5}$$

Scaling the complex eigenvector by c produces another complex eigenvector labeled $\boldsymbol{w}$ that forms a conjugate diameter description of the same ellipse described by $\boldsymbol{w}^*$. However, the real vector component of this eigenvector is aligned with the semi-major axis of the elliptical approximation of the invariant curve and the imaginary vector component is directed along the semi-minor axis, both measured from the fixed point at the center of the ellipse.

The relationship between real and imaginary components of the complex eigenvector and the principal axes of the approximated invariant curve in the phase space is conceptually illustrated in Figure 4.1. The real and imaginary vector components of the eigenvector returned by the eigendecomposition solver are represented as dashed red and blue vectors, respectively, originating at the fixed point along the periodic orbit, labeled t. These vectors form a set of conjugate diameters that describe a unique ellipse centered at the periodic orbit that forms the first-order approximation of the instantaneous invariant curve associated with the oscillatory mode. A set of principal semi-axes of this ellipse are illustrated in solid red and blue vectors, respectively. These vectors form an orthogonal pair of conjugate diameters for the same ellipse spanned by the real and imaginary components of the complex eigenvector, $\boldsymbol{w}^*$.

The real and imaginary components of the scaled complex eigenvector describe nonunique, principal semi-axes of an ellipse formed by an invariant curve of unspecified size relative to a fixed

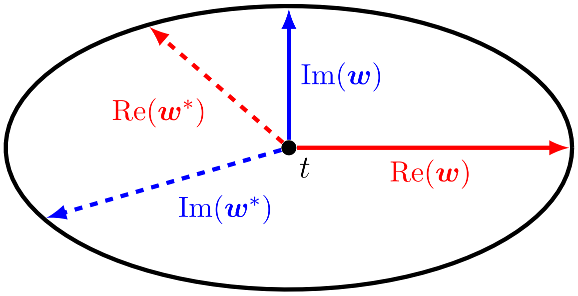

Figure 4.1: Real and imaginary components of the complex eigenvector with the principal axes of the approximated invariant curve. Reproduced with permission from Springer Nature [108].

point. Next, the complex eigenvector is scaled such that the magnitude of the projection of the semi-major axis of the ellipse onto the configuration space is equal to unity about the specific fixed point. After this step, the magnitude of the real position vector, $\boldsymbol{r}_r$, associated with the complex eigenvector is equal to unity such that $\boldsymbol{r}_r$ forms a unit vector in configuration space and $\boldsymbol{r}_i$ possesses a magnitude of less than unity. This normalization step is useful within the definition of the local toroidal coordinate sets to aid interpretation of the size of an approximated invariant torus in the configuration space.

Finally, the sign ambiguities that occur within an SVD must be addressed via a series of sign checks to ensure a consistent definition for $\boldsymbol{w}$. However, because of the variety of geometries of periodic orbits that admit oscillatory modes, a single set of sign checks may not be effectively defined for general application across periodic orbits in the CR3BP. Rather, sign checks may be defined on a case-by-case basis. A set of sign checks are defined that are applied throughout this investigation. First, if the perpendicular unit vector, $\hat{\boldsymbol{n}}$, is anti-parallel to the orbital angular momentum vector of the P_1-P_2 system, $\boldsymbol{w}$ is replaced with its complex conjugate. This enforces the constraint:

$$\hat{\boldsymbol{n}}^T \hat{\boldsymbol{z}} > 0 \tag{4.6}$$

The second sign check reflects the direction of $\boldsymbol{r}_r$ with respect to the axes of the rotating frame. For the first-order approximation of an invariant curve relative to a fixed points of periodic orbit located on the xz plane, the projection of $\boldsymbol{r}_r$ onto the xz plane is often observed to align with either the $\hat{\boldsymbol{x}}$ or $\hat{\boldsymbol{y}}$ axis, depending on specific orbit. To accommodate these two cases, the following constraint is enforced:

$$\hat{\boldsymbol{x}}^T\boldsymbol{r}_r + \hat{\boldsymbol{y}}^T\boldsymbol{r}_r > 0 \tag{4.7}$$

When satisfied, this constraint enforces the projection of $\boldsymbol{r}_r$ to lie in the positive direction of either axis. If this constraint is not satisfied, $-\boldsymbol{w}$ is used as the normalized eigenvector. The resulting components of the normalized complex eigenvector possess a unique and consistent description that is used within the mappings between relative Cartesian states and local toroidal coordinates.

The complex eigenvector of the monodromy matrices of the three reference orbits are normalized using the outlined process. For each orbit, the complex eigenvector is normalized at a crossing of the xz plane using the sign checks defined in Eq. (4.6) and Eq. (4.7). The selected fixed point and the value of the complex eigenvector formulated in the rotating frame for each orbit are listed in Table 4.1. The 8-day Earth-Moon L_2 southern NRHO and the 177-day Sun-Earth L_1 southern halo orbit are unstable, and each possess one oscillatory mode. The 7-day Earth-Moon DRO is stable, however, only the in-plane oscillatory mode is used in the investigation.

The invariant curve associated with the normalized complex eigenvector is labeled the normalized first-order invariant curve and supplies a reference ellipse within the definition of the local toroidal coordinate systems. The axes of the two introduced coordinates systems are derived from the real and imaginary position components of the normalized complex eigenvector as it naturally evolves over time. Once normalized, this eigenvector is integrated via the Jacobian matrix evaluated at states along the periodic orbit, or determined at a future fixed point via the state transition matrix. Thus, care must be taken when the starting point of the analysis is different from the fixed point along the periodic orbit at which the complex eigenvector is normalized. Furthermore, the state along the periodic orbit where the complex eigenvector is normalized must always be specified when using the toroidal coordinates systems to ensure consistent and repeatable implementation.

Table 4.1: Truncated initial conditions and normalized complex eigenvectors for the three reference periodic orbits, formulated in the rotating frame.

Reference orbit	Period (days)	Normalization location	State at normalization location	Normalized eigenvector
Earth-Moon L_2 southern NRHO	8	Apolune	$\boldsymbol{x} = \begin{bmatrix} 1.0776 \\ 0 \\ -0.20229 \\ 0 \\ -0.19523 \\ 0 \end{bmatrix}$	$\boldsymbol{w} = \begin{bmatrix} 0.89331 + 0i \\ 0 + 0.43774i \\ 0.44944 + 0i \\ 0 + 0.84533i \\ -2.0306 + 0i \\ 0 + 1.8099i \end{bmatrix}$
Earth-Moon distant retrograde	7	Negative $\hat{\boldsymbol{x}}$-axis crossing	$\boldsymbol{x} = \begin{bmatrix} 1.0951 \\ 0 \\ 0 \\ 0 \\ -0.46105 \\ 0 \end{bmatrix}$	$\boldsymbol{w} = \begin{bmatrix} 0 + 0.31624i \\ 1 + 0i \\ 0 + 0i \\ 3.1293 + 0i \\ 0 - 1.114i \\ 0 + 0i \end{bmatrix}$
Sun-Earth L_1 southern halo	177	Apogee	$\boldsymbol{x} = \begin{bmatrix} 0.98908 \\ 0 \\ -0.00401 \\ 0 \\ 0.01086 \\ 0 \end{bmatrix}$	$\boldsymbol{w} = \begin{bmatrix} 0 - 0.33309i \\ 1 + 0i \\ 0 + 0.87939i \\ 1.0778 + 0i \\ 0 + 1.3314i \\ -0.93246 + 0i \end{bmatrix}$

4.2 Nonsingular local toroidal coordinates

The nonsingular local toroidal coordinates are defined as three scalar quantities that, along with their respective time derivatives, describe the state of the chaser spacecraft relative to a target spacecraft located along a periodic orbit using basis vectors derived from the center eigenspace. The position vector locating the chaser spacecraft relative to a state along a periodic orbit may be constructed as a linear combination of the nonsingular local toroidal coordinates and the axes of the nonsingular toroidal coordinate frame. The relative position vector, $\boldsymbol{\rho}$, may be defined in terms of the nonsingular local toroidal coordinates, (α, β, h), as

$$\boldsymbol{\rho} = \alpha \boldsymbol{r}_r + \beta \boldsymbol{r}_i + h\hat{\boldsymbol{n}} \tag{4.8}$$

Figure 4.2 displays a conceptual illustration of the relative position vector, $\boldsymbol{\rho}$, locating a chaser spacecraft, c, from a target spacecraft, t, located on a periodic orbit using the basis vectors, $\{\boldsymbol{r}_r, \boldsymbol{r}_i, \hat{\boldsymbol{n}}\}$, and nonsinguar local toroidal coordinates.

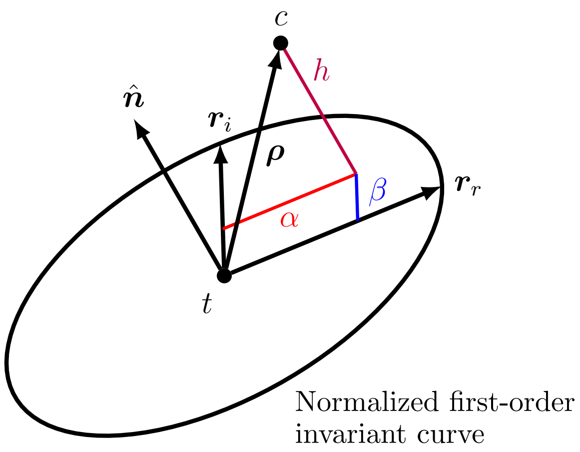

Figure 4.2: Nonsingular local toroidal coordinates (α, β, h) describing the position of a chaser spacecraft relative to a target spacecraft located on a periodic orbit with an oscillatory mode. Reproduced with permission from Springer Nature [108].

The three nonsingular local toroidal coordinates form a non-orthogonal, oblique coordinate set. The first and second coordinates, defined as α and β, express part of the relative position vector as a linear combination of the real and imaginary position components, $\boldsymbol{r}_r$ and $\boldsymbol{r}_i$, respectively, of the normalized complex eigenvector associated with the oscillatory mode evaluated at the state of the target spacecraft along the periodic orbit. The third coordinate, h, is defined as the distance of the chaser spacecraft from the plane spanning the projection of the center eigenspace onto the configuration space; a value of $h = 0$ indicates the chaser spacecraft is located within this plane. For a nonzero value of h, the sign reflects whether the relative position vector of the chaser spacecraft is parallel or anti-parallel to $\hat{\boldsymbol{n}}$, the unit vector that is normal to the plane formed by the projection of the center eigenspace onto the configuration space. Each coordinate is specified with dimensions of length and may be nondimensionalized using the characteristic length quantity associated with the CR3BP.

The nonsingular local toroidal coordinate frame is constructed using the real and imaginary position components of the normalized complex eigenvector associated with the oscillatory mode of a nearby state along a periodic orbit as well as the unit vector that is normal to the corresponding plane. Specifically, this new coordinate frame, labeled as $\mathscr{Z}$, is defined with the axes $\{\boldsymbol{r}_r, \boldsymbol{r}_i, \hat{\boldsymbol{n}}\}$, extracted from the normalized complex eigenvector evaluated at the fixed point along the periodic orbit locating the target spacecraft. These vectors form a non-orthogonal, right-handed reference frame with axes that do not necessarily possess unit length.

Because of their definition, the axes of the nonsingular local toroidal coordinate frame must be carefully and consistently computed over the time interval of interest. Recall that as a result of the normalization process detailed in Section 4.1, the magnitude of $\boldsymbol{r}_r$ is equal to unity at a specified initial epoch when calculated using a single initial state along the periodic orbit. However, the magnitudes of the basis vectors $\boldsymbol{r}_r$ and $\boldsymbol{r}_i$ are designed to vary at later instants of time, consistent with the invariant curve associated with a single invariant torus also evolving in size and shape relative to subsequent states along the reference periodic orbit. Thus, the normalized complex eigenvector used to compute the basis vectors within this system is integrated along with the state of the target spacecraft from a specified initial condition via the Jacobian matrix to capture the natural rotational frequencies of the center eigenspace. Furthermore, while the magnitude of $\boldsymbol{r}_r$ is greater than the magnitude of $\boldsymbol{r}_i$ at the normalization point, generally, the magnitude of $\boldsymbol{r}_r$ is not always greater than the magnitude of $\boldsymbol{r}_i$. For brevity, this frame is also referred to as simply the toroidal frame within this investigation.

The relative position vector locating the chaser spacecraft relative to the target spacecraft on the periodic orbit may be expressed in nonsingular toroidal coordinates via a 3 × 1 set. This set, labeled $\boldsymbol{z}$, is written as

$$\boldsymbol{z} = \begin{bmatrix} \alpha & \beta & h \end{bmatrix}^T \tag{4.9}$$

The time derivatives of the three scalar nonsingular local toroidal coordinates are determined by the time derivative of $\boldsymbol{z}$ for an observer fixed in the nonsingular local toroidal coordinate frame. The time derivative of the nonsingular coordinates for an observer fixed in the toroidal coordinate frame, indicated by the notation ${}^{\mathcal{Z}}(\ )'$, is defined as

$${}^{\mathcal{Z}}\boldsymbol{z}' = \begin{bmatrix} \dot{\alpha} & \dot{\beta} & \dot{h} \end{bmatrix}^T \tag{4.10}$$

whereas the second time derivative is defined as

$${}^{\mathcal{Z}}\boldsymbol{z}'' = \begin{bmatrix} \ddot{\alpha} & \ddot{\beta} & \ddot{h} \end{bmatrix}^T \tag{4.11}$$

for components formulated in the nonsingular toroidal frame.

To calculate the nonsingular local toroidal coordinates, a transformation is employed between the non-orthogonal toroidal coordinate frame and relative Cartesian coordinates in the rotating frame. The definition of the relative position vector in terms of the nonsingular local toroidal coordinates from Eq. (4.8) is rewritten as

$$\boldsymbol{\rho} = [\boldsymbol{R}]\boldsymbol{z} \tag{4.12}$$

where $[\boldsymbol{R}]$ is a 3 × 3 matrix containing the basis vectors of the nonsingular toroidal coordinate system expressed in the rotating frame, defined as

$$[\boldsymbol{R}] = \begin{bmatrix} \boldsymbol{r}_r & \boldsymbol{r}_i & \hat{\boldsymbol{n}} \end{bmatrix} \tag{4.13}$$

The columns of $[\boldsymbol{R}]$ are computed using the real and imaginary position components of the normalized complex eigenvector which has been integrated from the specified initial fixed point and evaluated at the current state of the target spacecraft along the periodic orbit. Using this definition, the nonsingular coordinates are then straightforwardly determined by inverting $[\boldsymbol{R}]$ as

$$\boldsymbol{z} = [\boldsymbol{R}]^{-1}\boldsymbol{\rho} \tag{4.14}$$

The matrix $[\boldsymbol{R}]$ is full rank and invertible so long as $\boldsymbol{r}_r$ and $\boldsymbol{r}_i$ are not collinear; this condition is satisfied when the oscillatory mode of a periodic orbit does not produce rectilinear motion in its associated Cartesian frame.

Next, consider the time derivative of the nonsingular local toroidal coordinates for an observer in the $\mathcal{Z}$ frame. Computing the time derivative of Eq. (4.12), the relative velocity of the chaser spacecraft for an observer in the rotating frame, $\boldsymbol{\rho}'$, is written as a function of the coordinates and coordinate rates as

$$\boldsymbol{\rho}' = [\boldsymbol{R}]\left({}^{\mathcal{Z}}\boldsymbol{z}'\right) + [\boldsymbol{R}]'\boldsymbol{z} \tag{4.15}$$

where $[\boldsymbol{R}]'$ is the time derivative of $[\boldsymbol{R}]$ for an observer in the rotating frame, written as

$$[\boldsymbol{R}]' = \begin{bmatrix} \boldsymbol{v}_r & \boldsymbol{v}_i & \hat{\boldsymbol{n}}' \end{bmatrix} \tag{4.16}$$

Each component of $[\boldsymbol{R}]'$ is derived from the normalized complex eigenvector which has been integrated from the specified initial fixed point and evaluated at the current state of the target spacecraft along the periodic orbit. In this expression, the time derivative of the normal unit vector for an observer in the rotating frame, $\hat{\boldsymbol{n}}'$, is calculated as

$$\hat{\boldsymbol{n}}' = \frac{\boldsymbol{n}'}{n} - \left(\boldsymbol{n}^T\boldsymbol{n}'\right)\frac{\boldsymbol{n}}{n^3} \tag{4.17}$$

where $\boldsymbol{n}' = \boldsymbol{v}_r \times \boldsymbol{r}_i + \boldsymbol{r}_r \times \boldsymbol{v}_i$. The time derivative of the nonsingular local toroidal coordinate set for an observer in the $\mathcal{Z}$ frame is then computed as a function of the relative Cartesian position and velocity vectors as

$$^{\mathcal{Z}}\boldsymbol{z}' = [\boldsymbol{R}]^{-1}\boldsymbol{\rho}' - [\boldsymbol{R}]^{-1}[\boldsymbol{R}]'[\boldsymbol{R}]^{-1}\boldsymbol{\rho} \tag{4.18}$$

This expression describes a transformation between the relative velocity vector for an observer fixed in the rotating frame to the relative velocity vector for an observer fixed in the non-orthogonal toroidal coordinate system.

To visualize the nonsingular local toroidal coordinate frame, consider a comparison between the coordinate grid lines of the rotating frame and the nonsingular local toroidal coordinate frame. Figure 4.3a illustrates a normalized first-order invariant curve, represented by a black ellipse, plotted relative to its associated periodic orbit. Several grid lines of the rotating frame, i.e., lines with a constant value of x or y separated by the unit lengths of $\hat{\boldsymbol{x}}$ and $\hat{\boldsymbol{y}}$. The same approximated invariant curve is plotted in Figure 4.3b with the grids lines of the nonsingular local toroidal coordinate frame, i.e. lines with a constant value of α and β, separated by the lengths of $\boldsymbol{r}_r$ and $\boldsymbol{r}_i$, respectively. In the nonsingular toroidal frame, the grid lines conform to the instantaneous orientation, size, and shape of the normalized invariant curve relative to the periodic orbit. Because the first two basis vectors of the nonsingular toroidal coordinate frame are neither orthogonal nor normalized to a magnitude of unity in Cartesian space, the transformation from the rotating frame to the nonsingular local toroidal coordinate frame is not area or shape-preserving [132]. Accordingly, while values of α and β are reported in this investigation using units of km, note that distances generally do not exactly translate between toroidal coordinate systems and a Cartesian coordinate system.

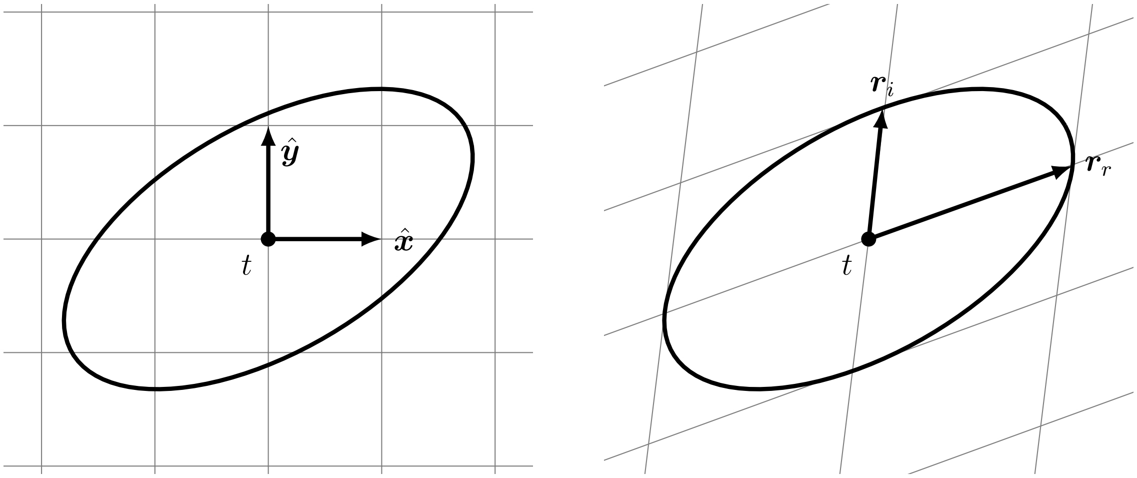

(a) Coordinate lines of the rotating frame

(b) Coordinate lines of the toroidal frame

Figure 4.3: Conceptual illustration of the reference first-order invariant curve and grid lines of unit length in the rotating frame and toroidal frame.

4.3 Geometric local toroidal coordinates

The geometric local toroidal coordinates modify the nonsingular local toroidal coordinates to express the state of the chaser spacecraft in terms of geometrically-interpretable quantities. The relative position vector for the chaser spacecraft measured from the target spacecraft is written as a nonlinear function of the geometric toroidal coordinates, (ε, θ, h), as

$$\boldsymbol{\rho} = \varepsilon \left(\boldsymbol{r}_r \cos\theta + \boldsymbol{r}_i \sin\theta \right) + h\hat{\boldsymbol{n}} \tag{4.19}$$

A conceptual illustration of the relative position vector, $\boldsymbol{\rho}$, and the geometric local toroidal coordinates describing the configuration of a chaser, c, spacecraft relative to a target spacecraft, t, located along a periodic orbit is displayed in Figure 4.4. In this illustration, the black curve represents the first-order invariant curve associated with the instantaneous position components of the normalized complex eigenvector.

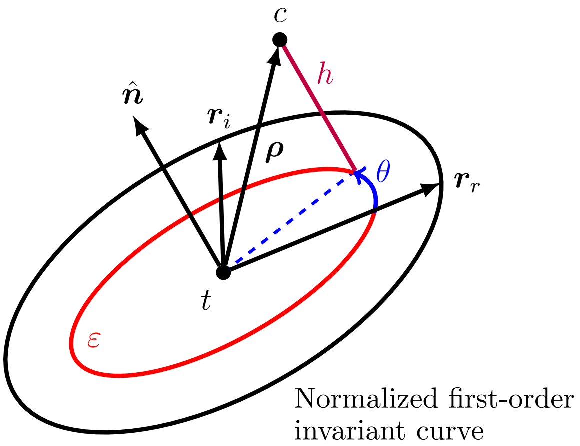

Figure 4.4: Geometric local toroidal coordinates (ε, θ, h) describing the position of a chaser spacecraft relative to a target spacecraft located on a periodic orbit with an oscillatory mode. Reproduced with permission from Springer Nature [108].

The three geometric local toroidal coordinates form a non-orthogonal, curvilinear coordinate set. The first coordinate, ε, indicates the size of the first-order approximation of the invariant curve that passes through the projection of the relative position vector of the chaser spacecraft onto the plane instantaneously spanned by $\boldsymbol{r}_r$ and $\boldsymbol{r}_i$. The ε coordinate is always positive and is expressed using length units. The second coordinate, θ, indicates the angular displacement of the chaser spacecraft about the ellipse formed by the first-order approximation of the invariant curve in configuration space, measured within the plane spanned by $\boldsymbol{r}_r$ and $\boldsymbol{r}_i$. Specifically, the angle is measured counterclockwise from $\boldsymbol{r}_r$ when viewed from the $\hat{\boldsymbol{n}}$ direction. The ε and θ coordinates are related to the nonsingular coordinates, α and β, as

$$\alpha = \varepsilon \cos\theta \tag{4.20}$$

$$\beta = \varepsilon \sin\theta \tag{4.21}$$

The third coordinate, h, possesses the same definition as in the nonsingular toroidal coordinate system. Once the nonsingular coordinates have been computed via Eq. (4.14), the first two geometric coordinates, ε and θ, are calculated as

$$\varepsilon = \sqrt{\alpha^2 + \beta^2} \tag{4.22}$$

$$\theta = \tan^{-1}\left(\frac{\beta}{\alpha}\right) \tag{4.23}$$

Along the $\hat{\boldsymbol{n}}$ axis, $\varepsilon = 0$ and a nonunique definition occurs in the mapping from geometric toroidal coordinates to Cartesian coordinates. When this condition is met, θ is undefined.

When the eigenvector normalization scheme described in Section 4.1 is applied, the geometric local toroidal coordinate ε reflects the maximum separation distance of the first-order approximation of the invariant curve from the periodic orbit at the location of the normalization of the complex eigenvector. Thus, it may be useful to specify this initial condition as a geometrically-meaningful fixed point. For example, if the normalized eigenvector is defined at an apsis of a periodic orbit, the physical interpretation of ε is the maximum separation distance of the approximated invariant curve defined by ε relative to the apsis.

The rates of change of the geometric toroidal coordinates are directly computed from the nonsingular coordinates and nonsingular toroidal coordinate rates. The rate of changes, $\dot{\alpha}$ and $\dot{\beta}$, are expressed as functions of the geometric local toroidal coordinates as

$$\dot{\alpha} = \dot{\varepsilon}\cos\theta - \varepsilon\sin\theta \tag{4.24}$$

$$\dot{\beta} = \dot{\varepsilon}\sin\theta + \varepsilon\cos\theta \tag{4.25}$$

The final coordinate rate, $\dot{h}$, also possesses the same definition as in the nonsingular toroidal coordinate rates. The geometric coordinate rates are calculated as nonlinear functions of the nonsingular coordinates and their respective rates as

$$\dot{\varepsilon} = \frac{\alpha\dot{\alpha} + \beta\dot{\beta}}{\varepsilon} \tag{4.26}$$

$$\dot{\theta} = \frac{\alpha\dot{\beta} - \beta\dot{\alpha}}{\varepsilon^2} \tag{4.27}$$

The value of the time derivative, $\dot{h}$, remains unchanged from the nonsingular coordinate set. The time derivative of Eq. (4.19) produces an expression for the relative velocity of the chaser spacecraft, $\boldsymbol{\rho}'$, in terms of the geometric coordinates and their rates as

$$\boldsymbol{\rho}' = \dot{\varepsilon}\big(\boldsymbol{r}_r\cos\theta + \boldsymbol{r}_i\sin\theta\big) + \varepsilon\big(\boldsymbol{v}_r\cos\theta - \boldsymbol{r}_r\sin\theta\dot{\theta} + \boldsymbol{v}_i\sin\theta + \boldsymbol{r}_i\cos\theta\dot{\theta}\big) + \dot{h}\hat{\boldsymbol{n}} + h\hat{\boldsymbol{n}}' \tag{4.28}$$

These expressions map the geometric local toroidal coordinates and respective coordinate rates to the relative position and velocity vectors expressed in the rotating frame and relative to a state along a periodic orbit.

The geometric toroidal coordinate system is a local, curvilinear coordinate system with basis vectors that are aligned with the amplitude, angle, and axial components of a reference invariant 2-torus. The geometric toroidal coordinate frame, labeled $\mathcal{E}$, is defined with axes $\{\boldsymbol{e}_\varepsilon, \boldsymbol{e}_\theta, \hat{\boldsymbol{n}}\}$, calculated as a function of both the complex eigenvector associated with the oscillatory mode and geometric coordinates as

$$\boldsymbol{e}_\varepsilon = \boldsymbol{r}_r\cos\theta + \boldsymbol{r}_i\sin\theta \tag{4.29}$$

$$\boldsymbol{e}_\theta = \varepsilon\left(-\boldsymbol{r}_r\sin\theta + \boldsymbol{r}_i\cos\theta\right) \tag{4.30}$$

These axes are defined as the partial derivatives of $\boldsymbol{\rho}$ with respect to ε and θ, respectively. Consistent with the nonsingular coordinate frame, the basis vectors are nonorthogonal, and the magnitudes of $\boldsymbol{e}_\varepsilon$ and $\boldsymbol{e}_\theta$ are generally not equal to unity. The axes of the geometric local toroidal coordinate frame may be grouped in a 3 × 3 matrix. This matrix, labeled $\boldsymbol{B}$, is defined as

$$[\boldsymbol{B}] = \begin{bmatrix} \boldsymbol{e}_\varepsilon & \boldsymbol{e}_\theta & \hat{\boldsymbol{n}} \end{bmatrix} \tag{4.31}$$

and is comparable to the $[\boldsymbol{R}]$ matrix defined for the nonsingular local toroidal coordinate frame. The time derivative of the columns of $[\boldsymbol{B}]$ for an observer in the rotating frame, $[\boldsymbol{B}]'$, is calculated by directly differentiating the columns of the matrix, and is equal to

$$[\boldsymbol{B}]' = \begin{bmatrix} \boldsymbol{e}'_\varepsilon & \boldsymbol{e}'_\theta & \hat{\boldsymbol{n}}' \end{bmatrix} \tag{4.32}$$

where the time derivative of the first two axes of the coordinate frame are equal to

$$\boldsymbol{e}'_\varepsilon = \boldsymbol{v}_r \cos\theta - \boldsymbol{r}_r \dot{\theta} \sin\theta + \boldsymbol{v}_i \sin\theta + \boldsymbol{r}_i \dot{\theta} \cos\theta \tag{4.33}$$

$$\boldsymbol{e}'_\theta = \dot{\varepsilon} \left(\boldsymbol{r}_i \cos\theta - \boldsymbol{r}_r \sin\theta \right) + \varepsilon \left(\boldsymbol{v}_i \cos\theta - \boldsymbol{r}_i \dot{\theta} \sin\theta - \boldsymbol{v}_r \sin\theta - \boldsymbol{r}_r \dot{\theta} \cos\theta \right) \tag{4.34}$$

The $[\boldsymbol{B}]$ matrix and its time derivative are used later in Chapter 6 with the formulation of various spacecraft control strategies leveraging local toroidal coordinates.

Unlike the nonsingular coordinates, the geometric coordinates do not map to relative position vectors as a linear combination of the basis vectors. However, it is convenient to express the values of the geometric toroidal coordinates in a 3 × 1 column vector, as

$$\boldsymbol{e} = \begin{bmatrix} \varepsilon & \theta & h \end{bmatrix}^T \tag{4.35}$$

The first and second time derivatives of the geometric toroidal coordinates are similarly grouped in 3 × 1 column vectors as

$${}^{\mathcal{E}}\boldsymbol{e}' = \begin{bmatrix} \dot{\varepsilon} & \dot{\theta} & \dot{h} \end{bmatrix}^T \tag{4.36}$$

and

$${}^{\mathcal{E}}\boldsymbol{e}'' = \begin{bmatrix} \ddot{\varepsilon} & \ddot{\theta} & \ddot{h} \end{bmatrix}^T \tag{4.37}$$

respectively. Compared to the nonsingular coordinate set, the geometric toroidal coordinates supply increased intuition into the position of the chaser spacecraft, at the expense of a singular point along the $\hat{\boldsymbol{n}}$ axis.

4.4 Properties of local toroidal coordinates

The two sets of local toroidal coordinates possess properties that render them useful for the analysis of quasi-periodic motion relative motion near a periodic orbit. First, equations of relative motion formulated in the nonsingular local toroidal coordinate frame are derived. Using these equations of motion, motion on the center eigenspace, i.e., in linearized dynamics, is demonstrated to possess a constant description using local toroidal coordinates. Next, the state transition matrix of a periodic orbit is reformulated in the nonsingular toroidal coordinate frame to supply an alternative perspective of motion in the vicinity of the periodic orbit. Finally, an analysis of the drift of motion initialized on the center eigenspace and propagated in the nonlinear CR3BP is presented.

4.4.1 Equations of relative motion in the nonsingular toroidal coordinate frame

The nonsingular local toroidal coordinates frame, $\mathcal{Z}$, supplies an alternative kinematic description of motion relative to a periodic orbit. Equations of relative motion may be formulated in this toroidal coordinate frame to directly assess the time history of a relative trajectory using toroidal coordinates. Consider the description of the relative velocity of the chaser spacecraft for an observer fixed in the rotating frame expressed in terms of the nonsingular local toroidal coordinates, expressed in Eq. (4.15). Rearranging this equation to solve for the rate of change of the toroidal coordinates, ${}^{\mathcal{Z}}\boldsymbol{z}'$, yields

$$ {}^{\mathcal{Z}}\boldsymbol{z}' = [\boldsymbol{R}]^{-1}\left(\boldsymbol{\rho}' - [\boldsymbol{R}]'[\boldsymbol{R}]^{-1}\boldsymbol{\rho}\right) \tag{4.38} $$

Next, an angular velocity-like term is defined using the transformation between the rotating and toroidal frame. This term is a 3 × 3 matrix, labeled $[\boldsymbol{\Omega}]$, and defined as

$$ [\boldsymbol{\Omega}] = -[\boldsymbol{R}]'[\boldsymbol{R}]^{-1} \tag{4.39} $$

This matrix is analogous to the angular velocity of the rotating frame with respect to the toroidal frame. However, because the transformation between the rotating and toroidal frame is not shape-preserving, $[\boldsymbol{\Omega}]$, is not skew-symmetric. Using this definition, the relative velocity vector for an observer in the toroidal frame may be written as

$$ {}^{\mathcal{Z}}\boldsymbol{z}' = [\boldsymbol{R}]^{-1}\left(\boldsymbol{\rho}' + [\boldsymbol{\Omega}]\boldsymbol{\rho}\right) \tag{4.40} $$

Taking the derivative of this equation yields an expression of the second time derivative of the nonsingular toroidal coordinates which simplifies as

$$ {}^{\mathcal{Z}}\boldsymbol{z}'' = [\boldsymbol{R}]^{-1}\left(\boldsymbol{\rho}'' + 2[\boldsymbol{\Omega}]\boldsymbol{\rho}' + [\boldsymbol{\Omega}][\boldsymbol{\Omega}]\boldsymbol{\rho} + [\boldsymbol{\Omega}]'\boldsymbol{\rho}\right) \tag{4.41} $$

These expressions require the time derivative of several expressions, including the time derivative of $[\boldsymbol{\Omega}]$, defined as

$$ [\boldsymbol{\Omega}]' = -[\boldsymbol{R}]''[\boldsymbol{R}]^{-1} + [\boldsymbol{R}]'[\boldsymbol{R}]^{-1}[\boldsymbol{R}]'[\boldsymbol{R}]^{-1} \tag{4.42} $$

the second derivative of the $[\boldsymbol{R}]$ matrix for an observer in the rotating frame, written as

$$ [\boldsymbol{R}]'' = \begin{bmatrix} \boldsymbol{a}_r & \boldsymbol{a}_i & \hat{\boldsymbol{n}}'' \end{bmatrix} \tag{4.43} $$

and finally, the second time derivative of the normal unit vector, $\hat{\boldsymbol{n}}$, for an observer in the rotating frame is defined as

$$ \hat{\boldsymbol{n}}'' = \frac{\boldsymbol{n}''}{n} - 2\left(\boldsymbol{n}^T\boldsymbol{n}'\right)\frac{\boldsymbol{n}'}{n^3} - (\boldsymbol{n}'' \cdot \boldsymbol{n} + \boldsymbol{n}' \cdot \boldsymbol{n})\frac{\boldsymbol{n}}{n^3} - 3(\boldsymbol{n} \cdot \boldsymbol{n}')\frac{\boldsymbol{n}}{n^5} \tag{4.44} $$

where $\boldsymbol{n}'' = (\boldsymbol{a}_r \times \boldsymbol{r}_i) + 2(\boldsymbol{v}_r \times \boldsymbol{v}_i) + (\boldsymbol{r}_r \times \boldsymbol{a}_i)$. Substituting Eq. (4.8), Eq. (4.15), and Eq. (4.42) into Eq. (4.41), the equations of relative motion may alternatively be expressed as a function of the nonsingular toroidal coordinates and coordinate rates as

$$ {}^{\mathcal{Z}}\boldsymbol{z}'' = [\boldsymbol{R}]^{-1}\left(\boldsymbol{\rho}'' - 2[\boldsymbol{R}]'({}^{\mathcal{Z}}\boldsymbol{z}') - [\boldsymbol{R}]''\boldsymbol{z}\right) \tag{4.45} $$

These equations of relative motion require the relative acceleration of the chaser spacecraft with respect to the target spacecraft as seen by an observer in the rotating frame. As time does not explicitly appear, this formulation of the equations of relative motion is autonomous.

Additional investigation into the angular velocity analog matrix reveals that the matrix is time periodic over the period of the associated periodic orbit, T. Consider the $[\boldsymbol{\Omega}]$ matrix defined at an initial time, t_0 and a final time $t_f = t_0 + T$, labeled $[\boldsymbol{\Omega}(t_0)]$ and $[\boldsymbol{\Omega}(t_f)]$, respectively. These matrices are expressed as

$$[\boldsymbol{\Omega}(t_0)] = -[\boldsymbol{R}(t_0)]'[\boldsymbol{R}(t_0)]^{-1}$$
$$[\boldsymbol{\Omega}(t_f)] = -[\boldsymbol{R}(t_f)]'[\boldsymbol{R}(t_f)]^{-1}$$

The matrix $[\boldsymbol{R}(t_f)]$ may be rewritten as a function of the vector components of the complex eigenvector at the initial time and the complex eigenvalue. First, a matrix, $[\boldsymbol{\Lambda}]$ is defined as a function of the complex eigenvalue as

$$[\boldsymbol{\Lambda}] = \begin{bmatrix} \lambda_r & \lambda_i & 0 \\ -\lambda_i & \lambda_r & 0 \\ 0 & 0 & 1 \end{bmatrix} \tag{4.46}$$

Examining the evolution of the components of the complex eigenvector after one revolution, as determined by the definition of eigenvalues and eigenvectors, $[\boldsymbol{M}]\boldsymbol{w} = \lambda\boldsymbol{w}$, $[\boldsymbol{R}]$ after one revolution may be expressed as

$$\begin{aligned}[\boldsymbol{R}(t_f)] &= \begin{bmatrix}(\lambda_r\boldsymbol{r}_r(t_0) - \lambda_i\boldsymbol{r}_i(t_0)) & (\lambda_i\boldsymbol{r}_r(t_0) + \lambda_r\boldsymbol{r}_i(t_0)) & \hat{\boldsymbol{n}}(t_0)\end{bmatrix} \\ &= [\boldsymbol{R}(t_0)][\boldsymbol{\Lambda}]\end{aligned}$$

Recall that in Section 3.3.2, the normal direction, $\hat{\boldsymbol{n}}$ is proven to be time-periodic such that $\hat{\boldsymbol{n}}(t_0) = \hat{\boldsymbol{n}}(t_f)$. The time derivative of $[\boldsymbol{R}]$ after one revolution is then equal to

$$\begin{aligned}[\boldsymbol{R}(t_f)]' &= \begin{bmatrix}(\lambda_r\boldsymbol{v}_r(t_0) - \lambda_i\boldsymbol{v}_i(t_0)) & (\lambda_i\boldsymbol{v}_r(t_0) + \lambda_r\boldsymbol{v}_i(t_0)) & \hat{\boldsymbol{n}}'(t_0)\end{bmatrix} \\ &= [\boldsymbol{R}(t_0)]'[\boldsymbol{\Lambda}]\end{aligned}$$

Using these expressions for $[\boldsymbol{R}(t_f)]$ and $[\boldsymbol{R}(t_f)]'$, $[\boldsymbol{\Omega}(t_f)]$ may be written as

$$\begin{aligned}[\boldsymbol{\Omega}(t_f)] &= -[\boldsymbol{R}(t_0)]'[\boldsymbol{\Lambda}]\left([\boldsymbol{R}(t_0)][\boldsymbol{\Lambda}]\right)^{-1} \\ &= [\boldsymbol{\Omega}(t_0)]\end{aligned}$$

Thus, $[\boldsymbol{\Omega}]$ is time-periodic over T, and the following holds:

$$[\boldsymbol{\Omega}(t_0)] = [\boldsymbol{\Omega}(t_0 + T)] \tag{4.47}$$

Because $[\boldsymbol{\Omega}]$ is an analog of the angular velocity between two frames, the norm of the matrix supplies insight into the rate at which the toroidal frame is rotating with respect to the rotating frame.

4.4.2 Describing motion on the center eigenspace

While any relative state may be expressed via the local toroidal coordinate systems, a state that lies along the center eigenspace is straightforward to describe via a sparse state representation, i.e., where only two of the six coordinates and coordinate rates possess nonzero values. This section demonstrates that states within the set $\boldsymbol{\varphi}$ are equilibrium solutions to the equations of relative motion that are linearized relative to a periodic orbit when expressed using local toroidal coordinates. This result is a direct consequence of defining the basis vectors of the local toroidal coordinate frames using the normalized complex eigenvector associated with the oscillatory mode, which is integrated along with the state of the target spacecraft. In nonsingular toroidal coordinates, all states within the set $\boldsymbol{\varphi}$ admit values of $h = \dot{h} = \dot{\alpha} = \dot{\beta} = 0$, while α and β are free parameters indicating the projection of the position vector onto the plane instantaneously spanned by $\boldsymbol{r}_r$ and $\boldsymbol{r}_i$. This property of the coordinate set is evident in Eqs. (4.8) and (4.15), where $h = \dot{h} = \dot{\alpha} = \dot{\beta} = 0$ results in a state along the set $\boldsymbol{\varphi}$ as defined in Eq. (3.29). Similarly, in geometric toroidal coordinates, all states within the set $\boldsymbol{\varphi}$ possess values of $h = \dot{h} = \dot{\varepsilon} = \dot{\theta} = 0$ due to the definitions of the geometric coordinates as a function of the nonsingular coordinates. The quantities ε and θ are analogous free parameters that, respectively, correspond to the size of and angle along the first-order approximation of the invariant curve associated with a fixed point.

The equations of relative motion that are linearized about a periodic orbit and the time derivative of the normalized complex eigenvector, $\boldsymbol{w}$, are both governed by the Jacobian matrix evaluated along the periodic orbit. The Jacobian matrix evaluated at the state of the target spacecraft located along a periodic orbit may be expressed using four 3 × 3 submatrices as

$$[\boldsymbol{A}]_t = \begin{bmatrix} [\boldsymbol{A}_{11}] & [\boldsymbol{A}_{12}] \\ [\boldsymbol{A}_{21}] & [\boldsymbol{A}_{22}] \end{bmatrix} \tag{4.48}$$

The time derivative of the eigenvector $\boldsymbol{w}$ for an observer in the rotating frame is then written as the sum of two 6 × 1 vectors containing the real and imaginary components as

$$\boldsymbol{w}' = \begin{bmatrix} \boldsymbol{v}_r \\ \\ \boldsymbol{a}_r \end{bmatrix} + i \begin{bmatrix} \boldsymbol{v}_i \\ \\ \boldsymbol{a}_i \end{bmatrix} \tag{4.49}$$

where $\boldsymbol{v}$ and $\boldsymbol{a}$ indicate velocity and acceleration components of the eigenvector, respectively, and the subscripts r and i indicate real and imaginary components, respectively. Using these definitions, $\boldsymbol{a}_r$ and $\boldsymbol{a}_i$, are then expressed as linear functions of the submatrices of the Jacobian as

$$\boldsymbol{a}_r = [\boldsymbol{A}_{21}]\boldsymbol{r}_r + [\boldsymbol{A}_{22}]\boldsymbol{v}_r \tag{4.50}$$

$$\boldsymbol{a}_i = [\boldsymbol{A}_{21}]\boldsymbol{r}_i + [\boldsymbol{A}_{22}]\boldsymbol{v}_i \tag{4.51}$$

An expression for the relative acceleration of a state within the set $\boldsymbol{\varphi}$ is derived by expressing the equations of relative motion that are linearized about a periodic orbit in terms of toroidal coordinates and the Jacobian. The linearized relative Cartesian acceleration is approximated as a function of the submatrices of the Jacobian and the relative position and velocity vectors as

$$\boldsymbol{\rho}'' \approx [\boldsymbol{A}_{21}]\boldsymbol{\rho} + [\boldsymbol{A}_{22}]\boldsymbol{\rho}' \tag{4.52}$$

The relative position vector for a state within the set $\boldsymbol{\varphi}$ in terms of nonsingular coordinates is written as

$$\boldsymbol{\rho}|_{\varphi} = \alpha \boldsymbol{r}_r + \beta \boldsymbol{r}_i \tag{4.53}$$

The associated relative velocity vector for an observer fixed in the rotating frame is written as

$$\boldsymbol{\rho}'|_{\varphi} = \alpha \boldsymbol{v}_r + \beta \boldsymbol{v}_i \tag{4.54}$$

Substituting Eq. (4.53) and Eq. (4.54) into Eq. (4.52), the relative acceleration of a state along the first-order approximation of the invariant curve is written as

$$\boldsymbol{\rho}''\big|_{\varphi} \approx \alpha \boldsymbol{a}_r + \beta \boldsymbol{a}_i \tag{4.55}$$

Accordingly, this expression relates the acceleration for a state located along the first-order approximation of the invariant curve to the time derivative of the complex eigenvector and the nonsingular coordinates, α and β.

An expression for the second time derivative of the nonsingular toroidal coordinates evaluated on the set $\boldsymbol{\varphi}$ is derived and used to prove that the set corresponds to an equilibrium solution to the equations of relative motion linearized about a periodic orbit. Tecall the equations of relative motion formulated in the nonsingular toroidal coordinate frame, written in Eq. (4.45). For states within the set $\boldsymbol{\varphi}$, the coordinate rates for an observer fixed in the $\mathcal{Z}$ frame, i.e., ${}^{\mathcal{Z}}\boldsymbol{z}'$, and the out-of-plane coordinate, h, are equal to zero. Consequently, the second time derivative of the nonsingular coordinate set evaluated along $\boldsymbol{\varphi}$ simplifies to

$$ {}^{\mathcal{Z}}\boldsymbol{z}''\big|_{\varphi} = [\boldsymbol{R}]^{-1}\left(\boldsymbol{\rho}''\big|_{\varphi} - \alpha\boldsymbol{a}_r - \beta\boldsymbol{a}_i\right) \tag{4.56} $$

Substituting Eq. (4.55), the expression for the linearized relative acceleration of the chaser spacecraft evaluated at a state within the set $\boldsymbol{\varphi}$, reveals that

$$ {}^{\mathcal{Z}}\boldsymbol{z}''\big|_{\varphi} \approx [\boldsymbol{R}]^{-1}\left(\alpha\boldsymbol{a}_r + \beta\boldsymbol{a}_i - \alpha\boldsymbol{a}_r - \beta\boldsymbol{a}_i\right) = \boldsymbol{0} \tag{4.57} $$

Because the first and second time derivatives of the geometric coordinates equal zero, a state within the set $\boldsymbol{\varphi}$ corresponds to an equilibrium solution to the equations of relative motion linearized about a periodic orbit. This result supplies a direct description of trajectories in the linear equations of relative motion that trace out the surface of a first-order approximation of an invariant torus via toroidal coordinates.

Since the description of motion on the center eigenspace of the periodic orbit is constant over time, first-order approximations of invariant tori relative to the periodic orbit are straightforwardly represented in the nonsingular toroidal coordinate frame. When α and β are represented along the horizontal and vertical axes, respectively, an invariant torus constructs a circle centered at the periodic orbit. States along this circle with zero coordinates rates are equilibrium solutions in the center eigenspace, i.e., in dynamics linearized about the periodic orbit.

An illustration of this representation is shown in Figure 4.5. In this visual representation of motion relative to the periodic orbit, the lengths of $\boldsymbol{r}_r$ and $\boldsymbol{r}_i$ are scaled to equal unity. The reference invariant curve constructed by the normalized complex eigenvector is represented by a circle that possess a radius of unity, represented in black. These circles may be defined using the nondimensional units of length of the CR3BP or dimensionalized by a unit of length, i.e., km. Additional invariant curves, defined by value of ε, are also plotted. This figure illustrates how nested first-order invariant 2-tori relative to the periodic orbit are straightforwardly represented in the nonsingular toroidal coordinate frame. Furthermore, this representation of invariant tori relative to a periodic orbit is the same for any periodic orbit in the CR3BP that possess an oscillatory mode, supplying a consistent approach for describing oscillatory motion near periodic orbits.

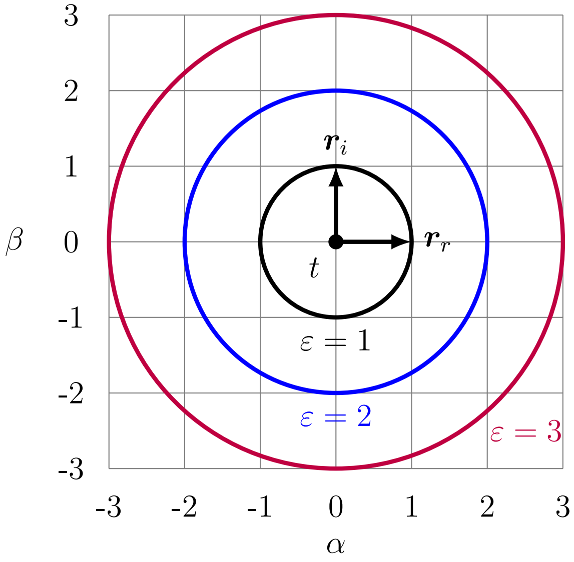

Figure 4.5: Representation of first-order invariant 2-tori in the nonsingular local toroidal coordinate frame defined by different values of ε.

4.4.3 State transition matrix formulated in the toroidal coordinate frame

A linear transformation is used to transform a relative state between the nonsingular local toroidal coordinate frame and rotating frame. Recall the 6 × 1 relative state vector, $\delta\boldsymbol{x}$, that describes the state of the chaser spacecraft relative to a target spacecraft location along the periodic orbit in components of the rotating frame:

$$\delta\boldsymbol{x} = \begin{bmatrix}\delta x & \delta y & \delta z & \delta\dot{x} & \delta\dot{y} & \delta\dot{z}\end{bmatrix}^T$$

An equivalent relative state vector is defined using the nonsingular local toroidal coordinates and coordinate rates as

$$\boldsymbol{\zeta} = \begin{bmatrix} \alpha & \beta & h & \dot{\alpha} & \dot{\beta} & \dot{h} \end{bmatrix}^T \tag{4.58}$$

A 6×6 transformation matrix, $[\boldsymbol{T}]$, that maps a state vector formulated in the toroidal coordinates frame to a state vector formulated in the rotating frame is defined as

$$[\boldsymbol{T}] = \begin{bmatrix} [\boldsymbol{R}] & [\mathbf{0}_3] \\ [\boldsymbol{R}]' & [\boldsymbol{R}] \end{bmatrix} \tag{4.59}$$

As the matrices $[\boldsymbol{R}]$ and $[\boldsymbol{R}]'$ are dependent on the associated fixed point along the periodic orbit, the transformation matrix is also dependent on the fixed point. The transformation from a relative state vector defined in the rotating frame, $\delta\boldsymbol{x}$, to a relative state in the toroidal coordinate frame, $\boldsymbol{\zeta}$, is then expressed as

$$\boldsymbol{\zeta} = [\boldsymbol{T}]^{-1}\delta\boldsymbol{x} \tag{4.60}$$

The transformation matrix is full-rank and invertible so long as the associated oscillatory mode doe not produce motion along a single axis in the rotating frame. Note that the transformation $[\boldsymbol{T}]$ is not periodic and instead corresponds to the quasi-periodic flow in the center eigenspace about the periodic orbit.

The STM evaluated along the periodic orbit in the CR3BP is formulated in the nonsingular local toroidal coordinate frame. Consider the STM between time t_0 and t formulated in the rotating frame, $[\boldsymbol{\Phi}(t, t_0)]$. The transformation matrix between the rotating and toroidal frame, $[\boldsymbol{T}]$, evaluated at times t_0 and t, is used to reformulate this STM into the toroidal coordinate frame, denoted ${}^{\mathcal{Z}}[\boldsymbol{\Phi}(t, t_0)]$. This transformation is expressed as

$${}^{\mathcal{Z}}[\boldsymbol{\Phi}(t, t_0)] = [\boldsymbol{T}(t)]^{-1}[\boldsymbol{\Phi}(t, t_0)][\boldsymbol{T}(t_0)] \tag{4.61}$$

The formulation of the STM in the toroidal coordinate frame describes the first-order mapping of initial and final deviations from the periodic orbit defined using the toroidal coordinate relative state vector, $\boldsymbol{\zeta}$, expressed as ${}^{\mathcal{Z}}[\boldsymbol{\Phi}(t, t_0)] = \partial\boldsymbol{\zeta}/\partial\boldsymbol{\zeta}_0$. Because motion on the center eigenspace has a constant description, the upper-left quadrant of the STM formulated in the toroidal frame, ${}^{\mathcal{Z}}[\boldsymbol{\Phi}_{11}] = \partial \boldsymbol{z}/\partial \boldsymbol{z}_0$, possesses the form

$$ {}^{\mathcal{Z}}[\boldsymbol{\Phi}_{11}] = \begin{bmatrix} 1 & 0 & * \\ 0 & 1 & * \\ 0 & 0 & * \end{bmatrix} \tag{4.62}$$

where $*$ indicates an unspecified value. This form of the STM is employed within the derivation of an impulsive station-keeping control algorithm in Chapter 6.

4.4.4 Sensitivity due to first-order approximations in initial conditions

The center eigenspace of a periodic orbit reflects a linear approximation of the center manifold and quasi-periodic motion in the nonlinear CR3BP. Thus, trajectories in the CR3BP initialized on the center eigenspace will eventually drift from the eigenspace due to the nonlinear effects of the model. Using a local toroidal coordinate state description, this drift of motion from the center eigenspace will be slowly time-varying and may be compared to the constant description of motion on the center eigenspace from the same initial conditions. To investigate the sensitivity in this drift, motion near members of the Earth-Moon L_2 southern halo orbit family is examined. An error analysis is performed to compare the trajectories generated in the nonlinear and linear models from the same initial conditions located on the center eigenspace. This error analysis is then performed for members across the orbit family and for tori of various sizes, represented using the geometric local toroidal coordinate set to facilitate interpretation.

An approximated invariant curve is calculated relative to apolune of the 8-day Earth-Moon L_2 southern NRHO. Initial conditions from this approximated invariant curve are used to generate the associated trajectories in each of the nonlinear and linearized models. First, 15 initial conditions are defined by values of the geometric toroidal coordinates of $\varepsilon = 10$ km and evenly distributed values of $\theta \in [0, 2\pi)$ rad; values of h and the coordinates rates that are all equal to zero at the initial conditions to indicate motion that lies within the center eigenspace. Each initial condition is integrated from relative to apolune in both the nonlinear CR3BP and linearized dynamical model for two revolutions of the NRHO, i.e., 16 days. The trajectories associated with these initial conditions and propagated in the nonlinear CR3BP are visualized relative to the halo orbit in Figure 4.6.

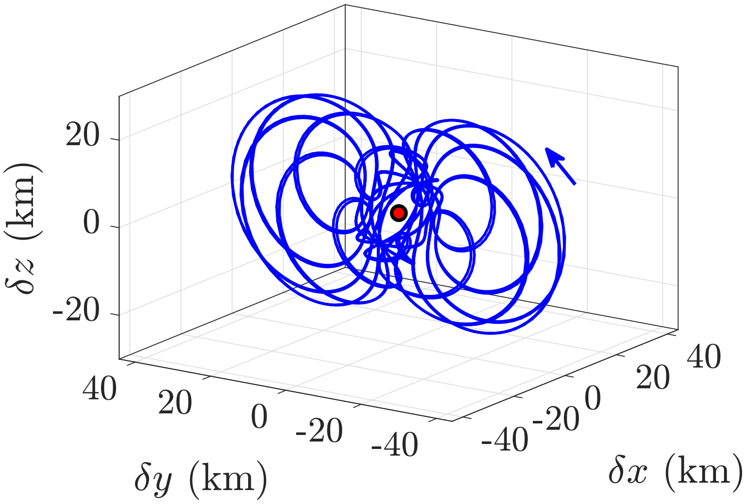

Figure 4.6: Trajectories propagated in the CR3BP relative to an 8-day Earth-Moon L_2 southern NRHO for two revolutions with initial conditions located along an approximated invariant curve with $\varepsilon = 10$ km and evenly distributed values of θ.

A single initial condition from the set displayed in Figure 4.6 is used to generate a trajectory in both the nonlinear and linear relative motion models to further examine the use of geometric toroidal coordinates. Specifically, consider an initial condition located along an invariant curve and described by $\varepsilon_0 = 10$ km and $\theta_0 = 0$ rad relative to apolune along the selected L_2 southern halo orbit. Recall that the initial value of h and all toroidal coordinate rates are equal to zero. This initial condition possesses a relative Cartesian description in the rotating frame of

$$\delta \boldsymbol{x}_0 = \begin{bmatrix} 8.9331 \text{ km} & 0 \text{ km} & 4.4944 \text{ km} & 0 \text{ m/s} & -0.054129 \text{ m/s} & 0 \text{ m/s} \end{bmatrix}^T$$

The state histories of the trajectory in the nonlinear and linear CR3BP expressed using geometric toroidal coordiantes are plotted in Figure 4.7, represented in blue and dotted black, respectively. Time is measured from apolune and normalized by orbit period. The values of the geometric coordinates and coordinate rates along the trajectory in the linearized dynamical model are verified to remain constant to within 10^{-14} nondimensional units, similar to the tolerances used in numerical integration of the initial conditions in the linearized dynamical model. For this example, the motion of the trajectory in the nonlinear model is observed to closely resemble the linearized model, with maximum error between the nonlinear and linear trajectories occurring at perilune.

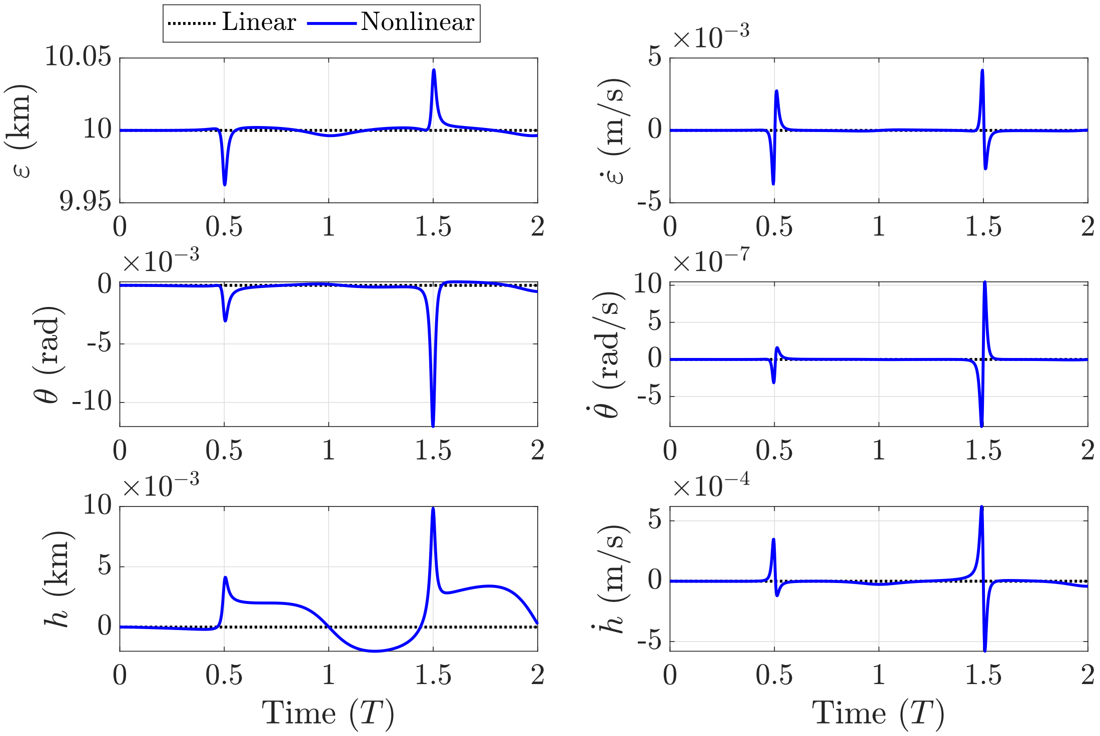

Figure 4.7: Geometric local toroidal coordinate description of the selected trajectory propagated using the nonlinear and linear equations of relative motion in the CR3BP.

This analysis is expanded to the divergence of nonlinear motion initialized along the center eigenspace for a wider variety of separations relative to members sampled across the computed segment of the Earth-Moon L_2 southern halo orbit family. Specifically, the geometric toroidal coordinates are used to define initial conditions relative to the state at apolune along members of the family for a range values of ε_0. This analysis supplies regions of validity for which the toroidal coordinates sufficiently predict initial conditions producing bounded motion in the nonlinear CR3BP. Values of ε_0 are selected within the range $\varepsilon_0 = [0, 100]$ km at an initial angle of $\theta_0 = 0$ rad along the first-order approximation of the associated invariant curve. Similar to the previous example, h_0 and the coordinate rates are all set to zero to ensure that the initial condition lies on an invariant curve relative to apolune. These initial conditions are then integrated from apolune for one revolution of the corresponding halo orbit using the nonlinear equations of relative motion. Errors in ε, θ, and h after one revolution, labeled as $\delta\varepsilon_f$, $\delta\theta_f$, and δh_f, respectively, are defined as the difference between the final and initial values of the coordinates. The orders of magnitude of the errors are visualized using color and plotted as a function of both the period of the associated L_2 southern halo orbit on the horizontal axis and the initial value of ε, i.e., the size of the initial invariant curve, on the vertical axis in Figures 4.8-4.10, respectively. Each figure includes two subfigures, corresponding to exciting one of the oscillatory modes associated with either s_1 or s_2 to generate quasi-periodic relative motion.

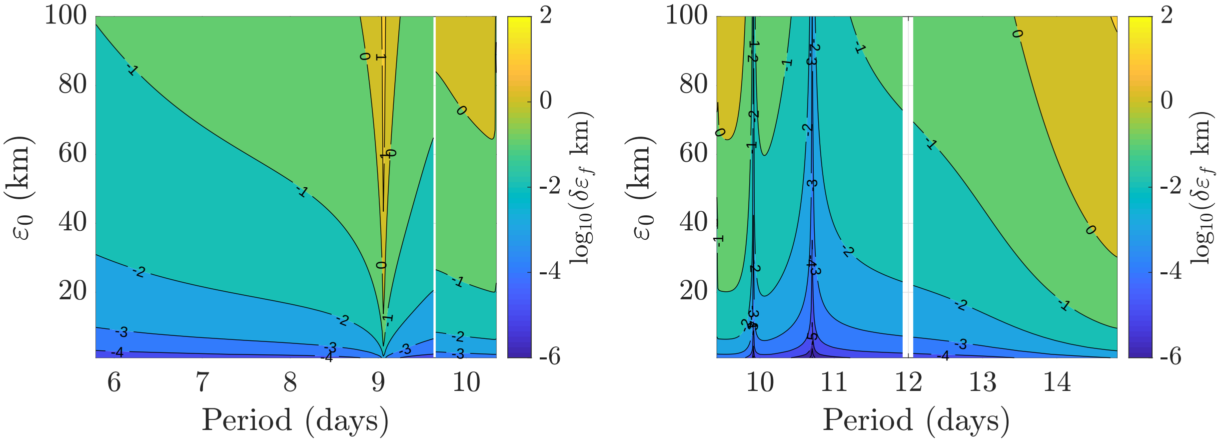

(a) Oscillatory modes associated with s_1

(b) Oscillatory modes associated with s_2

Figure 4.8: Error in ε of trajectories characterized by initial value of ε within the center eigenspace of a nearby Earth-Moon L_2 southern halo orbit, integrated in the CR3BP for one revolution of the periodic orbit. Reproduced with permission from Springer Nature [108].

Although the errors generally evolve smoothly across the orbit family, two discontinuities are observed in Figures 4.8-4.10. The first discontinuity is observed in the s_2 mode at the intersection of the s_2 stability index with -2, near an orbit possessing a period of approximately $T = 12$ days. Near this discontinuity, increased numerical sensitivity is observed in the computation of the approximated invariant curve due to the eigenvalues corresponding to the s_2 index possessing small imaginary components. Another discontinuity in the orbit family is observed in the s_1 mode near

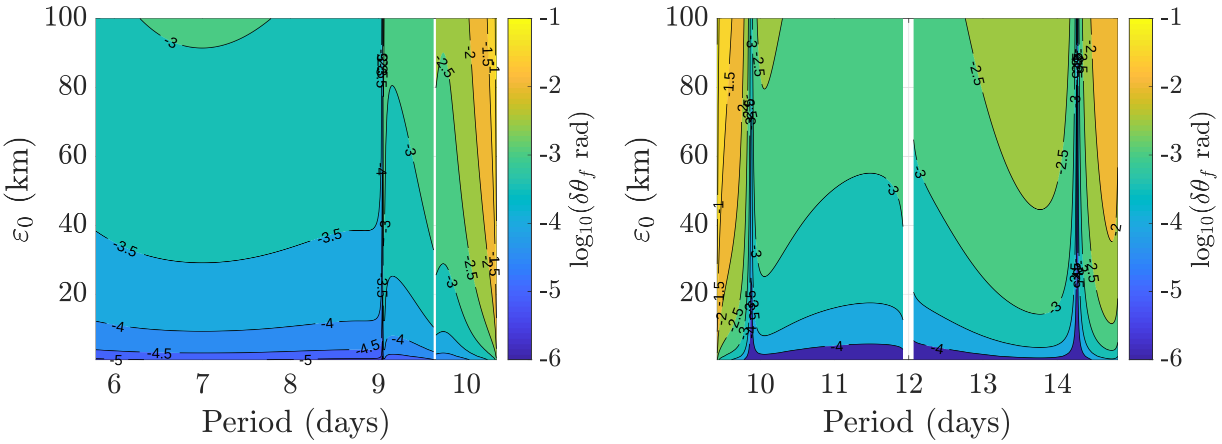

(a) Oscillatory modes associated with s_1

(b) Oscillatory modes associated with s_2

Figure 4.9: Error in θ of trajectories characterized by initial value of ε within the center eigenspace of a nearby Earth-Moon L_2 southern halo orbit, integrated in the CR3BP for one revolution of the periodic orbit. Reproduced with permission from Springer Nature [108].

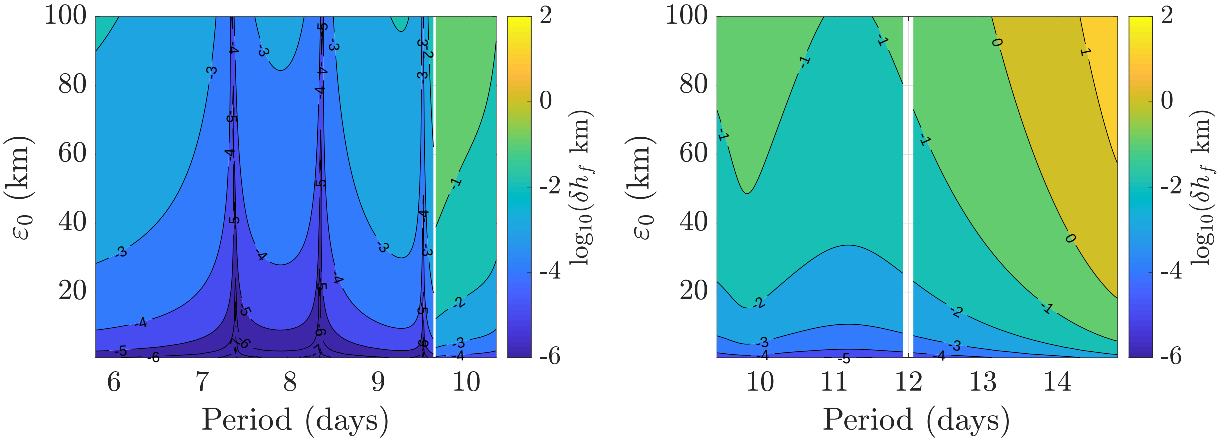

(a) Oscillatory modes associated with s_1

(b) Oscillatory modes associated with s_2

Figure 4.10: Error in h of trajectories characterized by initial value of ε within the center eigenspace of a nearby Earth-Moon L_2 southern halo orbit, integrated in the CR3BP for one revolution of the periodic orbit. Reproduced with permission from Springer Nature [108].

an orbit period of approximately $T = 9.6$ days. In this region of the halo orbit family, the geometry of the invariant curve at apolune corresponding to the s_1 index evolves such that the eccentricity of the ellipse instantaneously equals zero. When continuing the orbit family in either direction across this discontinuity, vectors aligned with the principal axes of the invariant curve switch, causing a discontinuity in the surfaces due to the normalization process of the complex eigenvector.

The differences between the nonlinear and linear trajectories, expressed in geometric toroidal coordinates, supply insight into the errors induced by the linear approximation of quasi-periodic relative motion across the orbit family. The investigation reveals that L_2 southern halo orbits near the bifurcation with the L_2 Lyapunov family, i.e., members that possess periods of approximately $T = 14.8$ days, exhibit greater drift after one period, likely corresponding to large unstable modes of orbits in this region. In addition, the oscillatory motion corresponding to the s_1 index reveals a region of increased errors near the range of halo orbits that possess a period of approximately 9 days. In this region, the invariant curve near apolune is nearly-rectilinear along the $\hat{\boldsymbol{y}}$ direction. Outside of this region, an error of less than 1 km is generally observed in both ε and h, plotted in Figures 4.8 and 4.9 respectively, for initial values of ε less than 50 km, i.e., the first-order torus with a maximum separation of 50 km from the periodic orbit at apolune. In Figure 4.9, the differences in the initial and final angle are observed to be generally less than 5×10^{-3} rad for the same initial conditions.

4.5 Describing motion tracing a nonlinear invariant 2-torus

The description of linearized relative motion exciting an oscillatory mode of a periodic orbit is constant over time using local toroidal coordinates. However, motion tracing an invariant torus in the nonlinear CR3BP measured from a periodic orbit possesses a time-varying description using local toroidal coordinates. To illustrate the state histories of quasi-periodic orbits in the nonlinear CR3BP formulated using toroidal coordinates, consider an invariant 2-torus in the Sun-Earth CR3BP that lies near the 177-day Sun-Earth L_1 southern halo orbit. Twelve quasi-periodic orbits that trace the surface of an invariant 2-torus are computed. The average value of ε for the initial relative positions of the 12 quasi-periodic orbits along the initial invariant curve is constrained to equal 1000 km and the average value of h is constrained to 0 km. Recall that the normalized complex eigenvector used to compute the local toroidal coordinates is computed at apogee of the L_1 halo orbit. For this invariant 2-torus, which lies near the associated halo orbit, the stroboscopic mapping time and Jacobi constant of the periodic orbits are similar to the orbit period and Jacobi constant of the halo orbit, respectively. Each quasi-periodic orbit is then integrated in the nonlinear CR3BP for one stroboscopic mapping time, approximately 1.3 seconds greater than the 177-day halo orbit period. The time histories of the 12 trajectories, measured from the halo orbit and expressed using geometric local toroidal coordinates, are plotted in Figure 4.11 as a function of time after apogee of the halo orbit and normalized by the halo orbit period. To better visualize the variation in θ, for each trajectory, the difference of the time history of θ and the initial value of θ, $\theta - \theta_0$, is plotted as a function of time.

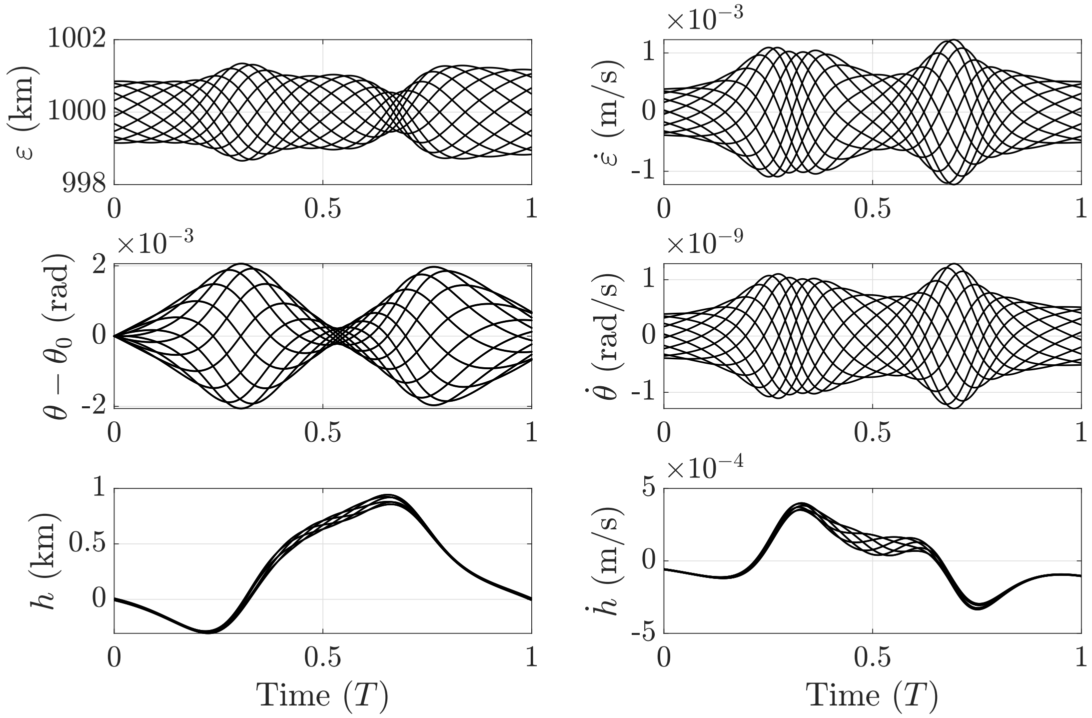

Figure 4.11: Geometric local toroidal coordinate description of quasi-periodic orbits tracing the surface of an invariant 2-torus in the nonlinear CR3BP relative to a 177-day Sun-Earth L_1 southern halo orbit.

The relative state descriptions of the quasi-periodic orbits in the nonlinear CR3BP reveal the differences between linearized motion on the center eigenspace of the halo orbit and its nonlinear counterpart at small separations from the periodic orbit. Specifically, the geometric local toroidal coordinate description reveals the variations in nonlinear motion not captured by first-order approximations, decomposed into components of the geometry of the instantaneous first-order invariant curve. The values of ε of the 12 trajectories are observed to be centered at 1000 km over time, and vary by less than 1.5 km from the constant linear approximation over the examined time interval. Values of θ are approximately distributed between $-\pi$ and π, and vary by less than approximately 0.002 rad over the examined time interval. However, the values of h for the nonlinear trajectories are centered at a varying, nonzero value. This structure in h, which reflects the out-of-plane separation of motion from the plane spanned by the projection of the center eigenspace onto the configuration space, may be caused by along-track phasing between motion on the nonlinear invariant torus and the linear approximation.

To further investigate the description of nonlinear quasi-periodic orbits using the presented local toroidal coordinates, quasi-periodic orbits that trace the surfaces of two different invariant 2-tori which lie further from the L_1 halo orbit are examined. First, quasi-periodic orbits that possess a stroboscopic mapping time equal to the period of the halo orbit, i.e., 177 days, are examined. Quasi-periodic orbits that satisfy this frequency matching between the stroboscopic mapping time and period of the associated periodic orbit orbit may be of particular interest to formation flying applications due to the elimination of secular drift between quasi-periodic orbits and a natural trajectory along the periodic orbit. The examined invariant 2-torus is constrained to possess an average value of ε along the initial invariant curve equal to 10^5 km. The time histories of the 12 quasi-periodic orbits, measured relative from the halo orbit and expressed using geometric local toroidal coordinates, are plotted in Figure 4.12 as a function of time normalized by the halo orbit period. Each quasi-periodic orbit is propagated for two stroboscopic mapping times.

The differences between the quasi-periodic orbits examined in Figure 4.12 and their linear approximations are much greater at this separation from the periodic orbit compared to the separation distances explored in Figure 4.11, indicated by the variation in the geometric toroidal coordinates over time. In fact, error in ε compared to a linear approximation of a constant value of $\varepsilon = 10^5$ km various by up to almost 50%. Large variations in θ is also observed, varying by up to 1.25 rad over the examined time interval. Similar to the previous example, the values of h of the 12 trajectories

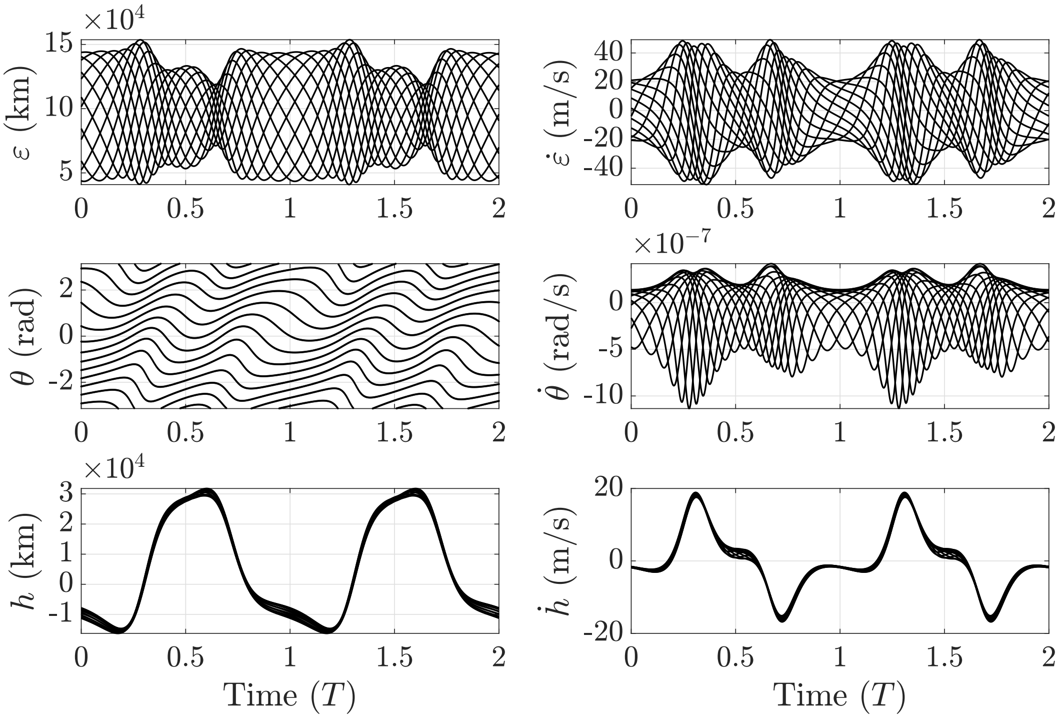

Figure 4.12: Geometric local toroidal coordinate description of quasi-periodic orbits tracing the surface of an invariant 2-torus with the same stroboscopic mapping time as the associated Sun-Earth L_1 southern halo orbit.

are centered at a nonzero and time-varying value, which varies by up to approximately 3×10^4 km. However, despite the time-varying descriptions and large differences between the nonlinear state histories and their linear counterparts, no secular drift is observed. This is attributed to the frequency matching between the quasi-periodic orbits and the associated periodic orbit.

Next, quasi-periodic orbits that possess a Jacobi constant equal to the Jacobi constant of the L_1 halo orbit are examined. The torus is also constrained to possess an average value of ε along the initial invariant curve equal to 10^5 km. The stroboscopic mapping time of this torus is equal to 177.421 days, about 10 hours greater than the period of the associated Sun-Earth L_1 halo orbit. The time histories of 12 quasi-periodic orbits, measured relative from the halo orbit and expressed using geometric local toroidal coordinates, are plotted as a function of time normalized by the halo orbit period in Figure 4.13 for two stroboscopic mapping times. Compared to the quasi-periodic orbits that trace the invariant torus with a same stroboscopic mapping time equal 177 days, the differences between the quasi-periodic orbits and their associated linear approximations are generally smaller. Values of ε vary by less than approximately 10% from the constant linear approximation, while values of θ vary by less than ± 0.2 rad over the examined time interval. A similar structure in the evolution of h is again observed, however, at smaller overall values than the previous example. However, due to the mismatch in frequencies between the invariant torus and periodic orbit, very slight secular drift is observed in the toroidal coordinates, which are measured from a natural state along the periodic orbit. As a result, error between the nonlinear motion and the linear approximations are generally slightly greater over the second half of the examined time interval.

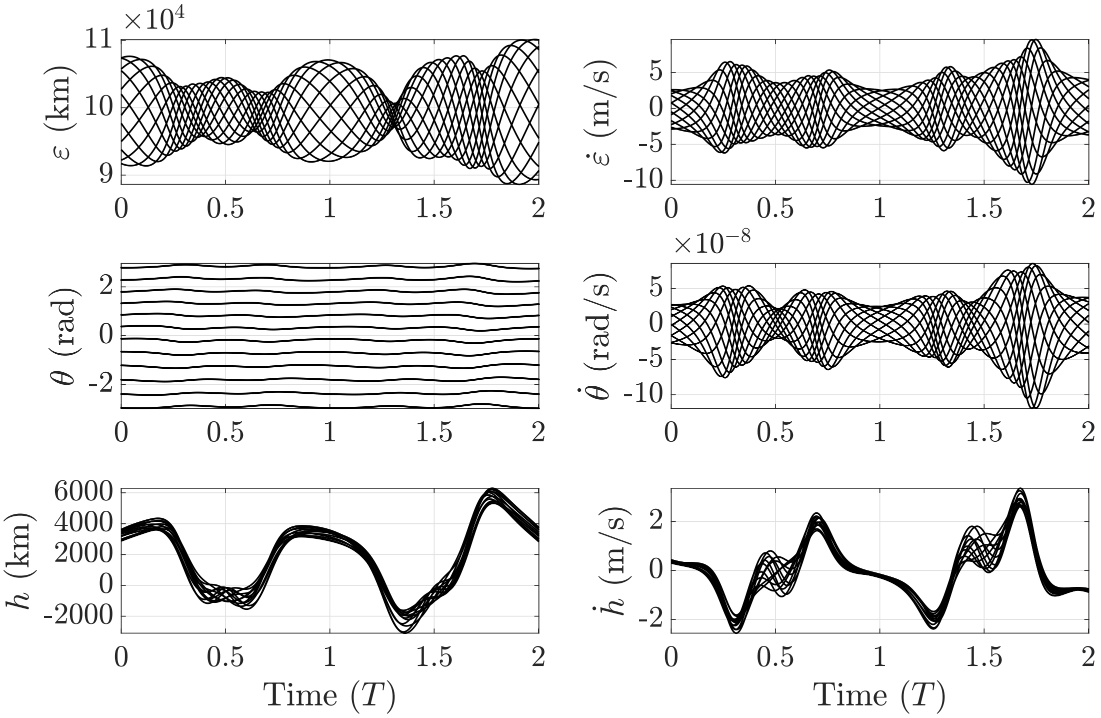

Figure 4.13: Geometric local toroidal coordinate description of quasi-periodic orbits tracing the surface of an invariant 2-torus with the same Jacobi constant as the associated Sun-Earth L_1 southern halo orbit.

As motion expands to greater separation distances from the periodic orbit, differences between the linear approximation and nonlinear quasi-periodic relative motion will increase. The general differences in the trends observed for quasi-periodic orbits tracing an invariant torus with the same stroboscopic mapping time as the period of the orbit and an invariant torus with the same Jacobi constant are also observed for quasi-periodic orbits that exist at further distances from the L_1 halo orbit. However, for small separation distances, this analysis reveals that motion tracing an invariant torus in the nonlinear model may have small differences to motion within the center eigenspace of a periodic orbit. Further investigation into the description of nonlinear quasi-periodic motion using local toroidal coordinate may reveal fascinating insight into this complex motion with application to spacecraft formation flying.

4.6 Using local toroidal coordinates in higher-fidelity models

While the local toroidal coordinate systems presented in this chapter are derived from the dynamics of the CR3BP, the coordinate systems may also be applied to the description of relative motion on higher-fidelity models, such as an ephemeris model. In the CR3BP, the local toroidal coordinate systems are applicable to the description of motion relative to periodic orbits that possess an oscillatory mode. However, in a higher-fidelity model, the coordinates may be used to describe motion relative to a reference trajectory that shares similar geometric characteristics as a periodic orbit in the CR3BP. Examples of such trajectories, computed via multiple-shooting, are illustrated in Section 3.4.5 using the three reference periodic orbits use throughout this dissertation.

The local toroidal coordinate systems require the normalized complex eigenvector of the monodromy matrix of the nearby periodic orbit to map between the rotating and toroidal coordinate frames. In this investigation, a cubic spline interpolation of the complex eigenvector may be used to supply a continuous representation of the eigenvector, calculated with a discrete number of data points over one revolution of the nearby periodic orbit. The data points are distributed evenly in time over a single revolution of the periodic orbit and each sample time is normalized by the orbit period. In the ephemeris model, a reference trajectory resembling a periodic orbit will generally no longer exhibit exact periodicity in the rotating frame. Accordingly, during use, the sample times of the complex eigenvector are re-normalized to span the actual duration between two reference points, e.g., subsequent plane crossings in the same direction or subsequent apoapses. After each revolution, the values of the complex eigenvector data points may be multiplied by the associated complex eigenvalue to construct a representation of the eigenvector for the next revolution.

In this investigation, implementation of the local toroidal coordinates in the ephemeris model approximates the complex eigenvector expressed in components of the rotating frame. Since a state in the ephemeris model is expressed using the axes of the ICRF, the relative state of the chaser spacecraft measured from the target spacecraft is first transformed to the rotating frame using the instantaneous states of the primaries from the ephemerides. Then, the components of the complex eigenvector are evaluated from the spline interpolation using the normalized time along the revolution, then used to transform the relative state formulating in the rotating frame into local toroidal coordinates and coordinate rates. The approximated complex eigenvector may then be dimensionalized by the characteristics quantities of the system. In this investigation, the eigenvector is dimensionalized by the constant, average characteristics quantities.

As an example, consider the complex eigenvector of the reference 177-day Sun-Earth L_1 southern halo orbit in the CR3BP. One revolution of the six real, nondimensional components of this eigenvector are approximated using a cubic spline approximation constructed using 11 samples of the eigenvector, evenly distributed in time between 0 and T. The actual and approximate components of the eigenvector are plotted for one revolution of the orbit in Figure 4.14 in red and blue, respectively, from initial conditions of the complex eigenvector normalized at apolune. The samples of the complex eigenvector are indicated using black markers. Despite the relatively small number of samples over time, the cubic spline approximation is observed to closely represent the true eigenvector. Generally, 100 evenly distributed samples in time is observed to sufficiently approximate the complex eigenvector for spacecraft control. However, periodic orbits that possess particular sensitive regions, such as close flybys with a primary body, may require additional samples. Additionally, future investigations of alternative methods for computing the complex eigenvector information in higher fidelity models may reduce error and improve the approximation of the complex eigenvector in the ephemeris model.

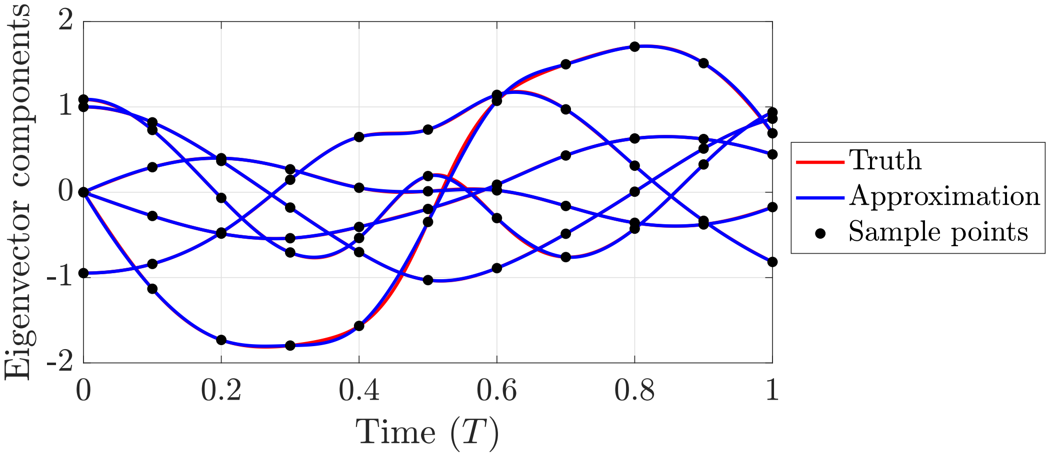

Figure 4.14: Spline interpolation of a complex eigenvector of the monodromy matrix of a 177-day Sun-Earth L_1 southern halo orbit over one period using sample points evenly distributed in time.

Chapter 5

Characterizing First-Order Oscillatory Relative Motion in the CR3BP

First-order approximations of invariant 2-tori relative to a periodic orbit in the CR3BP are useful in analyzing the fundamental solution space for naturally bounded motion relative to the orbit. In this chapter, methods to characterize motion on the center eigenspace of a periodic orbit are presented, leveraging insight supplied by the introduced local toroidal coordinate systems. First, quantities to parameterize the size, shape, and orientation of the projection of the elliptical, first-order approximation of the invariant curve in the configuration space are defined. These quantities are then applied to construct analytic maximum and minimum values of different characteristics of motion tracing the surface of the approximated invariant torus. As the approximation of the invariant curve relative to a periodic orbit evolves over time, corresponding to the natural evolution of an invariant torus, a set of differential equations are also presented to enable the computation of the principal axes of the approximated invariant curve over a revolution of the periodic orbit. Part of the material in this chapter was first published by Celestial Mechanics and Dynamical Astronomy in 2022 by Springer Nature [108].

5.1 Parameterizing an approximated invariant curve

In this section, several parameters that describe the size, shape, and orientation of the first-order approximation of an invariant curve relative to a periodic orbit are defined. Five parameters are required to describe the size and orientation of an ellipse: two parameters to describe size and shape, and three parameters to describe orientation with respect to the rotating frame.

5.1.1 Size and shape of the approximated invariant curve

In the derivation of the local toroidal coordinate systems in Chapter 4, the position components of the normalized complex eigenvector form are demonstrated form a conjugate diameter description of a unique two-dimensional ellipse in the configuration space [132]. This approximated invariant curve is then used a reference to determine the size and shape of an invariant curve described by ε. Using the normalization process described in Section 4.1, the real and imaginary components of the complex eigenvector are aligned with the principal axes of the elliptical approximation of the invariant curve. However, as the eigenvector evolves naturally over time, the real and imaginary components will no longer align with the principal axes. Because the magnitudes of the projection of the principal axes of the normalized invariant curve associated with the complex eigenvector onto the configuration space are useful for parameterizing the size and shape of the approximation, a process for computing the evolution of a set of principal semi-axes of the approximated invariant curve is presented.

The principal semi-axes of the invariant curve associated with the normalized complex eigenvector may be scaled by the desired value of ε to determine the size and shape in the configuration space of the approximated invariant curve defined by ε. This concept is illustrated in Figure 5.1. In this illustration, the projection onto the configuration space of an approximated invariant curve associated with the normalized eigenvector is represented by a dashed black ellipse centered at a fixed point of a periodic orbit, labeled t. A set of principal semi-axes of this ellipse are identified, plotted as red and blue vectors starting at the periodic orbit and intersecting the invariant curve at two vertices. The magnitudes of the principal semi-major axis and semi-minor axis, r_a and r_b, respectively, reflect the size and shape of this ellipse. Using these magnitudes, the size and shape of an approximated invariant curve defined by an arbitrary value of ε is is straightforwardly calculated by scaling the magnitudes by ε. An invariant curve defined by an arbitrary value of ε is plotted in Figure 5.1, represented with a solid black curve.

To compute the principal axes of the projection of an approximated invariant curve in the

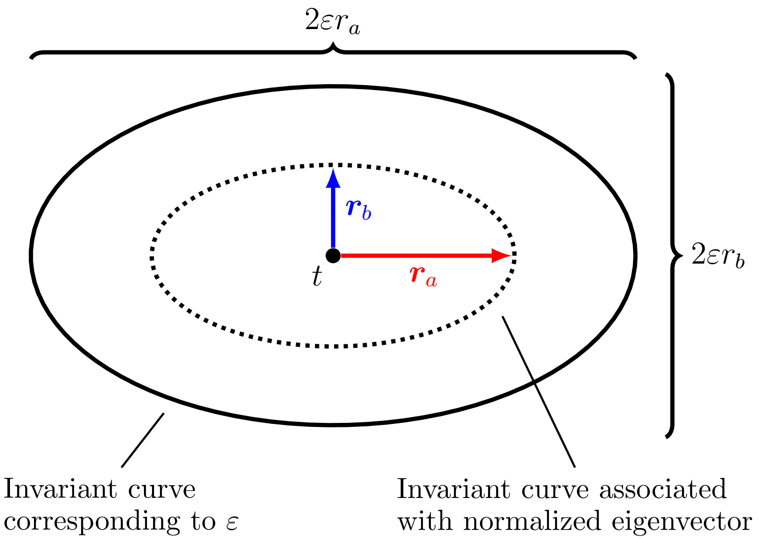

Figure 5.1: Relationship between the size of the approximated invariant curve associated with the normalized complex eigenvector and the size of the invariant curve described by ε.

configuration space, an SVD is again employed. This process modifies the principal axes analysis used in Section 4.1 to decompose a matrix constructed using only the real and imaginary position components of the normalized complex eigenvector. First, a 3×2 matrix, $[\boldsymbol{E}_r]$, is defined using the real and imaginary position components of the normalized complex eigenvector and ε as

$$[\boldsymbol{E}_r] = \varepsilon \begin{bmatrix} \boldsymbol{r}_r & \boldsymbol{r}_i \end{bmatrix} \tag{5.1}$$

This matrix is decomposed via an SVD as

$$[\boldsymbol{E}_r] = [\boldsymbol{U}_r][\boldsymbol{\Sigma}_r][\boldsymbol{V}_r]^T \tag{5.2}$$

where $[\boldsymbol{U}_r]$ is a 3×2 semi-orthogonal matrix containing the basis unit vectors of the principal axes in configuration space. Specifically, $[\boldsymbol{U}_r]$ is ordered with a unit vector aligned with a major axis in the left column and a unit vector aligned with a minor axis in the right columns as

$$[\boldsymbol{U}_r] = \begin{bmatrix} \hat{\boldsymbol{r}}_a & \hat{\boldsymbol{r}}_b \end{bmatrix} \tag{5.3}$$

The matrix $[\boldsymbol{\Sigma}_r]$ is a 2×2 diagonal matrix containing the magnitude of the semi-major axis, r_a, and the magnitude of the semi-minor axis, r_b, of the ellipse in the upper-left and lower-right, respectively, written as

$$[\boldsymbol{\Sigma}_r] = \varepsilon \begin{bmatrix} r_a & 0 \\ 0 & r_b \end{bmatrix} \tag{5.4}$$

The product of these two matrices is equal to a matrix containing a semi-major and semi-minor axes in the left and right columns, respectively, written as

$$[\boldsymbol{U}_r][\boldsymbol{\Sigma}_r] = \varepsilon \begin{bmatrix} \boldsymbol{r}_a & \boldsymbol{r}_b \end{bmatrix} \tag{5.5}$$

Using this process, a semi-major and semi-minor axis of the ellipse associated with the invariant curve are extracted. The magnitudes of the principal semi-axes may also be used to compute other geometric characteristics of the invariant curve, such as the eccentricity, e, of the invariant curve, computed as

$$e = \sqrt{1 - \frac{r_b^2}{r_a^2}} \tag{5.6}$$

to support interpretation of the shape of the invariant curve. Note that eccentricity is not a function of ε, thus, at a single fixed point, the nested approximations of invariant curves form a family of ellipses with constant eccentricity. Similar to the normalization process for the complex eigenvector, a set of sign checks must be defined to remove ambiguity in the computed set of principal semi-axes. For analyses in this investigation, the sign checks defined in Section 4.1 are again applied.

5.1.2 Orientation of the approximated invariant curve

An Euler angle set is used to describe the orientation of the approximated invariant curve in configuration space. Specifically, a 3-1-3 Euler angle set is used to describe the orientation of the approximated invariant curve with respect to the rotating frame of the CR3BP, consistent with the approach presented by Hsiao and Scheeres [88]. To compute the Euler angle set, a rotation matrix $[\boldsymbol{C}]$ is constructed using an orthogonal set consisting of the two unit vectors aligned with the principal axes of the approximated invariant curve, $\hat{\boldsymbol{r}}_a$ and $\hat{\boldsymbol{r}}_b$, and the vector, $\hat{\boldsymbol{n}}$, normal to the plane spanned by the center eigenspace. This rotation matrix is defined as

$$[\boldsymbol{C}] = \begin{bmatrix} \hat{\boldsymbol{r}}_a & \hat{\boldsymbol{r}}_b & \hat{\boldsymbol{n}} \end{bmatrix}^T \tag{5.7}$$

Using this rotation matrix, the 3-1-3 Euler angles, ψ_1, ψ_2, and ψ_3, are extracted from $[\boldsymbol{C}]$ as [40]

$$\psi_1 = \tan^{-1}\left(\frac{C_{31}}{-C_{32}}\right) \tag{5.8a}$$

$$\psi_2 = \cos^{-1}(C_{33}) \tag{5.8b}$$

$$\psi_3 = \tan^{-1}\left(\frac{C_{13}}{C_{23}}\right) \tag{5.8c}$$

where C_{ij} indicates the element of $[\boldsymbol{C}]$ in the i-th row and j-th column. The three Euler angles are conceptually illustrated in Figure 5.2 along with the basis vectors of the rotating frame and principal axes of the approximated invariant curve. The Euler angle set together with the magnitude of the semi-major and semi-minor axes provides a complete description of the size and orientation of the approximated invariant curve in the configuration space, relative to the associated fixed point along a periodic orbit. This Euler angle set may also be used to describe the orientation of the invariant curve with respect to other frames, such as a Hill frame.

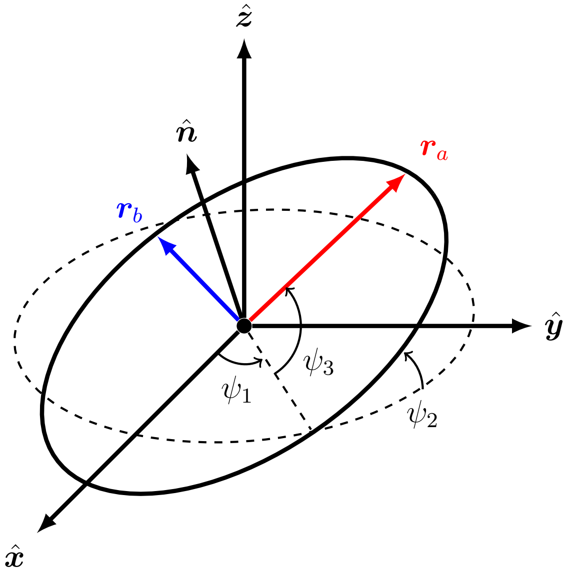

Figure 5.2: Schematic of the 3-1-3 Euler angle set used to describe the orientation of the first-order approximation of an invariant curve.

Each Euler angle possesses a physical interpretation of the orientation of the approximated invariant curve with respect to the rotating frame. The first angle, ψ_1, determines the location of the intersection of the invariant curve through the xy plane that ascends through the plane as θ increases. The second angle, ψ_2, determines the inclination of the invariant curve with respect to the xy plane and possesses values between 0° and 180°. A value of $\psi_2 = 0°$ indicates that oscillatory mode lies completely within the xy plane, while a value of $\psi_2 = 90°$ indicates that the plane spanned by oscillatory motion is perpendicular to the xy plane. Finally, the third angle, ψ_3, determines the orientation of the invariant curve within its plane. In the specific case of a center eigenspace that always spans the xy plane, i.e., the second Euler angle, ψ_2, is always equal to zero, the orientation of the invariant curve is described by a single angle, ψ, that measures the rotation of the $\boldsymbol{r}_a$ from the $\hat{x}$ axis in the direction of $\boldsymbol{r}_b$.

5.2 Integrating principal axes of the approximated invariant curve

The sequence of relative position vectors directed towards the vertices and co-vertices of the ellipse as it evolves over time does not correspond to a natural trajectory. Rather, the principal axes are geometric characteristics of the approximated invariant curve; they do not correspond to a continuous sequence of states generated using the linearized relative dynamics expressed in Eq. (2.49). Accordingly, a spacecraft initially aligned with the semi-major axis of the elliptical approximation of an invariant curve will not necessarily be located along the semi-major axis of the ellipse relative to a subsequent fixed point at a later instant of time.

A set of matrix differential equations for integrating the components of an SVD is leveraged to compute the principal axes of the invariant curve over a revolution of the periodic orbit. The matrix elements of the SVD of the matrix, $\boldsymbol{E}_r$, may be differentiated as [133, 134]

$$\begin{aligned}\frac{d}{dt}[\boldsymbol{U}_r] = [\boldsymbol{U}_r]\left([\boldsymbol{F}] \circ \left([\boldsymbol{U}_r]^T[\boldsymbol{E}_r'][\boldsymbol{V}_r][\boldsymbol{\Sigma}_r] + [\boldsymbol{\Sigma}_r][\boldsymbol{V}_r]^T(\boldsymbol{E}_r')^T[\boldsymbol{U}_r]\right)\right)\\ + \left([\boldsymbol{I}_3] - [\boldsymbol{U}_r][\boldsymbol{U}_r]^T\right)[\boldsymbol{E}_r'][\boldsymbol{V}_r][\boldsymbol{\Sigma}_r]^{-1}\end{aligned} \tag{5.9a}$$

$$\frac{d}{dt}[\boldsymbol{\Sigma}_r] = [\boldsymbol{I}_2] \circ \left([\boldsymbol{U}_r]^T[\boldsymbol{E}_r'][\boldsymbol{V}_r]\right) \tag{5.9b}$$

$$\begin{aligned}\frac{d}{dt}[\boldsymbol{V}_r] = [\boldsymbol{V}_r]\left([\boldsymbol{F}] \circ \left([\boldsymbol{\Sigma}_r][\boldsymbol{U}_r]^T[\boldsymbol{E}_r'][\boldsymbol{V}_r] + [\boldsymbol{V}_r]^T(\boldsymbol{E}_r')^T[\boldsymbol{U}_r][\boldsymbol{\Sigma}_r]\right)\right)\\ + \left([\boldsymbol{I}_2] - [\boldsymbol{V}_r][\boldsymbol{V}_r]^T\right)[\boldsymbol{E}_r']^T[\boldsymbol{U}_r][\boldsymbol{\Sigma}_r]^{-1}\end{aligned} \tag{5.9c}$$

where $[\boldsymbol{F}]$ is a 2×2 matrix function of the instantaneous values of r_a and r_b, defined as [133]

$$[\boldsymbol{F}] = \begin{bmatrix} 0 & \frac{1}{r_b^2 - r_a^2} \\ \frac{1}{r_a^2 - r_b^2} & 0 \end{bmatrix} \tag{5.10}$$

To support the integration of the SVD of $[\boldsymbol{E}_r]$, its time derivative is defined as

$$[\boldsymbol{E}_r]' = \varepsilon \begin{bmatrix} \boldsymbol{v}_r & \boldsymbol{v}_i \end{bmatrix} \tag{5.11}$$

The matrix components of the SVD of $[\boldsymbol{E}_r]$, i.e. $[\boldsymbol{U}_r]$, $[\boldsymbol{\Sigma}_r]$, and $[\boldsymbol{V}_r]$, are simultaneously integrated via the matrix differential equations in Eq. (5.9) together with the state of the target spacecraft and the complex eigenvector associated with the oscillatory mode. The vectors that appear in the columns of $[\boldsymbol{U}_r][\boldsymbol{\Sigma}_r]$ locate a vertex and co-vertex of the first-order approximation of an invariant curve. The other vertex and co-vertex of the invariant curve are straightforwardly calculated by mirroring the computed principal axes across the origin, i.e., the fixed point of the periodic orbit. This process may also be modified to compute the first-order approximation of the relative velocity magnitude between the chaser spacecraft exhibiting quasi-periodic relative motion and the target spacecraft located along a periodic orbit. In this case, the initial SVD is performed on the matrix containing columns composed of the real and imaginary velocity components of the complex eigenvector.

Two scenarios exist for which the numerical integration of the differential equations presented in Eq. (5.9) will fail. First, if the magnitude of one of the principal semi-axes reaches a value of zero, indicating the invariant curve is instantaneously rectilinear in the configuration space, the matrix of singular values, $[\boldsymbol{\Sigma}_r]$, is rank-deficient. In this event, $[\boldsymbol{\Sigma}_r]$ becomes nonsingular and numerical integration will be unable to continue. The second event that will cause a failure during numerical intergration is when the magnitudes of the semi-major and semi-minor axes possess equal values (i.e., $r_a = r_b$). When this occurs, the anti-diagonal components of the $[\boldsymbol{F}]$ matrix become undefined and numerical integration fails. This event corresponds to a circular invariant curve in the configuration space; thus, the direction of the principal axes are nonunique. In the event of these two occurrences, the periodic orbit may be discretized in time, then the value of the normalized complex eigenvector evaluated at each specified fixed point. At each point, a SVD may be applied to the $[\boldsymbol{E}_r]$ matrix constructed using the instantaneous values of the normalized eigenvector. From this SVD, the magnitude and direction of the principal semi-axes may be extracted. However, the direction of the principal semi-axes returned by the SVD is nonunique; when applying this method, the direction of the principal semi-axes must be compared with the direction at the previous time step to ensure that a continuous evolution of the axes is captured.

Integrating the SVD of the first-order approximation of the invariant curve for a revolution of the periodic orbit reveals fundamental insight into the separation between the target and chaser spacecraft. To demonstrate the variety of the size and shape of approximated invariant tori, recall the Earth-Moon L_2 southern halo orbit family. The stability indices computed for members of the orbit family are plotted in the centeral plot of Figure 5.3. The four selected members of the orbit family in Figure 3.9 are highlighted. For each orbit, the complex eigenvector is normalized at apolune and the magnitudes of the principal semi-axes are computed over one revolution. The time histories of the principal semi-axes along the tori constructed from the normalized complex eigenvector of these selected orbit members are plotted at the boundaries of Figure 5.3 reported using time measure past apolune nondimensionalized by the orbit period. In each subplot, the red and blue curves correspond to the semi-major axis magnitude and semi-minor axis magnitude, respectively, of the normalized invariant curve. Note that due to the definition of the normalization process, for each example, the magnitude of $\boldsymbol{r}_a$ is equal to unity at apolune.

This investigation illustrates the wide variety of geometries of invariant tori near members of the Earth-Moon L_2 southern halo orbit family. The principal semi-axes of the torus emanating from the NRHO, identified in magenta, exhibit a distinct peak at perilune. The stable halo oribt, identified in red, admits two oscillatory modes. Motion exciting the oscillatory mode associated with the s_1 index shares similar characteristics as motion exciting the oscillatory mode of the NRHO, for which the oscillatory mode is also associated with the s_1 index. Furthermore, comparing motion exciting the two oscillatory modes of the stable orbit, motion associated with s_1 exhibits a maximum semi-major axis at perilune, while motion associated with the s_2 index exhibits maximum semi-

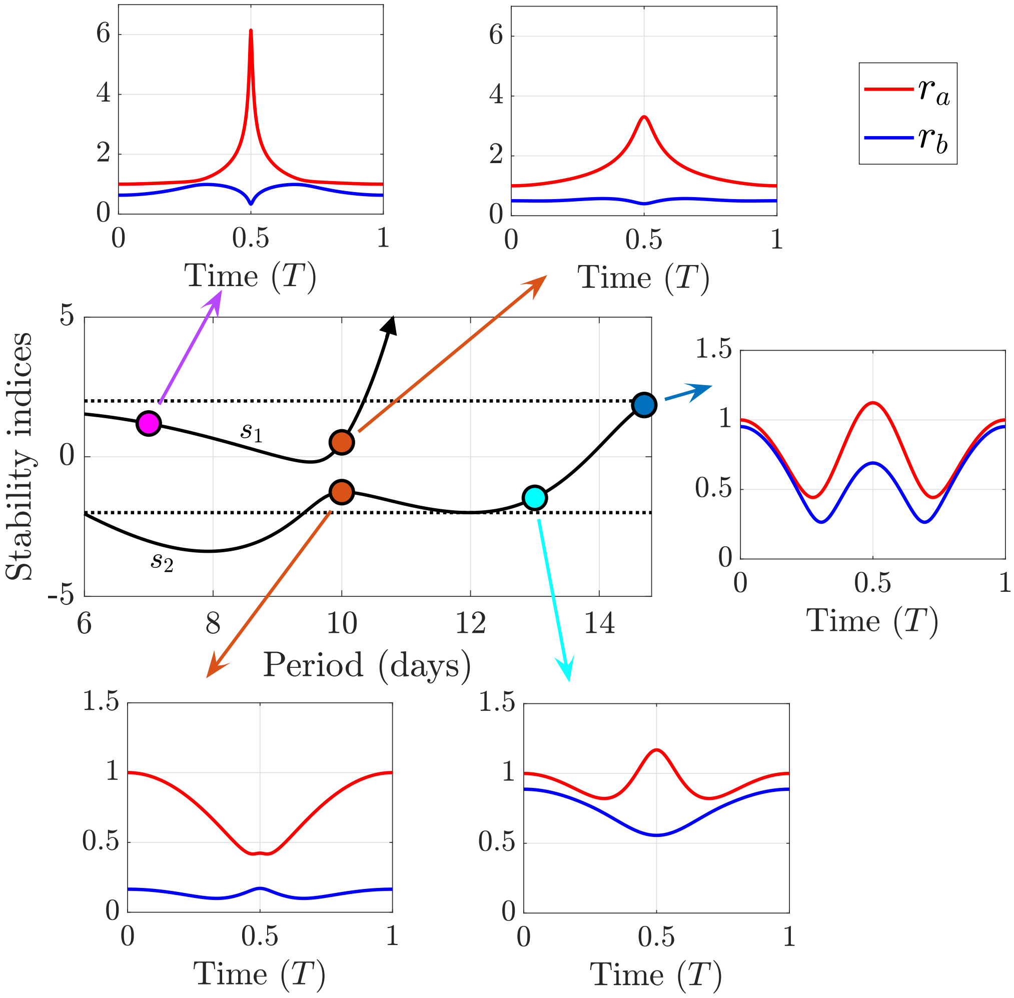

Figure 5.3: Stability of periodic orbits across the Earth-Moon southern L_2 halo orbit family and selected time histories of the principal semi-axes of first-order approximations of invariant 2-tori. Reproduced with permission from Springer Nature [108].

major axis at apolune. Rapid analysis of these characteristics across the orbit family may support the design of reference trajectories for spacecraft formations that seek to leverage naturally bounded motion relative to a periodic orbit but are subject to configuration constraints. The evolution of these curves are further examined in Chapter 7 for members of different periodic orbit families in the Sun-Earth and Earth-Moon CR3BP.

Investigation into the evolution of the direction of the principal semi-axes of the invariant curve after one revolution of the periodic orbit reveals that the direction of the semi-axes is not periodic for every orbit. Instead, the direction of the semi-axes may change sign after one revolution of the periodic orbit, then return to the original directions after two revolutions of the orbit. This behavior separates invariant tori relative to periodic orbits in the CR3BP into two categories: one group in which the paths traced by a set of principal semi-axes is time periodic over one period; and another group where the paths traced by a set of principal semi-axes is time periodic over two revolutions. This phenomenon is attributed to the fact that the paths traced by the principal semi-axes are not governed by the dynamics of the CR3BP, but instead represents a geometric characteristic of the 2-torus in the configuration space. This behavior is explored further in Chapter 7 during the analysis of the orientation of the approximated invariant curve relative to members of several orbit families in the CR3BP.

5.3 Defining bounds of motion in the center eigenspace

Because quasi-periodic trajectories exist in the center eigenspace, a trajectory initialized on the surface of an invariant torus will trace the entire structure over infinite time, regardless of the initial configuration on the torus. Because of this quasi-periodicity, the range of possible motion across the entire torus is assessed via analysis of the first-order approximation of the torus. Using the geometry of the first-order invariant curve, ranges of possible first-order motion are analytically defined, and provide the benefit of being independent of a specific initial configuration on a torus.

5.3.1 Separation between an invariant curve and periodic orbit

The magnitude of the principal axes of the approximated invariant curve correspond to the maximum and minimum possible separation of a spacecraft on the invariant curve from the associated fixed point along the periodic orbit. Evaluating this separation over an orbit period, the separation range of an approximation of an invariant 2-torus from a periodic orbit is determined. The separation between an approximated invariant curve and the associated fixed point along a periodic orbit may be straightforwardly proven by defining an angle parameter, θ^*, that reflects the location along an approximated invariant curve as measured from an instantaneous semi-major axis, $\boldsymbol{r}_a$. Using this parameter, the relative position vector is expressed as a function of this angle and the principal semi-axes as

$$\boldsymbol{\rho} = \varepsilon \left(\boldsymbol{r}_a \cos\theta^* + \boldsymbol{r}_b \sin\theta^* \right) \tag{5.12}$$

where $\boldsymbol{r}_a$ and $\boldsymbol{r}_b$ are principal semi-axes of the same ellipse calculated from the position components of the normalized complex eigenvector, i.e., $\boldsymbol{r}_r$ and $\boldsymbol{r}_i$. Using the principal axes to define the relative position vector, a value of $\theta^* = 0°$ indicates a position that lies along the direction of $\boldsymbol{r}_a$ and a value of $\theta^* = 90°$ indicates a position that lies along the direction of $\boldsymbol{r}_b$.

The maximum and minimum values of the separation distance for a state along the approximation of the invariant curve from the periodic orbit occur at the locations where the partial derivative of the separation distance with respect to θ^* is equal to zero. Separation distance from the periodic orbit is equal to the magnitude of the relative position vector, $\rho = \sqrt{\boldsymbol{\rho}^T \boldsymbol{\rho}}$. Substituting the expression for $\boldsymbol{\rho}$ defined into Eq. (5.12) and simplifying, the separation distance may be expressed as as a function of θ^* as

$$\rho = \varepsilon \sqrt{(r_a \cos\theta^*)^2 + (r_b \sin\theta^*)^2} \tag{5.13}$$

Taking the partial derivative of this expression with respect to θ^* yields

$$\frac{\partial \rho}{\partial \theta^*} = \frac{\varepsilon^2 (r_b^2 - r_a^2) \sin 2\theta^*}{\rho} \tag{5.14}$$

The roots of this expression are found at values of θ^* equal to integer multiples of 90°. The values of the maximum and minimum separations from the periodic orbit, ρ_{max} and ρ_{min}, respectively, are equal to

$$\rho_{\text{max}} = \varepsilon r_a \tag{5.15a}$$

$$\rho_{\text{min}} = \varepsilon r_b \tag{5.15b}$$

and occur at the top and bottom of the major and minor axes of the associated ellipse. The two maxima exist at values of $\theta^* = 0°, 180°$ and the two minima exist at values of $\theta^* = \pm 90°$. For an approximated invariant curve defined by ε, all possible separation distances lie between these two extrema, such that $\rho \in [\varepsilon r_b,\ \varepsilon r_a]$. Since the magnitude of the semi-principal axes are time-periodic, this range of separation distances also varies periodically in time over each revolution of the periodic orbit.

To illustrate how these separation bounds envelope the separation of an approximated invariant curve from a periodic orbit, an exampled is explored for motion relative to the reference 8-day Earth-Moon L_2 southern NRHO. In this example, 15 trajectories are defined with initial conditions on an approximated invariant curve at apolune, defined by $\varepsilon = 10$ km and evenly distributed by θ between 0 and 2π. Each trajectory is propagated using the linearized equations of relative motion for one revolution of the NRHO and plotted in the Earth-Moon rotating frame in Figure 5.4a. The separation distance of each trajectory from the periodic orbit is computed over time and plotted in Figure 5.4b, represented in black. Time is measured from apolune and normalized by the orbit period. Also plotted in Figure 5.4b are the maximum and minimum separations determined by Eq. (5.15), plotted in red and blue, respectively. In this linearized dynamical model, the separation of each trajectory is exactly bounded by the range defined by these extrema.

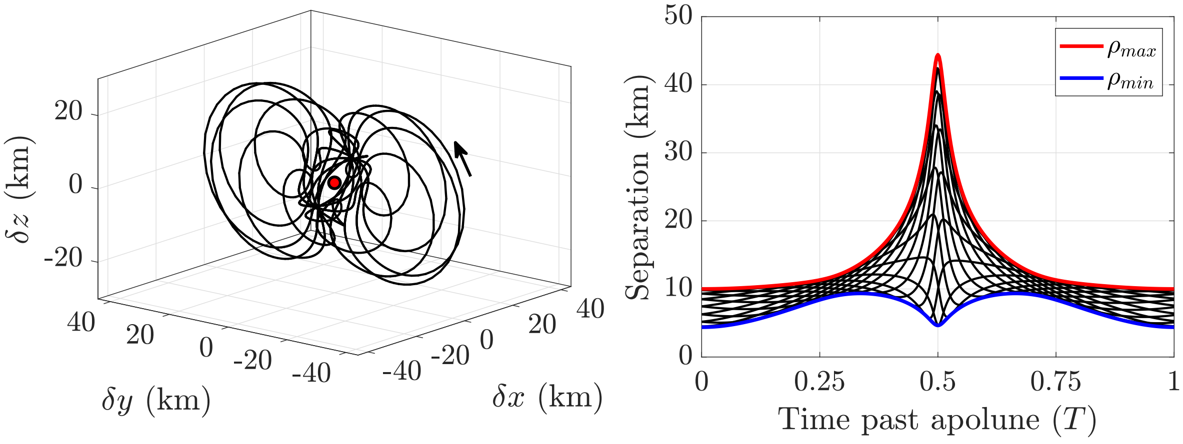

(a) Relative trajectories in the rotating frame

(b) Separation distance

Figure 5.4: Separation distance of the trajectories tracing the surface of an approximated invariant 2-torus described by $\varepsilon = 10$ km from an 8-day Earth-Moon L_2 southern NRHO.

5.3.2 Separation between two points on the same invariant curve

A useful quantity for trajectory design is the range of possible separation distances between two locations on the same invariant curve. For first-order motion in the center eigenspace, two points on the same invariant curve possess the same value of ε. Furthermore, since each point possesses a constant toroidal coordinate θ, the two points possess a constant toroidal angular difference, labeled $\delta\theta$. The two relative position vectors on an invariant curve deribed by ε, denoted as $\boldsymbol{\rho}_+$ and $\boldsymbol{\rho}_-$, are defined as a function of an angle, θ^*, and an angular difference, $\delta\theta$, such that $\boldsymbol{\rho}_+$ is defined with an angular toroidal coordinate of $(\theta^* + \delta\theta)$ and $\boldsymbol{\rho}_-$ is defined at $(\theta^* - \delta\theta)$. Using these definitions, the two relative position vectors are written as

$$\boldsymbol{\rho}_+ = \varepsilon\left(\boldsymbol{r}_a \cos\left(\theta^* + \frac{\delta\theta}{2}\right) + \boldsymbol{r}_b \sin\left(\theta^* + \frac{\delta\theta}{2}\right)\right) \tag{5.16a}$$

$$\boldsymbol{\rho}_- = \varepsilon\left(\boldsymbol{r}_a \cos\left(\theta^* - \frac{\delta\theta}{2}\right) + \boldsymbol{r}_b \sin\left(\theta^* - \frac{\delta\theta}{2}\right)\right) \tag{5.16b}$$

where $\boldsymbol{r}_a$ and $\boldsymbol{r}_b$ are the principal semi-axes of the ellipse corresponding to the normalized complex eigenvector. These relative position vectors and their separation distance, d, are conceptually illustrated in Figure 5.5 along with the principal semi-axes of the approximation of the invariant curve in the configuration space.

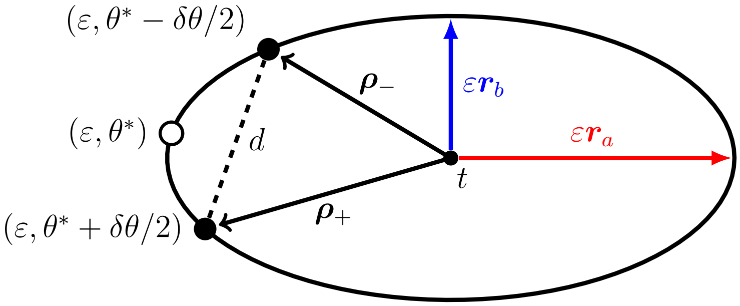

Figure 5.5: Schematic of the separation distance between two states on the same first-order approximation of an invariant curve.

The separation distance between two relative positions on the invariant curve is the Euclidean distance in configuration space, i.e., $d = \sqrt{\delta\boldsymbol{\rho}^T \delta\boldsymbol{\rho}}$, where

$$\delta\boldsymbol{\rho} = \boldsymbol{\rho}_+ - \boldsymbol{\rho}_- \tag{5.17}$$

Using the definitions in Eq. (5.16), the separation distance between the two position vectors simplifies to

$$d = 2\varepsilon \sin\left(\frac{\delta\theta}{2}\right)\sqrt{(r_b \sin\theta^*)^2 + (r_a \cos\theta^*)^2} \tag{5.18}$$

This separation distance is a function of θ^*, the toroidal angle difference, $\delta\theta$, the instantaneous magnitude of the principal axes, r_a and r_b, as well as the scaling of the ellipse, defined by ε. Taking the partial derivative of this relative separation distance with respect to θ^* yields

$$\frac{\partial d}{\partial\theta^*} = \frac{\varepsilon(r_b^2 - r_a^2)\sin(2\theta^*)\sin(\delta\theta/2)}{\sqrt{(r_b \sin\theta^*)^2 + (r_a \cos\theta^*)^2}} \tag{5.19}$$

The values of θ^* corresponding to the roots of this equation correspond to the major and minor axes of the associated ellipse; the maximum and minimum values of d are therefore, equal to

$$d_{\max} = 2\varepsilon r_a \sin\left(\frac{\delta\theta}{2}\right) \tag{5.20a}$$

$$d_{\min} = 2\varepsilon r_b \sin\left(\frac{\delta\theta}{2}\right) \tag{5.20b}$$

The minimum relative separation, $d_{\min}$ occurs when two positions are located symmetrically about the major axis, i.e., where $\theta^* = 0°, 180°$. The maximum relative separation, $d_{\max}$, occurs when two positions are symmetrically located about the minor axis, i.e., where $\theta^* = \pm 90°$. The extrema, $d_{\min}$ and $d_{\max}$ determine the range of possible separation distances between adjacent spacecraft, defined by a difference of $\delta\theta$.

The maximum possible separation between any two points on the same approximated invariant curve occurs when the two points are separated by a difference of $\delta\theta = 180°$ and both points lie along the major axis. In this case, the separation distance, and thus the maximum possible separation distance between any two points on the elliptical approximation, is equal to $2\varepsilon r_a$.

To demonstrate the bounds defined on the relative separation distance for linearized dynamics, consider the separation distance between the trajectories integrated in linearized dynamics plotted relative to an 8-day Earth-Moon L_2 southern NRHO in Figure 5.4a. The inter-spacecraft separation is examined between adjacent trajectories that are described each by $\varepsilon = 10$ km and an angular toroidal coordinate difference of $\delta\theta = 360°/15 = 24°$. The time histories of the separation between each adjacent trajectory over time is plotted in Figure 5.6 in black, along with the maximum and minimum possible inter-spacecraft separation distances calculated using Eq. (5.20) using the simulated values of ε and $\delta\theta$, plotted in red and blue, respectively. Using the linearized dynamical model, the relative separation bounds are observed to exactly capture the computed inter-spacecraft separation of each adjacent trajectory.

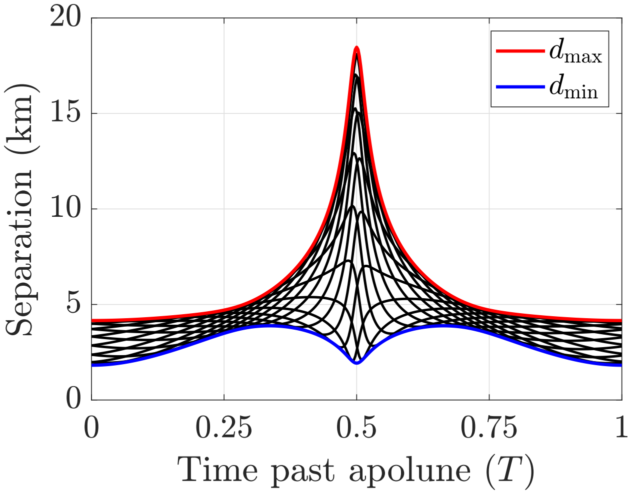

Figure 5.6: Separation distance between adjacent trajectories with a difference of $\delta\theta = 24°$ tracing the surface of an approximated invariant 2-torus described by $\varepsilon = 10$ km from an 8-day Earth-Moon L_2 southern NRHO.

5.3.3 Angle between two points on the same invariant curve

A useful quantity to understand the effect of the varying size and shape of the invariant curve on a spacecraft formation is the angle in configuration space between two states along the same invariant curve. For two spacecraft separated by a constant toroidal angle, the angle in configuration space between the two spacecraft generally varies over time. To derive the envelope of possible angles between spacecraft, the angle, ϕ, between two spacecraft on the same invariant curve in configuration space measured within the plane spanned by the invariant curve is equal to

$$\phi = \cos^{-1}\left(\frac{\boldsymbol{\rho}_+^T \boldsymbol{\rho}_-}{\rho_+ \; \rho_-}\right) \tag{5.21}$$

where the two relative position vectors, defined in Eq. (5.16), are functions of θ^* and $\delta\theta$. The roots of the partial derivative of ϕ with respect to θ^*, $\partial\phi/\partial\theta^*$, are again located at values of θ^* corresponding to the principal axes. Thus, the maximum and minimum separation angle between the two position vectors in configuration space are equal to

$$\phi_{\max} = \cos^{-1}\left(\frac{r_b\cos(\delta\theta/2) - r_a\sin(\delta\theta/2)}{r_b\cos(\delta\theta/2) + r_a\sin(\delta\theta/2)}\right) \tag{5.22a}$$

$$\phi_{\min} = \cos^{-1}\left(\frac{r_a\cos(\delta\theta/2) - r_b\sin(\delta\theta/2)}{r_a\cos(\delta\theta/2) + r_b\sin(\delta\theta/2)}\right) \tag{5.22b}$$

The two minimum values of ϕ occur when the two positions are symmetrically located about the major axis, i.e., $\theta^* = 0°, 180°$; the two maximum values of ϕ occur when the two positions are symmetrically located about the minor axis, i.e., where $\theta^* = \pm 90°$. The minimum and maximum angles in configuration space occur at the same values of θ^* where the minimum and maximum relative separation occur, respectively. Theses extrema define the range of possible angles between two locations on the same invariant curve and are functions of the geometry of the ellipse, captured by r_a and r_b, and the toroidal angle difference $\delta\theta$, but is independent of the value of ε.

To demonstrate the range of separation angle between locations on the same invariant curve, consider the 15 trajectories integrated in linearized dynamics about an 8-day Earth-Moon L_2 southern halo orbit plotted in Figure 5.4a. Each adjacent trajectory possesses an angular toroidal coordinate difference of $\delta\theta = 24°$. The angle, ϕ, between adjacent trajectories in the configuration is computed over one revolution of the NRHO using Eq. (5.21). The time histories of these angles are plotted in Figure 5.7 in solid black, along with the maximum and minimum possible values of this angle for the value of ε and $\delta\theta$, plotted in red and blue, respectively, computed using Eq. (5.22). For comparison, the angular toroidal coordinate difference, $\delta\theta = 24°$, is also represented with a constant dotted black line. The derived values for the maximum and minimum possible separations in the configuration space for trajectories defined by the same value of ε and a constant value of $\delta\theta$ are observed to exactly encapsulate the motion of the linearized relative trajectories.

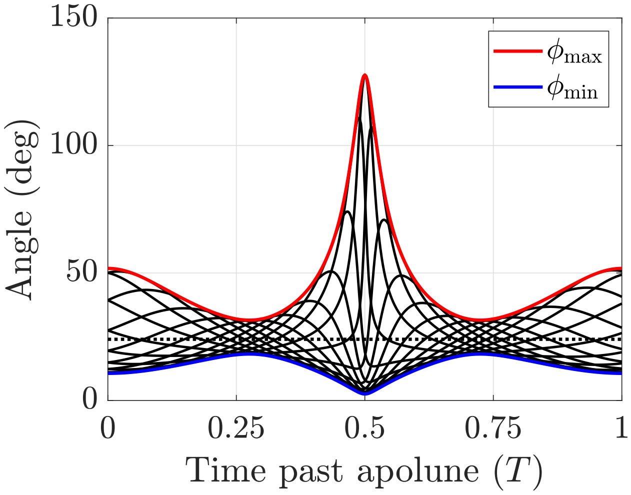

Figure 5.7: Angle between adjacent trajectories with a difference of $\delta\theta = 24°$ tracing the surface of an approximated invariant 2-torus described by $\varepsilon = 10$ km relative to an 8-day Earth-Moon L_2 southern NRHO.

For each of the three characteristics of motion examined in Figures 5.4 - 5.7, the linearized oscillatory motion is exactly bounded by the analytically defined ranges. In the nonlinear CR3BP or other nonlinear dynamical model, natural motion will gradually diverge from the linear approximation and motion will diverge from the defined bounds. However, with application of control, a spacecraft may track a reference trajectory developed from linear oscillatory motion that possesses motion within the analytically defined ranges. Thus, the defined ranges may support collision avoidance and other trajectory design considerations for multiple spacecraft leveraging oscillatory motion near a periodic orbit. An example comparing the controlled motion of spacecraft simulated in the ephemeris model near a trajectory resembling periodic orbit is included in Chapter 8. In Chapter 7, the characterization of the approximated invariant curve relative to periodic orbits in the Earth-Moon and Sun-Earth system is surveyed. Using the information in this survey, ranges of d and ϕ may be straightforwardly computed for desired values of ε and $\delta\theta$. An example of this type of application is additionally presented in Chapter 8 within the design of a constellation about a Sun-Earth L_1 southern halo orbit that satisfies various inter-spacecraft separation constraints.

Chapter 6

Spacecraft Control Strategies Leveraging Local Toroidal Coordinates

The intuition into motion on or near a center eigenspace of a periodic orbit provided by the introduced local toroidal coordinate systems is leveraged to develop various control strategies for spacecraft near periodic orbits with an oscillatory mode. Within the CR3BP, quasi-periodic orbits produce motion that is naturally-bounded near a periodic orbit such that no control effort is requirement to maintain a formation. However, in higher-fidelity dynamical models, the natural structures of the CR3BP (e.g., periodic orbits, invariant tori) are not exactly recovered. Thus, control strategies are required to maintain long-term bounded motion to a reference trajectory in a higher-fidelity dynamical model that shares geometric characteristics as a periodic orbit CR3BP.

In this chapter, control strategies are formulated using local toroidal coordinates for a chaser spacecraft flying in formation with a target spacecraft on a periodic orbit in the CR3BP, or a nearly-periodic reference trajectory recovered in an ephemeris model. First, variations of nonlinear feedback control laws are introduced using the nonsingular and geometric local toroidal coordinates and coordinate rates. Using a control Lyapunov function derivation, these feedback control laws are analytically proven to be asymptotically stabilizing to desired configurations relative to a periodic orbit in the CR3BP. Next, variations of impulsive control strategies are presented, including a targeting algorithm for designing maneuvers relative to a periodic orbit and an impulsive station-keeping strategy to enable a chaser spacecraft to maintain on specific location within the center eigenspace of a periodic orbit.

6.1 Nonlinear feedback control strategies

In this section, two nonlinear feedback control laws are derived using control Lyapunov function formulated using local toroidal coordinates and coordinate rates. The controllers are designed to track a specified desired trajectory relative to a periodic orbit in the CR3BP that admits an oscillatory mode. Quadratic-form Lyapunov functions are selected to produce globally asymptotically convergence to the desired trajectory without any constraints on control effort [135]. This formulation of Lyapunov function produces a control law with similar structure to Cartesian state feedback control laws [99, 41]. The performance of the presented continuous control strategies are comparable to continuous Floquet control methods, such as the strategies presented by Wiesel and Shelton [63] and Howell and Millard [98], as well as other feedback control strategies incorporating the stability of a periodic orbit, such as the method presented by Scheeres et al. [89].

For the derivations in this section, several notation choices are placed on the definition of vectors for brevity. Specifically, the relative position vector of the chaser spacecraft is assumed to correspond to the position expressed in the rotating frame, i.e., $\boldsymbol{\rho} = [\delta x, \delta y, \delta z]^T$. The relative velocity as seen by an observer in the rotating frame is denoted as $\boldsymbol{\rho}' = [\delta\dot{x}, \delta\dot{y}, \delta\dot{z}]^T$. The nonsingular and geometric local toroidal coordinate systems are expressed as $\boldsymbol{z} = [\alpha, \beta, h]^T$ and $\boldsymbol{e} = [\varepsilon, \theta, h]^T$, respectively. The time derivatives of these sets for an observer in their respective frames are defined as $\boldsymbol{z}' = [\dot{\alpha}, \dot{\beta}, \dot{h}]^T$ and $\boldsymbol{e}' = [\dot{\varepsilon}, \dot{\theta}, \dot{h}]^T$, for the nonsingular and geometric coordinate rates, respectively. Thus, the left superscript indicating the frame is omitted to simplify notation.

6.1.1 Nonsingular local toroidal coordinate formulation

First, a feedback control law is derived using a Lyapunov function constructed as a function of tracking errors expressed in terms of the nonsingular local toroidal coordinates and their respective rates. The coordinate tracking error, labeled $\delta\boldsymbol{z}$, and the coordinate rate tracking error, labeled

$\delta\boldsymbol{z}'$, are defined as

$$\delta\boldsymbol{z} = \boldsymbol{z} - \boldsymbol{z}_d \tag{6.1a}$$

$$\delta\boldsymbol{z}' = \boldsymbol{z}' - \boldsymbol{z}_d' \tag{6.1b}$$

where $\boldsymbol{z}_d$ and $\boldsymbol{z}_d'$ are the desired nonsingular toroidal coordinates and coordinate rates, respectively. Following a similar procedure for previously derived Cartesian control laws, the Lyapunov function, V, is defined as a radially unbounded, positive definite function of geometric coordinate and coordinate rate tracking errors as [40]

$$V(\delta\boldsymbol{z}, \delta\boldsymbol{z}') = \frac{1}{2}\delta\boldsymbol{z}^T[\boldsymbol{K}_1]\delta\boldsymbol{z} + \frac{1}{2}(\delta\boldsymbol{z}')^T\delta\boldsymbol{z}' \tag{6.2}$$

where $[\boldsymbol{K}_1]$ is a positive definite 3×3 gain matrix applied to the nonsingular toroidal coordinate error. The time derivative of V is

$$\dot{V} = (\delta\boldsymbol{z}')^T\left([\boldsymbol{K}_1]\delta\boldsymbol{z} + \delta\boldsymbol{z}''\right) \tag{6.3}$$

where the acceleration difference term, $\delta\boldsymbol{z}''$, is defined as

$$\delta\boldsymbol{z}'' = \boldsymbol{z}'' - \boldsymbol{z}_d'' \tag{6.4}$$

where $\boldsymbol{z}''$ is the relative acceleration of the chaser spacecraft applying a control input and $\boldsymbol{z}_d''$ is the desired relative acceleration formulated in nonsingular toroidal coordinates.

For this derivation, the control input of the chaser spacecraft is expressed in the rotating frame. Thus, an expression for the relative acceleration of the chaser spacecraft for an observer in the toroidal coordinate frame, $\boldsymbol{z}''$, is derived as a function of the control input in the rotating frame, $\boldsymbol{u}$. First, recall the expression for the relative velocity of the chaser spacecraft for an observer in the rotating frame is written as

$$\boldsymbol{\rho}' = [\boldsymbol{R}]'\boldsymbol{z} + [\boldsymbol{R}]\boldsymbol{z}' \tag{6.5}$$

Equating the time derivative of the right hand side of this equation to the sum of the natural relative acceleration, labeled $\boldsymbol{f}$, due to the CR3BP and a control acceleration, $\boldsymbol{u}$, yields the expression:

$$\boldsymbol{f} + \boldsymbol{u} = [\boldsymbol{R}]''\boldsymbol{z} + 2[\boldsymbol{R}]'\boldsymbol{z}' + [\boldsymbol{R}]\boldsymbol{z}'' \tag{6.6}$$

Solving for $\boldsymbol{z}''$, this acceleration term is written as

$$\boldsymbol{z}'' = [\boldsymbol{R}]^{-1}\left(\boldsymbol{f} - [\boldsymbol{R}]''\boldsymbol{z} - 2[\boldsymbol{R}]'\boldsymbol{z}'\right) + [\boldsymbol{R}]^{-1}\boldsymbol{u} \tag{6.7}$$

This expression is rewritten as the sum of the natural acceleration due to the CR3BP, labeled $\overline{\boldsymbol{z}}''$, and the acceleration due to the control as

$$\boldsymbol{z}'' = \overline{\boldsymbol{z}}'' + [\boldsymbol{R}]^{-1}\boldsymbol{u} \tag{6.8}$$

where the natural acceleration term is defined as

$$\overline{\boldsymbol{z}}'' = [\boldsymbol{R}]^{-1}\left(\boldsymbol{f} - [\boldsymbol{R}]''\boldsymbol{z} - 2[\boldsymbol{R}]'\boldsymbol{z}'\right) \tag{6.9}$$

With the total acceleration of the nonsingular coordinates defined in terms of the control acceleration vector expressed in the rotating frame, the acceleration difference between the current and desired trajectory is written as

$$\delta\boldsymbol{z}'' = \left(\overline{\boldsymbol{z}}'' + [\boldsymbol{R}]^{-1}\boldsymbol{u}\right) - \boldsymbol{z}_d'' \tag{6.10}$$

This expression may now be substituted into the time derivative of the Lyapunov function written in Eq. (6.3).

Continuing an analogous procedure to Cartesian control law derivations [40], the presented control law is selected to force the first time derivative of the Lyapunov function equal to a negative semidefinite function of the error terms, defined as

$$\dot{V}(\delta\boldsymbol{z}') = -\delta(\boldsymbol{z}')^T[\boldsymbol{K}_2]\delta\boldsymbol{z}' \tag{6.11}$$

where $[\boldsymbol{K}_2]$ is a positive definite 3×3 nonsingular toroidal coordinate rate feedback gain matrix. Equating Eq. (6.3) and Eq. (6.11) and solving for $\boldsymbol{u}$, the resulting tracking control law is

$$\boldsymbol{u} = -[\boldsymbol{R}]\left([\boldsymbol{K}_1]\delta\boldsymbol{z} + [\boldsymbol{K}_2]\delta\boldsymbol{z}' + \overline{\boldsymbol{z}}'' - \boldsymbol{z}_d''\right) \tag{6.12}$$

For a trajectory tracing a first-order approximation of an invariant torus, the acceleration of the geometric coordinates for dynamics linearized about the periodic orbit is equal to zero. When tracking this motion, the desired chaser acceleration is $\boldsymbol{z}_d'' = \mathbf{0}$ and the control law simplifies to

$$\boldsymbol{u} = -[\boldsymbol{R}]\left([\boldsymbol{K}_1]\delta\boldsymbol{z} + [\boldsymbol{K}_2]\delta\boldsymbol{z}' + \overline{\boldsymbol{z}}''\right) \tag{6.13}$$

In this form, the control law resembles the structure of a proportional-derivative controller and feedforward acceleration term, with a mapping from error defined in terms of coordinates and coordinate rates to a Cartesian acceleration vector via the transformation matrix, $[\boldsymbol{R}]$.

The presented feedback control law enables tracking of an arbitrary reference trajectory relative to the periodic orbit. Because the time derivative of V, defined in Eq. (6.11), is a negative semidefinite function of the toroidal coordinate and coordinate rate error terms, the asymptotic stability of the control law is verified by confirming that the first nonzero derivative of V evaluated on the set $\delta\boldsymbol{z}' = \mathbf{0}$ is a negative definite function of $\delta\boldsymbol{z}$ [40]. The third derivative of V evaluated on this set is equal to

$$\dddot{V}(\delta\boldsymbol{z}' = \mathbf{0}) = -2\delta\boldsymbol{z}^T[\boldsymbol{K}_1]^T[\boldsymbol{K}_2][\boldsymbol{K}_1]\delta\boldsymbol{z} \tag{6.14}$$

which is a negative definite function of $\delta\boldsymbol{z}$, verifying that the control law is asymptotically stabilizing in the CR3BP to the desired state described by $\boldsymbol{z}_d$ and $\boldsymbol{z}_d'$. The control law uses no additional linearization assumptions beyond the linear approximations within the definition of the geometric coordinates. However, tracking first-order quasi-periodic motion relative to a periodic orbit, as opposed to a path in the nonlinear system, results in small steady-state control usage with the advantage of less computational complexity. In addition, unknown perturbing accelerations on the chaser spacecraft in a higher-fidelity dynamical model will result in steady-state tracking error and control usage.

Applying continuous control modifies the equations of motion of a spacecraft. The equations of motion for a spacecraft applying continuous control in the CR3BP are

$$\ddot{x} = \frac{\partial U^*}{\partial x} + 2\dot{y} + u_x \tag{6.15a}$$

$$\ddot{y} = \frac{\partial U^*}{\partial y} - 2\dot{x} + u_y \tag{6.15b}$$

$$\ddot{z} = \frac{\partial U^*}{\partial z} + u_z \tag{6.15c}$$

where u_x, u_y, and u_z are the components of the control applied along the $\hat{\boldsymbol{x}}$, $\hat{\boldsymbol{y}}$, and $\hat{\boldsymbol{z}}$ directions, respectively. For simulating controlled motion in the ephemeris model, the total inertial acceleration of the a spacecraft relative to the central body, $\ddot{\boldsymbol{r}}_{i,sc}$, is modeled as

$$\ddot{\boldsymbol{r}}_{i,sc} = \overline{\ddot{\boldsymbol{r}}}_{i,sc} + \boldsymbol{u} \tag{6.16}$$

where $\overline{\ddot{\boldsymbol{r}}}_{i,sc}$ is the natural acceleration of the spacecraft in the ephemeris model as discussed in Section 2.3. Note that these sets of equations of motion do not incorporate a specific spacecraft or engine model, nor the dependency of the control acceleration on the mass of the spacecraft.

6.1.1.1 Demonstration of asymptotic stability in the CR3BP

The asymptotic stability of the control law is verified numerically via an example in the CR3BP. A simulation is constructed for a chaser applying feedback control near a target spacecraft located on the reference Earth-Moon DRO. The parameters of the simulation are summarized in Table 6.1, including the initial and desired relative configuration of the chaser spacecraft in toroidal coordinates, control gain values, and simulation duration. Note that for this simulation, the feedback gain matrices, $[\boldsymbol{K}_1]$ and $[\boldsymbol{K}_2]$, are hand-selected and defined using units nondimensionalized by the characteristic quantities of the Earth-Moon CR3BP.

Table 6.1: Parameters of the simulation in the CR3BP using the feedback control law formulated using nonsingular local toroidal coordinates.

Parameter	Value
Reference orbit	7-day Earth-Moon DRO
Simulation duration	$1T = 7$ days
Coordinate error gains	$[\boldsymbol{K}_1] = \text{diag}(1500, 1500, 1500)$ (nondim.)
Coordinate rate error gains	$[\boldsymbol{K}_2] = \text{diag}(100, 100, 100)$ (nondim.)
Initial configuration	$\boldsymbol{z}_0 = [10 \text{ km}, 0 \text{ km}, 1 \text{ km}]^T$ $\boldsymbol{z}_0' = [0 \text{ m/s}, 0 \text{ m/s}, 0 \text{ m/s}]^T$
Desired configuration	$\boldsymbol{z}_d = [5 \text{ km}, 5 \text{ km/s}, 0 \text{ km}]^T$ $\boldsymbol{z}_d' = [0 \text{ m/s}, 0 \text{ m/s}, 0 \text{ m/s}]^T$

The controlled trajectory of the chaser spacecraft applying nonlinear feedback control relative to the target spacecraft is examined. First, the relative trajectory of the chaser spacecraft is plotted in both the rotating coordinate frame and nonsingular local toroidal coordinate frame in Figures 6.1a and 6.1b, respectively. For each plot, the target spacecraft is represented by a red marker at the origin, the initial position of the chaser spacecraft is represented with a blue marker, and the final position of the chaser spacecraft is represented by a black cross. In the rotating frame, the relative trajectory is observed to remain in the vicinity of the target spacecraft at the origin over the specified time interval.

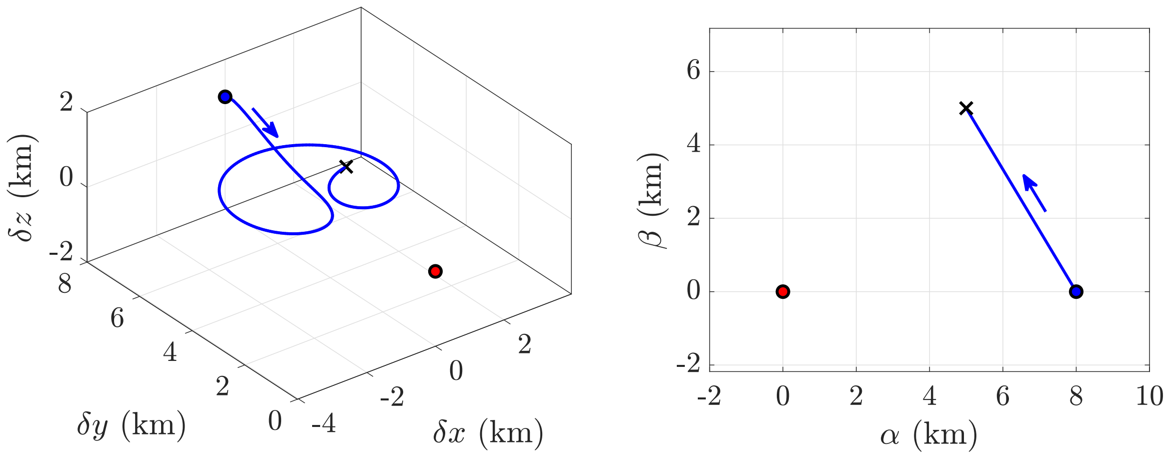

(a) Relative trajectory in the rotating frame

(b) Relative trajectory in the nonsingular local toroidal coordinate frame

Figure 6.1: Relative trajectory of the chaser spacecraft applying feedback control formulated using nonsingular local toroidal coordinates.

Examination of the same relative trajectory plotted in the nonsingular toroidal frame reveals that, in this state representation, the chaser spacecraft travels in a straight-line path from the initial to final relative position. This is a direct result of the definition of feedback error terms using nonsingular local toroidal coordinates and an example of the response of the chaser spacecraft represented in the toroidal coordinate frame. This type of response may be useful for the design of reconfiguration maneuvers that travel along the same plane in the configuration space spanned by the center eigenspace and that expand and contract over time with respect to the periodic orbit at a similar rate to natural motion on the center eigenspace. The time histories of the nonsingular local toroidal coordinates describing the relative state of the chaser spacecraft applying control are plotted as a function of time in Figure 6.2 in blue, with the desired configuration plotted in black.

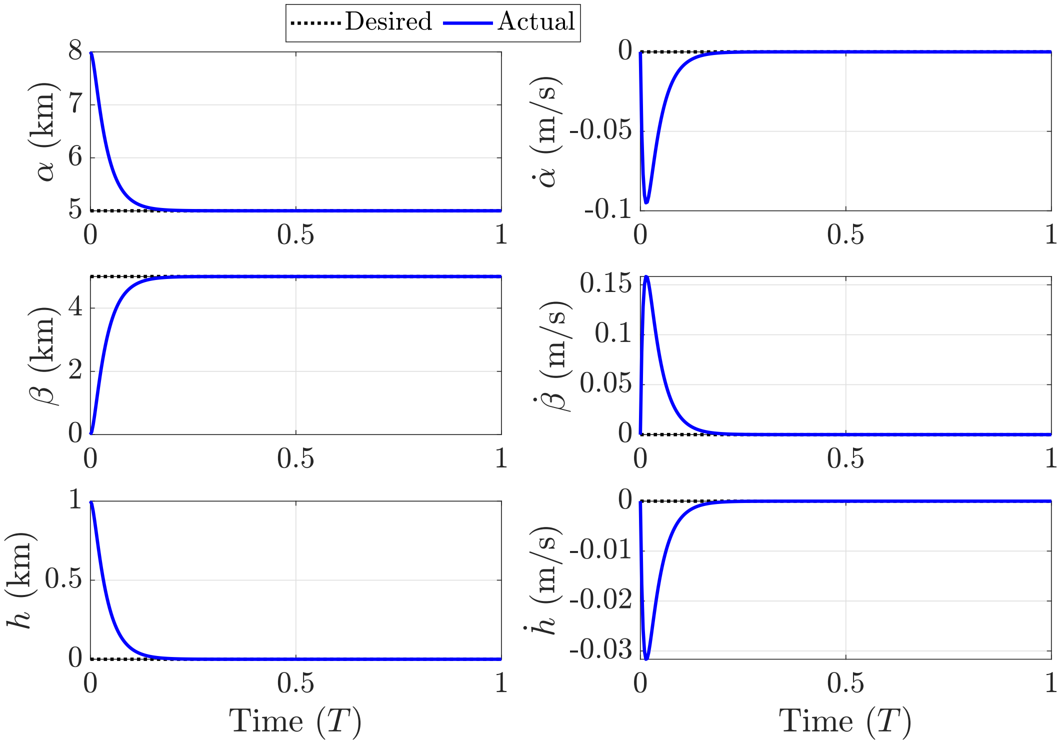

Figure 6.2: State history of the chaser spacecraft applying the feedback control law formulated using nonsingular toroidal coordinates.

Next, the error terms of the Lyapunov function and the chaser spacecraft's required control acceleration are examined. The coordinate error and coordinate rate error of the chaser spacecraft as a function of time are plotted in Figure 6.3a and the magnitude of the input control, u, is plotted as a function of time in Figure 6.3b. In Figure 6.3a, the two error terms are observed to asymptotically approach zero to within a small tolerances expected due to machine precision and the tolerances of the numerical integration scheme. Examining Figure 6.3b, a small steady-state control usage is observed. This required control in the nonlinear CR3BP is expected due to the linear approximations within the definition of the local toroidal coordinate systems. For this example, the total Δv required by the chaser spacecraft is approximately 0.23 m/s; of course, modifying the parameters of the example may change the results. Furthermore, the path of the chaser spacecraft taken from the initial to desired configuration has not been optimized to minimize a cost function.

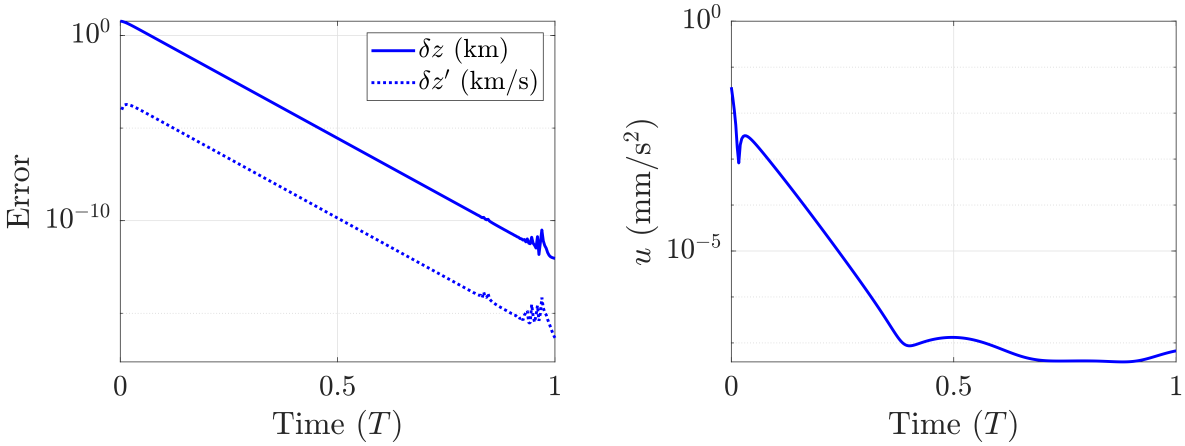

(a) Magnitude of error terms (b) Control acceleration magnitude

Figure 6.3: Lyapunov function error and control acceleration magnitude over time, demonstrating asymptotic convergence to the reference trajectory in the CR3BP.

6.1.2 Geometric local toroidal coordinate formulation

A second formulation of nonlinear feedback control is presenting using a Lyapunov function formulated using the geometric local toroidal coordinates and coordinate rates. For this formulation, the geometric local toroidal coordinate tracking error, labeled $\delta\boldsymbol{e}$, and the coordinate rate tracking error, labeled $\delta\boldsymbol{e}'$, are defined as

$$\delta\boldsymbol{e} = \boldsymbol{e} - \boldsymbol{e}_d \tag{6.17a}$$

$$\delta\boldsymbol{e}' = \boldsymbol{e}' - \boldsymbol{e}'_d \tag{6.17b}$$

where $\boldsymbol{e}_d$ and $\boldsymbol{e}'_d$ are the desired coordinates and coordinate rates, respectively. Following a similar procedure as the previous control law, the Lyapunov function, V, is defined as a radially unbounded, positive definite function of geometric coordinate and coordinate rate tracking errors as

$$V(\delta\boldsymbol{e}, \delta\boldsymbol{e}') = \frac{1}{2}\delta\boldsymbol{e}^T[\boldsymbol{K}_1]\delta\boldsymbol{e} + \frac{1}{2}\left(\delta\boldsymbol{e}'\right)^T \delta\boldsymbol{e}' \tag{6.18}$$

where $[\boldsymbol{K}_1]$ is a positive definite 3×3 gain matrix applied to the coordinates. The time derivative of the Lyapunov function is

$$\dot{V} = \delta(\boldsymbol{e}')^T \left([\boldsymbol{K}_1]\delta\boldsymbol{e} + \delta\boldsymbol{e}''\right) \tag{6.19}$$

where the acceleration error term, $\delta\boldsymbol{e}''$, is the difference between the controlled acceleration of the chaser spacecraft, and the desired acceleration, $\boldsymbol{e}''_d$, written as

$$\delta\boldsymbol{e}'' = \boldsymbol{e}'' - \boldsymbol{e}''_d \tag{6.20}$$

where $\boldsymbol{e}''$ is the acceleration of the geometric local toroidal coordinate due to natural gravitational influence of P_1 and P_2 and a control input acceleration.

To compute the acceleration of the geometric coordinates due as a function of a Cartesian control input vector defined in the rotating frame, first the relationship between the geometric and nonsingular local toroidal coordinate rates is derived. First, recall the expression for relative velocity of the chaser spacecraft in terms of nonsingular toroidal coordinates and coordinate rates, as defined in Eq. (4.15), rewritten here as

$$\boldsymbol{\rho}' = [\boldsymbol{R}]'\boldsymbol{z} + [\boldsymbol{R}]\boldsymbol{z}'$$

The second term of the right-hand side of this expression, $[\boldsymbol{R}]\boldsymbol{z}'$, may be expanded as

$$[\boldsymbol{R}]\boldsymbol{z}' = \begin{bmatrix} \dot{\alpha}\boldsymbol{r}_r & \dot{\beta}\boldsymbol{r}_i & \dot{h}\hat{\boldsymbol{n}}' \end{bmatrix} \tag{6.21}$$

Substituting in the expressions for $\dot{\alpha}$ and $\dot{\beta}$ in terms of the geometric toroidal coordinates and coordinate rates, expressed in Eq. (4.24) and Eq. (4.25), respectively, into Eq. (6.21), yields the following relation:

$$[\boldsymbol{R}]\boldsymbol{z}' = [\boldsymbol{B}]\boldsymbol{e}' \tag{6.22}$$

where $[\boldsymbol{B}]$ is the 3×3 matrix containing the axes of the geometric local toroidal coordinate frame, defined in Eq. (4.31).

Using this relationship between the nonsingular and geometric toroidal coordinate rates, an expression for the acceleration of the geometric local toroidal coordinates in terms of the Cartesian input control acceleration is derived. Using the relation defined in Eq. (6.22), the relative velocity of the chaser spacecraft may be expressed as

$$\boldsymbol{\rho}' = [\boldsymbol{R}]'\boldsymbol{z} + [\boldsymbol{B}]\boldsymbol{e}' \tag{6.23}$$

Equating the time derivative of the right hand side this equation to the sum of the relative acceleration due to the CR3BP, $\boldsymbol{f}$, and a control acceleration formulated in the rotating frame, $\boldsymbol{u}$, yields:

$$\boldsymbol{f} + \boldsymbol{u} = [\boldsymbol{R}]''\boldsymbol{z} + [\boldsymbol{R}]'\boldsymbol{z}' + [\boldsymbol{B}]'\boldsymbol{e}' + [\boldsymbol{B}]\boldsymbol{e}'' \tag{6.24}$$

where $[\boldsymbol{B}]'$ is the time derivative of the axes of the geometric toroidal coordinate frame for an observer in the rotating frame. The acceleration, $\boldsymbol{e}''$, is the acceleration of the geometric coordinates due to both the gravitational influences of P_1 and P_2 and the control acceleration. Solving for $\boldsymbol{e}''$ in Eq. (6.24), the acceleration is written as

$$\boldsymbol{e}'' = \overline{\boldsymbol{e}}'' + [\boldsymbol{B}]^{-1}\boldsymbol{u} \tag{6.25}$$

where the acceleration, $\overline{\boldsymbol{e}}''$, is the natural acceleration of the geometric toroidal coordinates at the current state, defined as

$$\overline{\boldsymbol{e}}'' = [\boldsymbol{B}]^{-1}\left(\boldsymbol{f} - [\boldsymbol{R}]''\boldsymbol{z} - [\boldsymbol{R}]'\boldsymbol{z}' - [\boldsymbol{B}]'\boldsymbol{e}'\right) \tag{6.26}$$

With the total acceleration of the geometric coordinates defined in terms of a Cartesian control acceleration vector, the feedback control law is derived via a control Lyapunov function.

$$\delta\boldsymbol{e}'' = \left(\overline{\boldsymbol{e}}'' + [\boldsymbol{B}]^{-1}\boldsymbol{u}\right) - \boldsymbol{e}_d'' \tag{6.27}$$

This expression may be used to define the time derivative of the control Lyapunov function expressed in Eq. (6.19) in terms of the control acceleration, $\boldsymbol{u}$.

Next, the presented control law is selected to force the the first time derivative of the Lyapunov function equal to a negative definite function of the coordinate rates and negative semidefinite function of all tracking error terms. Specifically, the desired form of the time derivative of the control Lyapunov function is defined as

$$\dot{V}(\delta \boldsymbol{e}') = -(\delta \boldsymbol{e}')^T [\boldsymbol{K}_2] \delta \boldsymbol{e}' \tag{6.28}$$

where $\boldsymbol{K}_2$ is a positive definite 3×3 coordinate rate feedback gain matrix. Equating Eq. (6.11) and Eq. (6.28) and solving for $\boldsymbol{u}$, the resulting tracking control law is

$$\boldsymbol{u} = -[\boldsymbol{B}] \left([\boldsymbol{K}_1] \delta \boldsymbol{e} + [\boldsymbol{K}_2] \delta \boldsymbol{e}' + \overline{\boldsymbol{e}}'' - \boldsymbol{e}_d'' \right) \tag{6.29}$$

For a trajectory tracing a first-order approximation of an invariant torus, the acceleration of the geometric coordinates for dynamics linearized about the periodic orbit is equal to zero. When tracking this motion, the desired chaser acceleration is $\ddot{\boldsymbol{e}}_d = \boldsymbol{0}$ and the control law simplifies to

$$\boldsymbol{u} = -[\boldsymbol{B}] \left([\boldsymbol{K}_1] \delta \boldsymbol{e} + [\boldsymbol{K}_2] \delta \boldsymbol{e}' + \overline{\boldsymbol{e}}'' \right) \tag{6.30}$$

In this form, the control law resembles the structure of a proportional-derivative controller and feedforward acceleration term, with a mapping from error defined in terms of geometric toroidal coordinates and coordinate rates to a Cartesian acceleration vector via the control influence matrix.

The asymptotic stability of the control law is verified by confirming that the first nonzero derivative of V evaluated on the set $\delta \boldsymbol{e}' = \boldsymbol{0}$ is a negative definition function of $\delta \boldsymbol{e}$. The third derivative of V is found as

$$\dddot{V}(\delta \boldsymbol{e}' = \boldsymbol{0}) = -2 \delta \boldsymbol{e}^T [\boldsymbol{K}_1]^T [\boldsymbol{K}_2] [\boldsymbol{K}_1] \delta \boldsymbol{e} \tag{6.31}$$

which is a negative definite function of $\delta \boldsymbol{e}$, verifying that the control law is asymptotically stabilizing to the desired state for a spacecraft formation in the CR3BP. Furthermore, despite the non-unique mapping that exists when $\varepsilon = 0$, the geometric coordinate control law is able to asymptotically approach $\varepsilon = 0$. As ε approaches zero, θ and angle error approach undefined values. However, as ε approaches zero, the magnitude of the corresponding column of the control influence matrix from Eq. (4.31) which determines effort spent on correcting the angle error also approaches zero. Thus, the control law is observed to allow asymptotic regulation to the periodic orbit.

The geometric interpretation of tracking errors and control gains enables a wide range of reference trajectories and control responses to be intuitively designed to achieve distinct formation flying objectives. In this formulation, gain matrices $[\boldsymbol{K}_1]$ and $[\boldsymbol{K}_2]$ may be manually tuned to achieve the desired control response with respect to quasi-periodic motion relative to a periodic orbit. Additionally, a useful property of this formulation of feedback control is that the decomposition of the position error of the chaser spacecraft in terms of geometric local toroidal coordinates supplies the ability to under-constrain the desired state of the chaser spacecraft. In particular, this is useful for when a desired torus size is defined but a specific location along the torus is free to vary. A similar variation may be implemented such that $\delta\theta$ is enforced and ε is allowed to vary.

6.1.2.1 Demonstration of asymptotic stability in the CR3BP

The asymptotic convergence of the feedback control law formulated using the geometric local toroidal coordinates is demonstrated in the CR3BP via an example formation reconfiguration maneuver in the Sun-Earth system. In this example, the target spacecraft is initially located at apolune of the reference 177-day Sun-Earth L_1 southern halo orbit. The chaser spacecraft is initialized on a first-order approximation of an invariant curve with small initial toroidal coordinate rates. The chaser spacecraft then applies feedback control to insert into a first-order invariant torus described by $\varepsilon = 1000$ km. To demonstrate the ability to under-constrain the desired configuration along the torus, the control law simulation is applied without defining a desired value of θ. This is implemented by setting the control gain in the $[\boldsymbol{K}_1]$ matrix associated with $\delta\theta$ equal to zero. The simulation parameters are summarized in Table 6.2. The chaser spacecraft is integrated while applying the control law for one half period of the orbit.

The response of the chaser spacecraft applying the feedback control law is examined. The relative trajectory of the chaser spacecraft is plotted in the Sun-Earth rotating frame and nonsingular local toroidal coordinate frame in Figures 6.4a and 6.4b, respectively. For each plot, the target spacecraft is represented by a red marker at the origin, the initial position of the chaser spacecraft is represented with a blue marker, and the final position of the chaser spacecraft is represented by

Table 6.2: Parameters of the simulation in the CR3BP using the feedback control law formulated using geometric local toroidal coordinates.

Parameter	Value
Reference orbit	177-day Sun-Earth L_1 southern halo orbit
Simulation duration	$T/2 = 88.5$ days
Coordinate error gains	$[\boldsymbol{K}_1] = \text{diag}(1000, 0, 1000)$ (nondim.)
Coordinate rate error gains	$[\boldsymbol{K}_2] = \text{diag}(100, 100, 100)$ (nondim.)
Initial configuration	$\boldsymbol{e}_0 = [250 \text{ km}, \pi/3 \text{ rad}, 1 \text{ km}]^T$ $\boldsymbol{e}'_0 = [2 \text{ m/s}, -10^{-5} \text{ rad/s}, 0 \text{ m/s}]^T$
Desired configuration	$\varepsilon_d = 1000$ km, $h_d = 0$ km $\boldsymbol{e}'_d = [0 \text{ m/s}, 0 \text{ m/s}, 0 \text{ m/s}]^T$

a black cross. In Figure 6.4a, the invariant curve that the desired state is defined on, described by $\varepsilon = 1000$ km, is plotted as a black dashed circle centered at the target spacecraft with a radius of 1000 km. When visualized in the nonsingular local toroidal coordinate frame, the maneuver of the chaser spacecraft to the desired invariant curve is straightforward to interpret.

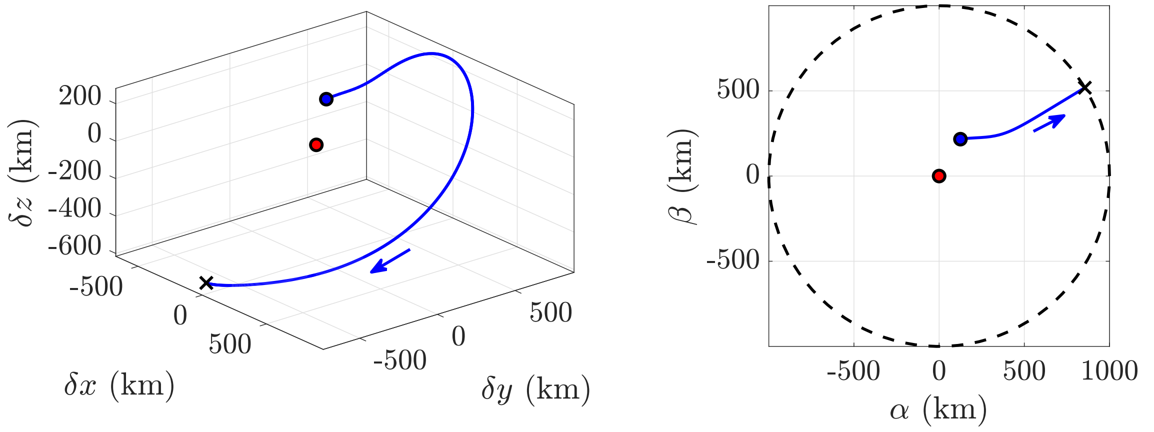

(a) Relative trajectory in rotating frame

(b) Relative trajectory in toroidal frame

Figure 6.4: Relative trajectory of the chaser spacecraft applying feedback control to maneuver to an approximated invariant curve without specifying a desired value of θ.

Over the simulation duration, the chaser spacecraft is observed to converge to the invariant curve described by $\varepsilon = 1000$ km at a value of $\theta = 0.545$ rad. Because of the initial toroidal coordinate rates defined for the chaser spacecraft, a curved path is observed in this nonsingular toroidal coordinate frame. The relative state history of the resulting chaser expressed in geometric local toroidal coordinate and their respective rates over time are plotted versus time in Figure 6.5 in blue. The desired state, which possesses a constant description using geometric local toroidal coordinates, is plotted in black. Note that when the initial toroidal coordinates rates are equal to zero, a straight-line path from the perspective of the nonsingular toroidal coordinate frame is again observed. In this case, the value of θ is observed to remain constant throughout the maneuver.

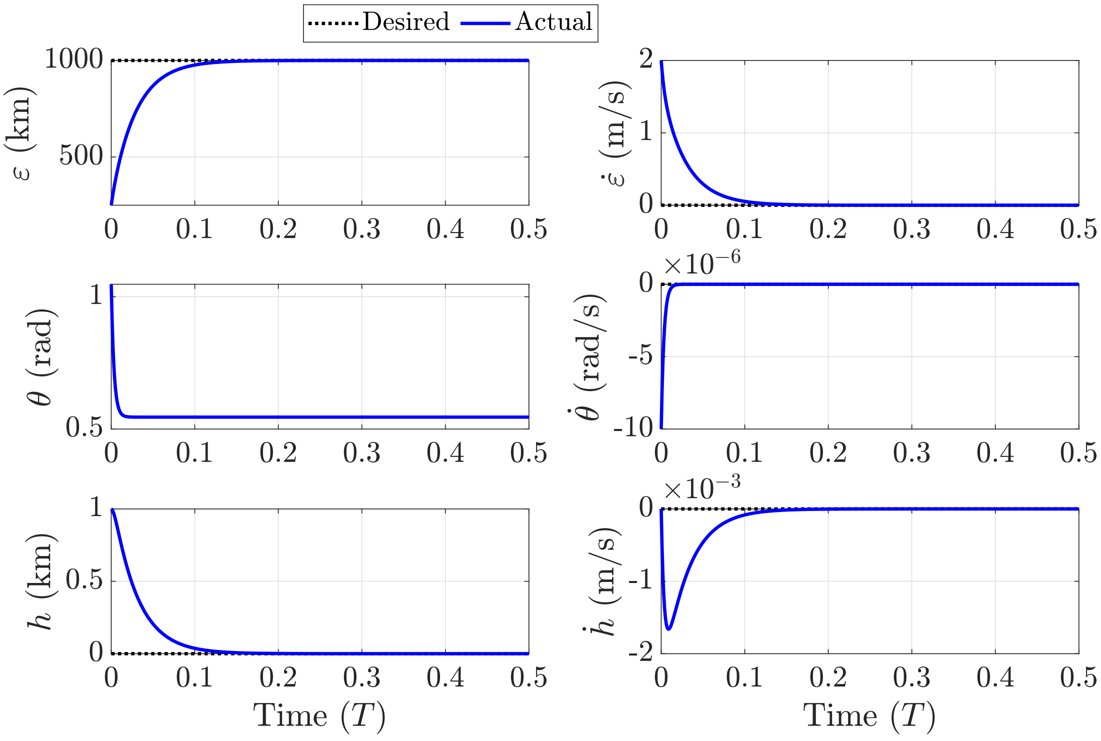

Figure 6.5: State history of the chaser spacecraft applying feedback control, expressed using geometric local toroidal coordinates.

Next, the asymptotic convergence of the chaser spacecraft to the desired configuration is assessed. The magnitude of the geometric coordinate and coordinate rate error of the trajectory is plotted versus time in Figure 6.6a. For this example, since a desired toroidal angle is undefined, the coordinates error term, δe, is calculated using only the error in ε and h. From this figure, the magnitude of each error term is observed to asymptotically approach zero until the numerical tolerances of the integration scheme in reached. Additionally, the required control acceleration magnitude over time is plotted in Figure 6.6b. The required control acceleration decreases over time until a small steady-state control acceleration is reached; this steady-state acceleration is expected due to the linear approximations within the definition of the local toroidal coordinate used to define the reference trajectory. For this example, a total cumulative Δv of 3.41 m/s is required over the course of 88.5 days.

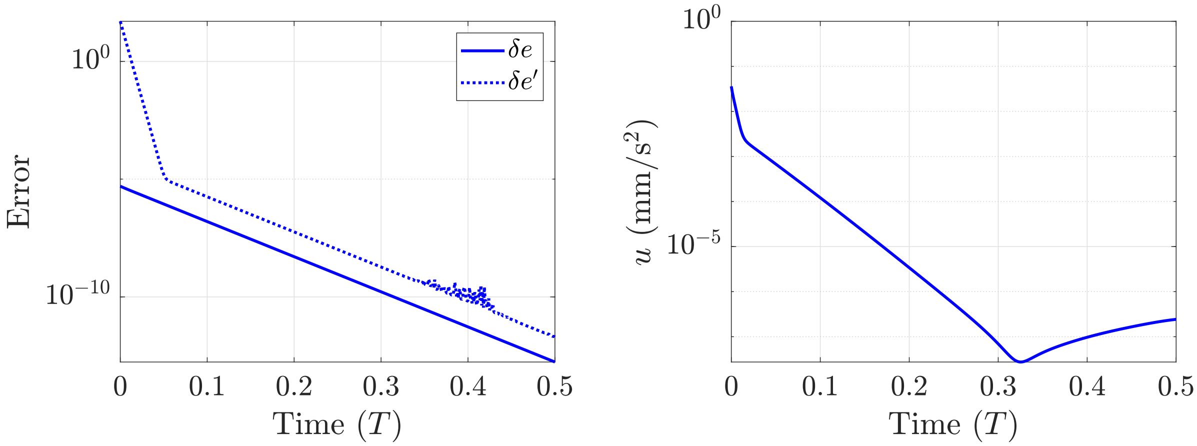

(a) Magnitude of error terms

(b) Control acceleration magnitude

Figure 6.6: Lyapunov function error and control acceleration magnitude over time, demonstrating asymptotic convergence to the reference trajectory in the CR3BP.

6.1.3 Comparison with a Cartesian feedback control formulation

In this section, a simulation compares the response of the chaser spacecraft using the feedback control law formulated using geometric toroidal coordinates compared to the response of the spacecraft using a feedback control law formulated using error terms defined using Cartesian states. A Cartesian-coordinate based control law is formulated using position error, labeled $\delta\boldsymbol{r}$, and velocity error, labeled $\delta\boldsymbol{v}$, defined as

$$\delta\boldsymbol{r} = \boldsymbol{r} - \boldsymbol{r}_d \tag{6.32}$$

$$\delta\boldsymbol{v} = \boldsymbol{v} - \boldsymbol{v}_d \tag{6.33}$$

where $\boldsymbol{r}_d$ is the desired position and $\boldsymbol{v}_d$ is the desired velocity of the spacecraft. Additionally, a feedforward term is defined using the current acceleration of the spacecraft, $\boldsymbol{f}$, and the natural acceleration of the reference trajectory, $\boldsymbol{f}_d$. Using these definitions, the Cartesian feedback control law is defined as [40]

$$\boldsymbol{u} = -[\boldsymbol{K}_1]\delta\boldsymbol{r} - [\boldsymbol{K}_2]\delta\boldsymbol{v} - (\boldsymbol{f} - \boldsymbol{f}_d) \tag{6.34}$$

When $\boldsymbol{f}$ captures the nonlinear dynamics of the CR3BP, this control law is asymptotically stabilizing in the CR3BP to the desired reference trajectory.

A simulation explores the performance of the geometric coordinate control law applied to reconfigure the chaser spacecraft relative to a target spacecraft following an 7-day Earth-Moon DRO. The responses of the two control laws are compared by separately integrating the chaser spacecraft using both controllers for one period of the DRO starting from the same initial conditions. The objective is to reconfigure the chaser spacecraft between two locations along the same invariant curve relative to the target spacecraft. The parameters used in the simulation are summarized in Table 6.3. Note that for comparison, the nondimensional gains for the geometric toroidal coordinate formulation are tuned by hand and are equal to the position and velocity gains for the Cartesian state controller. Because neither control formulation is designed to minimize control usage, this comparison focuses on differences between the two controlled paths relative to the target spacecraft.

After integrating the two controlled trajectories, both control laws demonstrate asymptotic convergence to the desired configuration. However, different responses are observed between the two trajectories produced by the two control schemes. The trajectories produced by two control schemes are illustrated in Figure 6.8 where the trajectory corresponding to the geometric control law is depicted in blue and the trajectory corresponding to the Cartesian control law is depicted in red. The relative trajectories are represented in both the rotating frame and the nonsingular toroidal coordinate frame. The initial and final states along each trajectory is indicated by a circular marker and cross marker, respectively. Although the two trajectories begin at the same

Table 6.3: Parameters of the example simulation comparing the responses of a feedback control law formulated using geometric local toroidal coordinates and Cartesian coordinates.

Parameter	Value
Reference orbit	7-day Earth-Moon DRO
Simulation duration	$1T = 7$ days
Coordinate error gains	$[\boldsymbol{K}_1] = \text{diag}(1000, 1000, 1000)$ (nondim.)
Coordinate rate error gains	$[\boldsymbol{K}_2] = \text{diag}(100, 100, 100)$ (nondim.)
Initial configuration	$\boldsymbol{e}_0 = [10\text{ km}, 2\text{ rad}, 0.001\text{ km}]^T$ $\boldsymbol{e}_0' = [0\text{ m/s}, 0\text{ rad/s}, 0\text{ m/s}]^T$
Desired configuration	$\boldsymbol{e}_d = [10\text{ km}, 0\text{ rad}, 0\text{ km}]^T$ $\boldsymbol{e}_d' = [0\text{ m/s}, 0\text{ rad/s}, 0\text{ m/s}]^T$

state and converge to the same desired trajectory, the paths exhibit distinct geometries due to the formulation of the control schemes. The state histories of the two trajectories corresponding to the two controllers are plotted over time in Figure 6.7, expressed using geometric local toroidal coordinates and respective coordinate rates, using a coloring scheme consistent with Figure 6.8.

The trajectory produced by the toroidal feedback law is observed to maintain constant a values of ε and traces along the torus until converging to the desired angle. This behavior is expected as from a geometric local toroidal coordinate error definition, the toroidal angle term is the only nonzero initial error. In contrast, the trajectory produced by the control law formulated using a Cartesian state description initially departs the torus and approaches the target spacecraft before ultimately returning to the torus at the desired angle. Because of the error definition in terms of relative position and velocity expressed in the rotating frame, the trajectory produced by the Cartesian controller is not influenced by the structure of the center eigenspace during the reconfiguration maneuver. This behavior is evident in Figure 6.8 as the chaser spacecraft using the Cartesian controller exhibits a closer approach to the target spacecraft than when the geometric control law is applied. In particular, the toroidal coordinate frame provides an interpretable depiction of the departure of the chaser spacecraft applying the Cartesian control law from the instantaneous invariant curve.

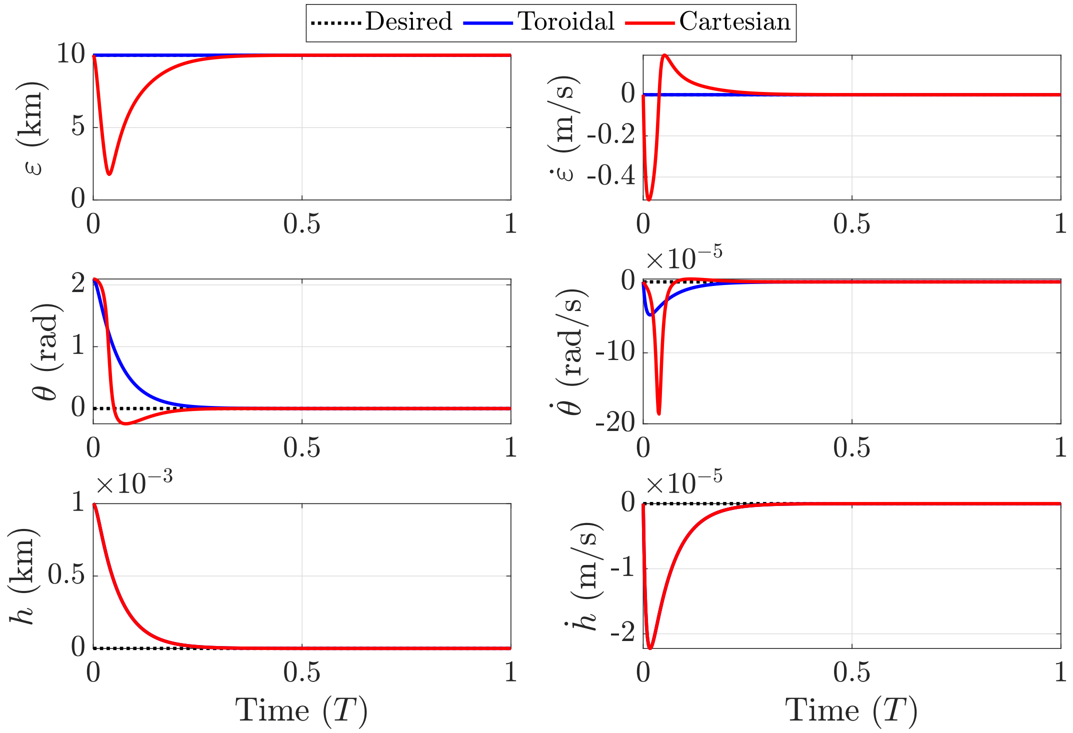

Figure 6.7: State histories of spacecraft applying feedback control laws formulated using geometric toroidal coordinates and Cartesian coordinates to reconfigure between two locations along the same approximated invariant curve.

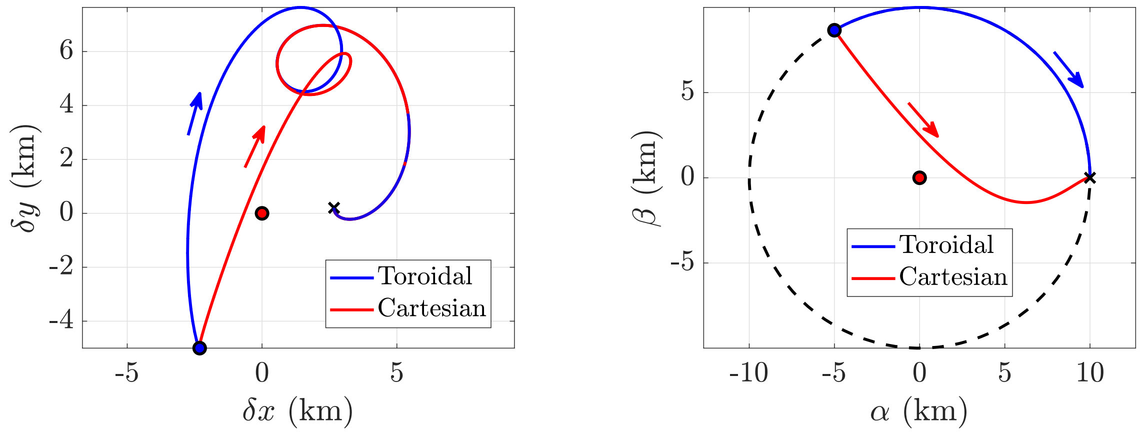

(a) Relative trajectories in rotating frame

(b) Relative trajectories in toroidal frame

Figure 6.8: Relative trajectories of spacecraft applying feedback control laws formulated using geometric toroidal coordinates and Cartesian coordinates to reconfigure between two locations along the same approximated invariant curve.

Though neither feedback control law is optimized to minimize control effort, comparison of the Δv required by each formulation of feedback control reveals a similar control profile. The magnitude of the control acceleration and the cumulative required Δv for two spacecraft are plotted as functions of time in Figure 6.9. The control law formulated using geometric local toroidal coordinates required a total of approximately 1 m/s of Δv, while the control law formulated using Cartesian coordinates required approximately 0.73 m/s of Δv. However, a similar profile in the acceleration magnitude is observed between the two trajectories as they both asymptotically approach the tracking reference, and both control laws require a small steady-state control effort due to the linear approximation of relative dynamics within the definition of the tracking reference.

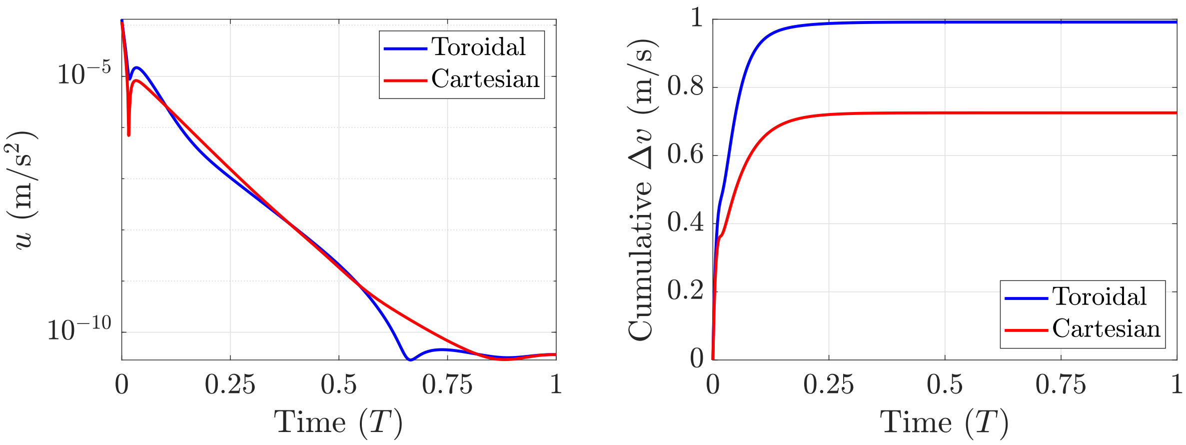

(a) Control acceleration magnitude

(b) Cumulative required Δv

Figure 6.9: Control effort of spacecraft applying feedback control laws formulated using geometric toroidal coordinates and Cartesian coordinates to reconfigure between two locations along the same approximated invariant curve.

While in this example, the control law formulated using geometric local toroidal coordinates required more Δv, varying the gains of each control law impacts the required total Δv. However, for this type of maneuver between two locations on the same approximated invariant torus, the formulation of the error terms using geometric local toroidal coordinates enables a controlled response that travels along the surface of the torus rather than departing and returning to the torus. Thus, the definition of feedback errors and gains corresponding the geometry of an invariant torus via geometric toroidal coordinates enables increased insight into the response of spacecraft feedback control. Furthermore, the description of reference trajectories within the center eigenspace using toroidal coordinates is more straightforward compared to a traditional control law formulated with Cartesian coordinates. The capability for the target spacecraft to trace the torus without defining a reference a priori, as demonstrated in this example, may also support collision avoidance measures for spacecraft flying in formation.

6.1.4 Demonstrations in the ephemeris model

A demonstration of the performance of nonlinear feedback control in a higher-fidelity dynamical model is presented through a simulation of three spacecraft relative to an Earth-Moon DRO recovered in the ephemeris model. To simulate this demonstration, first, the DRO reference orbit with a period of 7 days in the rotating frame is recovered in the point mass ephemeris model of the Earth, Moon, and Sun with an initial epoch of January 1, 2025 at 00:00:00.000 UTC. This reference trajectory is plotted in Figure 3.13 in Section 3.4.5. Furthermore, the complex eigenvector associated with the in-plane oscillatory mode of the nearby DRO in the CR3BP is captured for one revolution via a cubic-spline interpolation.

The nonlinear feedback control law formulated using the geometric local toroidal coordinates is applied. However, in this example, the feed-forward term of the control law is dropped. The small acceleration determined by the feedforward term, which enables asymptotic convergence in the CR3BP, is not observed to significantly impact the performance of the controller in the ephemeris model. Thus, the control law applied in the ephemeris model takes a proportional-derivative form, determined as

$$\boldsymbol{u} = -[\boldsymbol{B}]\Big([\boldsymbol{K}_1]\delta\boldsymbol{e} + [\boldsymbol{K}_2]\delta\boldsymbol{e}'\Big) \tag{6.35}$$

where the spline approximation of the complex eigenvector is used to compute the geometric local toroidal coordinate and coordinate rates. Since the equations of motion of the ephemeris model are formulated in the inertial frame, the control acceleration vector, which is determined in the rotating frame, is transformed to the inertial frame using the instantaneous relative state of the

Earth and Moon to compute the axes of the rotating frame expressed in the inertial frame. The three spacecraft, labeled Chasers A, B, and C, simulate a deployment from near the DRO reference to locations along the same invariant torus approximation described by $\varepsilon = 50$ km and evenly distributed in θ by $2\pi/3$ rad. The parameters of the simulation are summarized in Table 6.4. The control gains are tuned by hand and are equal for each spacecraft.

Table 6.4: Parameters of the example simulation applying feedback control formulated using local toroidal coordinates in the ephemeris model.

Parameter	Value
Reference orbit	7-day Earth-Moon DRO recovered in ephemeris model
Initial epoch	January 1, 2025 00:00:00.000 UTC
Simulation duration	1/2 revolution = 3.47 days
Coordinate error gains	$[\boldsymbol{K}_1] = \text{diag}(5000, 1000, 1000)$ (1/s^2)
Coordinate rate error gains	$[\boldsymbol{K}_2] = \text{diag}(250, 250, 250)$ (1/s)
Chaser A initial configuration Chaser A desired configuration	$\boldsymbol{e}_0 = [1 \text{ km}, 0 \text{ rad}, 0 \text{ km}]^T$ $\boldsymbol{e}_d = [50 \text{ km}, 0 \text{ rad}, 0 \text{ km}]^T$
Chaser B initial configuration Chaser B desired configuration	$\boldsymbol{e}_0 = [1 \text{ km}, 2\pi/3 \text{ rad}, 0 \text{ km}]^T$ $\boldsymbol{e}_d = [50 \text{ km}, 2\pi/3 \text{ rad}, 0 \text{ km}]^T$
Chaser C initial configuration Chaser C desired configuration	$\boldsymbol{e}_0 = [1 \text{ km}, -2\pi/3 \text{ rad}, 0 \text{ km}]^T$ $\boldsymbol{e}_d = [50 \text{ km}, -2\pi/3 \text{ rad}, 0 \text{ km}]^T$

After integrating each of the three chaser spacecraft for the simulation duration, the controlled trajectories in the ephemeris model are examined. The three trajectories relative to the reference trajectory in the ephemeris model are plotted in the Hill frame measured from the Moon and toroidal frame in Figures 6.10a and Figure 6.10b, respectively. The trajectory of Chaser A is represented in blue, Chaser B in red, and Chaser C in dark yellow. For each trajectory, a small out-of-plane component (< 5m) is not plotted. The invariant curve at the final time is plotted in both figures, represented as a black dashed line. The state history of the three chaser spacecraft are plotted versus time in Figure 6.11, using a coloring scheme consistent with Figure 6.10. Visualizing the relative trajectories in the Hill frame supplies a perspective of the relative motion that is commonly used in spacecraft formation flying analysis and illustrates the oscillatory motion of the chaser spacecraft relative to the reference trajectory. Examining the trajectories in the toriodal frame, the chaser spacecraft are observed to maneuver to their desired configurations by traveling generally along a path of near-constant value of θ.

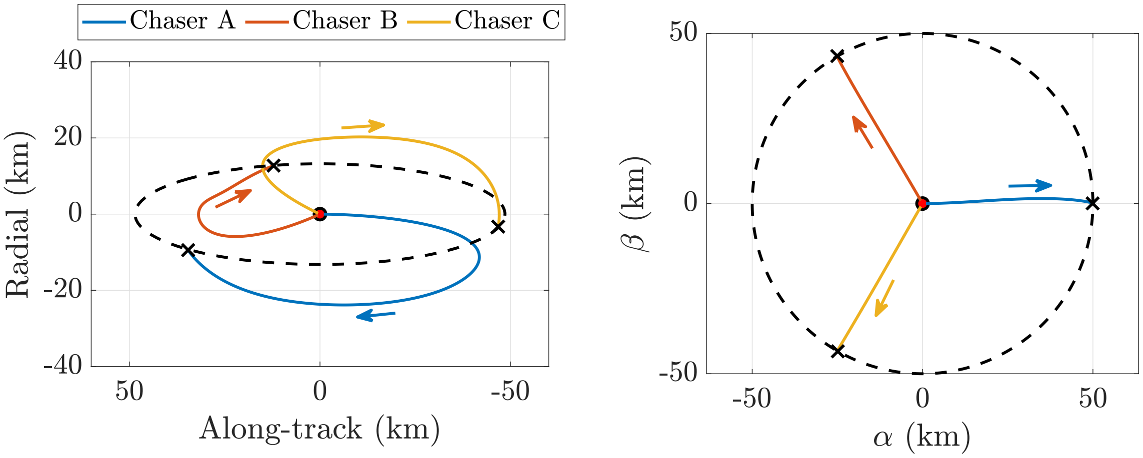

(a) Relative trajectories in the Hill frame (b) Relative trajectories in the toroidal frame

Figure 6.10: Relative trajectories of the three chaser spacecraft relative to the reference trajectory in the ephemeris model resembling a DRO.

The control efforts required by the chaser spacecraft are examined next. The acceleration of the control acceleration is plotted as a function of time in Figure 6.12a using a consistent coloring scheme as Figure 6.10. The magnitude of the required control acceleration suggests that this type of maneuver may be well-suited to a low-thrust enabled spacecraft [136]. Next, the cumulative Δv required is plotted in Figure 6.12b as a function of time. Chaser A requires a total of approximately 4.764 m/s, while Chaser B and C require a total Δv of approximately 2.562 m/s and 2.660 m/s, respectively; the average of the three spacecraft is 3.328 m/s. The variation in the required Δv between spacecraft may motivate the future optimization of deployment location onto an invariant torus for scenarios where the exact deployment location along the torus is a design variable.

6.1.4.1 Tracking a nonlinear vs linearized trajectory in the ephemeris model

Neither nonlinear nor linearized relative motion in the CR3BP is naturally recovered in an ephemeris model. Thus, the performance of feedback control applied in the ephemeris model track-

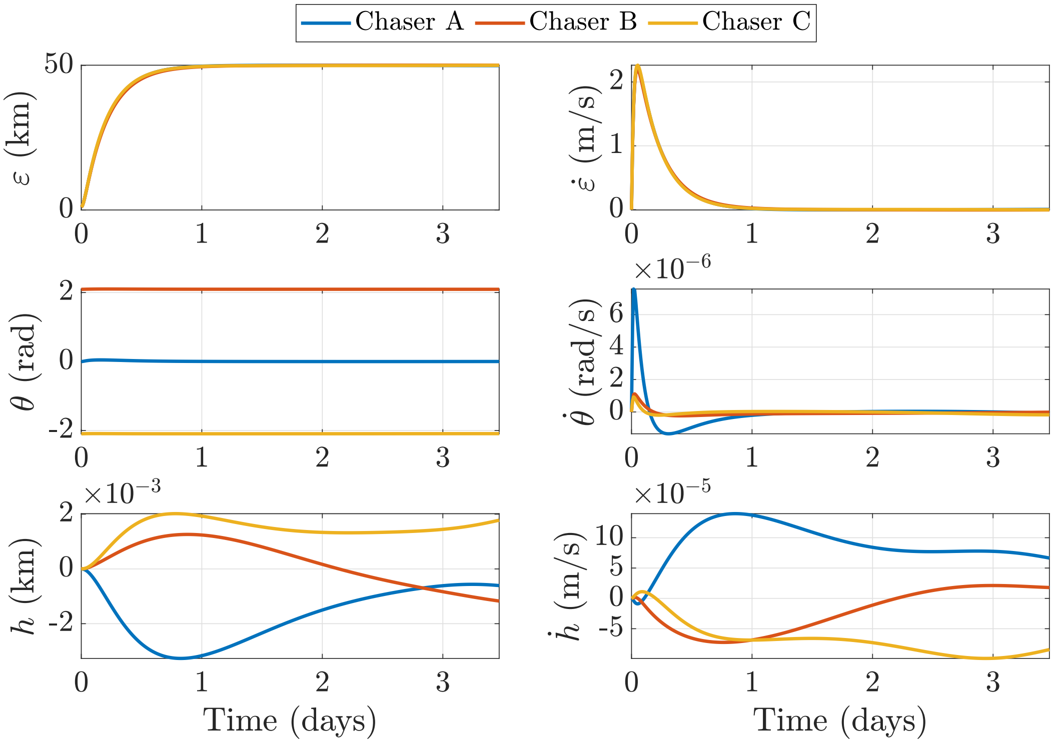

Figure 6.11: State histories of the three chaser spacecraft applying feedback control formulated using toroidal coordinates in the ephemeris model.

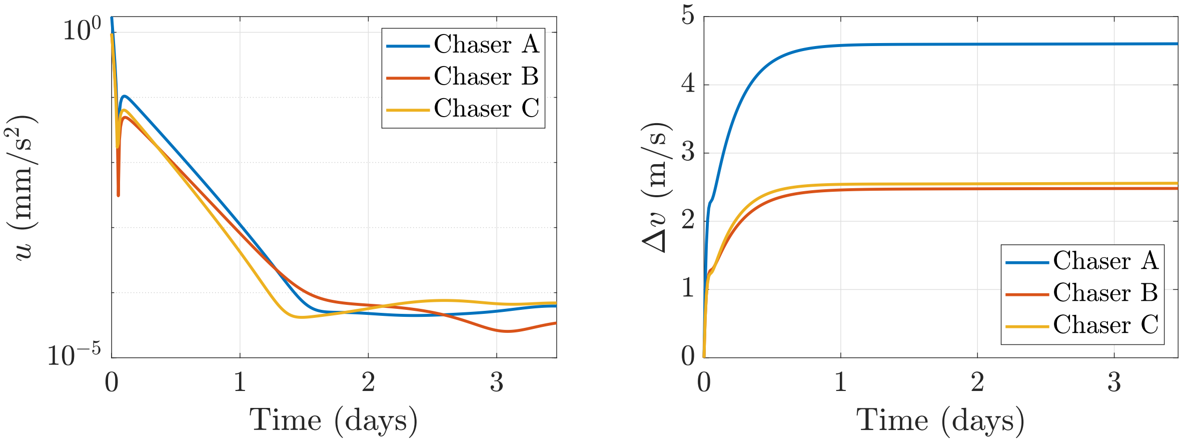

(a) Control acceleration magnitude

(b) Cumulative Δv required

Figure 6.12: Control acceleration and cumulative Δv required for the three chaser spacecraft applying feedback control in the ephemeris model.

ing a linear relative trajectory described via a constant geometric toroidal coordinated and tracking a nonlinear relative reference trajectory generated from a quasi-periodic orbit in the nonlinear CR3BP is investigated. Specifically, a simulation of spacecraft relative to the reference trajectory in the ephemeris model the resembles a 7-day Earth-Moon DRO is presented.

Quasi-periodic orbits that trace along the surface of an invariant torus in the nonlinear CR3BP near the 7-day DRO are computed using a process detailed by Olikara and Scheeres with a stroboscopic return time equal to the period of the DRO [70]. The exact invariant curve is determined by constraining the mean value of ε for a discrete number of initial conditions along the invariant curve to equal 50 km. A single nonlinear quasi-periodic orbit is selected that possesses a value near $\theta = 0$ rad. Two revolutions of this trajectory relative to the periodic orbit in the CR3BP are captured within a cubic spline interpolation for use within the feedback control algorithm in the ephemeris model. To compare to this trajectory, a single linearized quasi-periodic orbit is defined with a constant geometric local toroidal description of $\varepsilon = 50$ km and $\theta = 0$ rad. A summary of the specifications of the comparison simulations is included in Table 6.5. Chaser A is defined as the spacecraft applying control to track the linearizd quasi-periodic orbit and Chaser B applies control to track the nonlinear reference.

Table 6.5: Parameters of simulation in the ephemeris model comparing a spacecraft tracking a quasi-periodic orbit in the CR3BP versus a linearized approximation of a quasi-periodic orbit.

Parameter	Value
Reference orbit	7-day Earth-Moon DRO recovered in ephemeris model
Initial epoch	January 1, 2025 00:00:00.000 UTC
Simulation duration	2 revolutions = 13.9 days
Coordinate error gains	$[\boldsymbol{K}_1] = \mathrm{diag}(10^5, 10^5, 10^5)\ (1/\mathrm{s}^2)$
Coordinate rate error gains	$[\boldsymbol{K}_2] = \mathrm{diag}(10^3, 10^3, 10^3)\ (1/\mathrm{s})$
Chaser A initial and desired configuration	$\boldsymbol{e}_0 = [100\ \mathrm{km}, 0\ \mathrm{rad}, 0\ \mathrm{km}]^T$ $\boldsymbol{e}'_0 = [0\ \mathrm{m/s}, 0\ \mathrm{rad/s}, 0\ \mathrm{m/s}]^T$
Chaser B initial configuration	$\boldsymbol{e}_0 = [100.89\ \mathrm{km}, 0.003\ \mathrm{rad}, 0\ \mathrm{km}]^T$ $\boldsymbol{e}'_0 = [1.111 \times 10^{-3}\ \mathrm{m/s}, -1.253 \times 10^{-7}\ \mathrm{rad/s}, 0\ \mathrm{m/s}]^T$

Each chaser spacecraft is integrated for two revolutions of the reference trajectory in the ephemeris model. For each simulation, the spacecraft is initially located on the desired reference trajectory. The relative trajectories of the two spacecraft are plotted in both the Hill frame measured from the Moon and toroidal frame in Figure 6.13. The trajectory corresponding to a spacecraft tracking a linear approximation of a quasi-periodic orbit is plotted in blue, while the trajectory corresponding to the nonlinear quasi-periodic orbit reference is plotted in red. For the each subfigure, the first-order approximation of the invariant curve relative to the DRO in the CR3BP at the final time is represented as a dashed black line. In the Hill frame, the two trajectories are visually similar, however, when expressed in the nonsingular local toroidal frame, the differences between the two responses is more apparent. The chaser spacecraft that tracks the linearized reference remain in the close vicinity of the approximate invariant curve. The chaser spacecraft tracking the nonlinear reference oscillates around this linear solution, corresponding to the nonlinear invariant torus in the CR3BP.

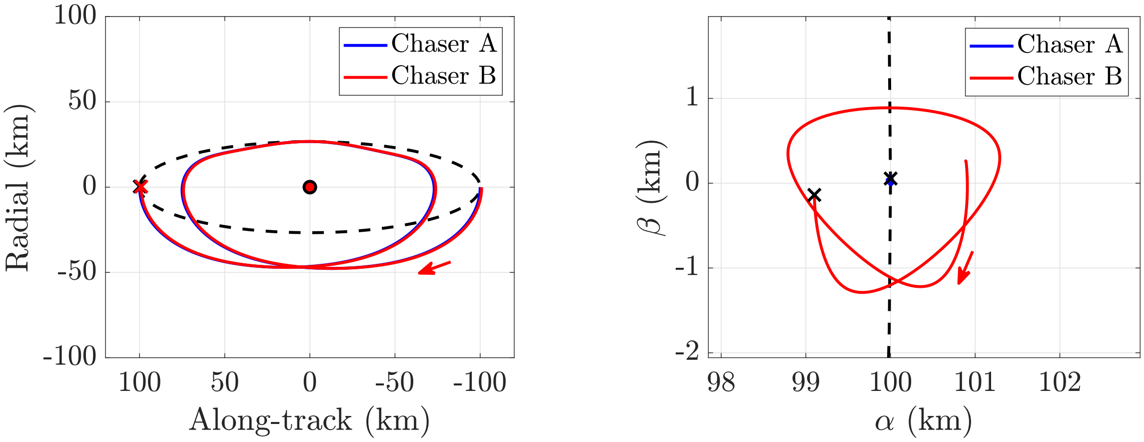

(a) Relative trajectories in the Hill frame

(b) Relative trajectories in the toroidal frame

Figure 6.13: Relative trajectories in the ephemeris model for a spacecraft tracking a quasi-periodic orbit in the CR3BP versus a linearized approximation of a quasi-periodic orbit.

The relative state histories of each trajectory are plotted as a function of time in Figure 6.14. This demonstration illustrates the slowly time-varying relative state description of quasi-periodic orbits in the nonlinear CR3BP formulation using toroidal coordinates. After one revolution of the simulation, a small, non-smooth evolution in the trajectory states is observed due to the interpolation scheme of the complex eigenvector and relative trajectory of the quasi-periodic orbit caused by the scaling of the interpolation of data evenly in time over each revolution of the reference trajectory in the ephemeris model, which is no longer exactly periodic.

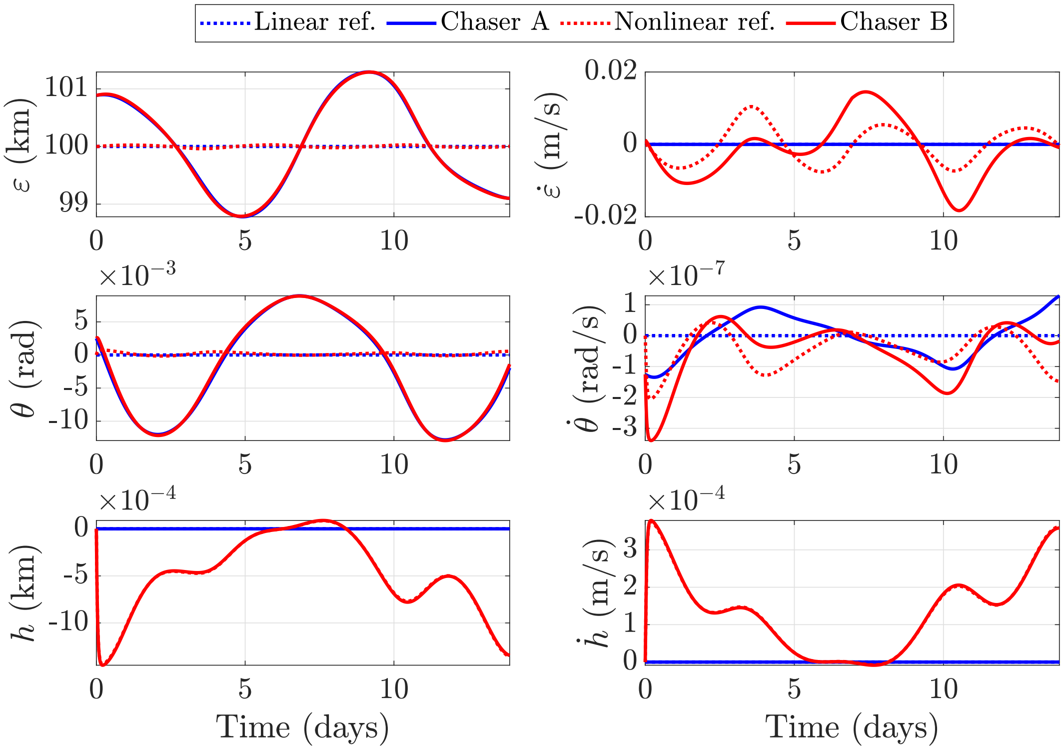

Figure 6.14: State histories of the controlled trajectories in the ephemeris model and their associated reference trajectories.

Finally, the Δv requirements of each controlled trajectory is compared. The cumulative Δv required by each trajectory is plotted versus time in Figure 6.15a using a consistent coloring scheme as Figure 6.13. The difference between the cumulative Δv is computed, defined as $\Delta v_{\text{linear}} - \Delta v_{\text{nonlinear}}$, and plotted in Figure 6.15b. This difference is observed to be very similar between the two controlled trajectories, which vary on the order of mm/s for this example. Furthermore, between some time intervals, the linear tracking reference requires more cumulative Δv than the nonlinear tracking reference, however, for the majority of the simulation, the linear tracking reference requires less Δv by a small amount.

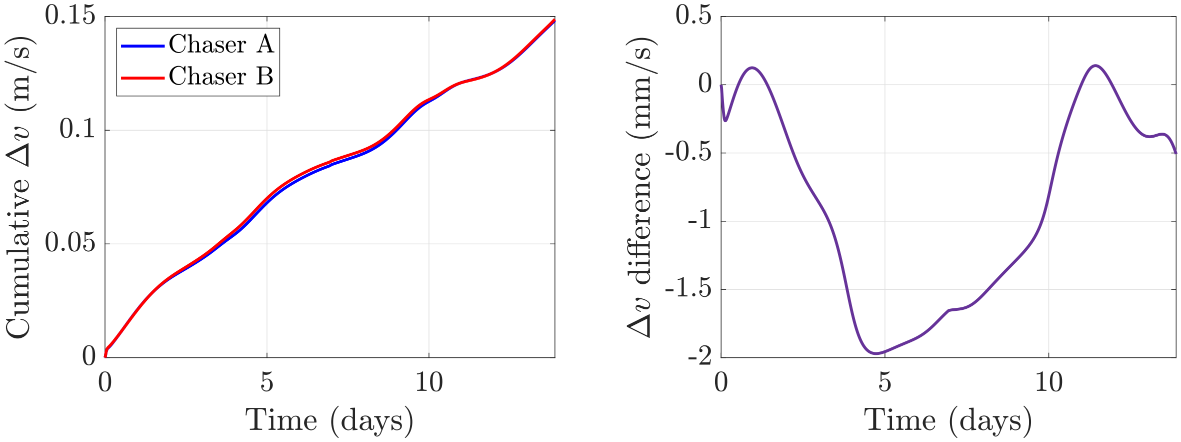

(a) Cumulative Δv required

(b) Difference between cumulative Δv required

Figure 6.15: Comparison of the Δv required to track each relative trajectory in the ephemeris model using the same control feedback formulation.

This experiment illustrates a single example comparing the performance of the feedback controller with reference formulated in the nonlinear CR3BP versus linearized dynamics. Similar results were observed when using a Cartesian proportional-derivative control law in the ephemeris model. The results suggest that for some scenarios, the use of nonlinear versus linearized quasi-periodic tracking reference may exhibit negligible Δv requirements in an ephemeris model. However, this demonstration reflects the performance of feedback control at small separations from the reference trajectory in the ephemeris model. For motion with a greater separation from the reference trajectory, the linearization about the periodic orbit in the CR3BP will provide a worse approximation, and capturing the nonlinear motion in the CR3BP may provide a better tracking reference for motion in the ephemeris model.

6.2 Impulsive control strategies

The local toroidal coordinates are used within the formulation of impulsive control strategies. The first strategy presented is a targeting algorithm to determine impulsive maneuvers for two-impulse transfers relative to a periodic orbit in the nonlinear CR3BP. Next, the slowly time-varying description of motion near the center eigenspace using local toroidal coordinate is leveraged to develop an impulsive station-keeping strategy that enables a spacecraft to stabilize motion near a specific location within the center eigenspace of a periodic orbit.

6.2.1 Targeting algorithm

The STM formulated in the toroidal frame is used to formulate a linear targeting scheme, which determines the impulsive maneuver required to intersect a desired deviation from the periodic orbit after a given time in a linearized dynamical model. Similar to previously derived linear targeting schemes formulated in the rotating frame [103], to calculate the required impulsive maneuver, the STM is defined using four quadrants. The quadrants of the STM formulated in the toroidal coordinate frame are defined as

$$^{\mathcal{Z}}[\boldsymbol{\Phi}(t_f, t_0)] = \begin{bmatrix} [\boldsymbol{\Phi}_{11}] & [\boldsymbol{\Phi}_{12}] \\ [\boldsymbol{\Phi}_{21}] & [\boldsymbol{\Phi}_{22}] \end{bmatrix} \tag{6.36}$$

Using these quadrant definitions, the first-order relation between an initial and final relative states defined using nonsingular toroidal coordinates is expressed as

$$\begin{bmatrix} \boldsymbol{z}_f \\ \boldsymbol{z}'_f \end{bmatrix} = \begin{bmatrix} [\boldsymbol{\Phi}_{11}] & [\boldsymbol{\Phi}_{12}] \\ [\boldsymbol{\Phi}_{21}] & [\boldsymbol{\Phi}_{22}] \end{bmatrix} \begin{bmatrix} \boldsymbol{z}_0 \\ \boldsymbol{z}'_0 + \Delta \boldsymbol{z}'_0 \end{bmatrix} \tag{6.37}$$

where $\Delta \boldsymbol{z}'_0$ is an instantaneous change in toroidal coordinate rates at t_0 corresponding to an impulsive maneuver. This instantaneous change in the coordinate rate relates to an instantaneous change in Cartesian velocity, $\Delta \boldsymbol{v}_0$, as

$$\Delta \boldsymbol{z}'_0 = [\boldsymbol{R}(t_0)]^{-1} \Delta \boldsymbol{v}_0 \tag{6.38}$$

This expression is derived by taking the partial derivative of the expression for the local toroidal coordinate rates, $^{\mathcal{Z}}\boldsymbol{z}'$, with respect to the relative velocity vector, $\boldsymbol{\rho}'$. Rearranging Eq. (6.37) and incorporating the relationship between $\Delta \boldsymbol{z}'_0$ and $\Delta \boldsymbol{v}_0$, the required impulsive change in Cartesian velocity required to reach the desired final configuration in linearized dynamics is

$$\Delta \boldsymbol{v}_0 = [\boldsymbol{R}(t_0)] \left([\boldsymbol{\Phi}_{12}]^{-1} \left(\boldsymbol{z}_d - [\boldsymbol{\Phi}_{11}] \boldsymbol{z}_0 \right) - \boldsymbol{z}'_0 \right) \tag{6.39}$$

Note that only the upper quadrants of the STM are required. In this formulation, the Δv determined by Eq. (6.39) is equivalent to the maneuver determined by a Cartesian linear targeting scheme using initial and final conditions converted from toroidal coordinates to relative Cartesian deviations.

Due to the linear approximations within the targeting maneuver, integration in the nonlinear CR3BP results in a small position error at the final time. Thus, the Δv determined by the linear targeting scheme may be used as an initial guess for a targeting algorithm in a nonlinear dynamical model. In these strategies, the three final position components of a reconfiguration maneuver would be constrained using a constraint vector, $\boldsymbol{F}$, defined as

$$\boldsymbol{F} = \boldsymbol{z}_d - \boldsymbol{z}_f$$

where $\boldsymbol{z}_f$ are the nonsingular local toroidal coordinates at the end of the transfer. The free variable vector, $\boldsymbol{V}$, may consist of the components of the maneuver Δv, defined as

$$\boldsymbol{V} = \Delta \boldsymbol{z}_0'$$

If desired, time of flight may also be included as a free variable. Using the free variable and constraint vectors, a Jacobian matrix is then constructed, either analytically or approximated via finite-differencing, to iteratively update the free variables using a multivariate root finding method. This algorithm may be used to determine a transfer that terminates at the desired position in the nonlinear CR3BP or a higher-fidelity dynamical model.

While the maneuvers determined by the targeting algorithm summarized in Eq. (6.39) produce the same response as an analogous formulation using relative Cartesian states, the nonsingular local toroidal coordinates supply geometric insight into the reconfiguration maneuver. The constant description of locations within the center eigenspace also provides the benefit of less complexity during formulation. For example, consider a chaser spacecraft that is maneuvering between two invariant tori relative to a target spacecraft following the reference Earth-Moon L_2 southern NRHO. For this example, the spacecraft is maneuvering between a location on the surface of an approximated invariant torus defined by $\varepsilon = 10$ km to another torus defined by $\varepsilon = 2$ km. Such a reconfiguration maneuver may be representative of an approach maneuver for proximity operations near a space station located on the NRHO.

The initial and desired relative configuration of the spacecraft is summarized in Table 6.6. The transfer time of the maneuver is fixed at four hours to simulate a relatively quick approach to the second invariant torus. Additionally, the value of θ for the initial and final configuration are offset by $\pi/3$ rad to avoid a reconfiguration maneuver that would closely approach the target spacecraft located on the NRHO should the second maneuver fail to occur. The first maneuver of the chaser spacecraft is occurs as the target spacecraft passes apolune of the L_2 southern NRHO.

Table 6.6: Parameters of the simulation of a reconfiguration maneuver between two approximated invariant curves relative to an 8-day Earth-Moon L_2 southern NRHO.

Parameter	Value
Reference orbit	8-day Earth-Moon L_2 southern NRHO
Initial target location	Apolune
Transfer time	4 hours = $0.021T$
Initial configuration	$\boldsymbol{e}_0 = [10\text{ km}, 0\text{ rad}, 0\text{ km}]^T$ $\boldsymbol{e}'_0 = [0\text{ m/s}, 0\text{ rad/s}, 0\text{ m/s}]^T$
Final configuration	$\boldsymbol{e}_d = [2\text{ km}, \pi/3\text{ rad}, 0\text{ km}]^T$ $\boldsymbol{e}'_d = [0\text{ m/s}, 0\text{ rad/s}, 0\text{ m/s}]^T$

Two impulsive maneuvers required for a transfer between the initial and final desired positions relative to the NRHO in the nonlinear CR3PB are computed. Specifically, the impulsive maneuver determined by the linear targeting algorithm in Eq. (6.39) is used as an initial guess for a single shooting algorithm to compute a transfer in the nonlinear CR3BP for a fixed transfer time of four hours. For this example, one iteration of Newton's method is required to determine a maneuver that results in a position error of less than 10^{-13} km in the nonlinear CR3BP. The magnitude of the first maneuver is equal to 0.694 m/s; the magnitude of the maneuver required to insert into motion on the center eigenspace, i.e., zero local toroidal coordinate rates, is equal to 0.697 m/s, for a total reconfiguration cost of 1.391 m/s.

The relative trajectory of the chaser spacecraft during the maneuver is plotted in the Earth-

Moon rotating frame in Figure 6.16a and in the nonsingular local toroidal coordinate frame in Figure 6.16b. The initial relative position of the chaser spacecraft is represented with a blue marker; the target spacecraft is represented with a red marker at the origin. In each plot, the first order approximation of the invariant curve corresponding to $\varepsilon = 10$ km at the initial time and the invariant curve corresponding to $\varepsilon = 2$ km at the final time are represented in black. In the Earth-Moon rotating frame, these invariant curves are represented by ellipses of different size, with a small orientation difference between the initial and final invariant curve. In the toroidal coordinate frame, each invariant curve is represented as circles on the $\alpha\beta$ plane, centered at the target spacecraft, with a radius equal to ε.

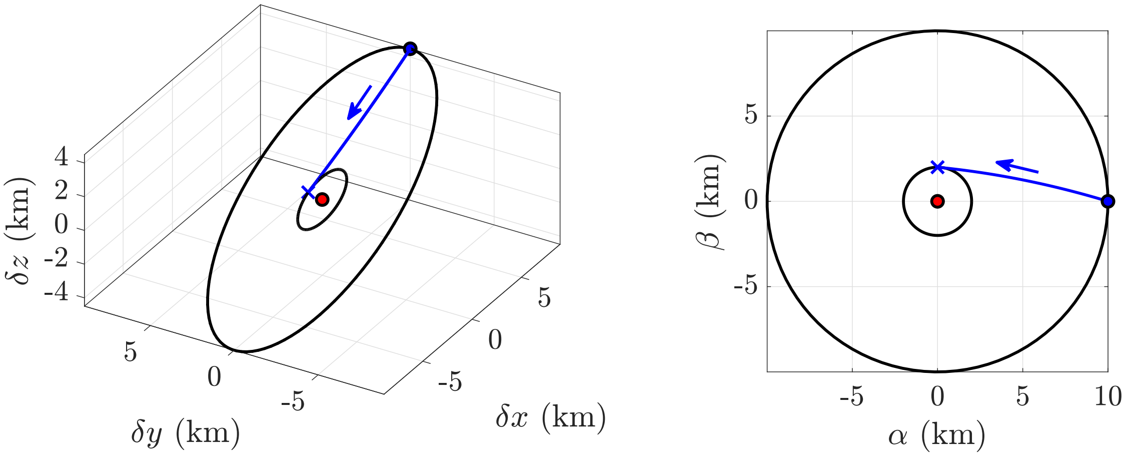

(a) Relative trajectories in rotating frame

(b) Relative trajectories in toroidal frame

Figure 6.16: Relative trajectory of a reconfiguration maneuver between two approximated invariant curves relative to an Earth-Moon L_2 southern NRHO in the CR3BP.

The four-hour transfer starting relative to apolune of the NRHO follows nearly straight-line motion with similar impulsive Δv maneuver magnitudes at the beginning and end of the transfer. The state history of the chaser spacecraft, measured relative to the target spacecraft and expressed in geometric local toroidal coordinates, is plotted versus time in Figure 6.17. The transfer, which travels between two distinct positions within the center eigenspace, is observed to depart the projection of the center eigenspace onto the configuration space during the transfer and the value of ε over the transfer drops slightly below 2 km before reaching the final desired value of 2 km. The nearly-straight-line motion observation reinforces the strategy to vary θ between the initial and final configuration to avoid a trajectory that would travel near the target spacecraft should the second maneuver fail to occur.

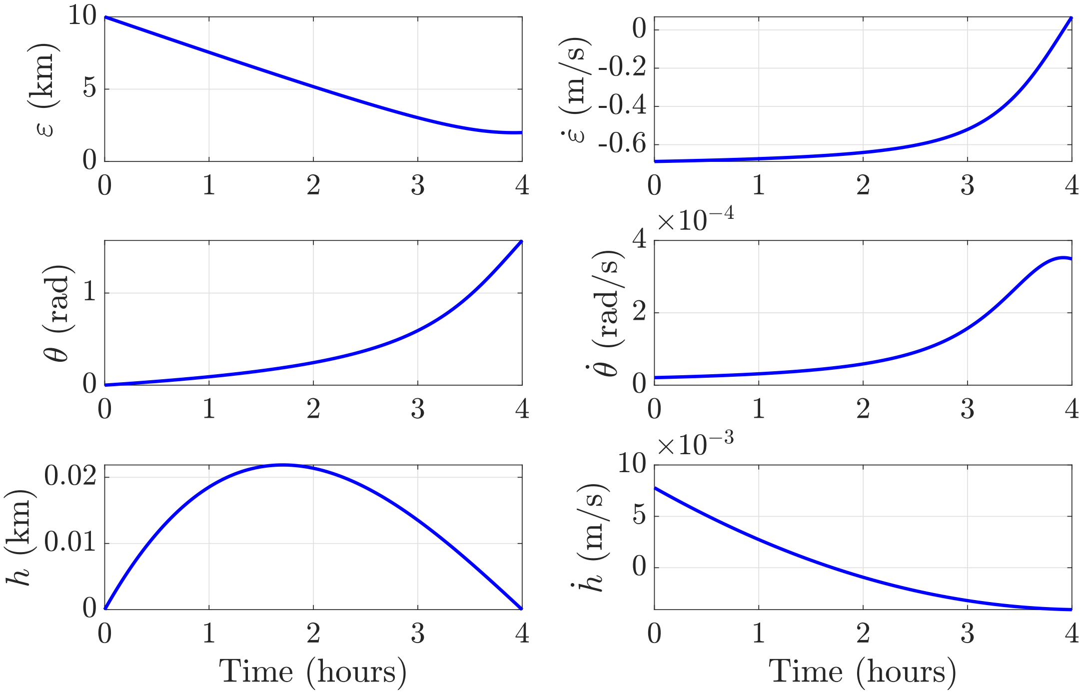

Figure 6.17: State history of the chaser spacecraft during the reconfiguration maneuver, expressed using geometric local toroidal coordinates.

6.2.2 Impulsive station-keeping strategy

A control strategy is introduced that determines successive impulsive maneuvers applied at a specified maneuver frequency to stabilize a spacecraft to a specific location on the center eigenspace of a periodic orbit. The strategy is formulated by combining the previously detail linear targeting algorithm with insight into the structure of the STM formulated in the nonsingular local toroidal coordinate frame as discussed in Section 4.4.3. An advantage of this strategy is that the STM is not required to be computed between maneuver epochs, resulting in a straightforward control strategy that is relatively computationally inexpensive.

The control strategy is formulated by assuming that the desired motion of the chaser spacecraft lies within the center eigenspace. Because motion along the center eigenspace is time-invariant when expressed in toroidal coordinates, the desired relative configuration is described by a constant description, $\boldsymbol{z}_d$. To derive the strategy, first, consider the first two terms of the Taylor series expansion of an STM formulated in the toroidal coordinate frame, ${}^{\mathcal{Z}}[\boldsymbol{\Phi}(t_f, t_0)]$, taken at t_0 [137]

$$
{}^{\mathcal{Z}}[\boldsymbol{\Phi}(t_f, t_0)] \approx [\boldsymbol{I}_6] + [\boldsymbol{A}(t_0)](t - t_0) = \begin{bmatrix} [\boldsymbol{I}_3] & [\mathbf{0}_3] \\ [\mathbf{0}_3] & [\boldsymbol{I}_3] \end{bmatrix} + \begin{bmatrix} [\mathbf{0}_3] & [\boldsymbol{I}_3] \\ [\boldsymbol{A}_{21}(t_0)] & [\boldsymbol{A}_{22}(t_0)] \end{bmatrix} (t - t_0) \tag{6.40}
$$

Using the terms of this Taylor series expansion to approximate the STM formulated in the toroidal coordinate frame, the upper-left quadrant of the STM is approximated as

$$[\boldsymbol{\Phi}_{11}] \approx [\boldsymbol{I}_3]$$

and the upper-right quadrant is approximated as

$$[\boldsymbol{\Phi}_{12}] \approx \Delta t [\boldsymbol{I}_3]$$

where $\Delta t = t_f - t_0$. Recall that the form of the state transition matrix formulation in the nonsingular local toroidal coordinate frame possesses the form:

$$
[\boldsymbol{\Phi}_{11}] = \begin{bmatrix} 1 & 0 & * \\ 0 & 1 & * \\ 0 & 0 & * \end{bmatrix}
$$

The upper-left quadrant of the STM formulated in the toroidal frame shares two columns with the approximation of the quadrant. In addition, these first two columns are multiplied by the dominant toroidal coordinate states components of a chaser spacecraft near the center eigenspace, α and β, while the remaining toroidal coordinate state components possess near-zero values for motion near the center eigenspace.

Applying the approximation of the quadrants of the STM formulated in the toroidal coordinate frame within the targeting control law, a straightforward control strategy is developed.

Substituting the approximated definitions of $[\boldsymbol{\Phi}_{11}]$ and $[\boldsymbol{\Phi}_{12}]$, the resulting impulsive control maneuver is determined as

$$\Delta \boldsymbol{v}_0 = -[\boldsymbol{R}(t_0)] \left(\frac{\boldsymbol{z}_0 - \boldsymbol{z}_d}{\Delta t} + \boldsymbol{z}_0' \right) \tag{6.41}$$

When the chaser spacecraft lies near the center eigenspace, h, and all three coordinate rates have near-zero values, minimizing the impact of the differences between the true and approximated values of $[\boldsymbol{\Phi}_{12}]$ and the third column of $[\boldsymbol{\Phi}_{11}]$. In fact, when the chaser spacecraft lies exactly on the center eigenspace, indicated by $h = \dot{\alpha} = \dot{\beta} = \dot{h} = 0$, the $\Delta \boldsymbol{v}_0$ determined by Eq. (6.41) and the linear targeting scheme summarized in Eq. (6.39) are equivalent. Ultimately, the simplifications remove the computation of the STM between successive maneuvers while enabling station-keeping of specified deviations from a periodic orbit that lies on the center eigenspace.

The derived station-keeping strategy is demonstrated in the CR3BP to maintain a spacecraft on the center eigenspace of the reference 177-day Sun-Earth southern L_1 halo orbit. First, the simplifications to the STM formulated in the toroidal coordinate frame is evaluated. A maneuver interval of 10 maneuvers per revolution is selected, corresponding to a time between maneuvers of approximately $\Delta t = 17.7$ days, or $\Delta t = 0.30452$ in nondimensional units of time. Starting from apogee, the nondimensionalized upper quadrants of the STM formulated in the toroidal frame evaluated along the periodic orbit for Δt are equal to

$$[\boldsymbol{\Phi}_{11}] = \begin{bmatrix} 1 & 0 & 0.01198 \\ 0 & 1 & -0.10148 \\ 0 & 0 & 1.2630 \end{bmatrix} \qquad [\boldsymbol{\Phi}_{12}] = \begin{bmatrix} 0.29997 & -0.10098 & -0.022618 \\ 0.096005 & 0.29769 & -0.024579 \\ 0.027662 & 0.0021548 & 0.32914 \end{bmatrix}$$

The form of $[\boldsymbol{\Phi}_{11}]$ is consistent with the expected form of the STM formulated in the nonsingular local toroidal coordinate frame. Furthermore, the diagonal terms of $[\boldsymbol{\Phi}_{12}]$ possess values near the nondimensional value of Δt and smaller off-diagonal terms. As the time between successive maneuvers decreases, the approximations of the STM quadrants better represent the true STM quadrants.

The station-keeping strategy applied to the control of a single chaser spacecraft relative to the Sun-Earth L_1 southern halo orbit is investigated. The desired relative trajectory is located on the surface of a first-order approximation of an invariant torus. The initial state of the chaser spacecraft is defined slightly perturbed from the desired location along the torus. The parameters of the simulation are summarized in Table 6.7. The spacecraft is simulated in the CR3BP for 5 revolutions of the halo orbit, applying impulsive maneuver determined in Eq. (6.41) at a maneuver frequecy of 10 maneuvers per revolution.

Table 6.7: Parameters of the simulation of the impulsive station-keeping strategy applied near a Sun-Earth L_1 southern halo orbit in the CR3BP.

Parameter	Value
Reference orbit	177-day Sun-Earth L_1 southern halo orbit
Initial target location	Apogee
Simulation duration	$5T = 2.42$ years
Maneuvers per revolution	$N = 10$
Initial configuration	$\boldsymbol{z}_0 = [10 \text{ km}, 0 \text{ km}, 1 \text{ km}]^T$ $\boldsymbol{z}_0' = [0 \text{ m/s}, 2 \text{ m/s}, 0 \text{ m/s}]^T$
Desired configuration	$\boldsymbol{z}_d = [5 \text{ km}, 5 \text{ km/s}, 0 \text{ km}]^T$ $\boldsymbol{z}_d' = [0 \text{ m/s}, 0 \text{ m/s}, 0 \text{ m/s}]^T$

The relative trajectory, maneuver history, and deviation of the controlled spacecraft from the desired reference are examined. First, the relative trajectory of the station-kept spacecraft measured from the halo orbit is plotted in Figure 6.18. The same relative trajectory is represented in the Sun-Earth rotating frame in Figure 6.18a and a planar view in the nonsingular local toroidal coordinate frame in Figure 6.18b. In both plots, the initial position of the maneuver spacecraft is represented with a blue marker and the final position is represented with a black cross. Examining the relative trajectory in the rotating frame, the response of the spacecraft is representative of the desired motion on the center eigenspace of the halo orbit. In Figure 6.18b, a zoomed-in view of the relative trajectory in the toroidal coordinate frame further reveals the response spacecraft applying the impulsive maneuvers to reduce the error with respect to the desired configuration along the approximated invariant torus, represented in the plot as a dashed black curve.

Next, the position error and maneuver magnitudes of the controlled trajectory are examined.

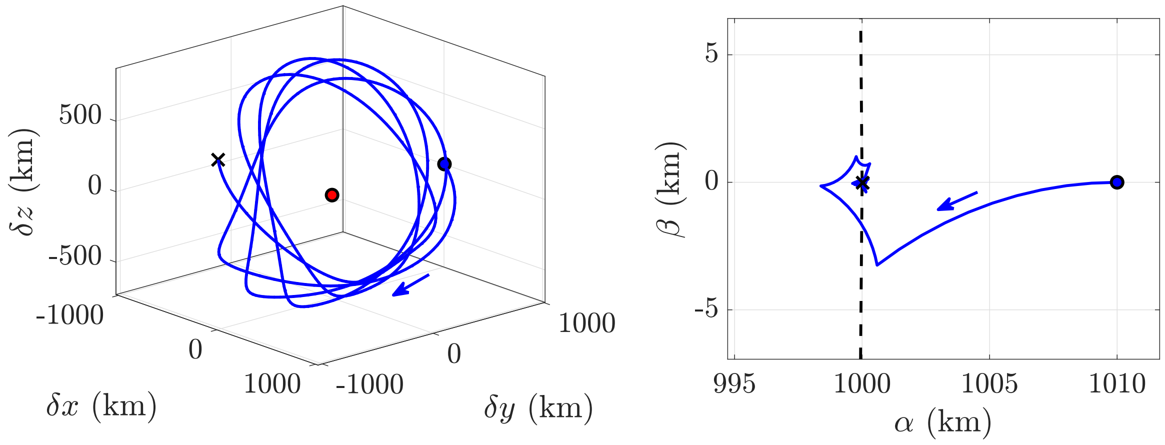

(a) Relative trajectory in the rotating frame (b) Relative trajectory in the toroidal frame

Figure 6.18: Relative trajectory of a spacecraft applying the impulsive station-keeping control near a 177-day Sun-Earth southern L_1 halo orbit in the CR3BP.

The position error versus time, defined as the separation between the spacecraft and the desired location along the invariant curve in the configuration space of the rotating frame, is plotted in Figure 6.19a. Analysis of this error reveals that the station-keeping spacecraft reduces the initial position error, then reaches a steady-state error of less than approximately 1 km. The magnitude of each maneuver of the simulation is plotted versus time in Figure 6.19b. Maneuvers early in the simulation possess a larger magnitude as the spacecraft reduces its position error. As the spacecraft enters a steady-state relative to the reference configuration, the maneuver magnitudes also reach an roughly constant magnitude of less than approximately 1 mm/s.

6.2.2.1 Varying maneuver frequency

The performance of the control strategy is assessed at different maneuver frequencies and separation distances from the 177-day Sun-Earth southern L_1 halo orbit. Values of the desired size of the torus, described by ε_d, near the Sun-Earth L_1 halo orbit are selected between 1 and 5000 km. The desired angle coordinate is kept constant at $\theta_d = 0$ rad, such that $\varepsilon_d = \alpha_d$ and $\beta_d = 0$ km. Three maneuver frequencies are simulated, corresponding to the number of maneuvers per revolution of $N = 5$, 10, 15, and 20. For each simulation, the controlled trajectory is initialized on the desired

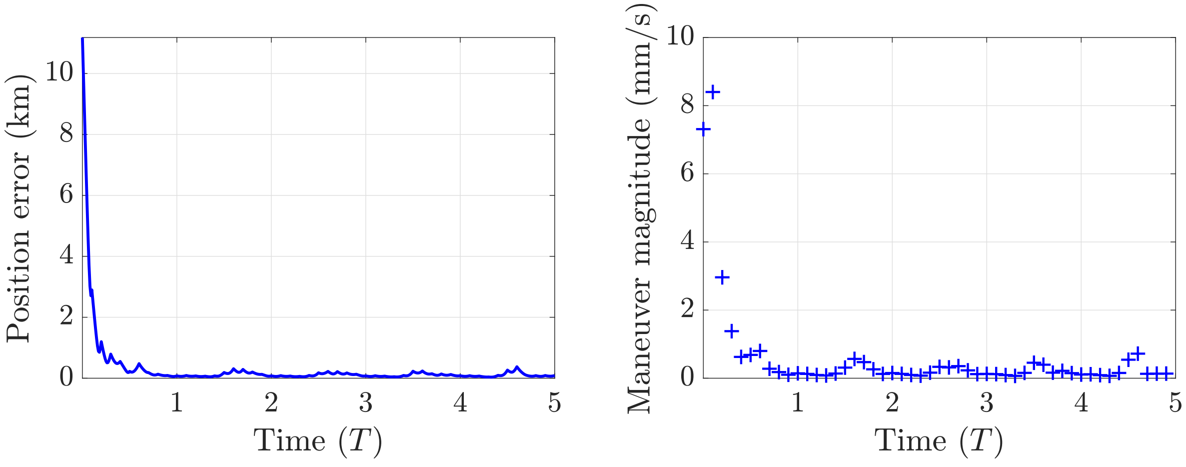

(a) Position error versus time

(b) Individual maneuver magnitude

Figure 6.19: Position error and maneuver magnitudes for the spacecraft applying the impulsive station-keeping control near the Sun-Earth L_1 southern halo orbit.

state relative to apogee of the reference orbit and propagated for five periods. The maximum position error is defined as the maximum magnitude of the Cartesian position difference between the spacecraft and the desired trajectory over the five periods. For each maneuver frequency, the Δv required per revolution and and maximum position error over the simulation are plotted as a function of ε_d in Figure 6.20a and Figure 6.20b, respectively.

For this particular periodic orbit, in general, a minimum number at least 8 maneuvers per revolution are required to maintain bounded motion for all values of ε_d, or a maneuver approximately every 22 days. At a maneuver frequency of $N = 5$, the controlled trajectory is observed to diverge from the desired reference, while maneuver frequencies of 10, 15, and 20, resulted in motion bounded to the desired relative configuration. To reduce the number of maneuvers require to maintain the desired configuration along the invariant torus, the targeting formulation using the full STM defined in Eq. (6.39) may be applied. When a sufficient number of maneuvers are applied, as the number of impulsive maneuvers per orbit increases, both the the cumulative Δv and maximum position error over time decreases. As the torus size relative to the periodic orbit increases, indicated by larger values of ε_d, the required Δv per orbit and maximum position error

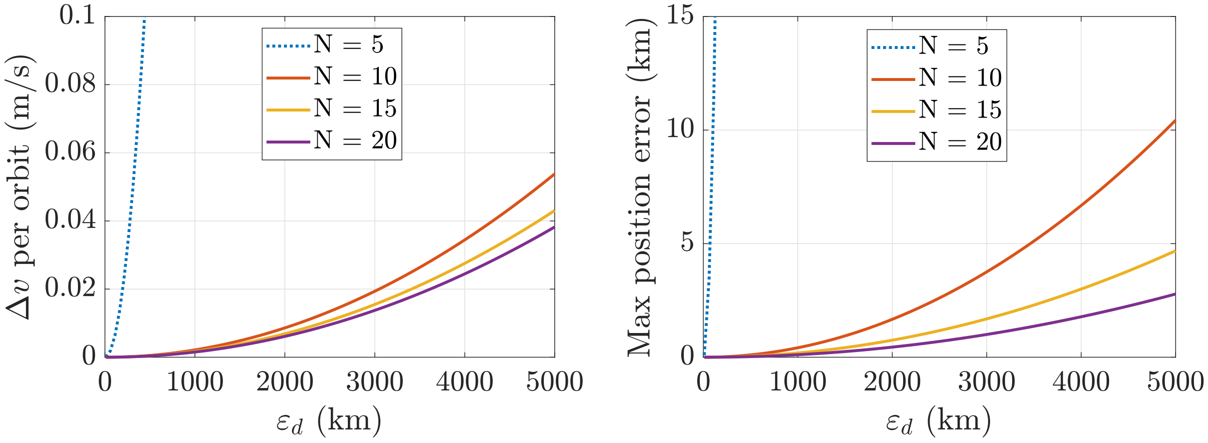

(a) Cumulative Δv per orbit

(b) Maximum position error

Figure 6.20: Cumulative Δv and maximum position error of spacecraft applying the impulsive station-keeping control strategy at different maneuver frequencies near the 177-day Sun-Earth southern L_1 halo orbit in the CR3BP .

also increases. However, for a sufficient number of maneuvers per revolution, the presented station-keeping strategy expressed in Eq. (6.41) using the approximation of the STM is demonstrated in this example to maintain a chaser spacecraft on a specific location along an approximated invariant torus for low required Δv.

6.2.3 Demonstration in the ephemeris model

To assess the performance of the presented control strategy in a higher-fidelity simulation, a Monte Carlo analysis of the control strategy is conducted in the ephemeris model. Compared to the Sun-Earth CR3BP, the higher-fidelity ephemeris model considers ephemeris positions of the Sun and Earth, the gravity of the Moon. Solar radiation pressure is also modeled for a spacecraft model with a surface-area-to-mass ratio of 0.01 m^2/kg and coefficient of reflectivity of 0.18. With the inclusion of SRP within the spacecraft model, a reference trajectory resembling the 177-day southern L_1 halo orbit is recovered in the ephemeris model using the same SRP parameters. To further increase fidelity, navigational errors and thruster firing errors are also considered, with 3σ values selected based on historical and theorized values at the Sun-Earth L_1 and L_2 equilibrium points [90, 138]. Injection errors are defined as the initial deviation of the chaser spacecraft from the desired trajectory error. Navigational errors are added to chaser spacecraft state within the determination of the required impulsive maneuver to simulate state estimation. Finally, thruster firing errors are defined as a magnitude percentage error of the implemented maneuver; however, thruster pointing errors are not simulated. To assess the performance of the control strategy, Monte Carlo simulations are conducted to average the results of 100 trials of the strategy applied using $N = 10, 15, 30$. The parameters of the Monte Carlo simulations are summarized in Table 6.8. For each simulation, the chaser spacecraft is initialized relative to the initial state of the reference trajectory at the southern crossing of the xz plane, approximately at apogee. Each controlled trajectory is then propagated for 10 revolutions in the rotating frame, approximately 1777.4 days or 4.86 years.

Table 6.8: Parameters of the Monte Carlo simulation of the impulsive station-keeping strategy in the ephemeris model.

Parameter	Value
Reference trajectory	Sun-Earth 177-day L_1 southern halo orbit recovered in ephemeris model
Initial epoch	January 1, 2025 00:00:00.000 UTC
Propagation duration	10 revolutions = 1777.4 days
Desired configuration	$\boldsymbol{z}_d = [1000\,\text{km}, 0\,\text{km}, 0\,\text{km}]^T$
Navigation and injection position error	$3\sigma_r = 10$ km
Navigation and injection velocity error	$3\sigma_v = 10$ mm/s
Maneuver magnitude error	$3\sigma_{\Delta v} = 3\%$
Maneuvers per revolution	$N = 10, 15, 20$

In the Monte Carlo simulations of the control of the chaser spacecraft in the ephemeris model, the control strategy maintains bounded motion to the reference trajectory with a reasonable Δv requirement. The control usage requirements and position error results averaged over the 100 trials of the Monte Carlo simulations are summarized in Table 6.9. For each maneuver frequency, the Δv requirements are less than 1 m/s per revolution. However, in contrast to the assessment in the

CR3BP, increasing the number of maneuvers per revolution instead results in an increase in the total Δv required. Increasing the number of maneuvers per revolution is observed to reduces the average and maximum position error.

Table 6.9: Results of the Monte Carlo simulation of the impulsive station-keeping strategy performance in the ephemeris model.

Maneuvers per revolution	Min of total Δv (m/s)	Mean of total Δv (m/s)	Max of total Δv (m/s)	Mean of max error (km)	Max of max error (km)
10	2.566	2.945	3.330	78.793	126.15
15	3.412	2.891	4.455	44.849	67.733
20	4.856	5.427	5.936	33.150	51.053

A single trajectory from the Monte Carlo simulation in analyzed in more detail. Specifically, a simulated trajectory in the ephemeris model apply maneuvers at a frequency of $N = 10$ is examined. The controlled trajectory of the chaser spacecraft is plotted in Figure 6.21a in the Sun-Earth rotating frame relative to the reference trajectory, indicated by a red marker at the origin. Oscillatory bounded motion relative to the reference trajectory is observed, with no secular drift towards or away from the reference orbit. Furthermore, the response of the controlled spacecraft relative to the reference trajectory in the ephemeris model shares similar characteristics with the response of the spacecraft applying control relative to the Sun-Earth L_1 southern halo orbit in the CR3BP, as visualized in Figure 6.18a. The corresponding position of this trajectory is plotted in the nonsingular local toroidal coordinate frame in Figure 6.21b.

The position error and magnitude of each maneuver of the example Monte Carlo simulation trajectory in the ephemeris model is examined. The position error versus time is plotted in Figure 6.22a and the maneuver magnitudes are plotted in Figure 6.22b. Compared to the simulation of a chaser spacecraft applying the impulsive station-keeping strategy in the CR3BP, larger position error and maneuver magnitudes are observed. However, this is an expected result of the increase in fidelity of the dynamical model as well as the introduction of navigation and thruster errors. The magnitude per each maneuver is observed to be similar to previously developed station-keeping

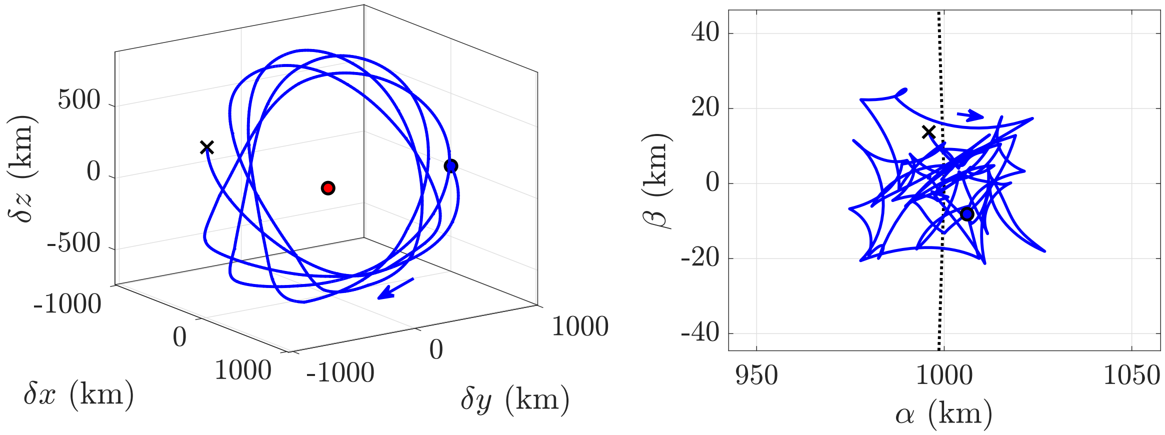

(a) Relative trajectory in the rotating frame (b) Relative trajectory in the toroidal frame

Figure 6.21: Relative trajectory of the spacecraft applying impulsive station-keeping control near a trajectory in the ephemeris model resembling a Sun-Earth L_1 southern halo orbit.

algorithms applied to spacecraft near Sun-Earth halo orbits [29], and the required Δv of less than 1 m/s/year is comparable to the station-keeping requirements of previously flown missions near Sun-Earth L_1 [92]. The results of the Monte Carlo analysis and the sampled trajectory illustrate an example where the impulsive control strategy formulated using local toroidal coordinates supports station-keeping to a specified deviation located on the surface on an approximated invariant torus. Of course, modification of the error parameters, dynamical model, or spacecraft properties may impact observations.

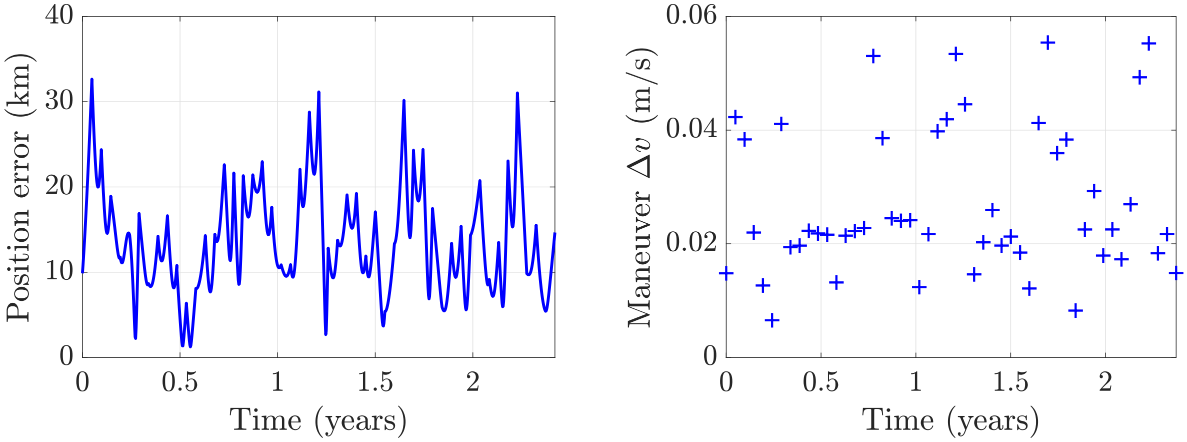

(a) Position error versus time

(b) Individual maneuver magnitude

Figure 6.22: Position error and maneuver magnitudes of the spacecraft applying impulsive stationkeeping control near the reference trajectory in the ephemeris model.

Chapter 7

Survey of First-Order Oscillatory Relative Motion in the CR3BP

In this chapter, the evolution of the size, shape, and orientation of the first-order invariant curve approximation is explored across numerous orbit families in the Earth-Moon and Sun-Earth CR3BP. This analysis reveals the variety of oscillatory motion geometries that exists in the CR3BP relative to periodic orbits, which may be leveraged for the preliminary trajectory design of spacecraft formations near periodic orbits using the center eigenspace. For each periodic orbit family, first, members of the family and their stabilities are computed to identify the regions of each family that admit one or more oscillatory modes. Then, using the characterization methods defined in Chapter 5, the size, shape, and orientation of the normalized invariant curve in the configuration space over each revolution of the associated periodic orbit is summarized using two-dimensional contour plots. Finally, discussions on the general trends and family-specific observations are included to identify considerations for spacecraft formations leveraging the center eigenspace of a periodic orbit within their trajectory design.

7.1 Earth-Moon periodic orbit families

First-order oscillatory motion relative to several periodic orbit families in the Earth-Moon CR3BP is assessed. These periodic orbit families include: the DRO family, the L_1 halo orbit family, the L_2 halo orbit family, the L_1 vertical orbit family, the L_2 vertical orbit family, the L_4 short period family, the L_5 short period family, and the 2:1 resonant orbit family. Although these families are not the only families that possess members that admit oscillatory motion in the Earth-

Moon system, they include many periodic orbits of potential interest for cislunar operations. A summary of the stability indices of each family that correspond to an applicable oscillatory mode is included in Table 7.1. Out-of-plane oscillatory motion relative to periodic orbits is not assessed, however, investigation of this type of oscillatory motion has been identified as a potential avenue of future work. Additionally, the location of the initial fixed point of each orbit at which the complex eigenvector is normalized and time is measured from is also summarized.

Table 7.1: Summary of explored periodic orbit families in the Earth-Moon system.

Orbit family	s_1	s_2	Initial fixed point
Distant retrograde	no	yes	$y = 0,\, \dot{x} < 0$
L_1 southern halo	yes	yes	$y = 0, z < 0$
L_2 southern halo	yes	yes	$y = 0, z < 0$
L_1 vertical	no	yes	$y = 0,\, \dot{z} > 0$
L_2 vertical	no	yes	$y = 0,\, \dot{z} > 0$
L_4 short period	no	yes	$y = \sqrt{3}/2,\, x > x_{L4}$
L_5 short period	no	yes	$y = -\sqrt{3}/2,\, x > x_{L5}$
2:1 resonant	no	yes	$x = 0, \dot{y} > 0$

For each orbit family, several figures are generated:

- Selected members over the examined range of the orbit family are plotted in the rotating frame. The initial fixed point of each orbit is represented with a black marker. The locations of the Earth and Moon, represented by blue and gray markers, respectively, and nearby equilibrium points, represented by red markers, may also be plotted for reference.
- The stability indices of orbits within the examined range of the family are plotted as a function of orbit period. The range of stability index values that corresponds to oscillatory motion, i.e., $s \in (-2, 2)$, is indicated via dashed black lines.
- For each stability index that corresponds to oscillatory motion, two-dimensional plots of the magnitudes of the principal semi-axes of the approximated invariant curve are generated. Periodic orbits are characterized along the horizontal axis, while time measured

from the initial fixed point, normalized by orbit period, is represented along the vertical axis. The size of the invariant curve reflects the normalized invariant curve associated with the normalized complex eigenvector and may be scaled linearly by ε to assess an invariant curve of any size.

- Two-dimensional plots of the description of the orientation of the normalized invariant curve with respect to the rotating frame are also generated. For planar oscillatory relative motion, the orientation of the invariant curve is described by a single angle, ψ. For spatial oscillatory relative motion, the orientation is described via the 3-1-3 Euler angle set. These angles are represented using a continuous color plot and a cyclic colormap.

Part of the material in this section was first published by Celestial Mechanics and Dynamical Astronomy in 2022 by Springer Nature [108].

7.1.1 Earth-Moon distant retrograde orbit family

Selected orbits and the stability indicies of members within the examined range of the Earth-Moon DRO family are plotted in Figure 7.1. Orbits in the DRO family admit in-plane oscillatory motion corresponding to the s_2 stability index and out-of-plane motion corresponding to s_1, which is not examined in this investigation.

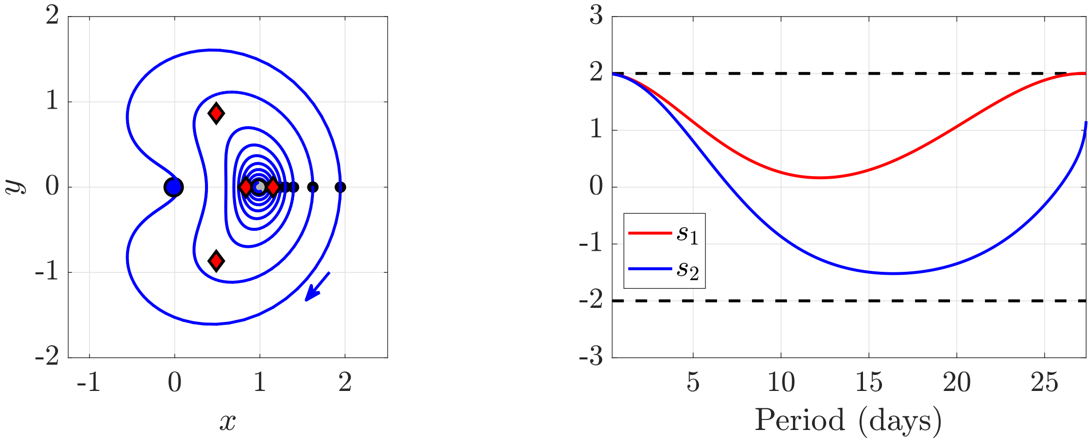

(a) Selected orbits in the rotating frame

(b) Stability indices

Figure 7.1: Selected orbits and stability indices computed for orbits within the examined range of the Earth-Moon DRO family.

The normalized size, shape, and orientation of the approximated invariant curve relative to orbits within the examined range of the Earth-Moon DRO family is summarized in Figure 7.2. As the s_2 index approaches 2 for orbits larger periods, the magnitude of the semi-major axis approaches infinity at $0.5T$, i.e., where DROs possess very low perigee radii. Orbits that possess a shorter period and lie near the Moon are near-circular and admit invariant curves with a ratio of semi-major to semi-minor axis magnitude of approximately 2:1. Motion on the center eigenspaces of orbits in this range may share similarities with the planar, bounded motion relative to circular orbits in a two-body environment, which trace 2:1 ellipses and exactly repeat after one orbital period [40]. As a result, spacecraft formation flying techniques for nearly-circular orbits in perturbed two-body environments may be applicable to the analysis of relative motion near short-period DROs.

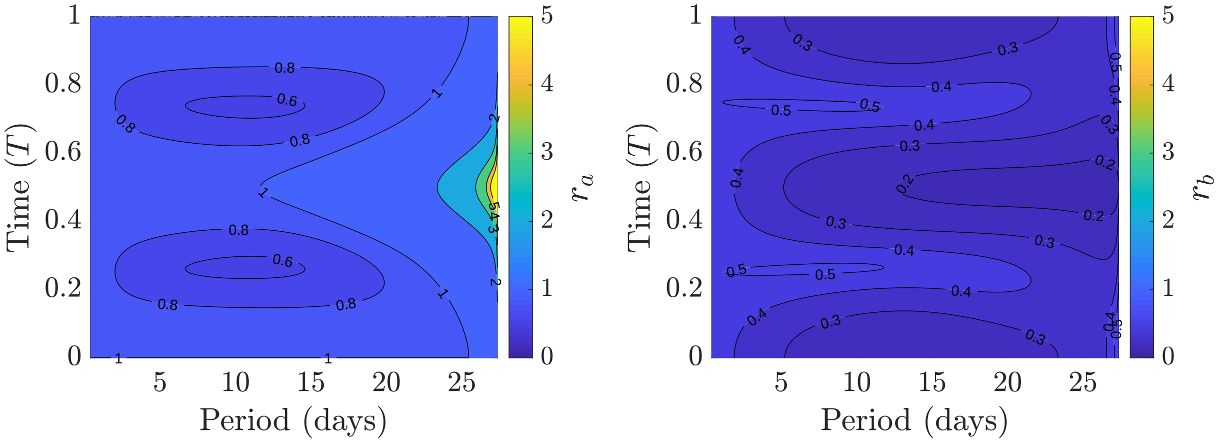

(a) Semi-major axis magnitude

(b) Semi-minor axis magnitude

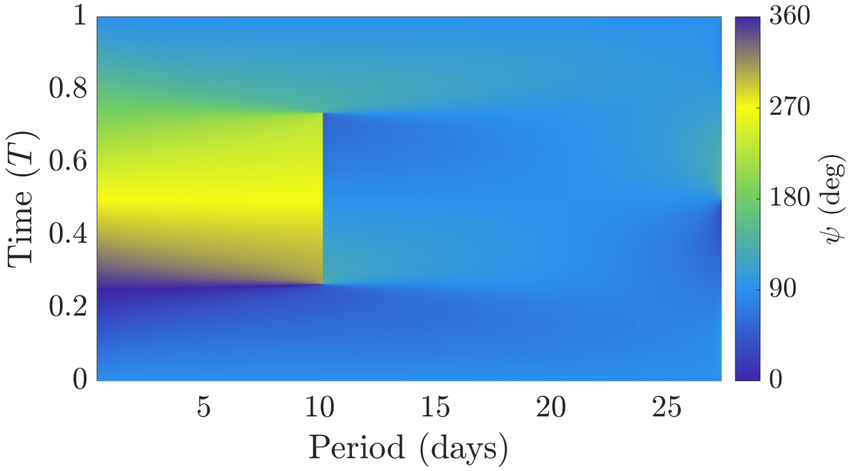

(c) Orientation with respect to the rotating frame

Figure 7.2: Description of the normalized first-order invariant curve relative to periodic orbits with oscillatory modes within the Earth-Moon DRO family.

At a DRO that possess an orbit period of approximately 10 days, at approximately $0.25T$ and $0.75T$ past the initial fixed point, the magnitudes of the semi-major and semi-minor axes of the approximated invariant curve are equal. As a result, the evolution of the orientation of the approximated curve has a discontinuity over this critical orbit. For orbits with a shorter period than this discontinuity, the orientation of the invariant curve is characterized by a full revolution of the semi-major axis about $\hat{\boldsymbol{z}}$, as indicated by the evolution of ψ. However, for DROs with a longer period, the semi-major axis does not make a full rotation about $\hat{\boldsymbol{z}}$ and instead oscillates near 90°.

To illustrate this discontinuity in the evolution of the orientation of the invariant curve across the Earth-Moon DRO family, two orbits on opposite sides of the discontinuity are compared. The angle, ψ, is computed over one revolution of a 9.5-day and 10.5-day DRO and plotted as a function of time, normalized by the orbit period, in Figure 7.3. Initially, the orientations of the two approximated invariant curves are similar, however, at approximately $0.25T$, the two time histories diverge. Thus, the orientation of the invariant curve is extremely sensitive to the exact orbit near this discontinuity. This is a direct result of the intersection between the magnitudes of the semi-major and semi-minor axes, at which point the approximated invariant curve becomes circular and the directions of the principal axes become undefined. Furthermore, numerical integration of the matrix differential equations written in Eq. 5.9 used to compute the principal semi-axes of the normalized invariant curve will fail. After this divergence, the invariant curve relative to the 9.5-day DRO performs a full revolution about $\hat{\boldsymbol{z}}$ while the orientation of invariant curve associated the 10.5-day DRO oscillates near $\psi = 90°$. Both orientations then re-converge after the location of the second intersection between the principal semi-axes magnitudes near $0.75T$ to complete the revolution similarly.

Despite the discontinuity in the invariant curve orientation across the family and different evolution of ψ over time, this analysis reflects the geometry of the invariant torus but not natural motion within the center eigenspace. In fact, the natural relative motion tracing an invariant torus near DROs that possess an orbit period close to this discontinuity is similar, and a discontinuity is not present in the evolution of the size and shape of the approximate invariant curve. However, this

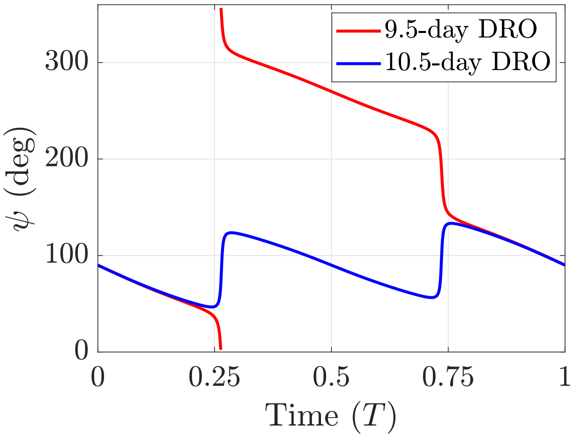

Figure 7.3: Orientation of the first-order invariant curve with respect to the rotating frame as a function of time for a 9.5-day and 10.5-day Earth-Moon DRO.

investigation highlights the complex evolution in invariant tori geometries relative to members of a single periodic orbit family. Studying the orientation of the approximated invariant curve supplies valuable insight into the minimum and maximum separation distances of the invariant curve from the associated periodic orbit.

7.1.2 Earth-Moon L_1 halo orbit family

The examined range of Earth-Moon L_1 halo orbit family is summarized in Figure 7.4. Because of the symmetry across the xy plane, this analysis is representative of both the northern and southern portions of the L_1 halo orbit family. For the purpose of illustration, only the southern portion of the family is visualized.

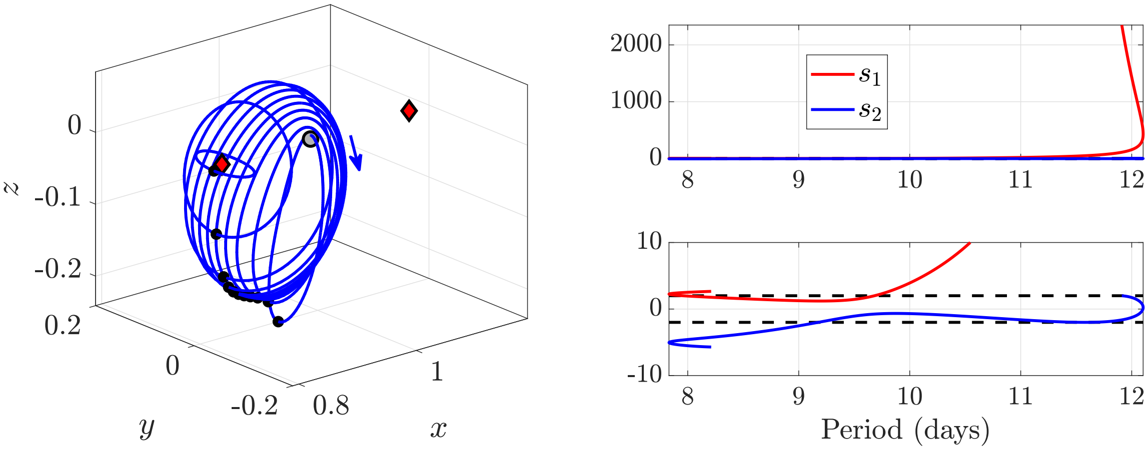

(a) Selected orbits in the rotating frame

(b) Stability indices

Figure 7.4: Selected orbits and stability indices computed for orbits within the examined range of the Earth-Moon L_1 halo orbit family.

The normalized size, shape, and orientation of the approximated invariant curve for motion exciting oscillatory modes corresponding to the s_1 index of the L_1 halo orbit family is summarized in Figure 7.5. This range includes the near-rectilinear members of the orbit family. Motion exciting oscillatory modes associated with the s_1 index is characterized by a large semi-major axis magnitude at perilune, at which the semi-major axis may possess a magnitude over 8 times greater than the semi-major axis magnitude at apolune. As a result, motion within the center eigenspace will experience significant and rapid expansion and contraction near perilune. When recovering similar relative motion into an ephemeris model, the sensitivity of motion near perilune may motivate specific investigation into the behavior between two spacecraft in these regimes. As the s_1 index approaches a value of 2 on either side of the examined range, the magnitude of the semi-minor

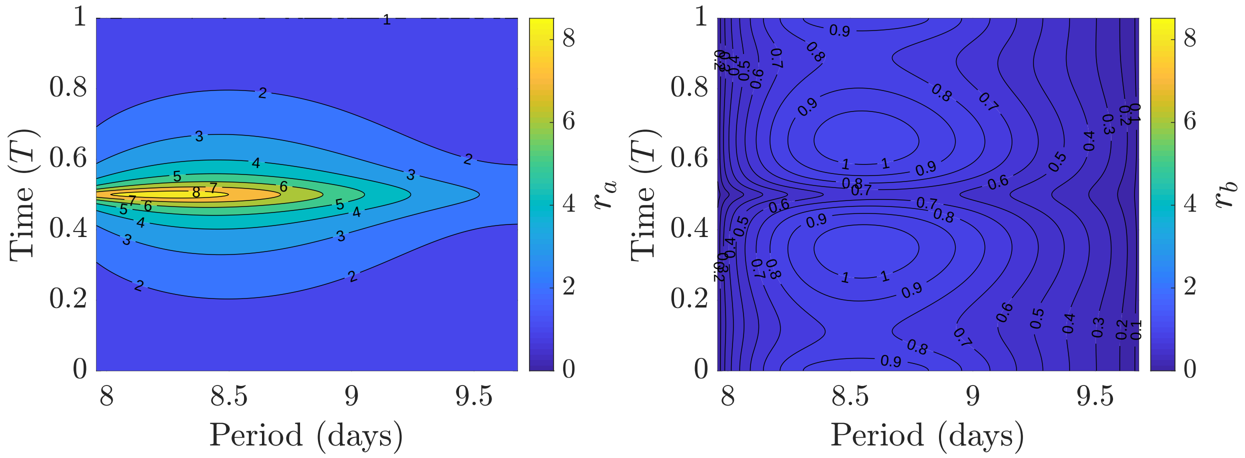

(a) Semi-major axis magnitude

(b) Semi-minor axis magnitude

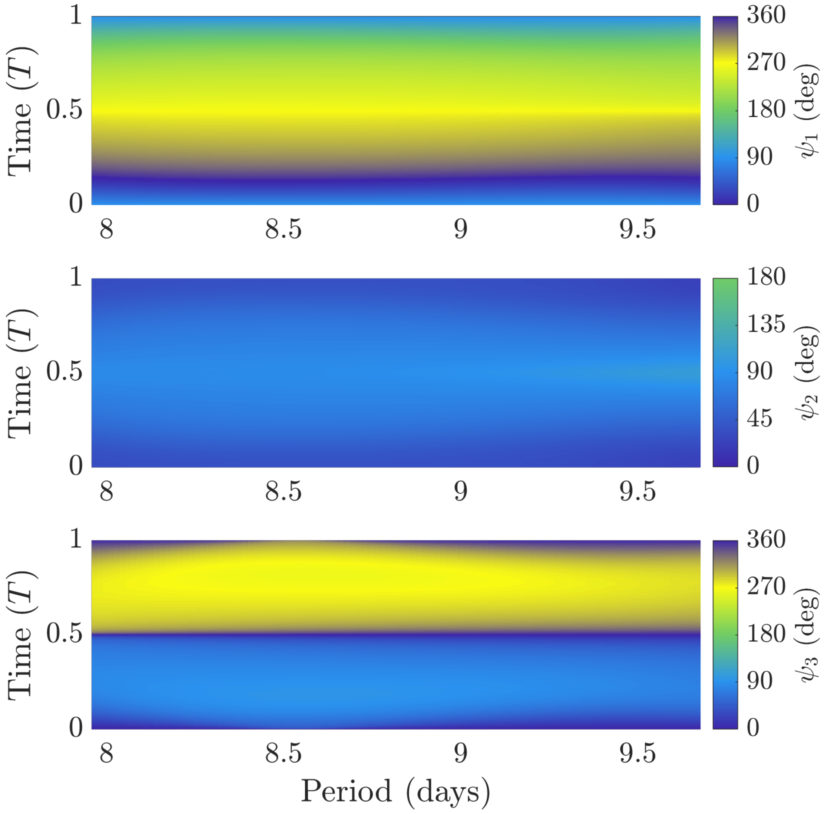

(c) Orientation with respect to the rotating frame

Figure 7.5: Description of the normalized invariant curve relative to periodic orbits with an oscillatory mode associated with s_1 within the Earth-Moon L_1 halo orbit family.

axis approaches zero. Consequently, halo orbits in these regions may be undesirable for locating a spacecraft formation leveraging the center eigenspace due to the significant contraction of the invariant curve. The orientation of the invariant curve relative to members of the orbit family is similar across this range and no discontinuities in the orientation are observed.

The normalized size, shape, and orientation of the approximated invariant curve for motion exciting oscillatory modes corresponding to the s_2 index of the orbit family is summarized in Figure 7.6. Since orbits characterized by orbit period across this range of the L_1 halo orbit family are non-unique, this subset of L_1 halo orbits are characterized via their apolune radius. Note that as apolune radius increases, orbital period generally decreases. A discontinuity is present in the data plotted in Figure 7.2 near an orbit that possess an apolune radius of approximately 3.3×10^5 km. This gap corresponds to where the value of s_2 index of the orbits possesses values near -2. In this region, motion corresponding to s_2 is nearly non-oscillatory, introducing numerical sensitivities in the computation of the first-order approximation of an invariant curve. This discontinuity is observed to separate regions of different characteristics of the approximated invariant curve relative to the associated periodic orbit.

Over the range of orbits with an apolune radius less than 3.3×10^5 km, a discontinuity is observed in the third Euler angle, ψ_3, at a halo orbit with a apolune of approximately 3.17×10^5 km. This discontinuity is caused by intersections of the semi-major and semi-minor axis magnitudes at two locations, similar to the example explored in the DRO family. For halo orbits with an apolune radius larger than 3.3×10^5 km, a complex evolution of the invariant curve geometry is observed. Several discontinuities exist in the description of the orientation of the invariant curve. Notably, a discontinuity is observed in all three Euler angles at an orbit with a apolune radius of approximately 3.42×10^5 km, at which point the invariant curve relative to apolune spans the yz plane of the rotating frame. Continuing along the family over this orbit, the discontinuity is caused by the normalization process applied to the complex eigenvector, which constrains $\hat{\boldsymbol{n}}^T \hat{\boldsymbol{z}} > 0$.

Three additional discontinuities are also observed in ψ_3, where the invariant curve becomes circular at perilune for orbits with an apolune radius of approximately 3.41×10^5 km, 3.42×10^5 km,

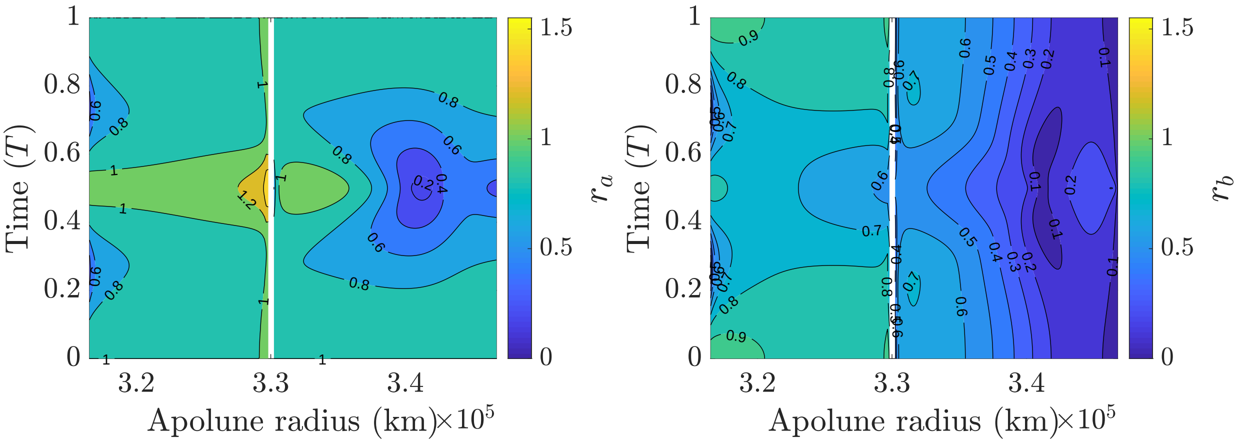

(a) Semi-major axis

(b) Semi-minor axis

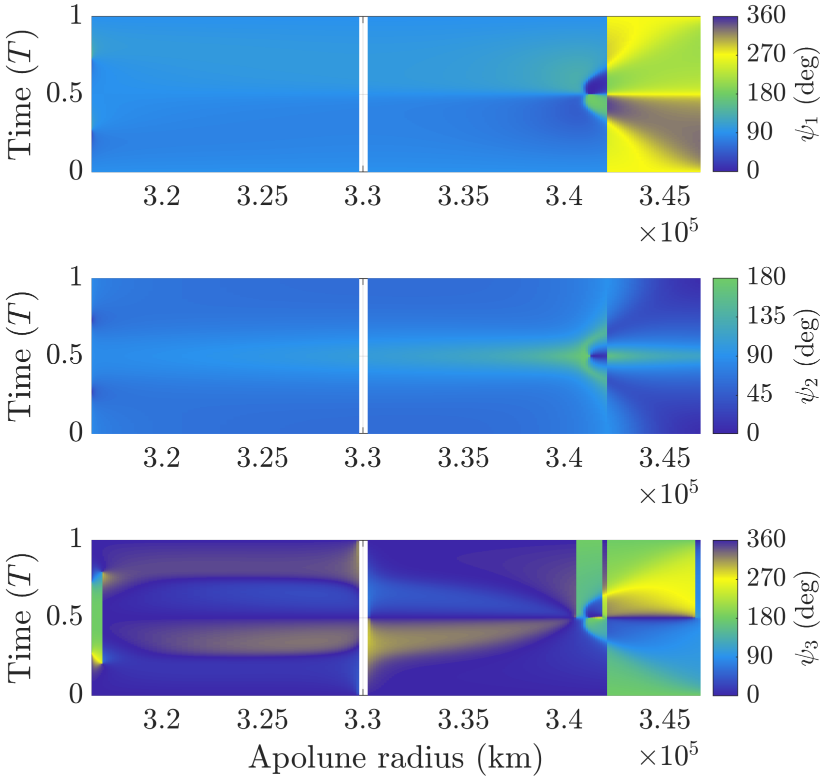

(c) Orientation with respect to the rotating frame

Figure 7.6: Description of the normalized invariant curve relative to periodic orbits with an oscillatory mode associated with s_2 within the Earth-Moon L_1 halo orbit family.

and 3.46×10^5 km. To visualize this phenomenon, consider the magnitude of the principal semi-axes of the approximated invariant curve relative to perilune, plotted as a function of apolune radius in Figure 7.7. The three intersections between the magnitude of the semi-major and semi-minor axes are visible as the magnitude of the semi-major axis appears to drop below the value of the semi-minor axis. However, due to their the definitions, the semi-major axis magnitude is always be greater than the semi-minor axis magnitude. Thus, the principal semi-axes magnitudes appear to switch at orbits where the two magnitudes intersect. These discontinuities separate regions of different periodicity in the orientation of the principal axes of the approximated invariant curve. For orbits with an apolune radius of between approximately 3.41×10^5 and 3.42×10^5 km and orbits with an apolune radius greater than 3.46×10^5 km, ψ_3 is periodic over $2T$. Elsewhere, ψ_3 is periodic over T. However, as generally observed, discontinuities in orientation due to an instantaneous circular invariant curve do not correspond to discontinuities in invariant curve size and shape. Because of the complex evolution of the size, shape, and orientation of the invariant curve with respect to the rotating frame in this region of the L_1 halo orbit family, formations leveraging the center eigenspace of orbits in this region may possess significantly different geometries despite being relative to nearby members of the same orbit family.

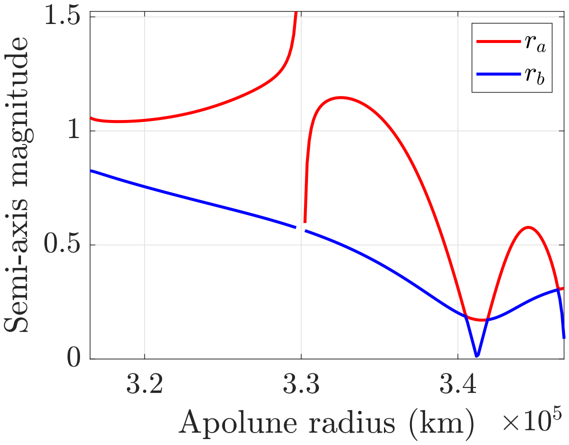

Figure 7.7: Magnitude of the semi-major and semi-minor axis of the normalized invariant curve relative to perilune of members of the Earth-Moon L_1 halo orbit family.

7.1.3 Earth-Moon L_2 halo orbit family

The examined range of Earth-Moon L_2 halo orbit family is summarized in Figure 7.8. Because of the symmetry across the xy plane, this analysis is representative of both the northern and southern portions of the L_2 halo orbit family.

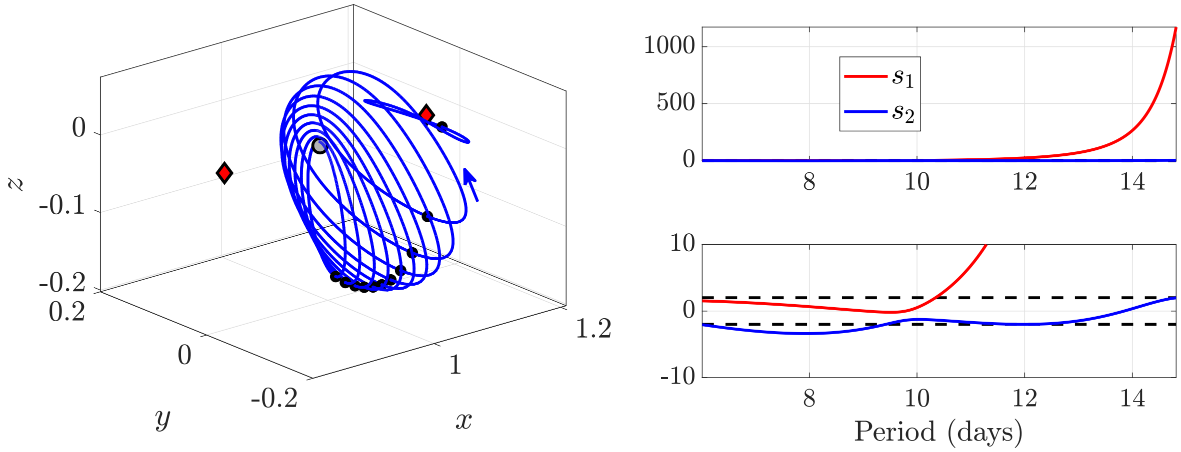

(a) Selected orbits in the rotating frame

(b) Stability indices

Figure 7.8: Selected orbits and stability indices computed for orbits within the examined range of the Earth-Moon L_2 halo orbit family.

The normalized size, shape, and orientation of the approximated invariant curve for motion exciting oscillatory modes corresponding to the s_1 index of the L_2 halo orbit family is summarized in Figure 7.9. Similar to the L_1 halo orbit family, this range includes NRHOs and oscillatory motion corresponding in this region is characterized by a large magnitude of the semi-major axis at perilune. A non-smooth evolution in the magnitude of the principal semi-axes and ψ_3 exists at an orbit with a period of approximately 9.6 days, caused by an intersection between the principal semi-axes magnitudes at the initial fixed point. Continuing over this orbit in either direction, the direction of the semi-major and semi-minor axes of the invariant curve relative to apolune switch. As a result of the normalization process for the complex eigenvector, this switch produces the non-smooth evolution in the parameterization of the invariant curve. Furthermore, a discontinuity is observed for all three Euler angles at an orbit with a period of approximately 9.05 days. At

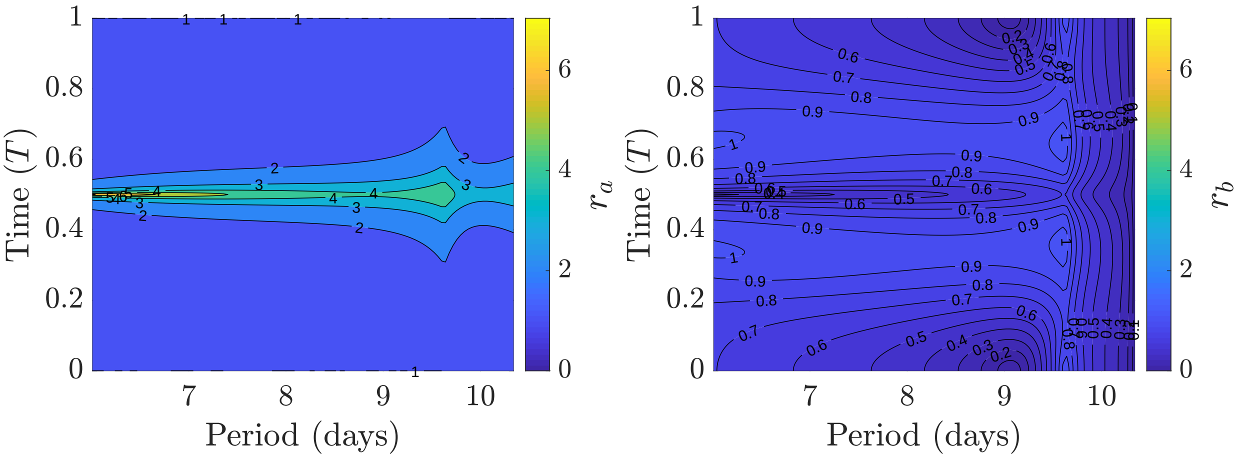

(a) Semi-major axis magnitude

(b) Semi-minor axis magnitude

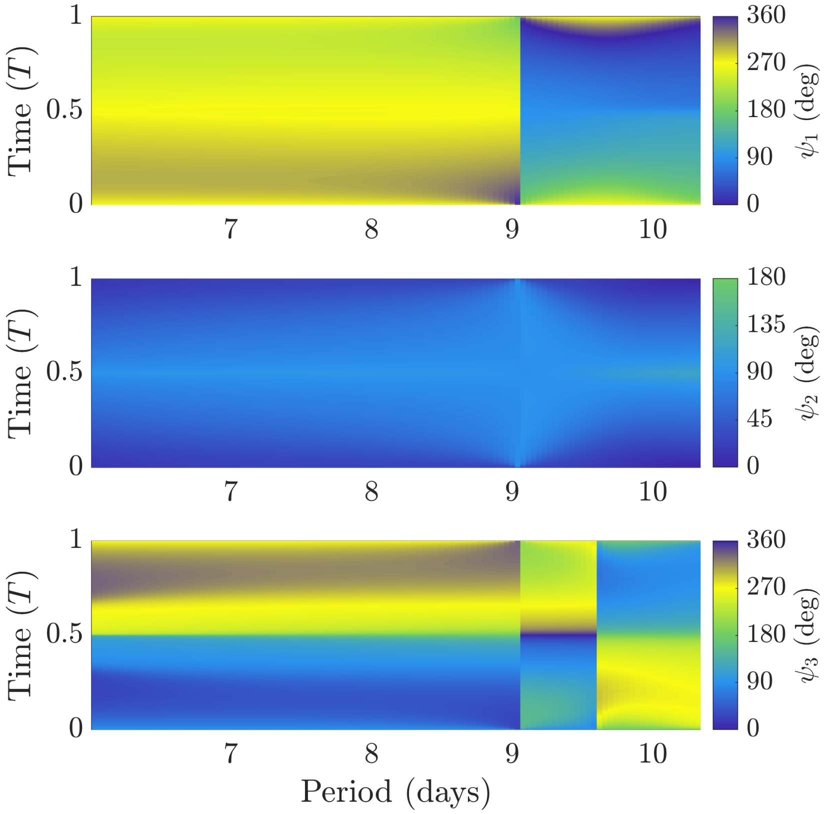

(c) Orientation with respect to the rotating frame

Figure 7.9: Description of the normalized invariant curve relative to periodic orbits with an oscillatory mode associated with s_1 within the Earth-Moon L_2 halo orbit family.

this orbit, the magnitude of the semi-major axis of the invariant curve relative to apolune is equal to zero. Accordingly, halo orbits near this orbit may be undesirable for locating a formation of spacecraft leveraging the center eigenspace due to collision risks between spacecraft on the torus and the periodic orbit.

The normalized size, shape, and orientation of the approximated invariant curve for motion exciting oscillatory modes corresponding to the s_2 index of the orbit family is summarized in Figure 7.10. Similar characteristics are shared between oscillatory motion across this range and oscillatory motion corresponding to the s_2 index of the Earth-Moon L_1 halo orbit family. Most notably, a discontinuity in the data exist near L_2 halo orbits that possesses a period of approximately 12 days, where the s_2 index possess a value near -2. For orbits with a period greater than 12 days, a single discontinuity is observed at an orbit with a period of approximately 14.7 days, where the approximated invariant curve becomes circular. For orbits with a period of less than 12 days, a discontinuity in all three Euler angles exists at an orbit with a period of approximately 9.85 days, caused by the normalization scheme. Two discontinuities also exist in ψ_3 caused by an instantaneously circular invariant curve becomes relative to perilune. These discontinuities separate regions of halo orbits that admit invariant curves where ψ_3 is periodic over $2T$, in this case between orbits with periods of approximately 10.05 and 10.2 days. However, at these discontinuities, the evolution of the size and shape of the invariant curve is smooth, and the natural relative motion of spacecraft within the center eigenspace of orbits near these discontinuities would be similar.

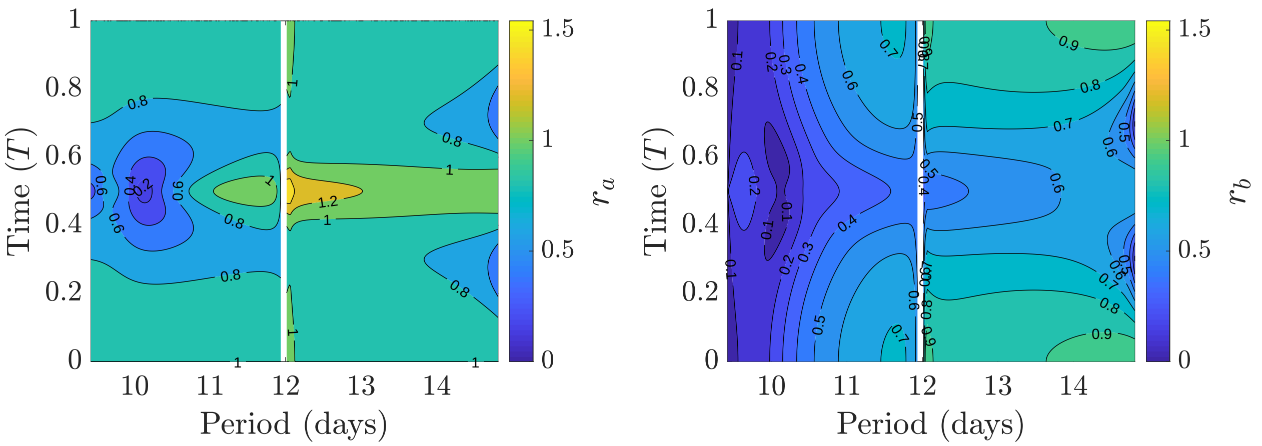

(a) Semi-major axis magnitude

(b) Semi-minor axis magnitude

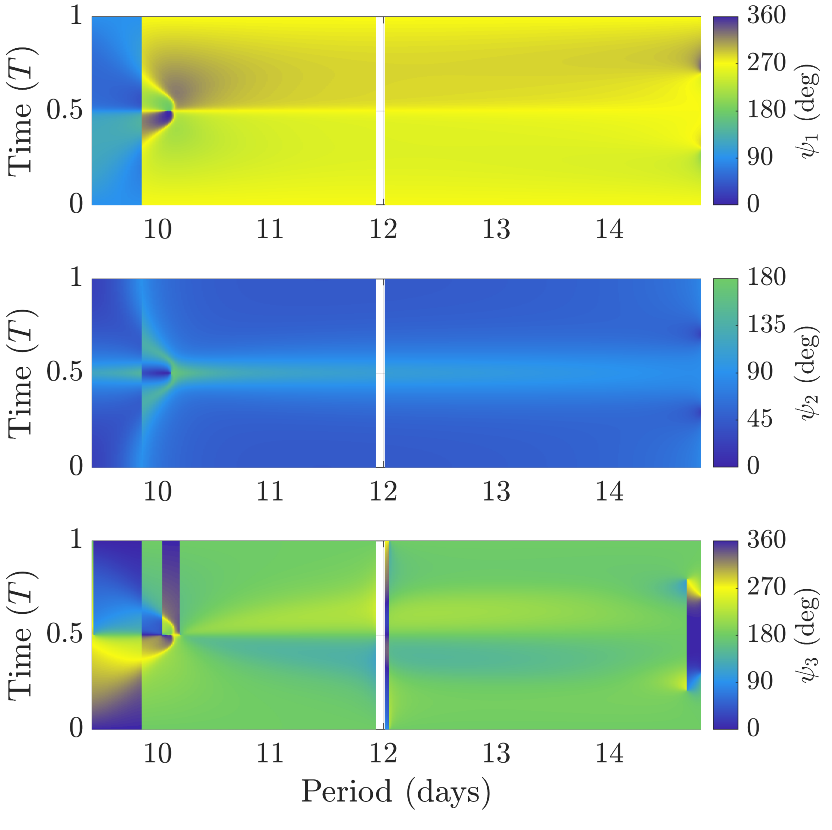

(c) Orientation with respect to the rotating frame

Figure 7.10: Description of the normalized invariant curve relative to periodic orbits with an oscillatory mode associated with s_2 within the Earth-Moon L_2 halo orbit family.

7.1.4 Earth-Moon L_1 vertical orbit family

Selected orbits and the stability indices computed for members within the examined range of the Earth-Moon L_1 vertical orbit family are plotted in Figure 7.11. Over the examined range of orbits, spatial oscillatory relative motion is admitted by modes corresponding to the s_2 index.

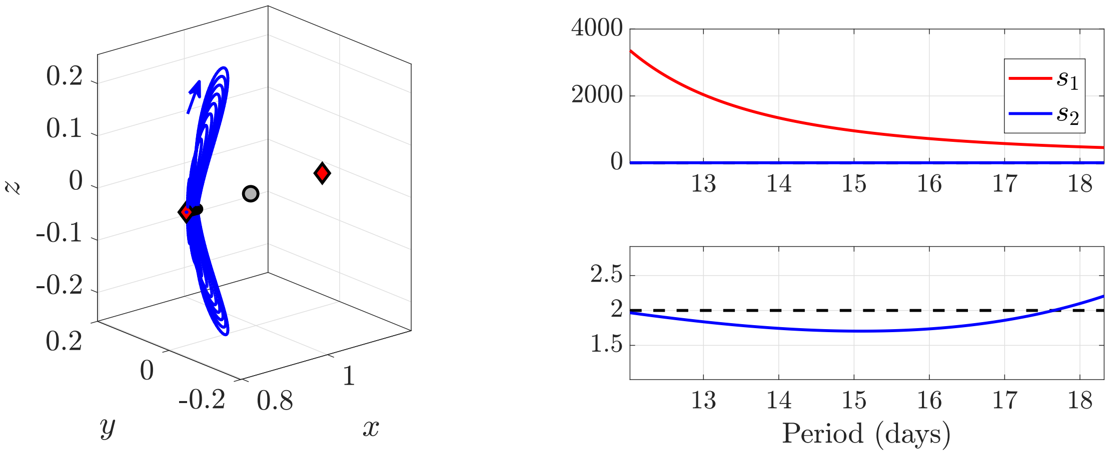

(a) Selected orbits in the rotating frame

(b) Stability indices

Figure 7.11: Selected orbits and stability indices computed for orbits within the examined range of the Earth-Moon L_1 vertical orbit family.

The normalized size, shape, and orientation of the approximated invariant curve for motion exciting oscillatory modes corresponding to the s_2 index of the orbit family is plotted in Figure 7.12. Across this examined range, the maximum magnitude of the semi-major axis is observed at the northern and southern-most points of each orbit, i.e., at times past the initial fixed point of approximately $0.25T$ and $0.75T$. In this orbit family, a single non-smooth evolution in the magnitude of the principal semi-axes and the orientation of the invariant curve exists near an orbit with a period of approximately 13.8 days. This discontinuity is a result of a circular first-order invariant curve relative to the initial fixed point, such that continuing along the family over this orbit, the direction of the principal axes of the invariant curve switch.

As the s_2 index approaches 2 on either side of the examined range of orbits, the magnitude of the semi-minor axis over time approaches zero. This indicates that motion within the center

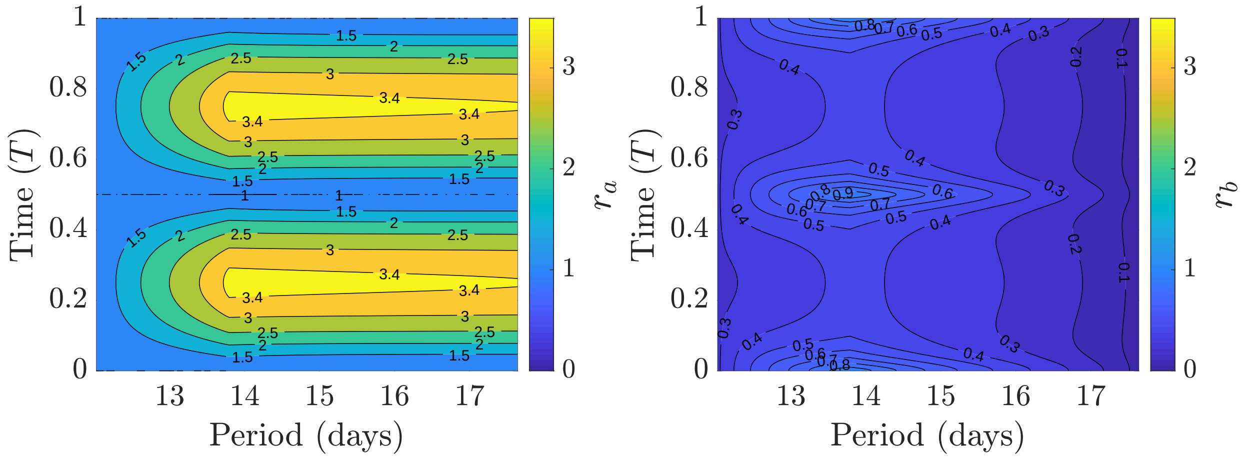

(a) Semi-major axis magnitude

(b) Semi-minor axis magnitude

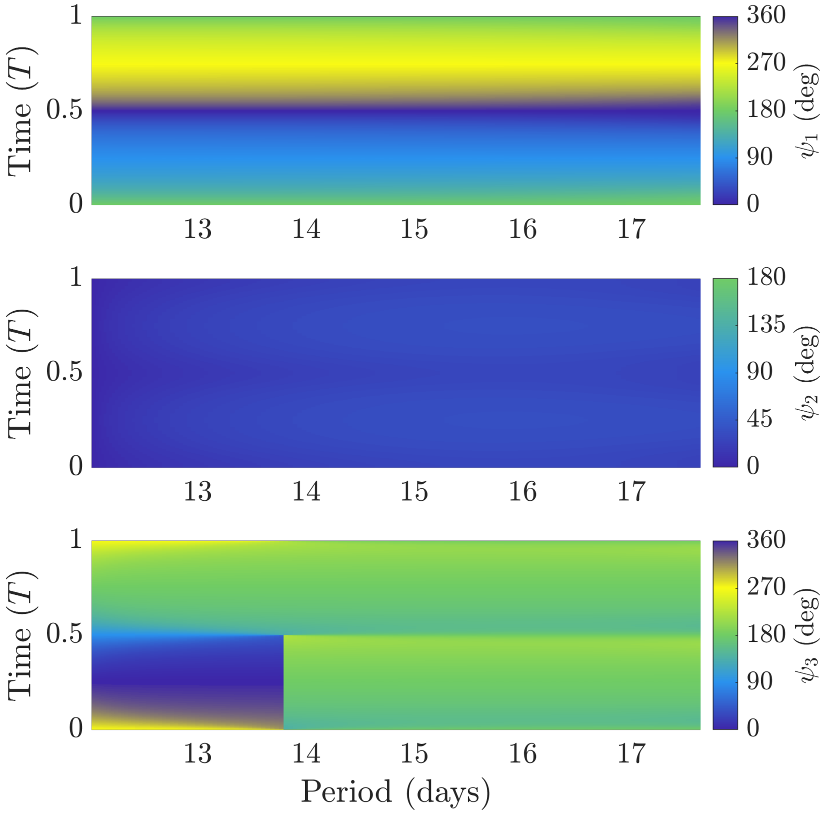

(c) Orientation with respect to the rotating frame

Figure 7.12: Description of the normalized first-order invariant curve relative to periodic orbits with oscillatory modes within the Earth-Moon L_1 vertical orbit family.

eigenspace of L_1 vertical orbits with either very low out-of-plane amplitude or very large out-of-plane amplitude will experience significant contraction towards the associated periodic orbit along the minor axis of the elliptical approximation, without significant contraction along the major axis. To investigate an example, consider first-order oscillatory motion relative to a 17.5-day L_1 vertical orbit, near the upper range of L_1 vertical orbits that admits oscillatory motion. Several discrete trajectories on the normalized invariant curve are plotted as a function of time in Figure 7.13 in black, along with the magnitudes of the semi-major and semi-minor axes in red and blue, respectively. The magnitude of the semi-minor axis varies much less than the semi-major axis and over time, and lies near zero over the entire revolution. Accordingly, the separation distance of motion near the minor axis of the ellipse is much smaller than motion near the major axis, introducing possible collision risks for spacecraft located within the center eigenspace.

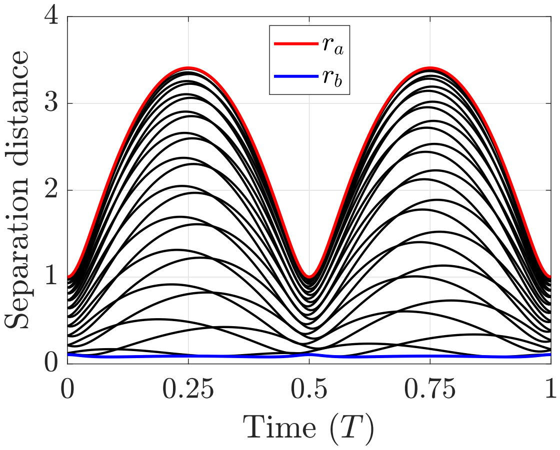

Figure 7.13: Separation distance of motion on the normalized invariant curve measured from a 17.5-day Earth-Moon L_1 vertical orbit.

Furthermore, due to the large magnitude of the unstable eigenvalue possessed by members in the examined range, motion initialized within the center eigenspace of a vertical orbit may quickly depart the vicinity of the orbit. This behavior is exhibit by motion initialized within the center eigenspaces of Earth-Moon L_2 halo orbits with large unstable eigenvalues, examined in Section 4.4.4. This rapid departure may motivate additional analysis for formations leveraging the center eigenspace of L_1 vertical orbits near in an ephemeris model.

7.1.5 Earth-Moon L_2 vertical orbit family

Selected orbits and the stability indices of members within the examined range of the Earth-Moon L_2 vertical orbit family are plotted in Figure 7.14. Over this range, spatial oscillatory motion is admitted by modes corresponding to the s_2 stability index.

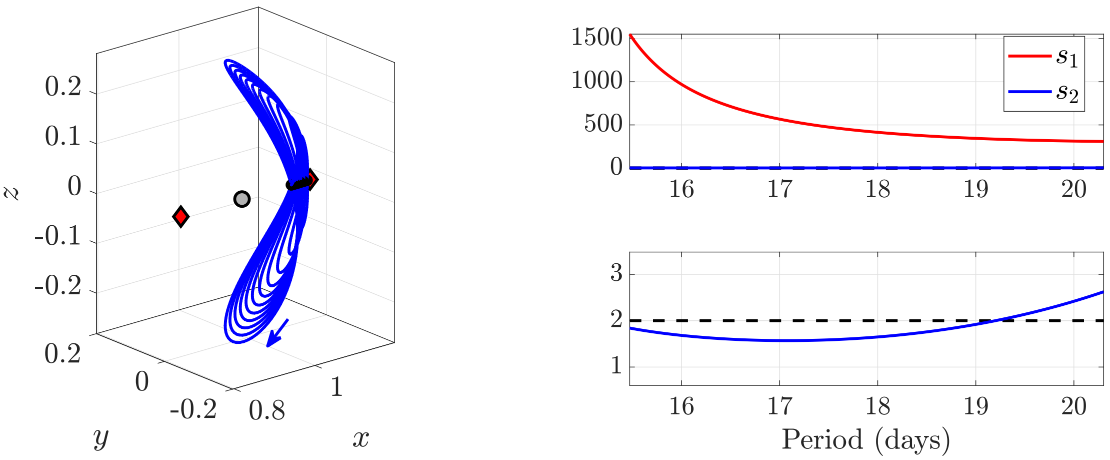

(a) Selected orbits in the rotating frame

(b) Stability indices

Figure 7.14: Selected orbits and stability indices computed for orbits within the examined range of the Earth-Moon L_2 vertical orbit family.

The normalized size, shape, and orientation of the approximated invariant curve for motion exciting oscillatory modes corresponding to the s_2 index of the orbit family is plotted in Figure 7.15. Similar trends are observed between oscillatory motion relative to members in the Earth-Moon L_1 and L_2 vertical orbit families, including the maximum magnitude of the semi-major axis occurring relative to the northern and southernmost points of each orbit. However, compared to the L_1 vertical orbit family, the maximum value of the semi-major axis in the L_2 vertical orbit family is slightly smaller. The family possesses a single discontinuity in the magnitude of the principal semi-axes and ψ_3 at an orbit with a period of approximately 16.25 days due to the switching of the direction of the principal axes at the initial fixed point. Additionally, L_2 vertical orbits also possess unstable eigenvalues with large magnitudes, possibly indicating challenges for maintaining bounded motion near trajectories resembling L_2 vertical orbits in an ephemeris model.

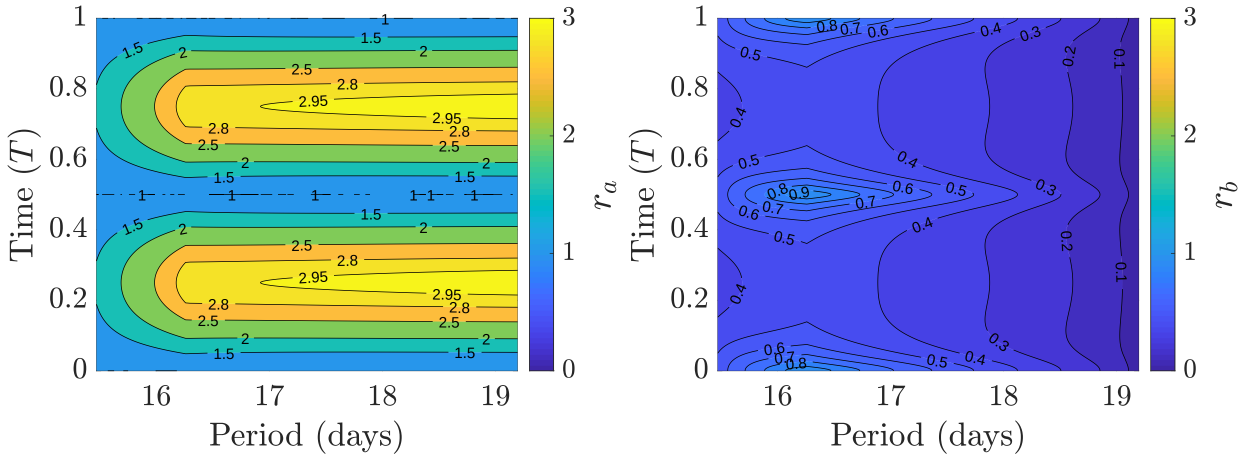

(a) Semi-major axis magnitude

(b) Semi-minor axis magnitude

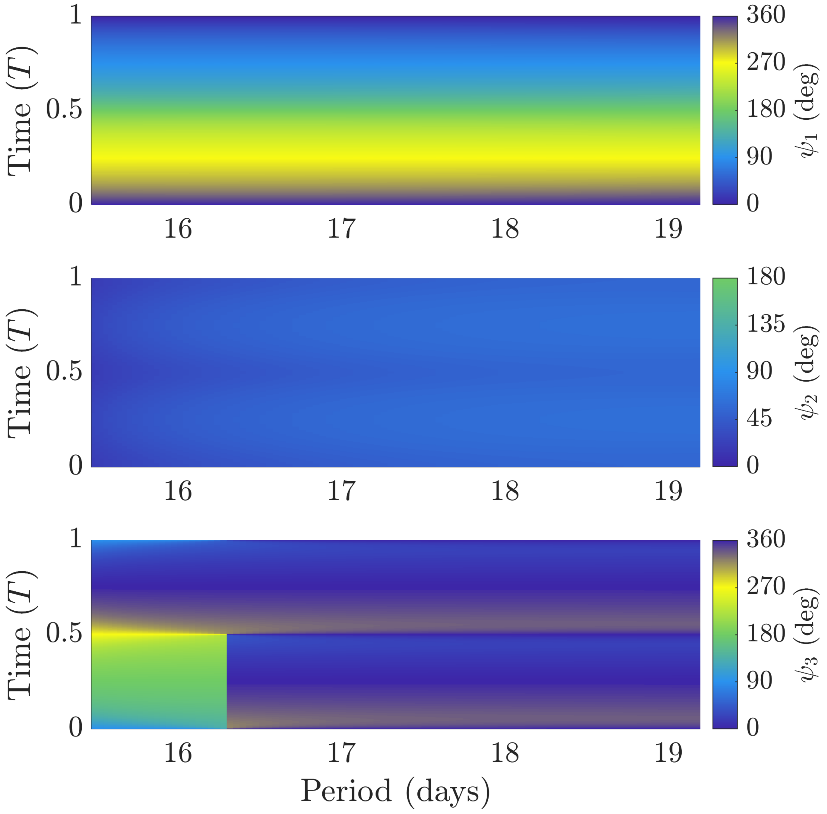

(c) Orientation with respect to the rotating frame

Figure 7.15: Description of the normalized first-order invariant curve relative to periodic orbits with oscillatory modes within the Earth-Moon L_2 vertical orbit family.

7.1.6 Earth-Moon L_4 short period family

Selected orbits and stability indices computed for members within the examined range of the Earth-Moon L_4 short period family are plotted in Figure 7.16. Over the examined range, in-plane oscillatory motion is admitted by modes corresponding to s_2.

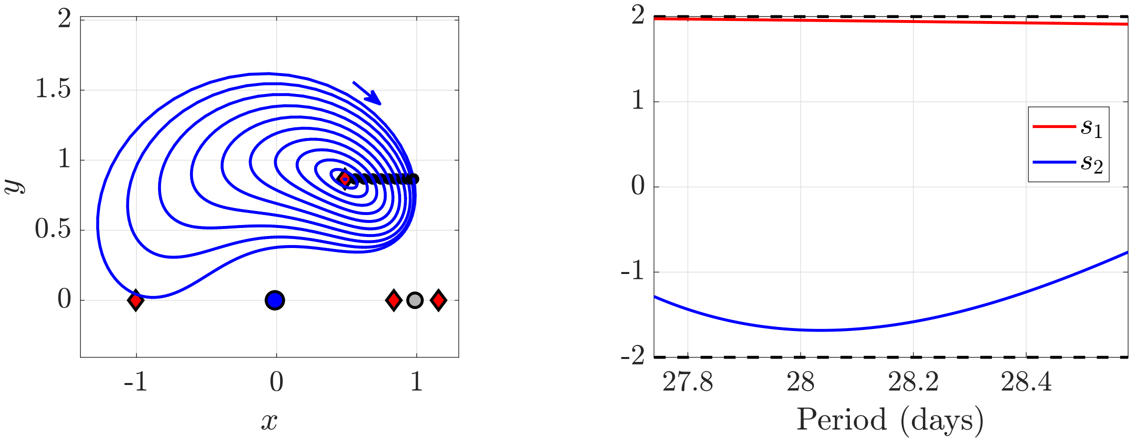

(a) Selected orbits in the rotating frame (b) Stability indices

Figure 7.16: Selected orbits and stability indices computed for orbits within the examined range of the Earth-Moon L_4 short period family.

The normalized size, shape, and orientation of the approximated invariant curve relative to members of the examined range of the L_4 short period family are plotted in Figure 7.17. In general, short period orbits with a shorter orbit period, i.e., that lie closer to L_4, exhibit a larger maximum semi-major axis than orbits with a larger period. Furthermore, the magnitude of the semi-minor axis is generally much smaller than the magnitude of the semi-major axis. Over the orbit family, the magnitudes of the principal semi-axes intersect at a single point, causing a discontinuity in the evolution of ψ. For orbits with a period of less than this discontinuity, the invariant curve revolves 180° about $\hat{\boldsymbol{z}}$ each period, while for orbits greater than this discontinuity ψ periodically oscillates over T. However, recall that this discontinuity reflects the geometry of the approximated invariant torus, and that the natural relative motion of spacecraft within the center eigenspace is similar across this discontinuity.

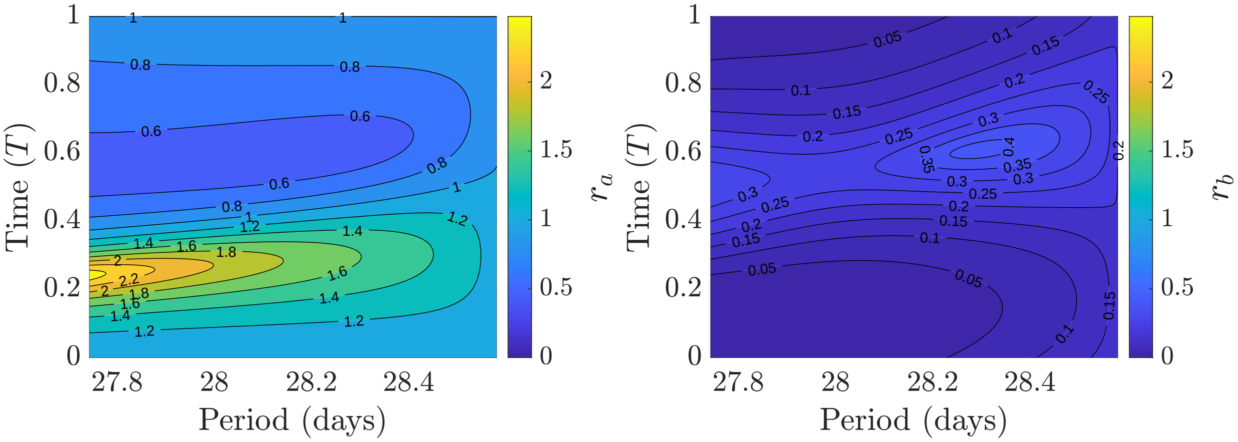

(a) Semi-major axis magnitude

(b) Semi-minor axis magnitude

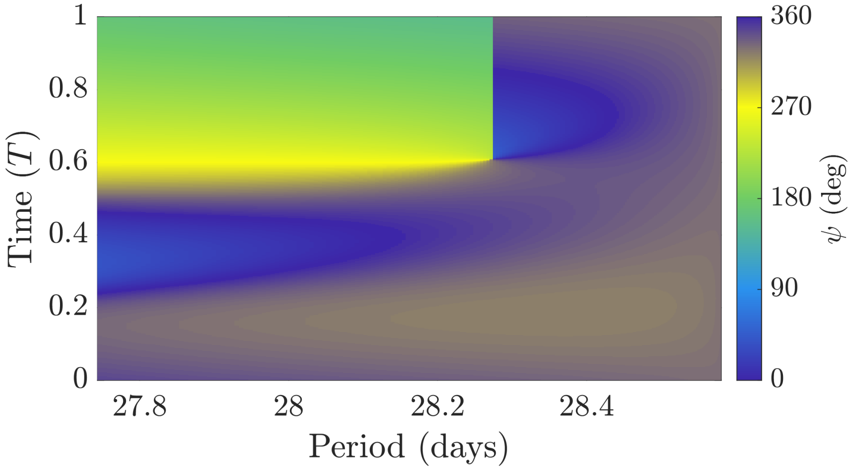

(c) Orientation with respect to the rotating frame

Figure 7.17: Description of the normalized first-order invariant curve relative to periodic orbits with oscillatory modes within the Earth-Moon L_4 short period family.

7.1.7 Earth-Moon L_5 short period family

Selected members and stability indices of orbits within the examined range of the Earth-Moon L_5 short period family are plotted in Figure 7.18. Over the examined range, in-plane oscillatory motion is admitted by modes corresponding to s_2.

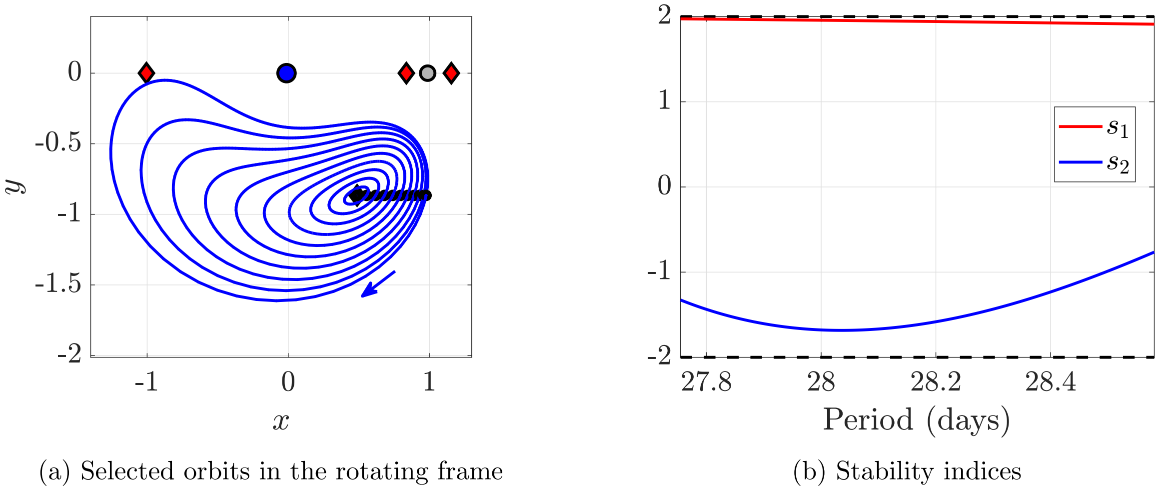

(a) Selected orbits in the rotating frame

(b) Stability indices

Figure 7.18: Selected orbits and stability indices computed for orbits within the examined range of the Earth-Moon L_5 short period family.

The normalized size, shape, and orientation of the approximated invariant curve relative to members of the examined range of the L_5 short period family are plotted in Figure 7.19. Similar to the L_4 short period orbit family, the maximum magnitude of the semi-major axis of the invariant curve is greater for orbits that lie closer to L_5, and the magnitude of the semi-minor axis is generally much smaller than magnitude of the semi-major axis. Furthermore, the magnitudes of the principal semi-axes intersect at an orbit with a period of approximately 28.3 days, causing a discontinuity in the orientation of the invariant curve and separating regions of different periodicity in the orientation of the invariant curve. While the periodicity of the principal axes has no significant impact on the relative motion with the center eigenspace, the description of the orientation supplies valuable insight into the directions of the maximum and minimum separation distances of an invariant curve from the associated periodic orbit.

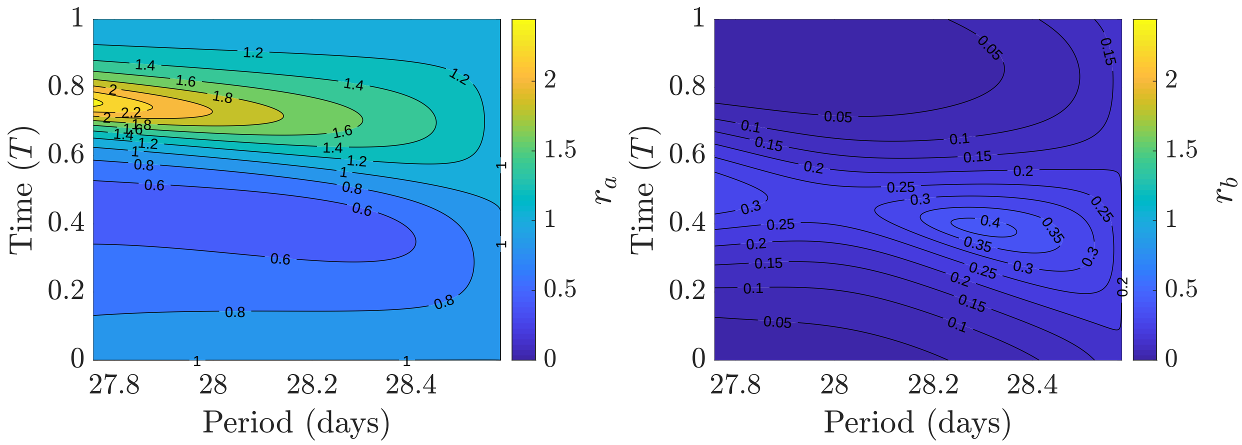

(a) Semi-major axis magnitude

(b) Semi-minor axis magnitude

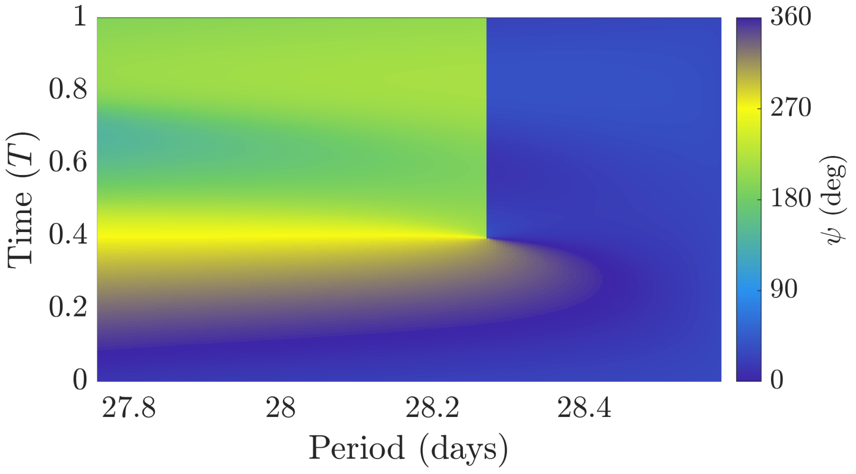

(c) Orientation with respect to the rotating frame

Figure 7.19: Description of the normalized first-order invariant curve relative to periodic orbits with oscillatory modes within the Earth-Moon L_5 short period family.

7.1.8 Earth-Moon 2:1 resonant orbit family

Selected members of the Earth-Moon 2:1 resonant orbit family and the stability of orbits across the examined range of the family are plotted in Figure 7.20. The family admits in-plane oscillatory motion associated with the s_2 index.

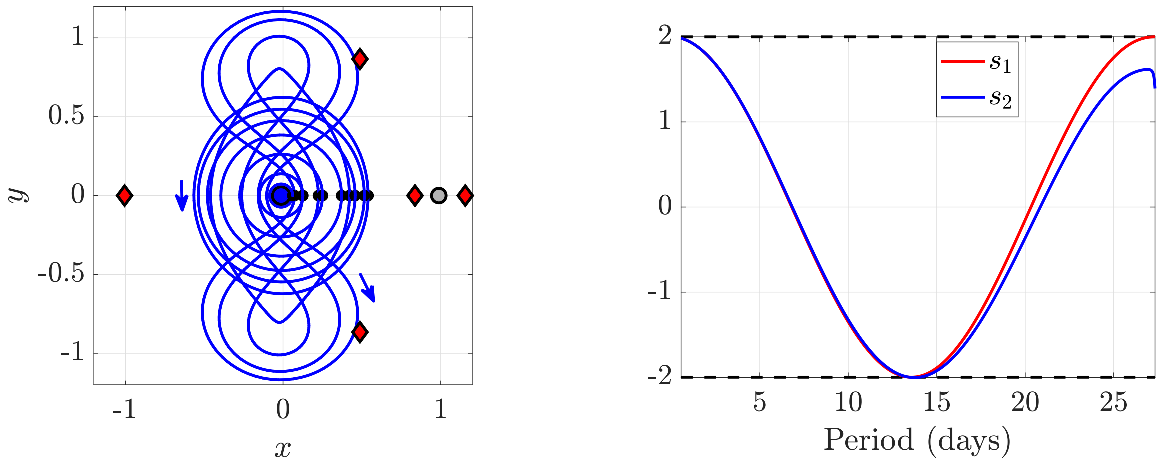

(a) Selected orbits in the rotating frame

(b) Stability indices

Figure 7.20: Selected orbits and stability indices compute for orbits within the examined range of the Earth-Moon 2:1 resonant orbit family.

The normalized size, shape, and orientation of the approximated invariant curve relative to members of the 2:1 resonant orbit family is plotted in Figure 7.21. The geometry of the invariant curve relative to members of this family admits a very complex variety of characteristics, with several distinct regions of behavior. First, consider 2:1 resonant orbits with the shortest orbit periods, which are nearly-circular about the Earth. Similar to members of the DRO family, in this region, an approximate 2:1 ratio of semi-major to semi-minor axis magnitude is observed, which may share similarities with bounded relative motion in two-body environments. As orbit period increases along the family, a discontinuity in all data exists at an orbit with a period of approximately 14 days, caused by sensitivities within the computation of the complex eigenvector for orbits that possess values of s_2 near -2. As observed with other families, this type of discontinuity separates regions of different characteristics within the center eigenspaces of orbits in the same family.

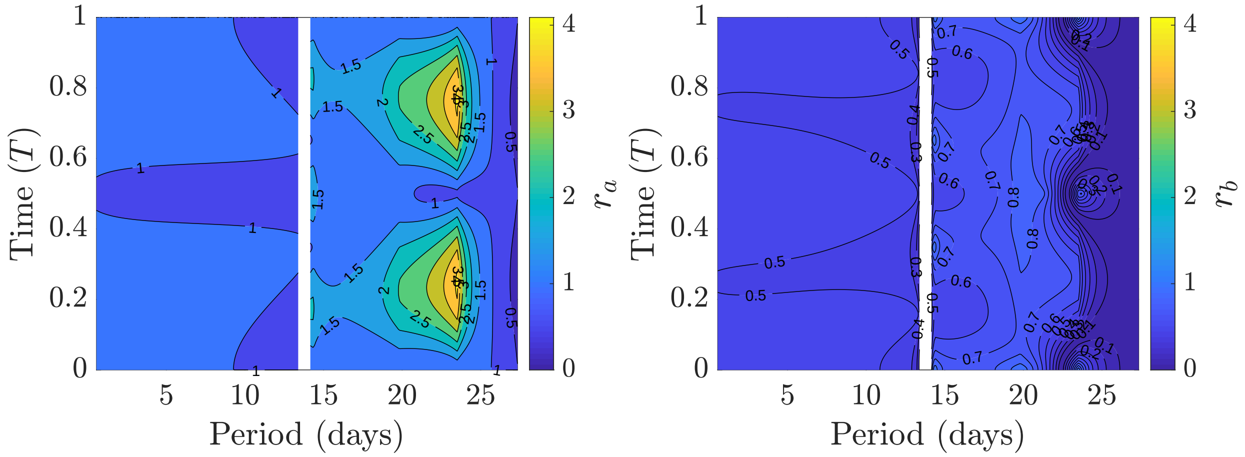

(a) Semi-major axis

(b) Semi-minor axis

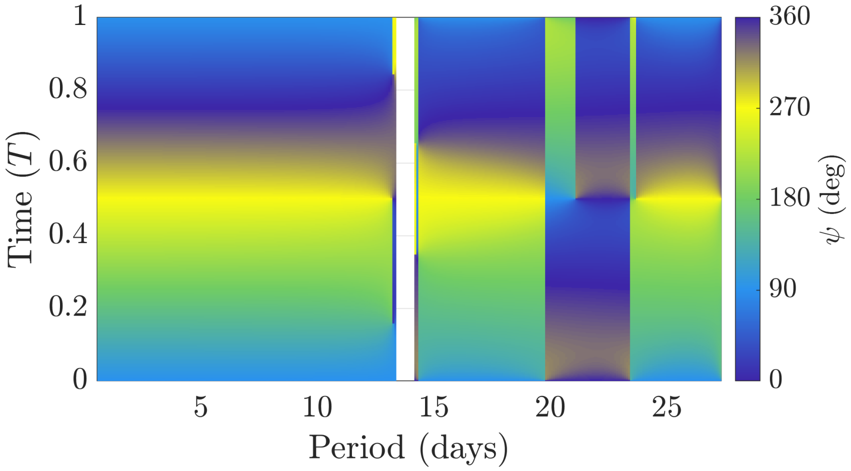

(c) Orientation with respect to the rotating frame

Figure 7.21: Description of the normalized first-order invariant curve relative to periodic orbits with oscillatory modes within the Earth-Moon 2:1 resonant orbit family.

For 2:1 resonant orbits with an orbit period greater than this discontinuity, multiple non-smooth transitions are observed. Discontinuities in the evolution of both the magnitudes of the principal axes and the orientation exist at orbits with periods of approximately 19.8 and 23.5 days caused by a circular approximated invariant curve relative to the initial fixed point, at which the direction of the principal axes switch. Furthermore, at orbits with periods of approximately 21.1 and 23.7 days, the magnitudes of the principal axes intersect after half a revolution, causing a discontinuity in time histories of ψ. These discontinuities bound ranges of 2:1 resonant orbits where the orientation of the invariant curve is periodic over $2T$, exhibited by orbits with a period of between approximately 19.8 and 21.1 days and orbits with a period greater than 23.7 days. The complex evolution of invariant curve geometries relative to members of this family, exhibit by both the size and shape of the approximate invariant curve its orientation, illustrates how insight into the in-plane oscillatory relative motion about one 2:1 resonant orbit may not translate well to another member of the same family. However, this analysis supplies a preliminary understanding of the geometry of formations leveraging the center eigenspace of a periodic orbit across different regions of this complex periodic orbit family.

For 2:1 resonant orbits with a period greater than approximately 22.5 days, the semi-minor axis of the invariant curve reaches one or motion instances of zero magnitude, indicating that the oscillatory relative motion is rectilinear in the configuration space. This occurrence causes the differential equations used to compute the principal semi-axes over time to fail. In these cases, the size of the invariant curve is calculated at discrete fixed points along the periodic orbit to construct the data shown in Figure 7.21. To illustrate an example of this occurrence, the magnitude of the principal semi-axes of the invariant curve relative to a 2:1 resonant orbit with a period of 26 days is plotted as a function of time in Figure 7.22. For this orbit, the magnitude of the semi-minor axis is observed to equal zero at four locations. At these locations, the first-order approximation of the invariant 2-torus associated with the oscillatory mode intersects the periodic orbit in the configuration space. This intersection may be undesirable for a constellation of spacecraft due to potential for collision between spacecraft on the periodic orbit or on the torus. However, this intersection of the invariant torus with the periodic orbit may also be exploited to determine a single impulsive maneuver required to transition a spacecraft from a periodic orbit to a quasi-periodic orbit. Unlike the other orbit families examined, where the semi-minor axis magnitude may equal zero at a distinct fixed point across the orbit family, this behavior is observed over a range of 2:1 resonant orbits and may occur multiple time per revolution.

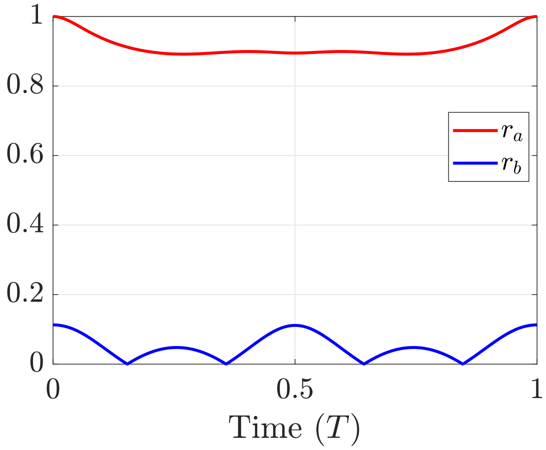

Figure 7.22: Magnitude of the principal semi-axes of the normalized invariant curve relative to an Earth-Moon 2:1 resonant orbit with a period of 26 days.

7.2 Sun-Earth periodic orbit families

First-order oscillatory motion relative to members of periodic orbits in several periodic orbit families in the Sun-Earth system is examined. The periodic orbit families in the Sun-Earth system explored include: the L_1 halo orbit family, the L_2 halo orbit family, the L_4 short period family, and the L_5 short period family. These families are not the only families that possess members that admit oscillatory motion in the Sun-Earth system, however, they include periodic orbits of interest due to their close proximity to the Earth or potential for scientific observations. The stability indices that are associated with oscillatory motion examined in this investigation and the initial fixed point of each orbit are summarized in Table 7.2. For each family explored, the same figures generated for the Earth-Moon periodic orbit families are generated and discussed.

Table 7.2: Summary of explored periodic orbit families in the Sun-Earth system.

Orbit family	s_1	s_2	Initial fixed point
L_1 southern halo	yes	yes	$y = 0, z < 0$
L_2 southern halo	yes	yes	$y = 0, z < 0$
L_4 short period	no	yes	$y = \sqrt{3}/2,\ x > x_{L4}$
L_5 short period	no	yes	$y = -\sqrt{3}/2,\ x > x_{L5}$

7.2.1 Sun-Earth L_1 halo orbit family

Selected members of the Sun-Earth L_1 southern halo orbit family and the stability of orbits across the examined range of the family are plotted in Figure 7.23. Because of the symmetry of the orbit family across the xy plane, the data in this analysis is representative of both the northern and southern portions of the L_1 halo orbit family. The data generated in this section is applied in Chapter 8 within the trajectory design of a conceptual constellation near a Sun-Earth L_1 southern halo orbit, demonstrating an application of the presented analysis to the trajectory design of a spacecraft formation within a multi-body environment.

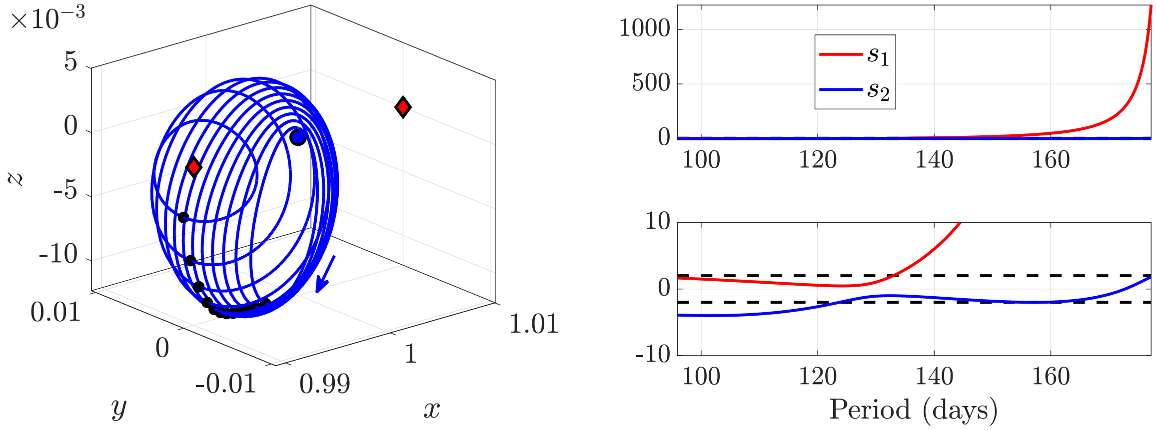

(a) Selected orbits in the rotating frame

(b) Stability indices

Figure 7.23: Selected orbits and stability indices computed over the examined range of the Sun-Earth L_1 halo orbit family.

The normalized size, shape, and orientation of the approximated invariant curve for motion exciting oscillatory modes corresponding to the s_1 index of the Sun-Earth L_1 halo orbit family is plotted in Figure 7.24. In general, the trends of the examined motion is similar to the relative motion near the same family in the Earth-Moon system. The invariant curve is circular relative to the initial fixed point of an orbit with a period of approximately 124 days causing a non-smooth evolution in the magnitudes of the principal axes and ψ_3 due to the normalization scheme. Additionally, at an orbit with a period of approximately 110 days, the magnitude of the semi-minor

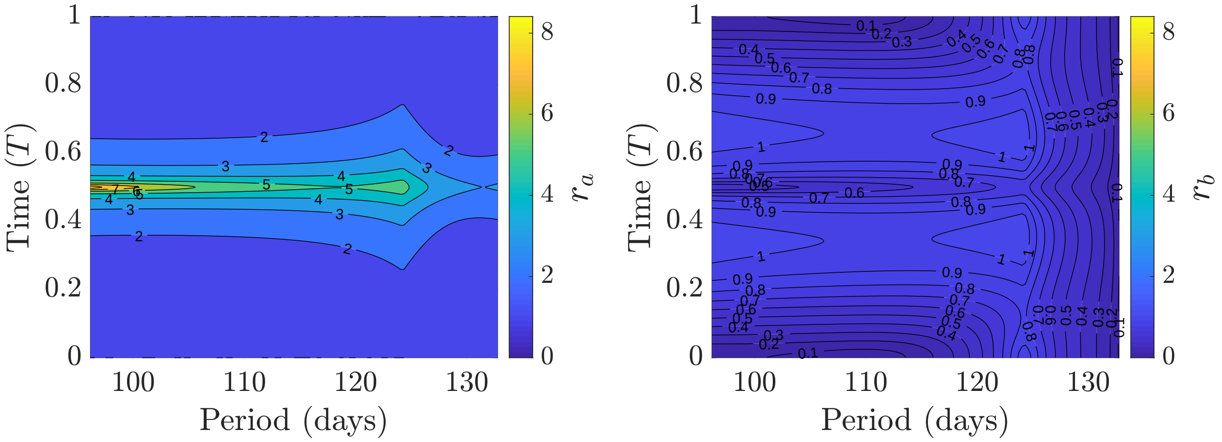

(a) Semi-major axis

(b) Semi-minor axis

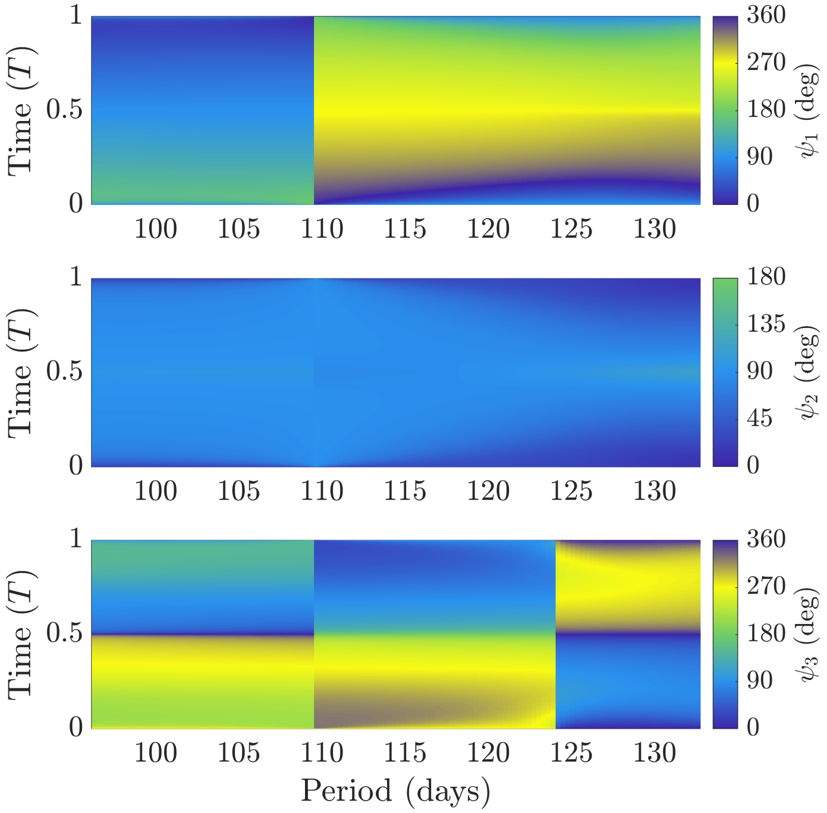

(c) Orientation with respect to the rotating frame

Figure 7.24: Description of the normalized first-order invariant curve relative to periodic orbits with an oscillatory mode associated with s_1 within the Sun-Earth L_1 halo orbit family.

axis of the invariant curve relative to apogee is equal to zero, causing a discontinuity in all three Euler angles.

The normalized size, shape, and orientation of the approximated invariant curve for motion exciting oscillatory modes corresponding to the s_2 index of the orbit family is plotted in Figure 7.25. A discontinuity is observed in the contour plots near an orbit that possesses a period of approximately 157 days, where s_2 possess a value of near -2. For orbits with a period less than the discontinuity near the 157-day orbit, the magnitude of the semi-minor axis of the invariant curve steadily decreases as the orbits decrease in period. As the orbits approach the critical orbit at which the s_2 index switches from corresponding to oscillatory to unstable motion, the semi-minor axes magnitude approaches zero. Similar to motion relative to the L_1 halo orbit family in the Earth-Moon the system, the invariant curve is circular relative to perigee of several orbits, which separate regions of different periodicity for the orientation of the invariant curve, as indicated by the evolution of ψ_3.

The region of Sun-Earth L_1 halo orbits with periods greater than the discontinuity near the 157-day orbit may be of particular interest for spacecraft formation flying applications due to their low out-of-plane amplitudes and use within the trajectory design of previous missions. Oscillatory motion within the center eigenspace of orbits in this range varies slowly as a function of orbit period, with no discontinuities in invariant curve geometry. Furthermore, the magnitude of the semi-minor axis does not approach near zero, indicating that motion within the center eigenspace of orbits in this range do not contract significantly towards the associated periodic orbit.

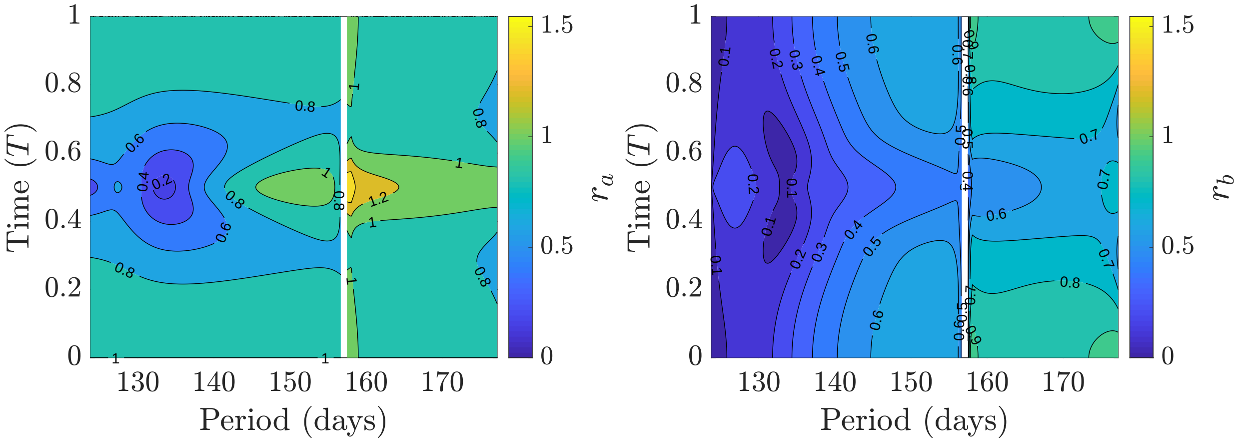

(a) Semi-major axis

(b) Semi-minor axis

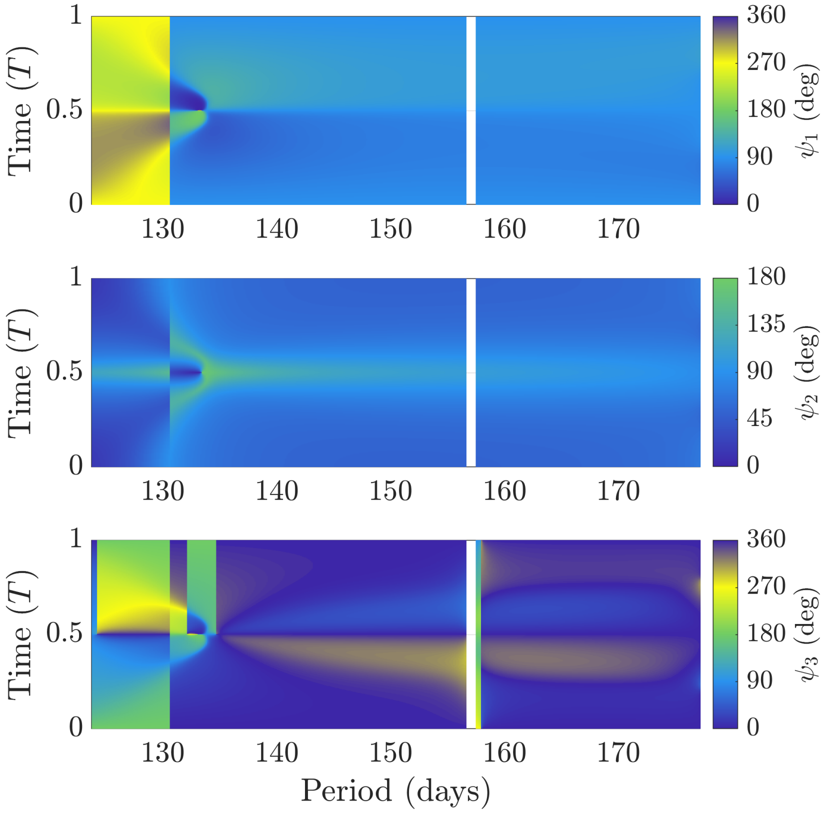

(c) Orientation with respect to the rotating frame

Figure 7.25: Description of the normalized first-order invariant curve relative to periodic orbits with an oscillatory mode associated with s_2 within the Sun-Earth L_1 halo orbit family.

7.2.2 Sun-Earth L_2 halo orbit family

Selected members of the Sun-Earth L_2 southern halo orbit family and the stability indices of orbits across the examined range of the family are plotted in Figure 7.26. Because of the symmetry of the family across the xy plane, the data in this analysis is representative of both the northern and southern portions of the orbit family.

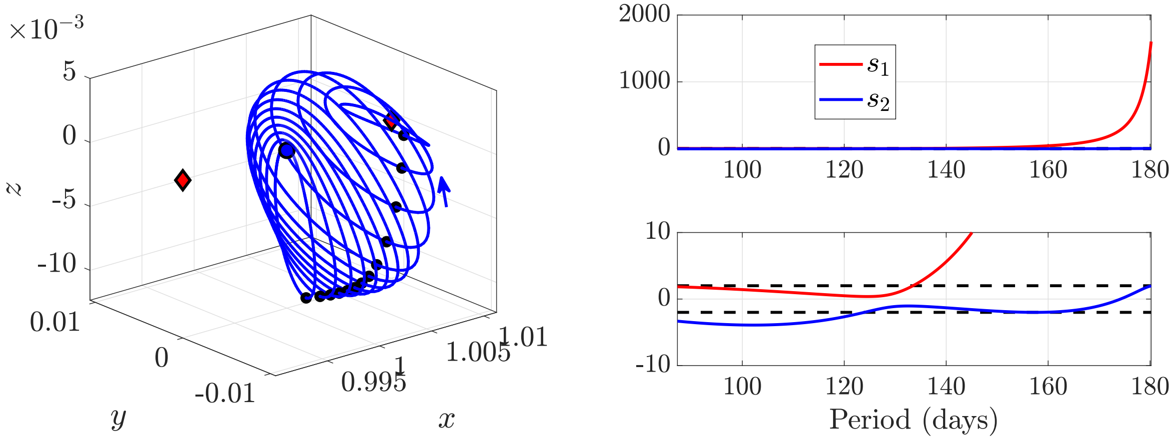

(a) Selected orbits in the rotating frame

(b) Stability indices

Figure 7.26: Selected orbits and stability indices computed over the examined range of the Sun-Earth L_2 halo orbit family.

The normalized size, shape, and orientation of the approximated invariant curve for motion exciting oscillatory modes corresponding to the s_1 index of the Sun-Earth L_2 halo orbit family is plotted in Figure 7.27. Similar to relative motion near members of the same orbit family in the Earth-Moon system, the invariant curve is characterized by large eccentricity relative to perigee for orbits with lower orbit period. As the s_1 approaches a value of 2 near an orbit with a period of approximately 133 days, the magnitude of the semi-minor axis approaches zero. The invariant curve relative to apogee is circular relative to a halo orbit with a period of approximately 125 days, such that the normalization process for the complex eigenvector causes a non-smooth evolution in the magnitude of the principal axes and ψ_3. Finally, at an orbit with a period of approximately 112 days, the magnitude of the semi-minor axis of the invariant curve relative to apogee is equal

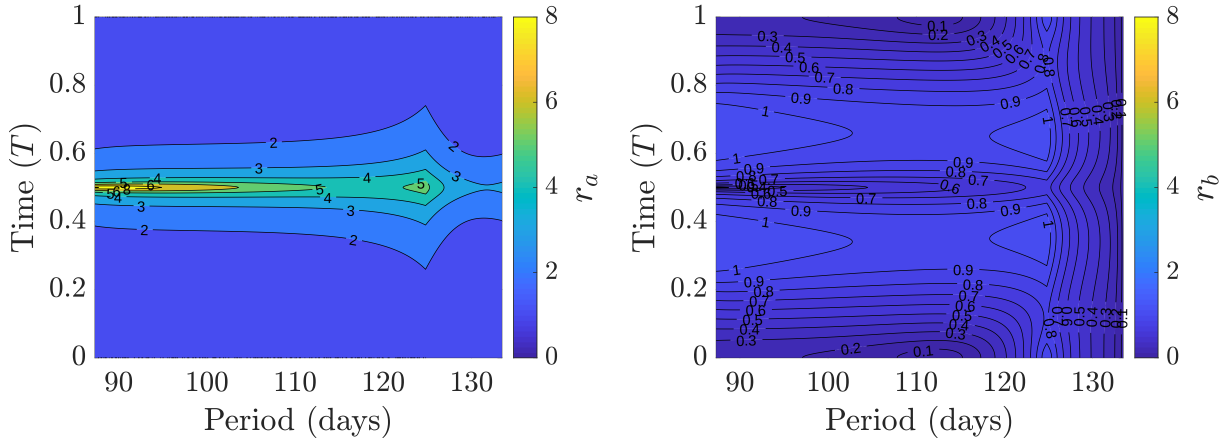

(a) Semi-major axis

(b) Semi-minor axis

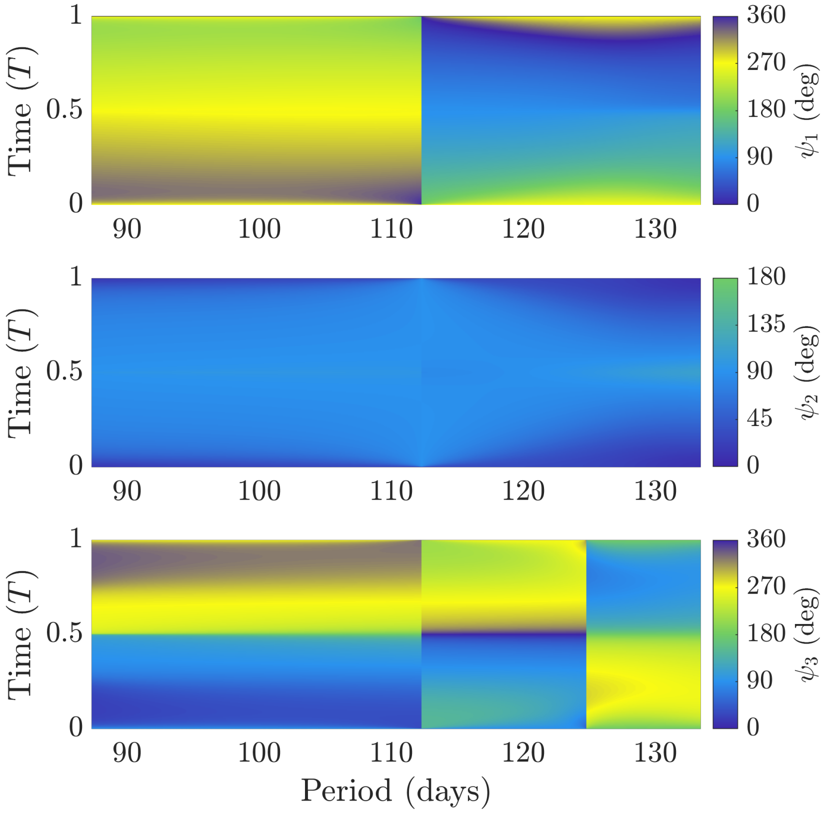

(c) Orientation with respect to the rotating frame

Figure 7.27: Description of the normalized first-order invariant curve relative to periodic orbits with an oscillatory mode associated with s_1 within the Sun-Earth L_2 halo orbit family.

to zero, causing a discontinuity in the evolution of the three Euler angles across this orbit.

Next, the normalized size, shape, and orientation of the approximated invariant curve for motion exciting oscillatory modes corresponding to the s_1 index of the Sun-Earth L_2 halo orbit family is plotted in Figure 7.28. Oscillatory motion associated with this stability index is separated by a discontinuity at an orbit with a period of approximately 158 days, caused by the numerical sensitivity of the computation of the approximated invariant curve. Similar trends in the discontinuities within the orientation of the invariant curve are observed between this range of orbits and the corresponding motion in the Sun-Earth L_1 halo orbit family.

Oscillatory motion relative to members of the Sun-Earth L_2 orbit family with larger orbit periods and smaller out-of-plane amplitudes may be of particular interest for the trajectory design of supporting spacecraft for in-space telescopes, such as servicing vehicles or starshades. These spacecraft may leverage quasi-periodic relative motion to maintain natural or efficient paths relative to a target spacecraft located on a trajectory resembling an L_2 halo orbit. The analysis of first-order oscillatory motion in this range suggests that the evolution of the invariant curve over time is less sensitive to the specific associated periodic orbit compared to other regions of the family.

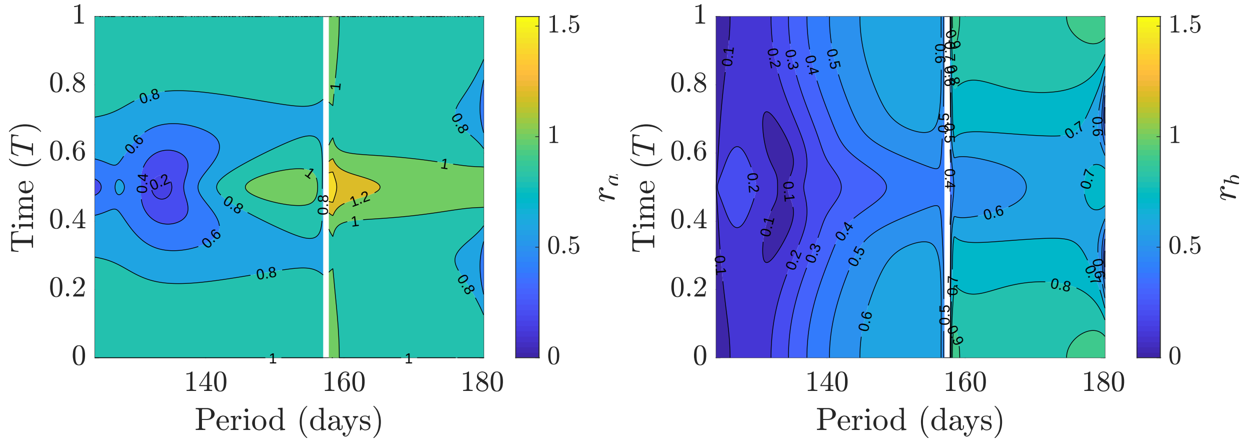

(a) Semi-major axis

(b) Semi-minor axis

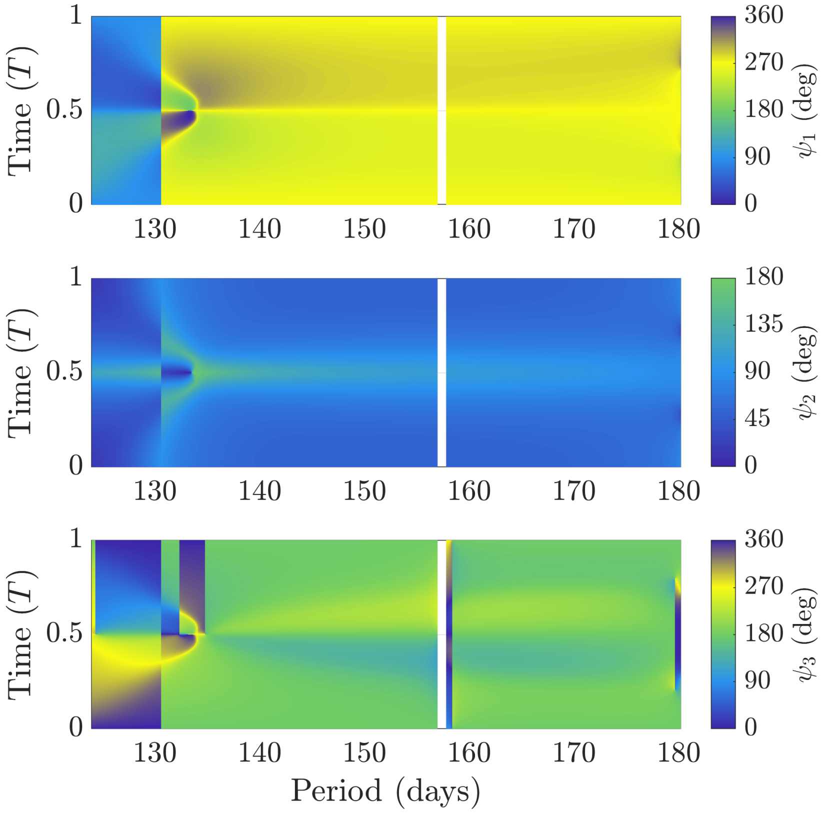

(c) Orientation with respect to the rotating frame

Figure 7.28: Description of the normalized first-order invariant curve relative to periodic orbits with an oscillatory mode associated with s_2 within the Sun-Earth L_2 halo orbit family.

7.2.3 Sun-Earth L_4 short period family

Selected members of the Sun-Earth L_4 short period family and the stability indices of orbits across the examined range of the family are plotted in Figure 7.29. Across the examined range, in-plane motion is admit by oscillatory modes associated with the s_2 index.

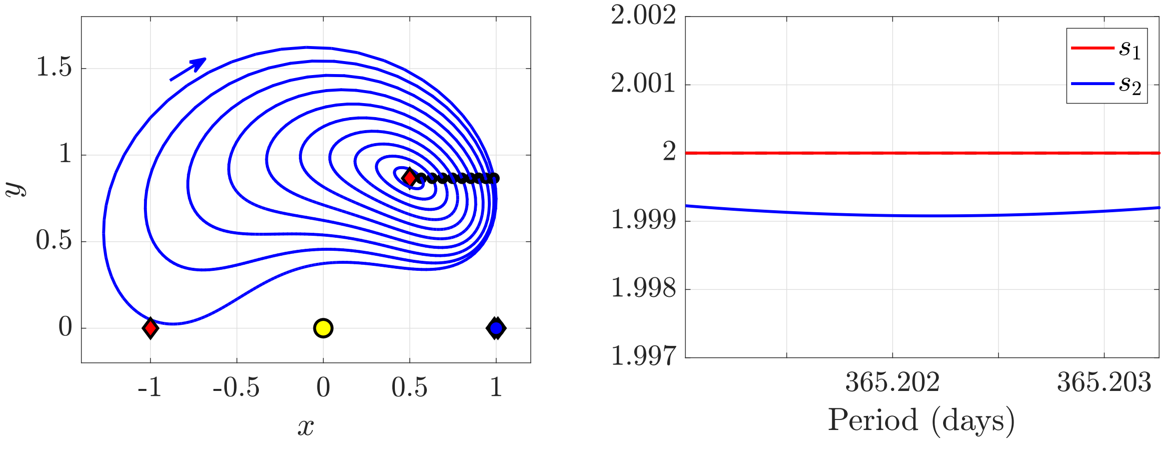

(a) Selected orbits in the rotating frame (b) Stability indices

Figure 7.29: Selected orbits and stability indices computed for orbits within the examined range of the Sun-Earth L_4 short period family.

The normalized size, shape, and orientation of the approximated invariant curve for motion exciting oscillatory modes corresponding to the s_2 index of the Sun-Earth L_4 short period family is plotted in Figure 7.30. Compared to the L_4 short period family in the Earth-Moon system, the magnitude of the semi-minor axis across the examined range is significantly lower, indicating motion on an invariant torus relative to a Sun-Earth L_4 short period orbit may closely approach the periodic orbit. Thus, the angle ψ supplies important insight into the direction of the maximum and minimum stretching distances of the invariant curve with respect to the rotating frame. Unlike the Earth-Moon L_4 short period family, the magnitudes of the principal semi-axes do not intersect over the examined range. The orientation of the invariant curve relative all members in the examined range is periodic with respect to the rotating frame over T and oscillates by less than 90° from the initial orientation.

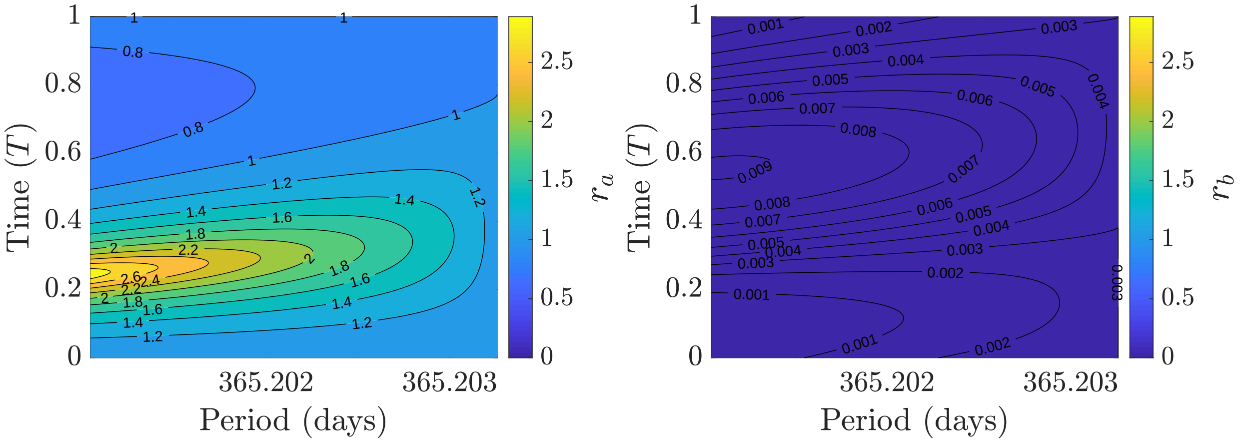

(a) Semi-major axis

(b) Semi-minor axis

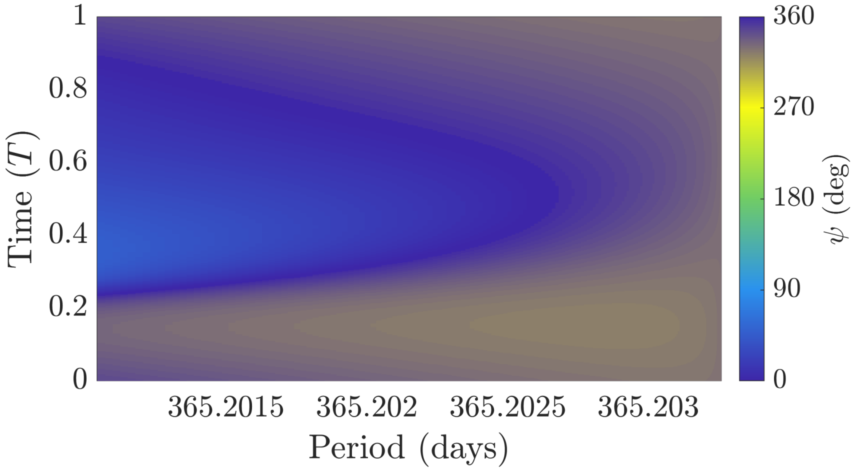

(c) Orientation with respect to the rotating frame

Figure 7.30: Description of the normalized first-order invariant curve relative to periodic orbits with an oscillatory mode within the Sun-Earth L_4 short period family.

7.2.4 Sun-Earth L_5 short period family

Selected members of the Sun-Earth L_5 short period family and the stability indices of orbits across the examined range of the family are plotted in Figure 7.31. Across the examined range, in-plane motion is admit by oscillatory modes associated with the s_2 index.

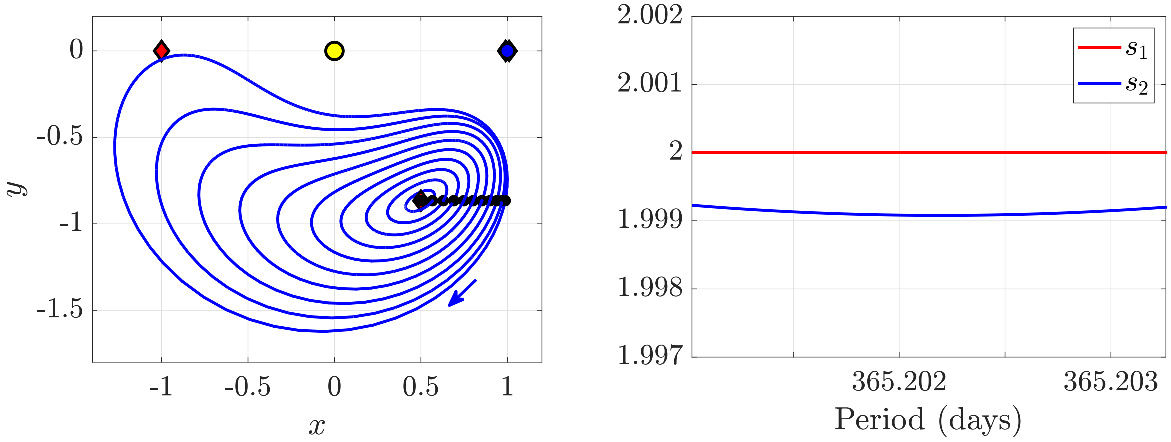

(a) Selected orbits in the rotating frame

(b) Stability indices

Figure 7.31: Selected orbits and stability indices computed over the examined range of the Sun-Earth L_5 short period family.

The normalized size, shape, and orientation of the approximated invariant curve for motion exciting oscillatory modes corresponding to the s_2 index of the Sun-Earth L_5 short period family is plotted in Figure 7.32. The resulting motion exhibits similar characteristics with the corresponding motion relative to the Sun-Earth L_4 short period family. The magnitude semi-minor axis across the examined range is much smaller than the semi-major axis, possessing an range of value between approximately 0.001 to 0.01. Similarly, the orientation of the invariant curve relative to all members in the examined range is periodic with respect to the rotating frame over T and oscillates by less than 90° from the initial orientation. As with the L_4 short period family, due to the high eccentricity of the invariant curve relative to L_5 short period orbits, the orientation of the invariant curve is important for understanding the direction the minimum and maximum separations distances of the invariant curve from the associated periodic orbit.

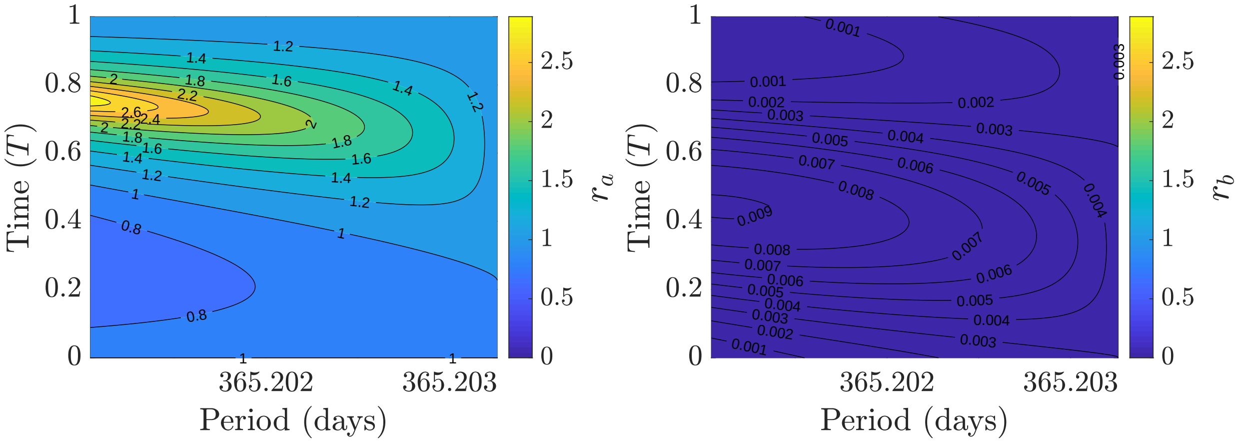

(a) Semi-major axis

(b) Semi-minor axis

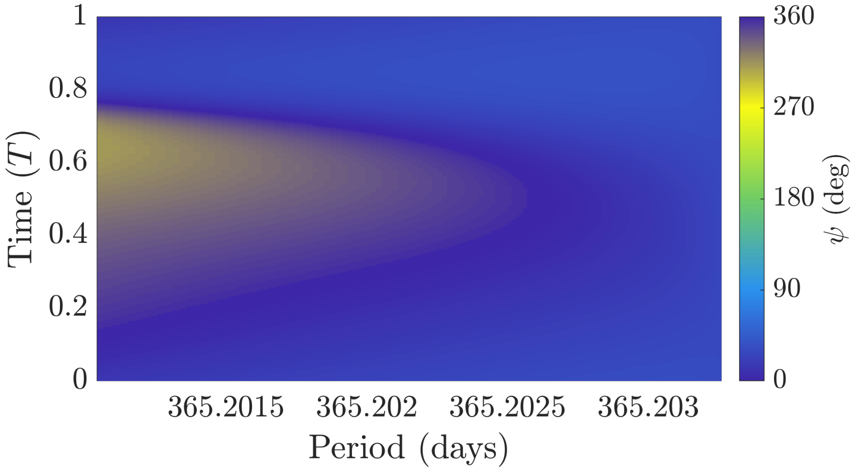

(c) Orientation with respect to the rotating frame

Figure 7.32: Description of the normalized first-order invariant curve relative to periodic orbits with an oscillatory mode within the Sun-Earth L_5 short period family.

Chapter 8

Application: Designing a Spacecraft Constellation near Sun-Earth L_1

An example of the design of a conceptual spacecraft constellation near Sun-Earth L_1 is presented to demonstrate an application of the strategies for oscillatory relative motion characterization, spacecraft control, and general use of local toroidal coordinate for spacecraft trajectory design. The spacecraft constellation is assumed to consist of six spacecraft following bounded motion near a Sun-Earth southern L_1 halo orbit that are tasked to observe the Sun. The Sun-Earth southern L_1 halo orbit family is examined due to its proximity between the Earth and the Sun, previous use in the ISEE-3 and SOHO missions [90], and potential as a future location for spacecraft to perform useful scientific observations for heliophysics.

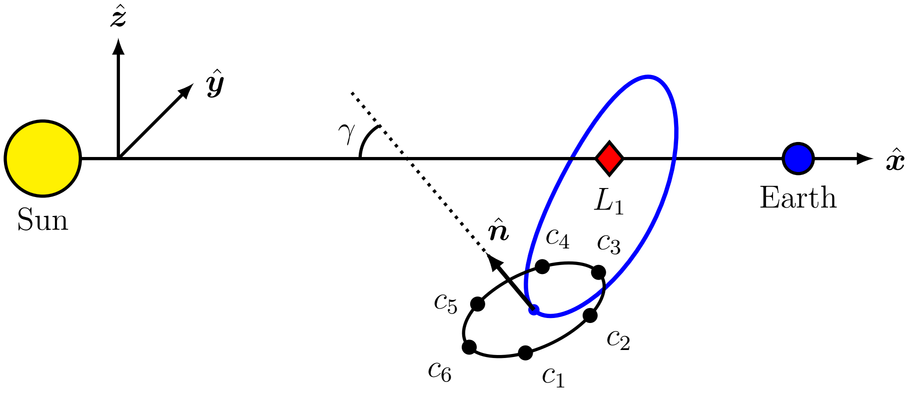

Figure 8.1: Conceptual illustration of a six-spacecraft constellation located on oscillatory motion near a Sun-Earth L_1 southern halo orbit (size and relative distances of objects exaggerated for visibility).

8.1 Formation trajectory design and constraints

Each spacecraft in the constellation is located at a small distance from the periodic orbit and within the center eigenspace to leverage the approximation of an invariant torus to supply naturally bounded motion. Each of the six-spacecraft are assumed to be evenly distributed along the same invariant curve relative to a Sun-Earth L_1 southern halo orbit, corresponding to a toroidal angle difference of $\delta\theta = 2\pi/6 = 60^\circ$. Figure 8.1 illustrates a conceptual schematic of the trajectory design of the spacecraft constellation, represented as black markers labeled as c_{1-6}. These spacecraft will be located near the Sun-Earth L_1 southern halo orbit, represented in blue. To design the trajectories of the constellation, the following process is followed:

(1) First, a stability analysis of the Sun-Earth southern L_1 halo orbit family is conducted to identify members of the orbit family that admit an oscillatory mode.

(2) Next, this oscillatory motion is examined across the identified members of the orbit family via analysis of the evolution of the size, shape, and orientation of the approximated invariant curve over an orbit period.

(3) Using the data generated from this analysis, a single reference orbit and torus size is selected to satisfy a given set of example trajectory design constraints and objectives.

(4) The selected reference trajectory is recovered in a higher-fidelity point mass ephemeris model and the desired configuration of the constellation is maintained with the impulsive station-keeping control strategy formulated using nonsingular local toroidal coordinates, presented in Section 6.

(5) The resulting motion of the constellation in the point mass ephemeris model is then assessed and compared to the estimated characteristics predicted by the CR3BP via the presented analysis techniques.

For this example design process, a simplified set of constraints are defined for this analysis. Two constraints on the inter-spacecraft separation between all six spacecraft are defined as:

- The inter-spacecraft separation must always be less than 1000 km such that each spacecraft may simultaneously communicate with the Earth
- The inter-spacecraft separation must always be greater than 250 km for collision avoidance considerations

In addition to these two constraints, the normal direction of the plane spanned by the constellation is also assessed to supply preliminary insight into the projection of the spacecraft onto the plane normal to the Sun-Earth line.

8.2 Selecting a reference orbit and invariant torus size

A preliminary analysis of the natural motion relative to periodic orbits in the CR3BP rapidly supplies estimates of the motion of the spacecraft in higher fidelity models. Example orbits across the examined range of Sun-Earth southern halo orbits are plotted in Figure 8.2a along with the location of the Earth, L_1, and L_2. The orbits in this subset of the Sun-Earth southern L_1 halo orbit family represent the portion of the orbit family with a low maximum out-of-plane extension. Along the examined range of L_1 halo orbits, each periodic orbit admits one stable/unstable eigenvalue pair and one complex conjugate eigenvalue pair corresponding to oscillatory motion. The stability indices of the examined range of Sun-Earth L_1 southern halo orbits are plotted in Figure 8.2b as a function of the out-of-plane amplitude of the periodic orbit. Across the examined range, the stability index corresponding to the stable/unstable eigenvalue pair, s_1, is represented in red and possesses a value greater than 2. In the lower subplot of Figure 8.2b, the values of the stability index corresponding to an oscillatory mode, s_2, represented in blue, indicates that the value of the index lies between -2 and 2 for the investigated range of orbits.

Following the computation and assessment of the stability indices across the Sun-Earth L_1 halo orbit family, oscillatory motion relative to the members of the orbit family is investigated. A subset of the data generated for the Sun-Earth L_1 halo orbit family in Section 7.2.1 is plotted over the range of interest. Recall for each orbit, the normalization process of the complex eigenvector

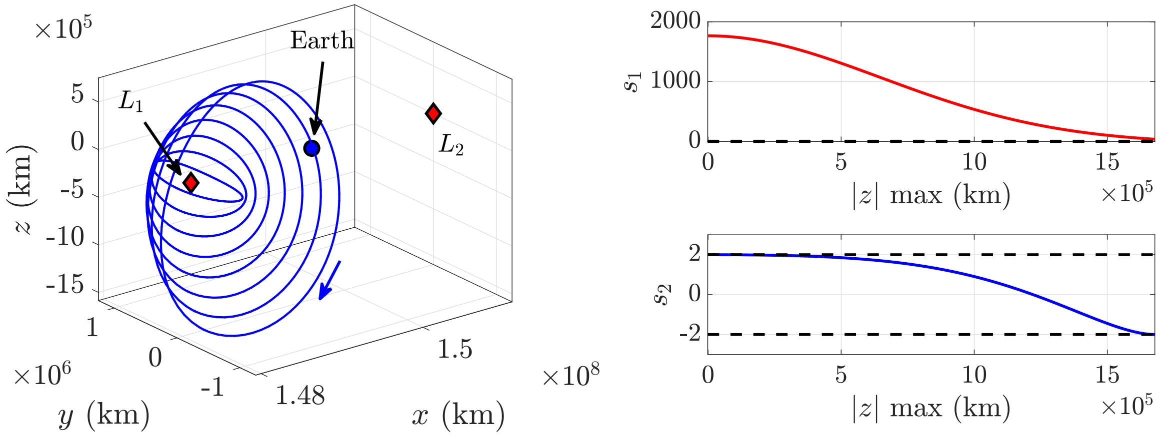

(a) Orbits plotted in the Sun-Earth rotating frame (b) Stability indices across the examined range

Figure 8.2: Selected members of the Sun-Earth southern L_1 halo orbit family and the stability indices of orbits across the examined range.

is applied at the apogee of each halo orbit. The magnitude of the semi-major axis of the invariant curve associated with the normalized eigenvector across each orbit and across the explored range of periodic orbits is displayed in Figure 8.3a and the magnitude of the semi-minor axis is displayed in Figure 8.3b. Time past apogee along each periodic orbit is represented on the vertical axis, normalized by the period of the orbit, T. Each orbit in the family is characterized by the dimensional out-of-plane amplitude, $|z|$ max, along the horizontal axis.

To interpret the angle of the normal vector of the invariant curve from the Sun-Earth line, the angle between the normal vector, $\hat{\boldsymbol{n}}$, and the $\hat{\boldsymbol{x}}$ axis of the rotating frame is computed. This angle, γ, is defined as

$$\gamma = \cos^{-1}\left(\hat{\boldsymbol{n}}^T\hat{\boldsymbol{x}}\right) \tag{8.1}$$

With this definition, γ is constrained to values between $0°$ and $180°$. A value of $\gamma = 0°$ indicates that the plane spanned by the invariant curve in the configuration space is exactly normal to $\hat{\boldsymbol{x}}$, i.e., it spans the yz plane. Furthermore, a value of $\gamma = 90°$ indicates that the normal vector of plane spanned by the invariant curve in the configuration space is perpendicular to the $\hat{\boldsymbol{x}}$ axis. Values of γ greater than $90°$ indicate that the normal direction lies in the opposite direction as $\hat{\boldsymbol{x}}$. This value

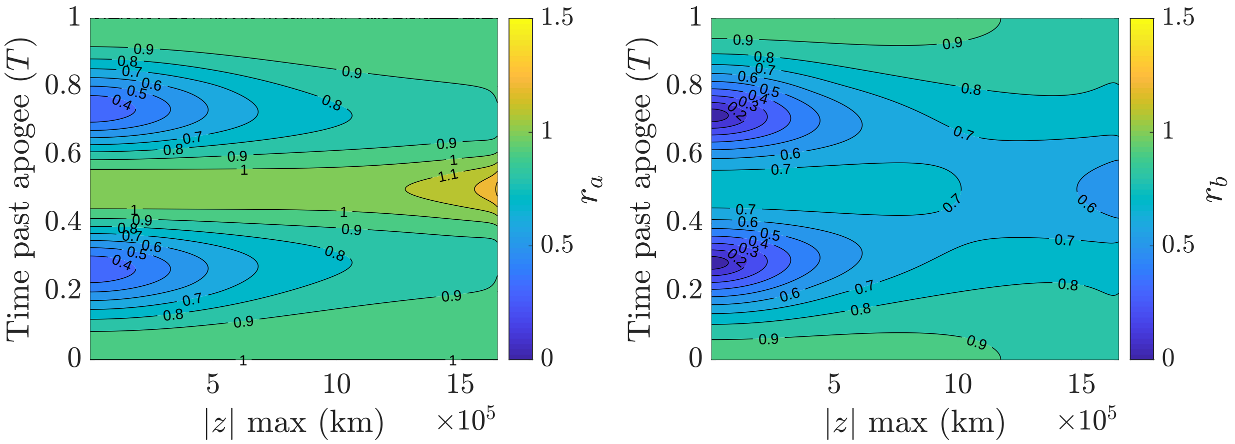

(a) Semi-major axis magnitude

(b) Semi-minor axis magnitude

Figure 8.3: Magnitude of the principal semi-axes of the normalized first-order invariant curve across the examined range of the Sun-Earth L_1 halo orbit family.

is potentially useful for spacecraft on an invariant curve which may need a desired spread along the plane normal to the viewing direction of one of the primaries bodies.

The evolution of γ is examined range of the halo orbit family. The two-dimensional plot of this angle across the orbit family appears in Figure 8.4. This investigation reveals regions of the southern halo orbit family where a invariant curve may exhibit more rotation over each revolution with respect to the rotating frame. In general, a invariant curve near orbits with a lower out-of-plane amplitude are observed to rotate more with respect to the rotating frame compared to orbits with larger out-of-plane amplitude. Notably, for orbits with lower out-of-plane amplitude, the angle indicates that the normal direction, $\hat{\boldsymbol{n}}$, lies near-perpendicular to the $\hat{x}$ axis near times past apogee of approximately $0.3T$ and $0.7T$ However, as orbits evolve across the family and increase in out-of-plane amplitude, the maximum angle between the normal direction and $\hat{x}$ axis generally decreases. For all orbits in the examined range, the minimum value of γ occurs at perigee. This angle may influence the design of a constellation for which the spacecraft are desired to be sufficiently distributed in either the yz or xy plane.

The data plotted in Figure 8.3 is used to compute the maximum and minimum inter-

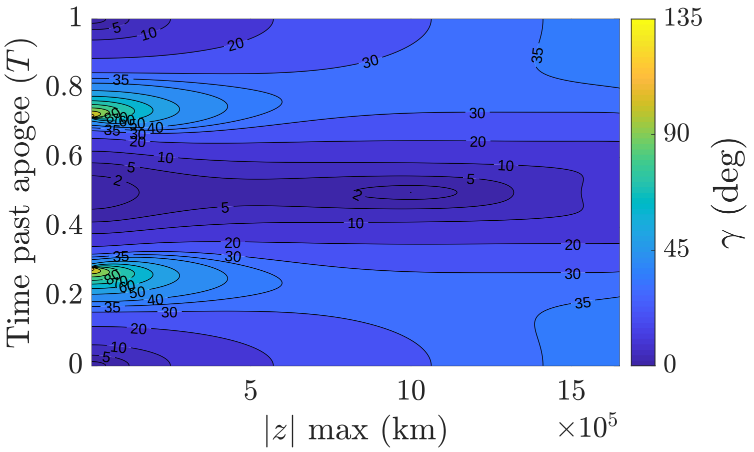

Figure 8.4: Angle between the normal direction to the approximated invariant curve and the $\hat{\boldsymbol{x}}$-axis of the Sun-Earth rotating frame over the examined range of the orbit family.

spacecraft separation for the conceptual six-spacecraft constellation. The six spacecraft are assumed to be evenly distributed along the invariant curve such that the relative toroidal angle between each spacecraft is equal to $\delta\theta = 60°$. From the strategies for assessing the relative separation between spacecraft on the same invariant curve detailed in Chapter 5, the minimum inter-spacecraft separation between any two spacecraft in the constellation is found using using Eq. (5.20). For two neighboring spacecraft separated by $\delta\theta = 60°$, the minimum possible separation is defined as a function of the instantaneous semi-minor axis of the invariant curve as

$$d_{\text{min}} = 2\varepsilon r_b \sin\left(\frac{60°}{2}\right) = \varepsilon r_b$$

The maximum inter-spacecraft separation between the two spacecraft on the same invariant curve occurs when $\delta\theta = 180°$ and is computed as a function of the instantaneous semi-major axis of the invariant curve as

$$d_{\text{max}} = 2\varepsilon r_a \sin\left(\frac{180°}{2}\right) = 2\varepsilon r_a$$

This value defines the separation between two-spacecraft located on opposing vertices along the major axis of an approximated invariant curve and reflects the upper bound of all inter-spacecraft separation in the constellation.

To summarize the inter-spacecraft separation over a revolution of each orbit, the maximum and minimum inter-spacecraft separation over each period is calculated and plotted as a function of the out-of-plane amplitude of the periodic orbit in Figure 8.5. These separation distances correspond to the invariant torus constructed by the normalized complex eigenvector, i.e., a torus described by a size of ε equal to unity. The maximum inter-spacecraft separation over each orbit, d^*_{max}, is plotted in red. The minimum inter-spacecraft separation over each orbit, d^*_{min}, is plotted in blue. This summary reveals that the maximum inter-spacecraft separation is roughly equal to 2.2ε for L_1 halo orbits with lower out-of-plane amplitude. As the orbits in the family grow to possess higher amplitude out of the plane, the maximum inter-spacecraft begins to increase. For orbits near the bifurcation with the L_1 Lyapunov orbit family, i.e., where $|z|$ max equals 0 km, the minimum inter-spacecraft separation over each orbit is near 0 km. As the halo orbits increase in the out-of-plane amplitude, the minimum inter-spacecraft separation increases, until a maximum value across the examined range of the orbit family is observed at an orbit possessing an out-of-plane amplitude of approximately 1×10^6 km.

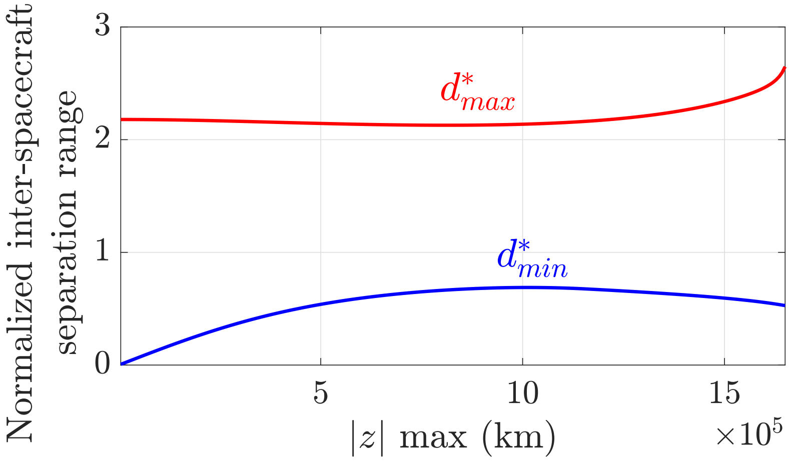

Figure 8.5: Maximum and minimum inter-spacecraft separation over each orbit for the approximate invarinat 2-torus constructed by the normalized eigenvector.

To determine a reference orbit and torus size that satisfies the constraints, the maximum and minimum inter-spacecraft separation distance as a function of ε are assessed. Using the separation of the torus constructed by the normalized complex eigenvector plotted in Figure 8.5, the maximum value of ε, ε_{max}, that satisfies the maximum separation constraint and the minimum value of ε, ε_{min}, that satisfies the minimum separation constraint are calculated across the orbit family. Theses limits are then used select a torus size and reference orbit that satisfies the trajectory design constraints. First, the maximum value of ε is computed across the family, equal to

$$\varepsilon_{\text{max}} = \frac{1000 \text{ km}}{d^*_{\text{max}}}$$

and is plotted in Figure 8.6 as a red line. The region under this curve reflects values of ε producing tori that meet the maximum separation constraint. Recall that the values generated in this analysis correspond to a complex eigenvector normalized at apogee of the orbit; modifying the fixed point along the periodic orbit at which the eigenvector is normalized will vary the results, i.e., the range of ε that satisfies the constraints.

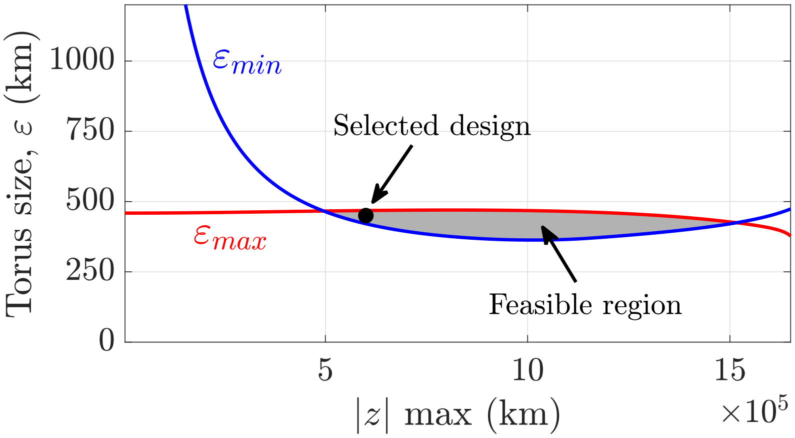

Figure 8.6: Identifying the feasible design range of the spacecraft constellation using insight into the oscillatory motion across the halo orbit family.

Next, the process is repeated to determine the orbits and values of ε that satisfy the minimum inter-spacecraft separation constraint. The value of ε that produces a minimum separation of 250 km over an orbit is plotted in Figure 8.6 as a solid blue line, equal to

$$\varepsilon_{\text{min}} = \frac{250 \text{ km}}{d^*_{\text{min}}}$$

The region above this line reflects values of ε that produce tori where the minimum separation constraint is satisfied. The feasible design range of reference halo orbit and ε is identified as the region that simultaneously lies below $\varepsilon_{\max}$ and above $\varepsilon_{\min}$, indicated by the gray shaded region in Figure 8.6. Feasible halo orbits are identified between a range of out-of-plane amplitude of approximately 500,000 km to 1,500,000 km, while feasible values of ε are approximately 350 - 470 km, depending on the specific periodic orbit. This feasible range indicates both the range of reference halo orbits and the range of possible values of ε for placing the constellation spacecraft to satisfy the constraints for first-order oscillatory motion.

With the feasible design range identified, a final reference trajectory and torus size is selected. The halo orbit with an out-of-plane amplitude equal to 600,000 km is selected as the reference orbit; this orbit possesses a period of 3.0468 nondimensional units, or approximately 177.1 days, in the CR3BP. A torus size for placing the constellation spacecraft of $\varepsilon = 450$ km, measured relative to apogee, is selected; the reference orbit and torus size pair is identified in Figure 8.6 via a black marker. This specific combination is selected as a design that lies within the feasible range with a lower out-of-plane amplitude. The principal axes of the invariant curve over time for the selected orbit and value of ε are plotted in Figure 8.7a. The maximum value of the magnitude of the semi-major axis occurs as the constellation center reaches perigee, at a value of approximately 480.6 km. Two minimum values of the magnitude of the semi-minor axis occur at times past apogee of $0.31T$ and $0.69T$, at a value of approximately 267.2 km. The 3-1-3 Euler angle description of the orientation of the invariant curve is additionally plotted in Figure 8.7b. The first angle, ψ_1, is consistently near a value of 90°. The inclination of the plane spanned by the center eigenspace, indicated by ψ_2, lies between values of 45° to 90°. Finally, ψ_3 indicates that orientation of the invariant curve rotates over time in the plane spanned by the center eigenspace, with regions of increased rotation occurring near minima in the magnitude of the semi-minor axis.

8.3 Simulation of the constellation in the ephemeris model

To demonstrate the use of a rapid analysis of quasi-periodic relative motion in the CR3BP to the trajectory design process, the selected reference orbit and torus are applied to the simulation of a spacecraft constellation in the ephemeris model including perturbation from SRP. To simulate the

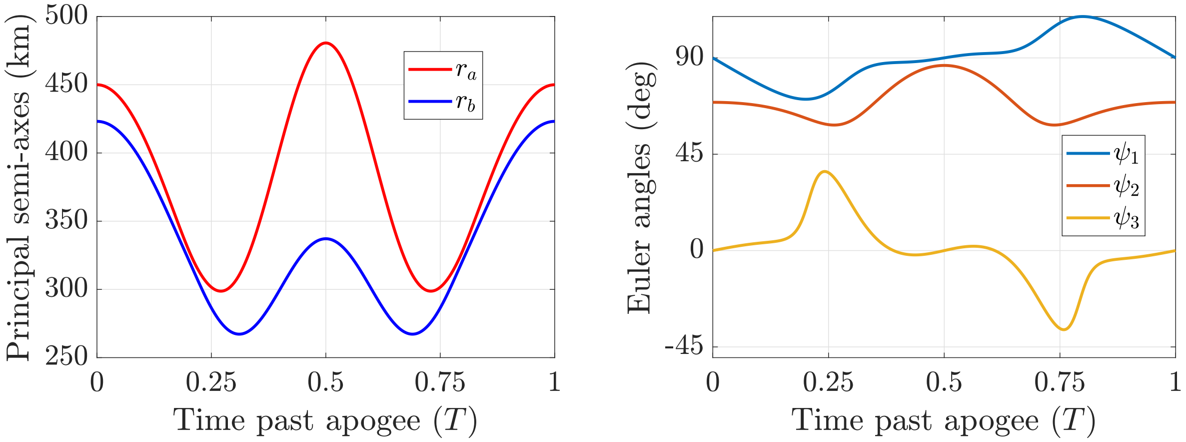

(a) Magnitude of principal semi-axes

(b) 3-1-3 Euler angle orientation description

Figure 8.7: Parameters describing the size, shape, and orientation of the approximated invariant curve relative to the selected Sun-Earth L_1 halo orbit, possessing a value of $\varepsilon = 450$ km measured relative to apogee.

spacecraft constellation in the ephemeris model, first, the selected Sun-Earth southern halo orbit is transitioned into the point mass ephemeris model of the Sun, Earth, and Moon with perturbations from SRP, detailed in Section 2.3. The desired motion of each spacecraft is then defined relative to this reference trajectory. In this simulation, each spacecraft is assumed to possess identical physical characteristics affecting the perturbation due to SRP. Thus, the reference trajectory is assumed to possess the same physical characteristics as the spacecraft in the constellation, despite not physically locating a spacecraft. A summary of the epoch, simulation duration, and the SRP parameters of the constellation spacecraft are listed in Table 8.1.

Using the multiple shooting algorithm described in Section 3.4.5, the constellation's reference trajectory is recovered in the ephemeris model using the selected Sun-Earth L_1 southern halo orbit. The reference trajectory in the ephemeris model is plotted in Figure 8.8 in the Sun-Earth rotating frame along with the orbit of the Moon and approximate location of Sun-Earth L_1. The initial condition of the trajectory is defined at the southern crossing of the xz plane, indicated with a black marker, and is simulated for 10 revolutions in the Sun-Earth rotating frame.

Due to the unstable mode of the Sun-Earth L_1 halo reference orbit and use of a higher-

Table 8.1: Summary of parameters used to simulate the spacecraft constellation center reference trajectory in the ephemeris model.

Parameter	Value
Reference orbit	177.1 day Sun-Earth L_1 southern halo orbit recovered in ephemeris model
Initial epoch	January 1, 2025 00:00:00.000 UTC
Simulation duration	10 revolutions = 4.86 years
Surface-area-to-mass-ratio	$A/m = 0.01$ m^2/kg
Reflectivity coefficient	$C_R = 1.8$

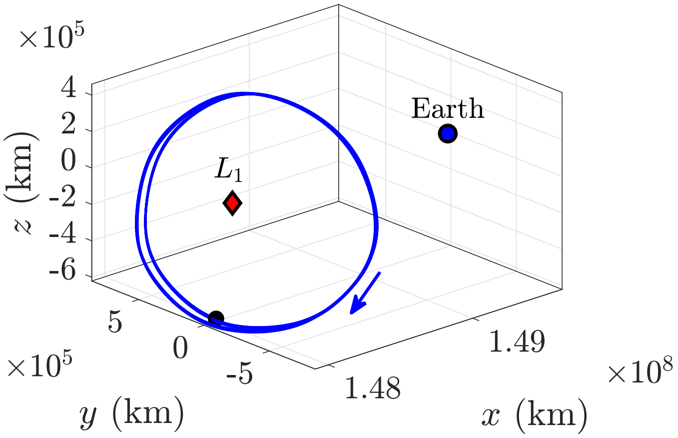

Figure 8.8: Constellation center trajectory recovered in the ephemeris model, plotted in the Sun-Earth rotating frame.

fidelity point mass ephemeris model, station-keeping is used to maintain the desired configuration constellation in this environment. Other station-keeping strategies may be applied, however, this control scheme is well-suited for the control of a constellation of this design which locates spacecraft relative to a reference trajectory in the ephemeris model using states defined within the center eigenspace of the periodic orbit in the CR3BP.

The six spacecraft in the constellation are tasked to station-keep to distinct configurations relative to the reference trajectory in the ephemeris model and are subject to navigation and maneuver errors. A summary of parameters used to simulate the constellation spacecraft is listed in Table 8.2. The desired relative configuration of the constellation is defined by the selected torus size of $\varepsilon = 450$ km for a complex eigenvector normalized at apogee, and evenly distributed values of θ between 0° and 360°. The desired out-of-plane toroidal coordinate, h and all coordinate rates are equal to zero to locate the desired configuration of each spacecraft within the center eigenspace. Each chaser spacecraft is initialized at the desired relative configuration with an added injection error drawn from a normal distribution; navigation errors are added to the inertial state of the chaser spacecraft before the computation of a maneuver. The selected error values are representative of the values observed for previous missions to Sun-Earth halo orbits [90]. For reference, without the application of control, the constellation of spacecraft initially located at the desired configuations from the reference trajectory depart a separation radius of 1000 km from the reference trajectory after approximately 150 days.

Table 8.2: Summary of parameters used to simulated the six constellation spacecraft applying station-keeping control in the ephemeris model.

Parameter	Value
Desired ε_d	450 km
Desired θ_d	$\theta_{1-6} = 0°, 60°, 120°, 180°, 240°, 300°$
Navigation and injection position error	$3\sigma_r = 10$ km
Navigation and injection velocity error	$3\sigma_v = 10$ mm/s
Maneuver magnitude error	$3\sigma_{\Delta v} = 3\%$
Maneuvers per revolution	$N = 10$

The trajectories of each of the six constellation spacecraft are simulated with station-keeping control for the total duration of the reference trajectory in the ephemeris model. The resulting trajectories relative to the reference trajectory in the ephemeris model are plotted in Figure 8.9. The relative trajectories are plotted in two different frames: the Sun-Earth rotating frame in Figure 8.9a, and the toroidal frame in Figure 8.9b. The trajectories visualized in the rotating frame reveal bounded, oscillatory motion relative to the periodic orbit, representative of oscillatory relative motion as predicted by the CR3BP. However, visualization of the relative trajectories in the toroidal frame better reveals the distinct deviation of each spacecraft from the reference trajectory.

In this frame, the first-order approximation of the invariant curve is represented as a circle that spans the $\alpha\beta$ plane with a radius of 450 km. Finally, the relative state histories of each spacecraft, expressed in geometric local toroidal coordinates and their respective rates, are plotted versus time in Figure 8.10. The ε and h coordinates, as well as the three coordinate rates, the state histories of each trajectory is centered a shared value while the θ value of each spacecraft is unique. Note that the time history of h reflects the out-of-plane component of each trajectory not visualized in the planar view plotted Figure 8.9b.

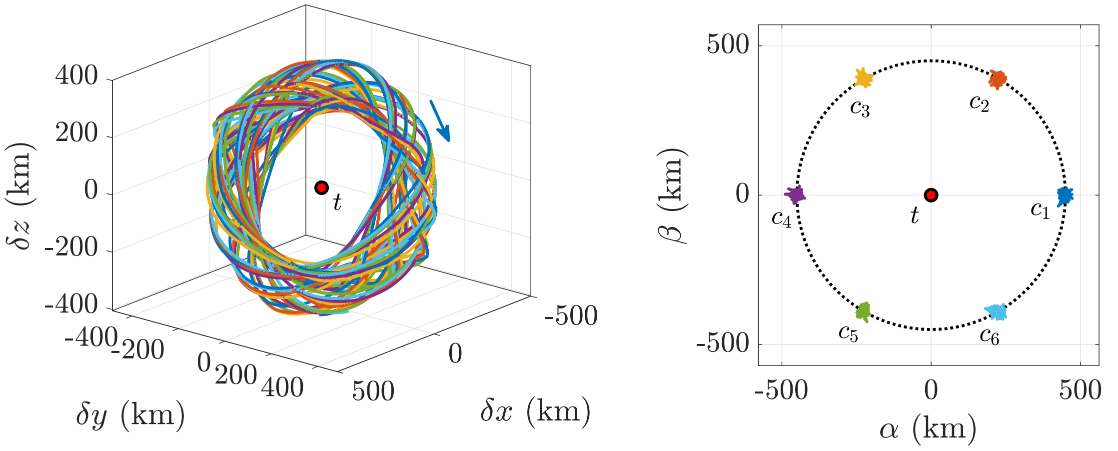

(a) Relative trajectories in the rotating frame

(b) Relative trajectories in the toroidal frame

Figure 8.9: Relative trajectories of the six-spacecraft constellation near a Sun-Earth L_1 halo orbit in the ephemeris model applying station-keeping control for 10 revolutions of the reference trajectory.

Next, the maneuver histories of the spacecraft in the constellation are assessed. The magnitude of each impulsive maneuver for each spacecraft is plotted in Figure 8.11a, using the same color scheme for each spacecraft as in Figure 8.9. The average magnitude of each maneuver by every spacecraft is approximately 2 cm/s. The cumulative required Δv is plotted in Figure 8.11b. A linearly-increasing Δv requirement is observed for each spacecraft in the constellation. The average total Δv required by each spacecraft is approximately 2 m/s, ranging between 1.85 m/s and 2.10 m/s, over the 4.8 year simulation. The required Δv is comparable to the station-keeping requirements of previously flown missions near Sun-Earth L_1 halo orbits [92]. Of course, varying

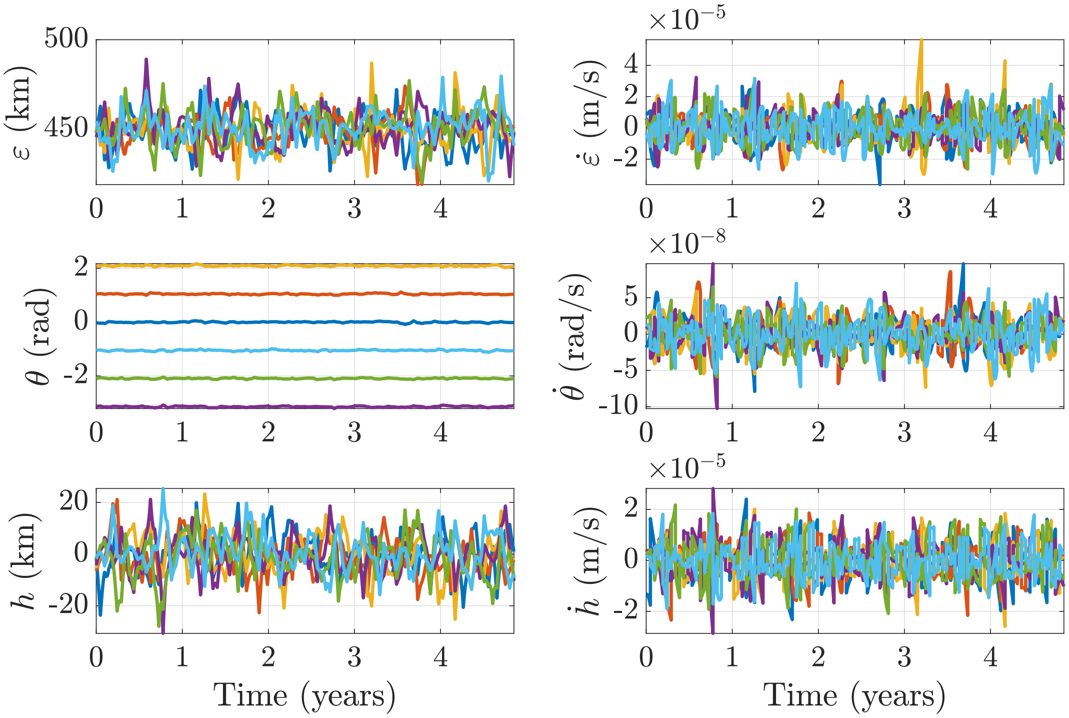

Figure 8.10: Relative state histories of the constellation spacecraft in the ephemeris model, expressed using geometric local toroidal coordinates.

the dynamical model and error model will vary the exact results and Δv requirements.

The resulting trajectories of the six spacecraft applying station-keeping control to maintain the defined configuration are plotted along with the estimates of motion characteristics derived using first-order approximations about the periodic orbit in the CR3BP. The trajectories of the constellation spacecraft over the first two revolutions of the reference trajectory are assessed. First, the inter-spacecraft separation between each spacecraft in the constellation is plotted over time in Figure 8.12, represented as 30 black lines, along with the estimated separation bounds. The maximum and minimum inter-spacecraft design constraints are also represented in this figure as dotted black lines. Also plotted in Figure 8.12 is the approximated range of possible inter-spacecraft for the six spacecraft evenly distributed along the invariant curve derived from the CR3BP, represented as the red shaded region, and the maximum and minimum inter-spacecraft design constraints, represented as dashed black lines. The inter-spacecraft separation distance is observed to always satisfy

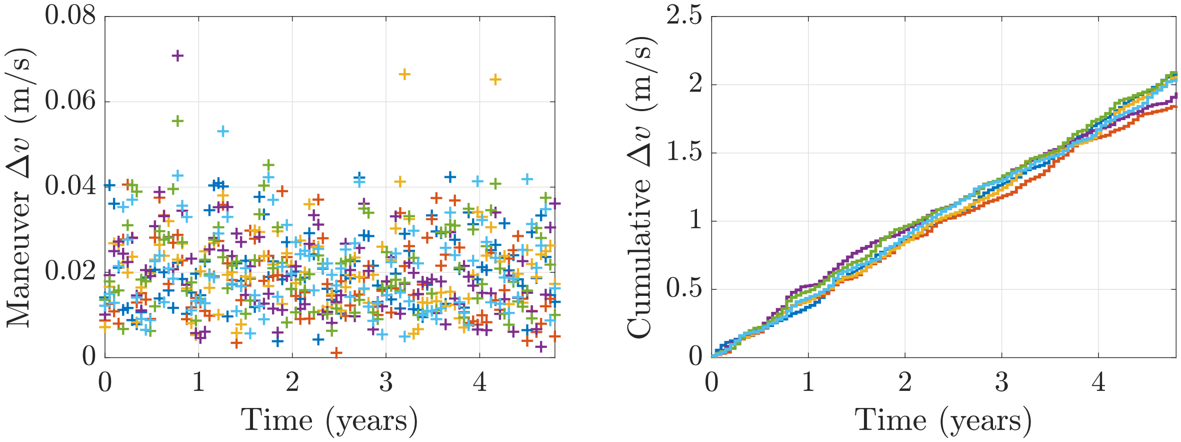

(a) Magnitude of each maneuver of each spacecraft (b) Cumulative Δv required by each spacecraft

Figure 8.11: Magnitude of each maneuver and cumulative Δv required by each spacecraft in the ephemeris model.

the constellation constraints of inter-spacecraft separation less than 1000 km and greater than 250 km. For this simulation, the maximum inter-spacecraft distance observed is approximately 965 km and the minimum separation distance is approximately 254 km.

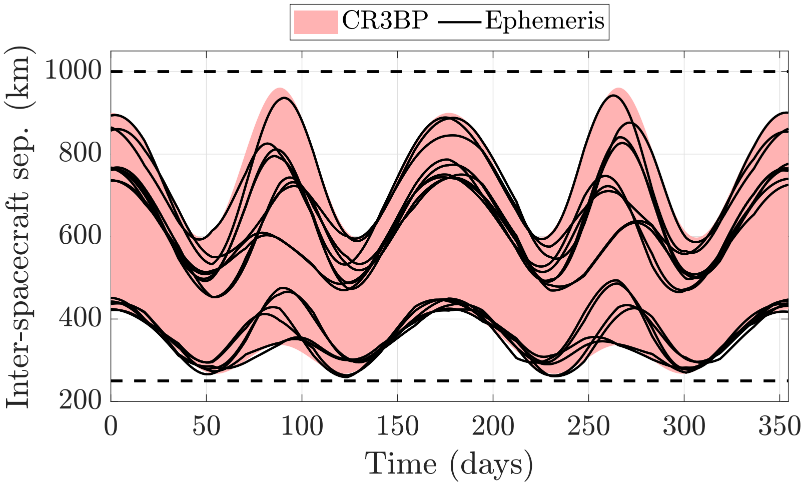

Figure 8.12: Inter-spacecraft separation between constellation spacecraft and the first-order approximation of the possible range of motion in the CR3BP.

Next, the separation distance between each spacecraft and the constellation center reference trajectory is plotted over time in Figure 8.13, represented as six black lines. The approximated range of possible separations of the invariant curve from the reference periodic orbit derived from the CR3BP is also represented in red. The maximum separation predicted by the first-order invariant torus is approximately 481 km. Over the first two revolutions of the simulation of the constellation applying station-keeping control, the maximum separation of any spacecraft from the reference trajectory is 476 km. Furthermore, the minimum separation predicted by the invariant curve is approximately 267 km and the actual minimum over the examined time interval is approximately 265 km. Overall, the bounds on the separation distance between each spacecraft and the reference trajectory is well-predicted by the insight from linearization in the CR3BP.

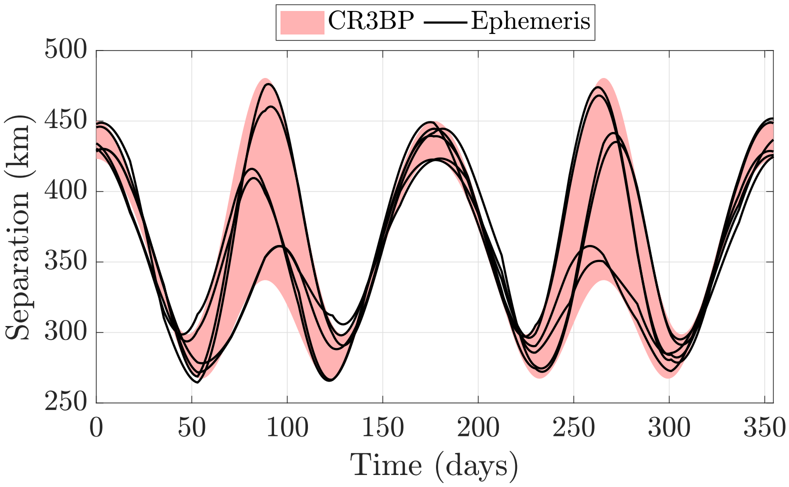

Figure 8.13: Separation between spacecraft and constellation center trajectory and the first-order approximation of the possible range of motion in the CR3BP.

Next, the angle between adjacent spacecraft in the configuration space, ϕ, is assessed for the constellation simulation in the ephemeris model. In Figure 8.14, the angle between adjacent spacecraft in the constellation in the configuration space and measured about the constellation center is plotted over time, represented as six black lines, along with the approximation of possible values of adjacent spacecraft angles in red. The true angle between adjacent spacecraft in the configuration space is observed to be predicted by the approximate angle range to within a maximum error of less than ±5°. Larger angle errors are observed at times where the invariant curve locating the reference motion is nearly-circular, e.g., near times of approximately 140 and 210 days after the initial epoch.

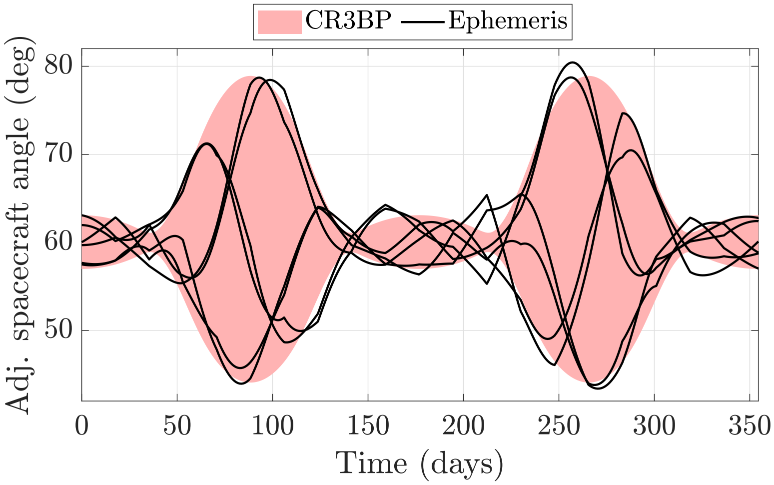

Figure 8.14: Angle in configuration spacecraft between adjacent spacecraft in the spacecraft constellation and first-order approximation of possible angle values in the CR3BP.

Finally, the angle, γ, between the direction normal to the plane spanned by the constellation spacecraft and the $\hat{x}$ axis of the Sun-Earth rotating frame is evaluated. Because the constellation spacecraft in the ephemeris simulation do not exactly span a single plane, the least-squares best-fit plane is used to compute a representative normal vector. Specifically, the best-fit plane is computed using a SVD of the relative positions of the six spacecraft measured from the reference trajectory. Using this approach, the best-fit plane determines the plane that minimizes the Euclidean norm of the separation of each spacecraft from the plane [118]. This angle in the ephemeris simulation is plotted in Figure 8.15 in black, along with the predicted value from the CR3BP, plotted in red. Overall, the value of γ in the ephemeris model simulation is well approximated by the angle computed using the CR3BP.

The evolution of the controlled spacecraft constellation trajectories in the ephemeris model reveal a strong resemblance with the ranges of motion calculated via the first-order analysis in the CR3BP. These analysis illustrate that the inter-spacecraft separation constraint are satisfied

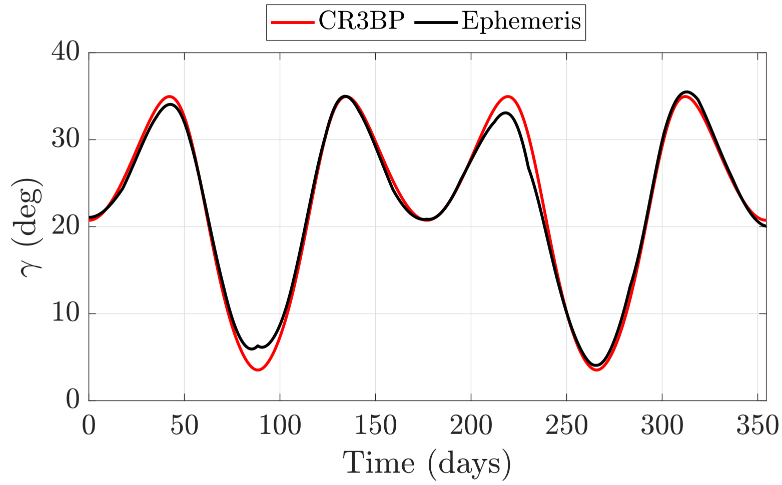

Figure 8.15: Angle between the normal direction of the best-fit plane spanned by the constellation and the $\hat{\boldsymbol{x}}$ axis of the Sun-Earth rotating frame in the ephemeris model and the first-order approximation in the CR3BP.

in the ephemeris model. These results indicate that the predicted ranges of motion developed by analyzing approximated invariant tori in the CR3BP, i.e., separation from the periodic orbit, inter-spacecraft separation, and relative angle in configuration space, may supply useful insight into spacecraft motion in an ephemeris model. The satisfaction of the specified constraints of the design process supports the use of the presented techniques to assist preliminary trajectory design in other high-fidelity models and scenarios. Future applications of this analysis may include more complex constellation designs, including spacecraft located on multiple tori, as well as the incorporation of higher-fidelity constellation design constraints and objectives.

Chapter 9

Conclusions and Recommendations

9.1 Concluding remarks

The design of trajectories relative to periodic orbits in multi-body environments encompasses a large and complex solution space. A key element of relative trajectory design is the capability for spacecraft to leverage bounded, quasi-periodic motions relative to periodic orbits to naturally reduce propellant usage and support collision avoidance considerations. For spacecraft formation flying applications, this motion is well approximated by the center eigenspace of the periodic orbit when the formation is sufficiently close to the periodic orbit. By leveraging the CR3BP and techniques from dynamical systems theory, this investigation introduces new local coordinate systems for the description of spacecraft motion relative to periodic orbit that possess an oscillatory mode. This new framework is used to design strategies for trajectory design and spacecraft control relative to periodic orbits in multi-body environments.

These local coordinate systems are formulated to supply a geometrically-interpretable description of oscillatory relative motion about periodic orbits that possess an oscillatory mode that possesses consistent interpretation across different reference orbits. The geometric local toroidal coordinates including a size coordinate, ε, which, in combination with the presented normalization scheme for the complex eigenvector of the monodromy matrix, serves as a single descriptor for specifying unique first-order approximation of an invariant 2-torus relative to the periodic orbit. While this coordinate helps distinguish between nested tori surrounding a periodic orbit, methods for analyzing the size, shape, and orientation of the instantaneous first-order approximation of an invariant curve in the configuration space are also introduced. The combination of paramterization of invariant 2-tori in the linearized model and better understanding of the range of separation of tori from periodic orbit may support the development of new heuristics for rendezvous and docking procedures near periodic orbits. For example, these heuristics may include the future definition of "safety tori" about space stations following periodic orbits as a analog to the safety ellipsoid currently defined about the International Space Station in low Earth orbit.

In Chapter 5 of this investigation, the evolution of the size and shape of the first-order approximation of the invariant curve relative to periodic orbits of several orbit families in the Sun-Earth and Earth-Moon CR3BP is examined. This survey reveals the complex solution space available to relative trajectory design about periodic orbits leveraging naturally bounded motion on the center eigenspace. The data generated in this survey may be used to support preliminary trajectory design for future spacecraft formations operating in these environments. Additionally, to support future analyses, this investigation details the necessary tools to recreate this type of analysis for different periodic orbit families in the Earth-Moon and Sun-Earth systems, as well as other three-body environments.

To support spacecraft formations operating near periodic orbits, the local toroidal coordinate systems are applied to the derivation of new continuous and impulsive spacecraft control strategies, including perturbations from SRP and models of navigation and thruster errors. Two nonlinear feedback control laws are presented that support tracking of arbitrary relative trajectories to periodic orbits using error terms formulated using the geometric characteristics of invariant 2-torus. An advantage of the formulation of the error terms is the ability to adjust control gains to modify the response of controlled motion in terms of the geometry of nearby invariant 2-tori, i.e., the torus size, angle about the periodic orbit, and separation from the center eigenspace. These control laws support the design of deployment or reconfiguration maneuvers for low-thrust enabled spacecraft between periodic orbits and nearby invariant tori.

In addition to the presented feedback control strategies, an impulsive station-keeping strategy is introduced that enables spacecraft to maintain a desired configuration along the center eigenspace of a periodic orbit via regular impulsive maneuvers. By approximating the state transition matrix evaluated along the periodic orbit between maneuvers and formulated in the nonsingular local toroidal coordinate frame, the strategy is demonstrated to stabilize spacecraft without the computation of the state transition matrix between subsequent maneuvers. This simplification may reduce operational complexity for station-keeping spacecraft and enable future constellations operating near periodic orbits with numerous spacecraft operating in close proximity.

While the presented local toroidal coordinate systems are derived using the CR3BP, the coordinates are demonstrated within higher fidelity, ephemeris models of spacecraft motion. Examples are presented throughout the investigation of the use of the coordinates to design desired relative motion about reference trajectory in the ephemeris model and the application of the presented control strategies to follow these trajectories. Furthermore, these strategies are applied within a comprehensive demonstration of the constrained design of a spacecraft constellation about a Sun-Earth L_1 southern halo orbit. In this example, the trajectory design strategies formulated in the CR3BP are used to rapidly assesses the design space in the approximated model; the resulting motions of the constellation spacecraft in a higher fidelity simulation are observed to satisfy the original design constraints placed on inter-spacecraft separation.

9.2 Recommendations for future investigation

Several items may be worthwhile for future investigation into the development of the presented strategies and applications of the presented trajectory design and control strategies. Recommendations for further investigation into the formulation and study of the presented local coordinate systems include:

- Analysis of a more generalizable and robust process the normalization of the complex eigenvector of the monodromy matrix would mitigate opportunities for issues within the reproduction of trajectories caused by the ambiguity of the eigenvector.
- Modification of the local toroidal coordinate systems to accommodate the construction of

axes using an oscillatory mode with rectilinear motion in the configuration space would support the description of motion in reference to the 2-tori associated with these types of oscillatory modes.

- Investigation into the periodicity of the principal axes directions for the approximated invariant curve may reveal fascinating new understanding of the size and shape of invariant 2-tori and the factors that contribute to their geometry.
- Development of relative state representation constructed using insight into higher dimensional tori that exist relative to stable periodic orbits may reveal new methods for describing oscillatory relative motion that shares similar geometric benefits of the presented toroidal coordinate systems formulated using the first-order approximation of 2-tori.
- Investigation into alternative methods for computing or approximating the complex eigenvector for application in an ephemeris model may reduce the differences observed between relative motion in the ephemeris model and the motion along the center eigenspace of a periodic orbit, particularly for trajectories with close flybys of a primary body.

In addition to these recommendations for the extended development of the presented local coordinate systems, recommendations for future investigations incorporating the presented relative trajectory design and control strategies include:

- Further investigation into the relative state histories of quasi-periodic orbits in the nonlinear CR3BP with respect to a periodic orbit using geometric local toroidal coordinate may reveal insight into the geometry of the nonlinearities of the trajectories.
- Study of the optimization of impulsive transfers between a periodic orbit and invariant torus or between invariant tori using the local toroidal coordinate state description would reveal new insights into optimal orbit phasing and timing for these transfers.

Bibliography

[1] D. Folta and M. Beckman, “Libration orbit mission design: applications of numerical and dynamical methods,” in Libration Point Orbits and Applications, 2002, pp. 85–113.

[2] J. Burt and B. Smith, “Deep space climate observatory: The DSCOVR mission,” in IEEE Aerospace Conference, Big Sky, MT, 2012, https://doi.org/10.1109/AERO.2012.6187025.

[3] J. Gardner, J. Mather, M. Clampin, R. Doyon, M. Greenhouse, H. Hammel, J. Hutchings, P. Jakobsen, S. Lilly, K. Long, J. Lunine, M. Mccaughrean, M. Mountain, J. Nella, G. Rieke, M. Rieke, H.-W. Rix, E. Smith, G. Sonneborn, and G. Wright, “The James Webb Space Telescope,” Space Science Reviews, vol. 123, pp. 485–606, 2009, https://doi.org/10.1007/s11214-006-8315-7.

[4] D. Spergel, N. Gehrels, C. Baltay, D. Bennett, J. Breckinridge, M. Donahue, A. Dressler, B. S. Gaudi, T. Greene, O. Guyon, C. Hirata, J. Kalirai, N. J. Kasdin, B. Macintosh, W. Moos, S. Perlmutter, M. Postman, B. Rauscher, J. Rhodes, Y. Wang, D. Weinberg, D. Benford, M. Hudson, W. S. Jeong, Y. Mellier, W. Traub, T. Yamada, P. Capak, J. Colbert, D. Masters, M. Penny, D. Savransky, D. Stern, N. Zimmerman, R. Barry, L. Bartusek, K. Carpenter, E. Cheng, D. Content, F. Dekens, R. Demers, K. Grady, C. Jackson, G. Kuan, J. Kruk, M. Melton, B. Nemati, B. Parvin, I. Poberezhskiy, C. Peddie, J. Ruffa, J. K. Wallace, A. Whipple, E. Wollack, and F. Zhao, “Wide-field infrared survey telescope-astrophysics focused telescope assets,” 2015, arXiv:1503.03757.

[5] NASA, “Nancy Grace Roman Space Telescope,” 2021. [Online]. Available: https://roman.gsfc.nasa.gov

[6] W. Belvin, B. R. Doggett, J. Watson, J. T. Dorsey, J. Warren, T. C. Jones, E. Komendera, T. Mann, and L. Bowman, “In-space structural assembly: Applications and technology,” in AIAA Spacecraft Structures Conference, 2016.

[7] NASA Goddard Space Flight Center, “On-orbit satellite servicing study,” 2010. [Online]. Available: https://nexis.gsfc.nasa.gov/images/NASA_Satellite%20Servicing_Project_Report_0511.pdf

[8] J. Le Moigne, “Distributed spacecraft missions (DSM) technology development at NASA Goddard Space Flight Center,” in Institute of Electrical and Electronics Engineers International Geoscience and Remote Sensing Symposium, 2018, pp. 293–296, https://doi.org/10.1109/IGARSS.2018.8519065.

[9] A. Farres, C. Webster, and D. Folta, "High fidelity modeling of SRP and its effect on the relative motion of starshade and WFIRST," in AIAA/AAS Space Flight Mechanics Meeting, 2018, https://doi.org/10.2514/6.2018-2227.

[10] NASA Jet Propulsion Laboratory, "Sun radio interferometer space experiment (SunRISE)," 2021. [Online]. Available: https://www.jpl.nasa.gov/missions/sun-radio-interferometer-space-experiment

[11] J. Kasper, J. Lazio, A. Romero-Wolf, J. Lux, and T. Neilsen, "The sun radio interferometer space experiment (SunRISE) mission concept," in 2019 IEEE Aerospace Conference, 2019, pp. 1–11, https://doi.org/10.1109/AERO.2019.8742146.

[12] C. Beichman, G. Gómez, M. Lo, J. Masdemont, and L. Romans, "Searching for life with the terrestrial planet finder: Lagrange point options for a formation flying interferometer," Advances in Space Research, vol. 34, no. 3, pp. 637–644, 2004, https://doi.org/10.1016/j.asr.2003.05.032.

[13] NASA Goddard Space Flight Center, "Microarcsecond x-ray imaging mission (MAXIM)." [Online]. Available: https://blackholeimager.gsfc.nasa.gov/pathfinder.html

[14] K. G. Carpenter, C. J. Schrijver, and M. Karovska, "The stellar imager (SI) vision mission," in SPIE Astronomical Telescopes and Instrumentation, 2006, https://doi.org/10.1117/12.669713.

[15] ESA, "Darwin overview." [Online]. Available: https://www.esa.int/Science_Exploration/Space_Science/Darwin_overview

[16] J. C. Crusan, R. M. Smith, D. A. Craig, J. M. Caram, J. Guidi, M. Gates, J. M. Krezel, and N. B. Herrmann, "Deep space gateway concept: Extending human presence into cislunar space," in IEEE Aerospace Conference. IEEE, 2018, pp. 1–10.

[17] D. E. Lee, "Gateway destination orbit model: A continuous 15 year NRHO reference trajectory," 2019, NASA Technical Report.

[18] NASA, "Gateway," 2021. [Online]. Available: https://www.nasa.gov/gateway/overview

[19] NASA Johnson Space Center, "Gateway: Images," 2021. [Online]. Available: https://www.nasa.gov/gateway/images

[20] A. Verdun, "Leonhard Euler's early lunar theories 1725–1752," Archive for history of exact sciences, vol. 67, no. 5, pp. 477–551, 2013.

[21] J. Vickers, Poincaré and the three body problem, History of Mathematics. American Mathematical Society, 1997, vol. 11.

[22] C. Wilson, "The three-body problem," Companion Encyclopedia of the History and Philosophy of the Mathematical Sciences, vol. 2, pp. 1054–1062, 2004.

[23] V. Szebehely, Theory of Orbits. Academic Press, 1967, https://doi.org/10.1016/B978-0-12-395732-0.50016-7.

[24] W. S. Koon, M. W. Lo, J. E. Marsden, and S. D. Ross, Dynamical Systems, the Three-Body Problem and Space Mission Design. Marsden Books, 2006.

[25] V. Szebehely and G. E. Giacaglia, “On the elliptic restricted problem of three bodies,” The Astronomical Journal, vol. 69, p. 230, 1964.

[26] S. S. Huang, “Very restricted four-body problem,” NASA Technical Note D-501, 1960.

[27] T. A. Pavlak, “Trajectory design and orbit maintenance strategies in multi-body dynamical regimes,” Ph.D. dissertation, Purdue University, West Lafayette, IN, 2013.

[28] N. Bosanac, “Leveraging natural dynamical structures to explore multi-body systems,” Ph.D. dissertation, Purdue University, West Lafayette, IN, 2016.

[29] N. Bosanac, C. M. Webster, K. C. Howell, and D. C. Folta, “Trajectory design for the wide field infrared survey telescope mission,” Journal of Guidance, Control, and Dynamics, vol. 42, no. 9, pp. 1899–1911, 2019, https://doi.org/10.2514/1.G004179.

[30] D. Guzzetti, N. Bosanac, A. Haapala, K. C. Howell, and D. C. Folta, “Rapid trajectory design in the Earth–Moon ephemeris system via an interactive catalog of periodic and quasi-periodic orbits,” Acta Astronautica, vol. 126, pp. 439–455, 2016, https://doi.org/10.1016/j.actaastro.2016.06.029.

[31] R. W. Farquhar, “The utilization of halo orbits in advanced lunar operations,” NASA Technical Note D-6365, 1971.

[32] J. V. Breakwell and J. V. Brown, “The ‘halo’ family of 3-dimensional periodic orbits in the Earth-moon restricted 3-body problem,” Celestial Mechanics, vol. 20, no. 4, pp. 389–404, 1979.

[33] K. C. Howell, “Three-dimensional, periodic, ‘halo’ orbits,” Celestial Mechanics, vol. 32, no. 1, pp. 53–71, 1984.

[34] R. W. Farquhar, D. P. Muhonen, C. R. Newman, and H. S. Heubergerg, “Trajectories and orbital maneuvers for the first libration-point satellite,” Journal of Guidance and Control, vol. 3, no. 6, pp. 549–554, 1980, https://doi.org/10.2514/3.56034.

[35] ESA and NASA, “Solar and Heliospheric Observatory,” 2022. [Online]. Available: https://sohowww.nascom.nasa.gov/

[36] E. C. Stone, A. Frandsen, R. Mewaldt, E. Christian, D. Margolies, J. Ormes, and F. Snow, “The advanced composition explorer,” Space Science Reviews, vol. 86, no. 1, pp. 1–22, 1998.

[37] C. L. Bennett, M. Bay, M. Halpern, G. Hinshaw, C. Jackson, N. Jarosik, A. Kogut, M. Limon, S. S. Meyer, L. Page, D. N. Spergel, G. S. Tucker, D. T. Wilkinson, E. Wollack, and E. L. Wright, “The microwave anisotropy probe mission,” The Astrophysical Journal, vol. 583, no. 1, pp. 1–23, 2003.

[38] J. L. Goodman, “History of space shuttle rendezvous and proximity operations,” Journal of Spacecraft and Rockets, vol. 43, no. 5, pp. 944–959, 2006, https://doi.org/10.2514/1.19653.

[39] K. A. Young and J. D. Alexander, “Apollo lunar rendezvous,” Journal of Spacecraft and Rockets, vol. 7, no. 9, pp. 1083–1086, 1970, https://doi.org/10.2514/3.30106.

[40] H. Schaub and J. Junkins, Analytical Mechanics of Space Systems, 3rd ed., ser. AIAA Education Series. American Institute of Aeronautics and Astronautics, Incorporated, 2014.

[41] K. Alfriend, S. R. Vadali, P. Gurfil, J. How, and L. Breger, Spacecraft Formation Flying: Dynamics, Control and Navigation. Elsevier, 2009, vol. 2.

[42] W. H. Clohessy and R. S. Wiltshire, "Terminal guidance system for satellite rendezvous," Journal of the Aerospace Sciences, vol. 27, no. 9, pp. 653–658, 1960, https://doi.org/10.2514/8.8704.

[43] J. Tschauner and P. Hempel, "Rendezvous zu einem in elliptischer bahn umlaufenden ziel," Acta Astronautica, vol. 11, no. 2, pp. 104–109, 1965.

[44] P. Sengupta and S. R. Vadali, "Relative motion and the geometry of formations in keplerian elliptic orbits with arbitrary eccentricity," Journal of Guidance, Control, and Dynamics, vol. 30, no. 4, pp. 953–964, 2007, https://doi.org/10.2514/1.25941.

[45] T. Bennett and H. Schaub, "Continuous-time modeling and control using nonsingular linearized relative-orbit elements," Journal of Guidance, Control, and Dynamics, vol. 39, no. 12, pp. 2605–2614, 2016, https://doi.org/10.2514/1.G000366.

[46] H. Schaub, "Relative orbit geometry through classical orbit element differences," Journal of Guidance, Control, and Dynamics, vol. 27, no. 5, pp. 839–848, 2004, https://doi.org/10.2514/1.12595.

[47] H. Schaub and K. T. Alfriend, "Impulsive feedback control to establish specific mean orbit elements of spacecraft formations," Journal of Guidance, Control, and Dynamics, vol. 24, no. 4, pp. 739–745, 2001, https://doi.org/10.2514/2.4774.

[48] E. Gill, S. D'Amico, and O. Montenbruck, "Autonomous formation flying for the PRISMA mission," Journal of Spacecraft and Rockets, vol. 44, no. 3, pp. 671–681, 2007, https://doi.org/10.2514/1.23015.

[49] O. Montenbruck, R. Kahle, S. D'Amico, and J.-S. Ardaens, "Navigation and control of the TanDEM-X formation," Journal of the Astronautical Sciences, vol. 56, no. 3, pp. 341–357, 2008, https://doi.org/10.1007/BF03256557.

[50] J. Stuart, A. Dorsey, F. Alibay, and N. Filipe, "Formation flying and position determination for a space-based interferometer in GEO graveyard orbit," in IEEE Aerospace Conference, 2017, pp. 1–19, https://doi.org/10.1109/AERO.2017.7943705.

[51] T. E. Carter, "State transition matrices for terminal rendezvous studies: Brief survey and new example," Journal of Guidance, Control, and Dynamics, vol. 21, no. 1, pp. 148–155, 1998, https://doi.org/10.2514/2.4211.

[52] J. Sullivan, S. Grimberg, and S. D'Amico, "Comprehensive survey and assessment of spacecraft relative motion dynamics models," Journal of Guidance, Control, and Dynamics, vol. 40, no. 8, pp. 1837–1859, 2017, https://doi.org/10.2514/1.G002309.

[53] C. W. T. Roscoe, S. R. Vadali, and K. T. Alfriend, "Third-body perturbation effects on satellite formations," Journal of the Astronautical Sciences, vol. 60, no. 3, pp. 408–433, 2013, https://doi.org/10.1007/s40295-015-0057-x.

[54] M. Bakhtiari, K. Daneshjou, and E. Abbasali, “A new approach to derive a formation flying model in the presence of a perturbing body in inclined elliptical orbit: Relative hovering analysis,” Astrophysics and Space Science, vol. 362, no. 2, p. 36, 2017, https://doi.org/10.1007/s10509-016-2968-9.

[55] P. Gurfil and N. Kasdin, “Stability and control of spacecraft formation flying in trajectories of the restricted three-body problem,” Acta Astronautica, vol. 54, no. 6, pp. 433–453, 2004, https://doi.org/10.1016/S0094-5765(03)00170-X.

[56] R. Luquette and R. Sanner, “Linear state-space representation of the dynamics of relative motion, based on restricted three body dynamics,” in AIAA Guidance, Navigation, and Control Conference and Exhibit, 2004, https://doi.org/10.2514/6.2004-4783.

[57] G. Franzini and M. Innocenti, “Relative motion dynamics in the restricted three-body problem,” Journal of Spacecraft and Rockets, vol. 56, no. 5, pp. 1322–1337, 2019, https://doi.org/10.2514/1.A34390.

[58] J. D. Meiss, Differential Dynamical Systems, 2007, https://doi.org/10.1137/1.9780898718232.ch9.

[59] À. Jorba and J. Villanueva, “Numerical computation of normal forms around some periodic orbits of the restricted three-body problem,” Physica D: Nonlinear Phenomena, vol. 114, no. 3, pp. 197–229, 1998, https://doi.org/10.1016/S0167-2789(97)00194-2.

[60] À. Jorba, “A methodology for the numerical computation of normal forms, centre manifolds and first integrals of Hamiltonian systems,” Experimental Mathematics, vol. 8, no. 2, pp. 155 – 195, 1999, https://doi.org/10.1080/10586458.1999.10504397.

[61] W. E. Wiesel, “Perturbation theory in the vicinity of a periodic orbit by repeated linear transformations,” Celestial Mechanics, vol. 23, no. 3, pp. 231–242, 1981, https://doi.org/10.1007/BF01230728.

[62] W. E. Wiesel and D. J. Pohlen, “Canonical Floquet theory,” Celestial Mechanics and Dynamical Astronomy, vol. 58, no. 1, pp. 81–96, 1994, https://doi.org/10.1007/BF00692119.

[63] W. E. Wiesel and W. Shelton, “Modal control of an unstable periodic orbit,” Journal of the Astronautical Sciences, 1983.

[64] D. P. Scharf, F. Y. Hadaegh, and S. R. Ploen, “A survey of spacecraft formation flying guidance and control (Part I): Guidance,” in Proceedings of the 2003 American Control Conference. IEEE, 2003, pp. 1733–1739.

[65] D. P. Scharf, F. Y. Hadaegh, and S. R. Ploen, “A survey of spacecraft formation flying guidance and control. (Part II): Control,” in Proceedings of the 2004 American Control Conference. IEEE, 2004, pp. 2976–2985.

[66] M. W. Lo, “Satellite-constellation design,” Computing in Science and Engineering, vol. 1, pp. 58–67, 1999, https://doi.org/10.1109/5992.743623.

[67] G. Gómez, J. Masdemont, and C. Simó, “Quasihalo orbits associated with libration points,” Journal of the Astronautical Sciences, vol. 46, no. 2, pp. 135–176, 1998, https://doi.org/10.1007/BF03546241.

[68] À. Jorba and J. Masdemont, "Dynamics in the center manifold of the collinear points of the restricted three body problem," Physica D: Nonlinear Phenomena, vol. 132, no. 1, pp. 189–213, 1999, https://doi.org/10.1016/S0167-2789(99)00042-1.

[69] E. Kolemen, N. Kasdin, and P. Gurfil, "Multiple Poincaré sections method for finding the quasiperiodic orbits of the restricted three body problem," Celestial Mechanics and Dynamical Astronomy, vol. 112, pp. 47–74, 10 2012, https://doi.org/10.1007/s10569-011-9383-x.

[70] Z. P. Olikara and D. J. Scheeres, "Numerical methods for computing quasi-periodic orbits and their stability in the restricted three-body problem," in Advances in the Astronautical Sciences, 2012, pp. 911–930.

[71] B. T. Barden and K. C. Howell, "Fundamental motions near collinear libration points and their transitions," Journal of the Astronautical Sciences, vol. 46, no. 4, pp. 361–378, 1998, https://doi.org/10.1007/BF03546387.

[72] B. T. Barden and K. C. Howell, "Formation flying in the vicinity of libration point orbits," in Advances in the Astronautical Sciences, 1998, pp. 969–988.

[73] B. T. Barden and K. C. Howell, "Dynamical issues associated with relative configurations of multiple spacecraft near the Sun-Earth/Moon L1 point," in AAS/AIAA Astrodynamics Specialist Conference, 1999.

[74] K. C. Howell and B. G. Marchand, "Natural and non-natural spacecraft formations near the L1 and L2 libration points in the Sun-Earth/Moon ephemeris system," Dynamical Systems, vol. 20, no. 1, pp. 149–173, 2005, https://doi.org/10.1080/1468936042000298224.

[75] N. Baresi, D. J. Scheeres, and H. Schaub, "Bounded relative orbits about asteroids for formation flying and applications," Acta Astronautica, vol. 123, pp. 364–375, 2016, https://doi.org/10.1016.

[76] N. Baresi and D. J. Scheeres, "Design of bounded relative trajectories in the Earth zonal problem," Journal of Guidance, Control, and Dynamics, vol. 40, no. 12, pp. 3075–3087, 2017, https://doi.org/10.2514/1.G002603.

[77] W. D. Sanchez, "Towards fuel-efficient formation flying of an observatory and external occulter at Sun-Earth L2," Ph.D. dissertation, Massachusetts Institute of Technology, 2020.

[78] D. B. Henry and D. J. Scheeres, "Expansion maps: Designing relative trajectories on quasi-periodic orbits," Journal of Guidance, Control, and Dynamics, vol. 44, no. 3, pp. 457–468, 2021, https://doi.org/10.2514/1.G005492.

[79] B. P. McCarthy and K. C. Howell, "Leveraging quasi-periodic orbits for trajectory design in cislunar space," Astrodynamics, vol. 5, no. 2, pp. 139–165, 2021, https://doi.org/10.1007/s42064-020-0094-5.

[80] P. Schnizer, E. Fischer, and B. Schnizer, "Cylindrical circular and elliptical, toroidal circular and elliptical multipoles fields, potentials and their measurement for accelerator magnets," 2014, arXiv:1410.8090.

[81] R. D. Hazeltine and J. D. Meiss, Plasma Confinement. Dover Publications, 2003.

[82] P. Schnizer, Advanced Multipoles for Accelerator Magnets: Coordinate Systems. Springer, 2017.

[83] V. Klema and A. Laub, "The singular value decomposition: Its computation and some applications," in IEEE Transactions on Automatic Control, vol. 25, no. 2, 1980, pp. 164–176, https://doi.org/10.1109/TAC.1980.1102314.

[84] C. R. Short, D. Blazevski, K. C. Howell, and G. Haller, "Stretching in phase space and applications in general nonautonomous multi-body problems," Celestial Mechanics and Dynamical Astronomy, vol. 122, p. 213–238, 2015, https://doi.org/10.1007/s10569-015-9617-4.

[85] D. Guzzetti, E. M. Zimovan, K. C. Howell, and D. C. Davis, "Stationkeeping analysis for spacecraft in lunar near rectilinear halo orbits," in 27th AAS/AIAA Space Flight Mechanics Meeting. American Astronautical Society San Antonio, Texas, 2017, pp. 1–20.

[86] V. Muralidharan and K. C. Howell, "Leveraging stretching directions for stationkeeping in earth-moon halo orbits," Advances in Space Research, vol. 69, no. 1, pp. 620–646, 2022, https://doi.org/10.1016/j.asr.2021.10.028.

[87] A. Héritier and K. C. Howell, "Dynamical evolution of natural formations in libration point orbits in a multi-body regime," Acta Astronautica, vol. 102, pp. 332–340, 2014, https://doi.org/10.1016/j.actaastro.2013.10.017.

[88] F.-Y. Hsiao and D. J. Scheeres, "The dynamics of formation flight about a stable trajectory," Journal of the Astronautical Sciences, vol. 50, no. 3, pp. 269–287, 2002, https://doi.org/10.1007/BF03546252.

[89] D. J. Scheeres, F.-Y. Hsiao, and N. X. Vinh, "Stabilizing motion relative to an unstable orbit: Applications to spacecraft formation flight," Journal of Guidance, Control, and Dynamics, vol. 26, no. 1, pp. 62–73, 2003, https://doi.org/10.2514/2.5015.

[90] D. W. Dunham and C. E. Roberts, "Stationkeeping techniques for libration-point satellites," Journal of the Astronautical Sciences, vol. 49, no. 1, pp. 127–144, 2001, https://doi.org/10.1007/BF03546340.

[91] D. Folta, T. Pavlak, K. C. Howell, M. Woodard, and D. Woodfork, "Stationkeeping of lissajous trajectories in the Earth-Moon system with applications to ARTEMIS," in Advances in the Astronautical Sciences, 2010.

[92] M. Shirobokov, S. Trofimov, and M. Ovchinnikov, "Survey of station-keeping techniques for libration point orbits," Journal of Guidance, Control, and Dynamics, vol. 40, no. 5, pp. 1085–1105, 2017, https://doi.org/10.2514/1.G001850.

[93] B. G. Marchand, "Spacecraft formation keeping near the libration points of the Sun-Earth/Moon system," Ph.D. dissertation, Purdue University, West Lafayette, IN, 2004.

[94] B. G. Marchand and K. C. Howell, "Control strategies for formation flight in the vicinity of the libration points," Journal of Guidance, Control, and Dynamics, vol. 28, no. 6, pp. 1210–1219, 2005, https://doi.org/10.2514/1.11016.

[95] L. Millard and K. C. Howell, "Optimal reconfiguration maneuvers for spacecraft imaging arrays in multi-body regimes," Acta Astronautica, vol. 63, pp. 1283–1298, 12 2008, https://doi.org/10.1016/j.actaastro.2008.05.016.

[96] M. Bando and A. Ichikawa, "Formation flying along halo orbit of circular-restricted three-body problem," Journal of Guidance, Control, and Dynamics, vol. 38, no. 1, pp. 123–129, 2015, https://doi.org/10.2514/1.G000463.

[97] R. A. Calico and W. E. Wiesel, "Control of time-periodic systems," Journal of Guidance, Control, and Dynamics, vol. 7, no. 6, pp. 671–676, 1984, https://doi.org/10.2514/3.19911.

[98] K. C. Howell and L. D. Millard, "Control of satellite imaging formations in multi-body regimes," Acta Astronautica, vol. 64, no. 5-6, pp. 554–570, 2009, https://doi.org/10.1016/j.actaastro.2008.10.008.

[99] H. Schaub, S. Vadali, J. Junkins, and K. Alfriend, "Spacecraft formation flying control using mean orbit elements," The Journal of the Astronautical Sciences, vol. 48, pp. 69–87, March 2000, https://doi.org/10.1007/BF03546219.

[100] C. Simó, G. Gómez, J. Llibre, R. Martínez, and J. Rodríguez, "On the optimal station keeping control of halo orbits," Acta Astronautica, vol. 15, no. 6-7, pp. 391–397, 1987, https://doi.org/10.1016/0094-5765(87)90175-5.

[101] A. Farrés and À. Jorba, "A dynamical system approach for the station keeping of a solar sail," The Journal of the Astronautical Sciences, vol. 56, no. 2, pp. 199–230, 2008, https://doi.org/10.1007/BF03256549.

[102] T. Pavlak and K. C. Howell, "Strategy for optimal, long-term stationkeeping of libration point orbits in the earth-moon system," in AIAA/AAS Astrodynamics Specialist Conference, 2012.

[103] K. C. Howell and B. T. Barden, "Trajectory design and stationkeeping for multiple spacecraft in formation near the Sun-Earth L1 point," in IAF 50th International Astronautical Congress., 1999.

[104] R. Qi, S. Xu, and M. Xu, "Impulsive control for formation flight about libration points," Journal of Guidance, Control, and Dynamics, vol. 35, no. 2, pp. 484–496, 2012, https://doi.org/10.2514/1.54383.

[105] K. C. Howell and H. J. Pernicka, "Station-keeping method for libration point trajectories," Journal of Guidance, Control, and Dynamics, vol. 16, no. 1, pp. 151–159, 1993, https://doi.org/10.2514/3.11440.

[106] K. C. Howell and S. Gordon, "Orbit determination error analysis and a station-keeping strategy for Sun-Earth L1 libration point orbits," Journal of the Astronautical Sciences, vol. 42, pp. 207–228, 1994.

[107] D. A. Vallado and W. D. McClain, Fundamentals of Astrodynamics and Applications, 4th ed., ser. Space Technology Library. Microcosm Press, 2013.

[108] I. Elliott and N. Bosanac, "Describing relative motion near periodic orbits via local toroidal coordinates," Celestial Mechanics and Dynamical Astronomy, vol. 134, no. 19, 2022, https://doi.org/10.1007/s10569-022-10074-8.

[109] H. K. Khalil, Nonlinear Systems. Prentice Hall, 2002.

[110] NASA Navigation and Ancillary Information Facility, “SPICE Toolkit,” 2021. [Online]. Available: https://naif.jpl.nasa.gov/naif/aboutspice.html

[111] J. O. Cappellari, C. E. Vélez, and A. J. Fuchs, Mathematical Theory of the Goddard Trajectory Determination System. Goddard Space Flight Center, 1976.

[112] S. P. Hughes, “General Mission Analysis Tool (GMAT),” in International Conference on Astrodynamics Tools and Techniques (ICATT), 2016.

[113] E. J. Doedel, V. A. Romanov, R. C. Paffenroth, H. B. Keller, D. J. Dichmann, J. Galán-Vioque, and A. Vanderbauwhede, “Elemental periodic orbits associated with the libration points in the circular restricted 3-body problem,” International Journal of Bifurcation and Chaos, vol. 17, no. 08, pp. 2625–2677, 2007, https://doi.org/10.1142/S0218127407018671.

[114] B. D. Tapley, B. E. Schutz, and G. H. Born, Statistical Orbit Determination. Burlington: Academic Press, 2004, https://doi.org/10.1016/B978-012683630-1/50023-0.

[115] D. J. Scheeres, Orbital motion in strongly perturbed environments: Applications to asteroid, comet and planetary satellite orbiters. Springer, 2016.

[116] M. J. Bolliger, “Cislunar mission design: Transfers linking near rectilinear halo orbits and the butterfly family,” Master’s thesis, Purdue University, West Lafayette, IN, 2019.

[117] K. C. Howell and T. M. Keeter, “Station-keeping strategies for libration point orbits - target point and floquet mode approaches,” Spaceflight Mechanics 1995, pp. 1377–1396, 1995.

[118] B. Noble and J. W. Daniel, Applied Linear Algebra. Prentice-Hall, 1969.

[119] D. J. Dichmann, R. Lebois, and J. P. Carrico, “Dynamics of orbits near 3:1 resonance in the Earth-Moon system,” Journal of the Astronautical Sciences, vol. 60, no. 1, pp. 51–86, 2013, https://doi.org/10.1007/s40295-014-0009-x.

[120] L. Perko, Differential Equations and Dynamical Systems, 3rd ed. Springer, 2001.

[121] Z. P. Olikara, “Computation of quasi-periodic tori and heteroclinic connections in astrodynamics using collocation techniques,” Ph.D. dissertation, University of Colorado Boulder, Boulder, CO, 2016.

[122] B. P. McCarthy, “Characterization of quasi-periodic orbits for applications in the Sun-Earth and Earth-Moon systems,” Master’s thesis, Purdue University, West Lafayette, IN, 2004.

[123] W. E. Wiesel, “Canonical Floquet theory II: Action-angle variables near conservative periodic orbits,” The Journal of the Astronautical Sciences, vol. 68, no. 2, pp. 391–401, 2021, https://doi.org/10.1007/s40295-021-00258-z.

[124] C. Zwikker, The Advanced Geometry of Plane Curves and Their Applications: The Ellipse. Dover Publications, 1963.

[125] Mathworks, “ode113,” 2021. [Online]. Available: https://www.mathworks.com/help/matlab/ref/ode113.html

[126] GNU Scientific Library, “Ordinary differential equations,” 2021. [Online]. Available: https://www.gnu.org/software/gsl/doc/html/ode-initval.html

[127] NASA Goddard Space Flight Center, “General Mission Analysis Tool,” 2016. [Online]. Available: https://software.nasa.gov/software/GSC-17177-1

[128] R. L. Burden, J. D. Faires, and A. M. Burden, Numerical analysis. Cengage, 2016.

[129] H. B. Keller, “Numerical solution of bifurcation and nonlinear eigenvalue problems.” in Applications of Bifurcation Theory, 1977, pp. 359–384.

[130] W. J. Beyn, A. Champneys, E. Doedel, W. Govaerts, Y. A. Kuznetsov, and B. Sandstede, “Numerical continuation, and computation of normal forms,” in Handbook of dynamical systems III: Towards applications, 2001.

[131] T. A. Pavlak, “Mission design applications in the earth-moon system: Transfer trajectories and stationkeeping,” Master’s thesis, Purdue University, West Lafayette, IN, 2010.

[132] B. J. McCartin, “A matrix analytic approach to conjugate diameters of an ellipse,” Applied Mathematical Sciences, vol. 7, no. 36, pp. 1797–1810, 2013.

[133] J. Townsend, “Differentiating the singular value decomposition,” 2016. [Online]. Available: https://j-towns.github.io/papers/svd-derivative.pdf

[134] M. Seeger, A. Hetzel, Z. Dai, E. Meissner, and N. D. Lawrence, “Auto-differentiating linear algebra,” 2017, arXiv:1710.08717.

[135] H. K. Khalil, Nonlinear Control. Pearson, 2015.

[136] J. R. Wertz, D. F. Everett, and J. J. Puschell, Space Mission Engineering: The New SMAD, ser. Space Technology Library. Microcosm Press, 2011.

[137] L. Markley, “Approximate cartesian state transition matrix,” The Journal of the Astronautical Sciences, vol. 34, no. 2, pp. 161–169, 1986.

[138] B. Sease, J. Myers, J. Lorah, and C. Webster, “Preliminary analysis of ground-based orbit determination accuracy for the wide field infrared survey telescope (WFIRST),” in AAS/AIAA Astrodynamics Specialist Conference, 2017.